NORTHWESTERN UNIVERSITY

# Biomaterials for Orthopaedic Implants and Bone Regeneration

A DISSERTATION

SUBMITTED TO THE GRADUATE SCHOOL
IN PARTIAL FULLFILLMENT OF THE REQUIREMENTS

for the degree

DOCTOR OF PHILOSOPHY

Field of Materials Science & Engineering

By

Timothy David Sargeant

EVANSTON, ILLINOIS

December 2007

# ABSTRACT

**Biomaterials for Orthopaedic Implants and Bone Regeneration**

Timothy David Sargeant

For bone regeneration, there is need for biodegradable, synthetic scaffolds that direct the formation of *de novo* mineralized tissue. Orthopaedic implants additionally require mechanical function. The work described herein attempts to address both of these needs. The general strategy involves integrating molecularly designed tissue engineering scaffolds with porous metallic foams to create hybrid materials to direct cellular behaviour.

Peptide amphiphiles (PAs) that self-assemble into nanofibers were designed to template hydroxyapatite mineral under biological conditions. The molecular design incorporated either serine (S) or phosphoserine S(P) and was mixed with RGDS-bearing PA to evaluate of the key parameters for mineral formation. This led to the discovery of nanoscale hydroxyapatite spheres templated on both S- and S(P)-bearing PA nanofibers. Stem cells were encapsulated in these gels and RT-PCR showed osteoblastic differentiation in all samples. Osteoblast maturation was increased in S-bearing PA compared to S(P)-bearing PA, although the reason is not yet understood.

A method to create robust PA nanofiber coatings on NiTi was developed by optimizing the NiTi oxide surface chemistry, optimizing silane vapor deposition, and covalently attaching the PAs to the silanized substrate. The surfaces were characterized by XPS, SIMS, AFM, and fluorimetry. *In vitro* experiments demonstrated the importance of covalent attachment for cellular adhesion and proved the materials were not cytotoxic.

Orthopaedic hybrid materials were created by triggering PA self-assembly within the interconnected pores of Ti foams developed by the Dunand research group. *In vitro* experiments demonstrate that pre-osteoblasts adhere to, proliferate on, and migrate into PA-Ti hybrids made with S(P)- and RGDS-bearing PA mixtures. The cells differentiate into mature osteoblasts and remain viable up to 28 days.

*In vivo* studies using a rat model demonstrate osteointegration and boney ingrowth into bare Ti foams and PA-Ti hybrids. Histology suggests that the PA-filled Ti foams may improve *de novo* bone formation and boney ingrowth compared to bare Ti foams, particularly with the serine PA, which correlates with the *in vitro* results.

These findings suggest that molecularly designed self-assembling PAs are an excellent system to study biomimetic mineralization and offer potential as an osteogenic material for bone regeneration and orthopaedic implant modification.

# THESIS COMMITTEE

**Thesis Supervisor:**

Samuel I. Stupp ..... Board of Trustees Professor of
Materials Science, Chemistry, and Medicine
Director, Institute for BioNanotechnology in Medicine
Northwestern University

**Thesis Committee:**

L. Catherine Brinson .....Professor of Mechanical Engineering and Materials Science
Northwestern University

David Dunand ..... Professor of Materials Science and Engineering
Northwestern University

Lonnie Shea ..... Associate Professor of Chemical and Biological Engineering
Northwestern University

# ACKNOWLEDGEMENTS

This work could not have been completed without the help of many people. In particular, I would like to thank the following people:

Prof. Samuel I. Stupp, for allowing me to join his research group and work on such an enjoyable and challenging project. He always pushed me to expand my horizons and look at the big picture, and I am grateful for these things.

My committee members, Prof. Dunand, Prof. Brinson, and Prof. Shea, for taking the time to go through my qualification and thesis defense.

The members, past and present, of the Stupp group, who have created a wonderful and fruitful working environment. These include Dr. Erik Spoerke, whose project I eventually took over and who guided me during my first year as a graduate student; Dr. Mukti Rao, who worked with me extensively on the silanization work; Dr. Daniel Harrington, Dr. Hannah Storrie, Dr. James Hulvat, Dr. Jack Donners, and Dr. Krista Niece, who were all invaluable in their help and mentoring; Dr. Mustafa Guler, who made a lot of the PAs used in portions of this work; Dr. Ramille Capito, who has played a huge role in my last year as a graduate student with her tissue engineering expertise, thesis editing, and friendship; Dr. Conrado Aparicio, who worked along side me and performed a lot of the mineralization work, including FT-IR and some SEM; Dr. Alvaro Mata, who tested his skills as an orthopaedic surgeon, and without whom the *in vivo* work would not have happened; Dr. Josh Goldberger and Dr. Honggang Cui for their TEM expertise; Dr. Liam Palmer for paper and thesis reviewing; Shuming Zhang for his help with RT-PCR and many years of thoughtful input; Chung-Yan Koh and Lorraine Hsu for their PA synthesis and purification help; Steve Soukasene, Lesley Chow, and Tommy Pashuck for making the Bio-subgroup an enjoyable and productive group to be in; Christina Newcomb and Stuart Kaltz for their eagerness and quickness to learn and help me wrap up my final experiments; and Jonathan Schwartz, Alok Vij, and Karen Shu, each of whom I had the pleasure of mentoring as undergraduate students during my years in graduate school.

Many Northwester collaborators, colleagues, and staff, including Dr. Scott Oppenheimer from the Dunand group, who supplied all the Ti foam used in this work; Jena Donovan from the Cheng group, who taught me to do cell transfection and always brought a smile to the office;

Andrew Gargus from IBNAM, who did a lot of the *in vivo* histology quantification; Janet Martinez from the Kibbe group, who taught me to do histology; Dr. Sue Crawford and Dr. Philip Fitchev from Pathology for there help with the *in vivo* histology; the wonderful facilities staff at Northwestern University, including Dr. Shuyou Li and Ben Myers (EPIC Staff), Dr. Gajendra Shekhawat (NIFTI Staff), Dr. Nick Wu (Keck II), and Dr. Bill Russin and Ramona Walsh (BIF); the superb staff that have made the Stupp group run, including Donnie Young, Chris Gilchrist and Sharon Jacknow; Alexandra Kolot, Nicole Papariello, and the IBNAM staff who have kept the facility running smoothly amidst all the changes, and the Materials Science and Engineering staff.

I would like to acknowledge my funding from the U.S. Department of Energy, the National Science Foundation, and the National Institutes of Health.

Most importantly, I would like to thank my parents and family, who have always given me unlimited love, support, and opportunity; my wife, Elizabeth, who has been a constant source of strength and encouragement; and Jesus Christ, who has given me all things.

# LIST OF ABBREVIATIONS

AFM – Atomic force microscopy

ALP – Alkaline phosphatase

APDMES – Aminopropyldimethylethoxysilane

APTES – Aminopropyltriethoxysilane

CPAE – Bovine pulmonary artery endothelial cells

EC – Endothelial cells

EDS – Energy dispersive spectroscopy

ESI – Electron spray ionization

FT-IR – Fourier transform infrared spectroscopy

GFP-MC3T3-E1 Cells – MC3T3-E1 cells transfected with GFP

hMSC – Human mesenchymal stem cells

HPLC – High performance liquid chromatography

MC3T3-E1 Cells – Mouse calvarial pre-osteoblastic cells

NiTi – Nickel-titanium

OP – Osteopontin

PA – Peptide Amphiphile

QRT-PCR – Quantitative real-time reverse transcription polymerase chain reaction

RGD(S) – Arginine-Glycine-Aspartic Acid-(Serine)

S – Serine

S(P) – Phosphoserine

SEM – Scanning electron microscopy

SMC – Smooth muscle cells

TEM – Transmission electron microscopy

Ti - Titanium

ToF-SIMS – Time-of-flight secondary ion mass spectroscopy

XPS – X-ray photoelectron spectroscopy

# DEDICATION

*This work is dedicated to*

*my parents, David and Diane Sargeant*

*and my wife, Elizabeth.*

# TABLE OF CONTENTS

**ABSTRACT** ..... **3**

**THESIS COMMITTEE** ..... **4**

**ACKNOWLEDGEMENTS** ..... **5**

**LIST OF ABBREVIATIONS** ..... **7**

**DEDICATION** ..... **8**

**LIST OF FIGURES** ..... **13**

**LIST OF TABLES** ..... **20**

**CHAPTER 1: GENERAL INTRODUCTION** ..... **21**

1.1 Background ..... 21

*1.1.1 Bone replacements and Orthopaedic Implants* ..... *22*
*1.1.2 Biomedical Alloys for Orthopaedic Implants* ..... *24*
*1.1.3 Design Improvements in Orthopaedic Implants* ..... *27*
*1.1.4 Regenerative Medicine & Tissue Engineering* ..... *28*
*1.1.5 Peptide Amphiphiles* ..... *31*

1.2 Experimental Approach ..... 34

*1.2.1 Specific Aims* ..... *35*
*1.2.2 Hypotheses* ..... *36*

**CHAPTER 2: MINERALIZATION OF PEPTIDE AMPHIPHILES FOR BONE APPLICATIONS** ..... **38**

2.1 Introduction ..... 38

2.2 Materials and Methods ..... 40

*2.2.1 Synthesis and Preparation of Peptide Amphiphiles* ..... *40*
*2.2.2 Cell Culture* ..... *40*
*2.2.3 Biological Analysis* ..... *41*
*2.2.4 Mineral Characterization* ..... *42*
*2.2.5 Statistical Analysis* ..... *43*

2.3 Results and Discussion ..... 44

*2.3.1 Mineralization of Peptide Amphiphile Nanofibers* ..... *44*
*2.3.2 Differentiation of hMSCs in Mineralizing Peptide Amphiphile Gels* ..... *57*

2.4 Conclusions ..... 63

**CHAPTER 3: SURFACE MODIFICATION OF METALLIC IMPLANTS WITH PEPTIDE AMPHIPHILES ..... 64**

3.1 Introduction ..... 64

3.2 Materials and Methods ..... 66

*3.2.1 Mechanical and Chemical Preparation of NiTi Substrates ..... 67*
*3.2.2 Vapor Deposition of OrganoSilanes on NiTi Substrates ..... 69*
*3.2.3 Synthesis of Peptide Amphiphiles ..... 71*
*3.2.4 Covalent Attachment of Self-Assembled Peptide Amphiphile Nanofibers on Silanized NiTi Substrates ..... 71*
*3.2.5 X-ray Photoelectron Spectroscopy (XPS) ..... 72*
*3.2.6 Time-of-Flight Secondary Ion Mass Spectroscopy (ToF-SIMS) ..... 72*
*3.2.7 Atomic Force Microscopy (AFM) ..... 73*
*3.2.8 Fluorimetric Analysis of PA Nanofibers Attached on Silanized NiTi ..... 73*
*3.2.9 Cell Quantification Assays on Modified NiTi substrates ..... 74*
*3.2.10 Cell Morphology Assessment by Scanning Electron Microscopy (SEM) ..... 75*
*3.2.11 Statistical Analysis ..... 76*

3.3 Results and Discussion ..... 76

*3.3.1 Optimization of NiTi Surfaces for Silane Coating ..... 76*
*3.3.2 Optimization and Characterization of Vapor Deposited APTES ..... 80*
*3.3.3 Characterization of Optimized APTES Vapor Deposition ..... 83*
*3.3.4 Covalent Attachment of Peptide Amphiphiles ..... 93*
*3.3.5 Cellular Response to PA Coated NiTi Samples ..... 99*

3.4 Conclusions ..... 105

**CHAPTER 4: THE DEVELOPMENT OF PEPTIDE AMPHIPHILE – TITANIUM FOAM (PA-Ti) HYBRIDS FOR BONE APPLICATIONS ..... 107**

4.1 Introduction ..... 107

4.2 Materials and Methods ..... 108

*4.2.1 Ti-6Al-4V Foam Processing ..... 109*
*4.2.2 Peptide Amphiphile Synthesis and Preparation ..... 110*
*4.2.3 Cell Culture Experiments ..... 110*
*4.2.4 PA-Ti Hybrid Preparation ..... 111*
*4.2.5 Cell Encapsulation ..... 112*
*4.2.6 Biological Analysis ..... 112*

4.3 Results and Discussion ..... 114

*4.3.1 Ti-6Al-4V Foam Processing ..... 114*
*4.3.2 Preparation of the PA-Ti Hybrid ..... 116*

*4.3.3 Mineralization of the PA Matrix in PA-Ti Hybrids ..... 119*
*4.3.4 In vitro Assessment of Potential PA Cytotoxicity ..... 121*
*4.3.5 Encapsulation of Cells within Nanofiber Matrix of PA-Ti hybrid ..... 122*

4.4 Conclusions ..... 126

**CHAPTER 5: *IN VITRO* ASSESSMENT OF PA-Ti HYBRIDS USING A ROTATING BIOREACTOR ..... 127**

5.1 Introduction ..... 127

5.2 Materials and Methods ..... 128

*5.2.1 PA-Ti Hybrid Preparation ..... 129*
*5.2.2 Transfection and Culture of GFP-MC3T3-E1 Cells ..... 130*
*5.2.3 Rotating Bioreactor Experiments ..... 131*
*5.2.4 Additional Culture Experiments ..... 131*
*5.2.5 Cell Quantification ..... 132*
*5.2.6 PA-Ti Hybrid Imaging ..... 132*
*5.2.7 Determination of Cell Differentiation ..... 133*
*5.2.8 Statistical Analysis ..... 133*

5.3 Results and Discussion ..... 134

*5.3.1 Cellular Proliferation ..... 134*
*5.3.2 Cellular Colonization of Hybrid ..... 138*
*5.3.3 Cellular Differentiation ..... 144*

5.4 Conclusions ..... 147

**CHAPTER 6: *IN VIVO* ASSESSMENT OF PA-Ti HYBRIDS USING A RAT FEMUR MODEL ..... 149**

6.1 Introduction ..... 149

6.2 Materials and Methods ..... 150

*6.2.1 PA-Ti Hybrid Preparation ..... 151*
*6.2.2 Rat Femur Model and Surgical Technique ..... 152*
*6.2.3 Sample Preparation for Histology ..... 152*
*6.2.4 Sample Preparation for SEM ..... 153*
*6.2.5 Statistical Analysis ..... 153*

6.3 Results and Discussion ..... 155

*6.3.1 SEM Analysis ..... 157*
*6.3.2 Histological Analysis ..... 160*

6.4 Conclusions ..... 175

**FUTURE WORK ..... 176**

**FINAL CONCLUSIONS..... 180**

**REFERENCES..... 185**

**APPENDIX A: PROTOCOLS FOR BIOLOGICAL ASSAYS ..... 200**

**APPENDIX B: RAW DATA FROM *IN VIVO* STUDIES ..... 206**

**VITA..... 208**

# LIST OF FIGURES

Figure 1.1 Schematic of the general chemical structure of a peptide amphiphile (A) and the nanofibers formed by self-assembly in aqueous conditions (B). The PA is composed of 3 segments: a hydrophobic tail that drives self-assembly in water (1), a β-sheet forming peptide sequence that gives the self-assembled structure order (2), and a charged, hydrophilic segment that can be tailored for bioactivity (3). It is the latter portion of the PA (segment 3) that is presented on the exterior of the nanofiber when assembled, as shown in (B). ..... 33

Figure 2.1 Chemical structures of the 3 PAs used to create nanofiber gels: A) net negatively charged serine-bearing PA, B) net negatively charged phosphoserine-bearing PA, and C) net positively charged RGDS-bearing PA. ..... 44

Figure 2.2 SEM images of 10 mM PA gels mineralized for 3 days (left column) and 7 days (right column) in hMSC osteogenic medium supplemented with 20 mM $CaCl_2$ (mineralization medium). From top to bottom, 100% S PA (A, E), 95% S/5% RGDS PA (B, F), 100% S(P) PA (C, G), and 95% S(P)/5% RGDS PA (D, H). All PAs show the formation of spherical nodules of calcium phosphate mineral associated with the PA nanofibers. ..... 46

Figure 2.3 High resolution SEM image of mineralized PA nanofibers. The PA has the amino acid sequence $C_{16}$-VVVAAAEES(P)G and was mineralized under the same conditions as the other PAs used here. The mineral can be clearly seen templated on the nanofibers. Furthermore, the mineral is spherical, not platelike or needlelike as is commonly observed in other systems. Image courtesy of Prof. Conrado Aparicio. ..... 47

Figure 2.4 FT-IR spectra of S(P) PA (A) and S PA (B) mineralized for 2 weeks in hMSC osteogenic medium supplemented with 20 mM $CaCl_2$ (culture medium). Mineralized PA gels were washed to remove medium components and then burned at various temperatures to remove the PA, leaving behind only mineral. Peaks that correspond to the PA (Amide I, II, III) and carbonated hydroxyapatite (C-O, P-O, and P-OH) are indicated. ..... 49

Figure 2.5 TEM images, diffraction patterns, and EDS spectra from mineralized S(P) PA (left) and S PA (right) after washing and burning at 350˚C to remove residual medium components and the PA. The remaining mineral from both PAs each produce a diffraction pattern corresponding to hydroxyapatite..... 52

Figure 2.6 TEM images of embedded and cross-sectioned 10 mM S(P) PA gels mineralized in hMSC osteogenic medium supplemented with 20 mM $CaCl_2$ (culture medium). From top to bottom: S(P) PA mineralized for 24 hours with no stain (A), S(P) PA mineralized for 24 hours with UA stain (B), and S(P) PA mineralized for 72 hours with UA stain (C)..... 54

Figure 2.7 TEM images of embedded and cross-sectioned 10 mM PA gels mineralized for 24 and 72 hours in hMSC osteogenic medium supplemented with 20 mM $CaCl_2$ (culture medium).

All PAs show the formation of mineral along the nanofibers, but mineral formation appears to occur quicker on the S(P)-bearing PA nanofibers (A, E). ..... 55

Figure 2.8 QRT-PCR data for hMSCs cultured in 100% S PA, 95% S/5% RGDS PA, 100% S(P) PA, and 95% S(P)/5% RGDS PA. Samples were assayed for alkaline phosphatase (ALP) gene expression (A) and osteopontin (OP) gene expression (B)..... 59

Figure 2.9 QRT-PCR data for hMSCs cultured on 100% S PA or 100% S(P) PA gels that were pre-mineralized or not. Samples were assayed for alkaline phosphatase (ALP) gene expression (A) and osteopontin (OP) gene expression (B). The results indicate that there is no overall effect of pre-mineralization on ALP or OP gene expression. ..... 60

Figure 2.10 Immunohistochemistry of ALP and OP on cryo-sectioned PA gels with hMSCs cultured for 4 weeks. Dark brown areas, illustrated with arrows, indicate the presence of ALP or OP, respectively. In confirmation of the PCR data, ALP and OP are produced by hMSCs in each of the PA nanofiber gels. ..... 62

Figure 3.1 Image of the Teflon© air tight container and matching custom made sample holder used to vapor deposit silane onto NiTi. ..... 70

Figure 3.2 Quantitative XPS data for the Si content (top) and Ni/Ti ratio (bottom) for NiTi subjected to various plasma and acid treatments, followed by vapor deposition of APDMES.... 79

Figure 3.3 Quantitative SIMS data for the Si peak, normalized to the Ti + Ni peaks, for NiTi subjected to various plasma and acid treatments, followed by vapor deposition of APDMES.... 79

Figure 3.4 Schematic of the reaction that occurs between the hydroxyl groups present in the NiTi surface oxide and the ethoxy groups on the silane. The advantage of using APTES is the reaction of adjacent molecules to create a polymerized network, making the coating more robust and decreasing the rate of hydrolysis at the NiTi interface. ..... 82

Figure 3.5 Quantitative SIMS of b$H_2O$ treated NiTi subjected to vapor deposition of APDMES at varying times and temperatures. ..... 82

Figure 3.6 Quantitative SIMS of APTES and b$H_2O$ NiTi fragments after vapor deposition of APTES onto b$H_2O$-treated NiTi for various times. ..... 83

Figure 3.7 Typical XPS survey spectra of T and ST NiTi surface showing observed elements. 85

Figure 3.8 High resolution XPS spectra for Oxygen 1s for T NiTi surface (left) and ST NiTi surface (right). Dotted lines indicate smoothed spectra, dashed lines indicate deconvoluted peaks, and solid lines indicate sum of deconvoluted peaks. ..... 87

Figure 3.9 SIMS spectra of T NiTi surface (dashed) and ST NiTi surface (solid) normalized so maximum counts are equal for comparison. ..... 89

Figure 3.10 AFM images of P NiTi surface (A), T NiTi (B), and ST NiTi surface (C) showing topography changes after acid treatment and then APTES vapor deposition. ..... 92

Figure 3.11 Chemical structures of APTES (A), the peptide amphiphile (PA) used for AFM, SEM, and biological assays (B), the peptide amphiphile (pyr-PA) used for the fluorimetry assay and AFM (C), and schematics for the various NiTi surfaces obtained in the process to create covalently bound PA nanofibers substrates (D-F). ..... 95

Figure 3.12 AFM images of ST (A), C16-RGDS PA as DC-PA (B) and CA-PA (C), ST+CA (D), and pyr-RGDS PA as DC-PA (E) and CA-PA (F). B & C and E & F show that the PA nanofiber structure is maintained after covalent attachment. D is a control to show no change in topography due the covalent attachment process. ..... 96

Figure 3.13 Fluorimetry spectra of pyr-PA coatings on NiTi. Graph (A) shows the spectra for ST NiTi and a typical DC-PA NiTi sample (left scale bar), and the pyr-PA in solution (right scale bar). Upon self-assembly of the PA molecules when dried on the NiTi, an excimer signal is observed. Graph (B) shows the elimination of the characteristic pyr-PA signal after washing DC-PA, while graph (C) shows conservation of the pyr-PA excimer signal after washing CA-PA, indicating the covalent coupling reaction enabled the retention of assembled pyr-PA on the NiTi. ..... 99

Figure 3.14 7-day CyQuant® proliferation assay results for MC3T3-E1 and CPAE cells on various modified NiTi substrates (A) and quantification by CyQuant® assay for the number of cells detached during medium changing (B). In (A), DC-PA and T+PA are both significantly different from T, ST, ST+CA, and CA-PA ($P<0.01$). T+PA is also significantly different from DC-PA ($P<0.05$). In (B), DC-PA is significantly different from T and CA-PA at day 1 ($P<0.05$) and day 3 ($P<0.01$). ..... 101

Figure 3.15 SEM images of MC3T3-E1 cells (top row) and CPAE cells (bottom row) on NiTi: (A, F) T; (B, G) ST; (C, H) DC-PA; (D, I) CA-PA, and (E, J) ST+CA, all showing initial attachment and spreading after cell seeding. ..... 102

Figure 3.16 SEM images of MC3T3-E1 (top row) and CPAE (bottom row) cells on NiTi: (A, E) T, Day 3; (B, F) CA-PA, Day 3; (C, G) DC-PA, Day 3; (D, H) CA-PA, Day 7. There is a drastic reduction in cell attachment when the PA nanofibers are not covalently bound to the silanized NiTi (DC-PA), whereas cells attach and grow to confluency on the CA-PA surfaces. ..... 103

Figure 4.1 SEM micrograph of polished, bare Ti-6Al-4V foam in cross-section. The mean line intercept was 110 μm, corresponding to a pore diameter of 165 μm. The pores are irregular in shape and equiaxed, showing no preferential orientation. ..... 115

Figure 4.2 (A) Chemical structure of the peptide amphiphile (PA) used to infiltrate and fill the pores of the Ti-6Al-4V foam. Scanning electron microscopy (SEM) images of (B) the bare Ti-6Al-4V foam; (C) Ti-6Al-4V foam filled with PA gel; (D) higher magnification of the self-assembled PA nanofibers forming a three dimensional matrix within the pores; and (E) higher magnification of the PA coating the Ti-6Al-4V foam surface and filling the pores. ..... 117

Figure 4.3 Chemical structure of the biotinylated PA used for the confocal microscopy without cells (A), and the resulting confocal microscopy images of the biotinylated PA-Ti hybrids embedded in acrylic and cross-sectioned, showing (B) the fluorescence of avidin-FITC bound to biotinylated PA gelled throughout the cross-section of Ti-6Al-4V foam, (C) no fluorescence from a control sample of Ti-6Al-4V foam and biotin-PA without avidin-FITC, and (D) no fluorescence from a second control of Ti-6Al-4V in acrylic without PA..... 119

Figure 4.4 Chemical structures of the S(P) PA and RGDS PA used to create PA-Ti Hybrids for mineralization (A, B). SEM images (C-E) show nanoscale bead-like mineral formation on the PA nanofibers. High magnification images (D-E) show the mineral formation only on the nanofibers, and not on the metal surface, indicating templating by the PA nanofibers. EDS quantification reveals a Ca:P ratio for the mineral as 1.71+/-0.18, in line with hydroxyapatite. 120

Figure 4.5 Optical (A) and fluorescence (B) microscopy images of non-transfected MC3T3-E1 cells encapsulated within the nanofiber matrix of the PA shown in Figure 2(A). Almost all cells fluoresced green due to the conversion of calcein AM to calcein, indicative of live cells. The hazy red areas are background fluorescence due to the interaction of the PA with EthD-1..... 121

Figure 4.6 Quantification of cells encapsulated within PA-Ti hybrids at different seeding densities, showing a direct correlation between seeding density and encapsulated cell number. ..... 123

Figure 4.7 SEM of GFP-transfected MC3T3-E1 cells encapsulated within PA-Ti hybrids. Cells encapsulated near the surface of the PA gel can be visualized spreading and pulling on the nanofibers presenting the RGDS cellular adhesion motif..... 125

Figure 4.8 Confocal microscopy of GFP-transfected MC3T3-E1 cells encapsulated within PA-Ti hybrids (cross-section). Left image is reflectance mode, while right image is fluorescence, showing cell suspended in an interior pore. The metal shows artificial fluorescence due to reflectance at the wavelength collected. The difference between the images is the true fluorescence of the cells, indicated by the arrows. ..... 125

Figure 5.1 Structure of the peptide amphiphiles used to create the hybrid bone implant materials. Top: a phosphoserine-bearing PA used as a "filler" PA. Bottom: an RGDS-bearing PA for cellular adhesion. ..... 134

Figure 5.2 Cell quantification as a function of days cultured on PA-Ti hybrids in a rotating bioreactor, n=8. There is a statistical effect of time on cell number ($\alpha$=0.05, P=1.00). At particular time points, significant differences are indicated by asterisks ($\alpha$=0.05). There appears to be a critical cell density that is reached between 2 and 3 weeks, with a mean value of $3.6 \times 10^5$ cells at day 28..... 135

Figure 5.3 Cell quantification assay of MC3T3-E1 cells cultured in PA gels without RGDS epitopes. The assay was performed using the same concentrations of S(P) PA (A) as in Figure 2, but instead mixed with a PA with a non-specific epitope (B). The non-statistically different

results at day 14 confirm that the increase in cell proliferation in the PA-Ti hybrids is due to the RGDS epitope presentation, and is not a function of the S(P) residues. ..... 137

Figure 5.4 SEM images of MC3T3-E1 pre-osteoblastic cells cultured for 1 day on 15% RGDS PA-Ti hybrids in a rotating bioreactor. Image A shows cells, indicated by arrows, spread on the exterior of the hybrid. Image B shows a high magnification of the boxed area in image A, illustrating the filopodia of the cell reaching out to the underlying PA nanofibers..... 139

Figure 5.5 SEM images of 15% RGDS PA-Ti hybrids cultured for 1 (A), 7 (B) and 21 (C) days. After 1 day of culture, cells have adhered and begin to spread on the exterior of the hybrids (A). By day 7, the cells have covered a significant amount of the hybrid exterior (B). By day 21, the exterior of the implant is completely covered with cells (C)..... 140

Figure 5.6 SEM images of MC3T3-E1 pre-osteoblastic cells cultured for 7 days on 15% RGDS PA-Ti hybrids in a rotating bioreactor. Image A shows a cell that is stretched across a gap and adhering to the PA matrix, indicated with arrows. Image B shows a cell that is migrating into the PA matrix-filled porosity of the PA-Ti hybrid (arrow). ..... 142

Figure 5.7 Confocal fluorescent images of cross-sectioned 15% RGDS PA-Ti hybrids at days 1, 7, and 28 showing GFP-transfected MC3T3-E1 pre-osteoblastic cellular ingrowth and proliferation. The cells are shown in green, with the top surface of the metal reflecting white, and the PA matrix not visible. As seen at day 1 (shown left), cells adhere to the exterior of the implant and proceed to migrate and proliferate into the core of the PA-Ti hybrid up to 28 days (shown right), where cells are observed both adjacent to the pore wall as well as in the PA matrix in the center of the pores..... 143

Figure 5.8 Alkaline phosphatase (ALP) and osteocalcin (OC) expression as a function of days cultured in a bioreactor, n=4. There is a significant effect of time on both ALP production ($\alpha$=0.05, P=0.9719) and OC production ($\alpha$=0.05, P=1.00). The data indicates the maturation of the pre-osteoblasts into mature osteoblasts as evident by the decrease in ALP expression and increase in OC expression..... 147

Figure 6.1 Chemical structures of the 3 PAs used to create PA-Ti hybrids for the *in vivo* rat femur model. Two hybrids were used: 1) 95% S(P) PA with 5% RGDS PA, and 2) 95% S PA with 5% RGDS PA. ..... 154

Figure 6.2 Schematic illustrating the sample preparation for imaging by SEM of the intact Ti foams and hybrids with cross-sectioned femur. SEM images are taken from the “Front View”. ..... 155

Figure 6.3 Schematic of the site of implantation (left) and an image of the actual surgical site (right). Ti foam and hybrid implants were positioned inside 2 mm diameter holes that were ~ 1.5 cm apart..... 156

Figure 6.4 SEM image of a sectioned bare Ti foam implanted in a rat femur, demonstrating the placement of the implant. Bone marrow can be seen (bright contrast) in the core of the

diaphysis, and soft tissue can be seen at the top of the implant on the exterior of the bone (arrow)..... 158

Figure 6.5 SEM images of S(P)/RGDS PA-Ti hybrid illustrating the attachment and migration of cells to the implant, and the deposition of ECM and proteins on the surface. Image A shows the implant positioned adjacent to cortical bone (right side) and the soft tissue attached to the outer surface (top side). Image B show many cells adhering and spreading on the implant surface. Image C shows cells migrating into the porosity of the implant (center). ..... 159

Figure 6.6 Histological images of bare Ti foams implanted into a rat femur for 2 (A) and 4 (B) weeks. The plastic embedded sections are stained with methylene blue and basic fuchsin. The images show *de novo* bone growing from the adjacent cortical bone towards the implant, making direct contact with the Ti foam and also forming a rim around the implant. ..... 161

Figure 6.7 Images of histological sections of a S(P)/RGDS PA-Ti hybrid implanted in a rat femur after 4 weeks. Non-decalcified, plastic embedded samples were stained with Goldner's Trichrome. When staining bone, green indicates highly mineralized bone; red indicates newly formed, immature bone. As seen in Image A, new, mineralized bone is seen growing from the cortical bone (CM) towards the PA-Ti hybrid in the bone marrow (BM), and infiltrating the open porosity (arrows). Image B shows newly formed, fully mineralized bone adherent to the PA-Ti hybrid exterior. An artery (A) is observed adjacent to the implant, indicating neo-vascularization around the PA-Ti hybrid. ..... 163

Figure 6.8 Images of histological sections of a S(P)/RGDS PA-Ti hybrid implanted in a rat femur after 4 weeks. Non-decalcified, plastic embedded samples were stained with methylene blue and basic fuchsin. Image A shows mineralized bone formation (blue) within an interior pore of the PA-Ti hybrid. Image B shows new bone formation adjacent to and into the PA-Ti hybrid. The location and formation of these bone spicules are evidence of osteoconduction, with new mineralized bone (NMB, deep blue) on the exterior, new unmineralized bone (NUB, pink) in the middle, and collagenous fibers (C) against the PA-Ti hybrid. ..... 164

Figure 6.9 Histological image of S(P)/RGDS PA-Ti hybrid after 2 weeks implantation. Goldner's Trichrome stain demonstrates the *de novo* bone formation commonly observed in the bone marrow in association with PA matrix (left). The cortical bone has grown into direct with the hybrid implant, and infiltrates the PA filled porosity (right). ..... 166

Figure 6.10 Histological image of each sample after 4 weeks of implantation. New bone formation is observed to form around the implants, both adjacent to the cortical bone and often in the bone marrow. The *de novo* bone makes direct contact with the bare Ti foam, but often is observed to be separated by collagenous tissue (left). More often with the hybrid implants (middle and right), the *de novo* bone makes increased direct contact with the implant, infiltrating the porous implant..... 167

Figure 6.11 Quantification of the new tissue formed within the porosity of the implants. After 2 weeks of implantation, the S/RGDS PA-Ti hybrid had significantly more tissue ingrowth than

the S(P)/RGDS PA-Ti hybrid and the bare Ti foam. By 4 weeks of implantation, there is no significant difference between the different implants..... 170

Figure 6.12 Quantification of the new tissue formed adjacent to the exterior of the implants from the cortical bone. After 2 weeks of implantation, the S/RGDS PA-Ti hybrid had significantly higher new tissue rimming the implant compared to the bare Ti foam. By 4 weeks of implantation, there is no significant difference between the different implants. ..... 171

Figure 6.13 Quantification of the total new bone formed in and around the implants, including in the bone marrow. The numbers represent the average of the best histological image for each sample, normalized to the bare Ti foams at week 2 (n=5-6). Error bars represent 95% confidence interval (α=0.05). ..... 172

# LIST OF TABLES

Table 1.1 Mechanical properties of orthopaedic implant materials and cortical bone ..... 26

Table 3.1 Nomenclature used for NiTi samples ..... 67

Table 3.2 Physical and chemical treatments for NiTi surface modification. ..... 68

Table 3.3 Parameters for silane coating optimization experiments ..... 70

Table 3.4 XPS characterizations of P and T NiTi, both before and after silanization (SP and ST). Numbers in brackets indicate 95% confidence interval. ..... 85

Table 3.5 Characteristic XPS binding energies of Ni, O, and Ti for P, T, SP, and ST NiTi surfaces, and the proposed assignments to surface functionalities. Numbers in brackets indicate standard deviation. ..... 86

# CHAPTER 1: GENERAL INTRODUCTION

## *1.1 Background*

While the study of biomaterials has only existed as we know it since the middle of the twentieth century, there is evidence that humans have used non-biological materials to repair bodily function for thousands of years[1]. There is evidence of the use of sutures by people nearly 32000 years ago, then the early Egyptians, and the Europeans in the Middle Ages; dental implants were implemented as early as 600 A.D. by the Mayans; Leonardo DaVinci conceptualized contact lenses in 1508, which was later made a reality by Adolf Fick around 1860[1]. However, without an understanding of biocompatibility and sterility, most implants prior to the 1950's were most likely unsuccessful. This led to the idea of creating materials that would meet the functional requirements without eliciting a negative biological response[2]. These "first generation" modern biomaterials typically took materials developed for other applications and were intended to be *bioinert*. In the last few decades of the twentieth century, advancements in the understanding of the biological-material relationship led to the development of "second generation" biomaterials capable of eliciting a desired response from the host tissue. These *bioactive* materials included the creation of bioglasses and ceramics for orthopaedic and dental implants; implantable polymers for controlled, local drug release; and biodegradable materials for applications such as sutures[2]. Recently, progress has been made in the development of "third generation" biomaterials, which combine engineered surfaces and bulk properties to control the interaction with the host tissue at the molecular level and regenerate functional tissue[2]. Facilitated by the overlapping advancements in biological understanding, engineering

nanotechnology, and chemistry, we have entered the era of regenerative medicine and tissue engineering. The work described herein attempts to add to the development of the "third generation" of biomaterials in the overlapping areas of bone regeneration and orthopaedic implants. The strategy is two-fold, including the development of novel tissue engineering scaffolds using molecular design for bone regeneration, and using them to create hybrid materials for orthopaedic implants capable of directing cellular behaviour.

### 1.1.1 Bone replacements and Orthopaedic Implants

The orthopaedic implant and bone graft market is extremely large; in the United States alone, over 1 million bone restoration surgeries[3] and approximately 500 000 bone graft procedures[4] are performed annually. Globally, orthopaedic sales reached approximately $14 billion in 2002, which is expected to grow at an annual rate of 7-9%[5]. This represents about 700 000 hip and knee replacement surgeries, respectively[5]. With the life expectancy increasing in most parts of the world and an increasing number of skeletal injuries to younger people, these numbers are expected to increase with time.

The current gold standard for bone replacement is the autologous bone graft, in which bone from another area of the patient, such as the iliac crest, is harvested and implanted at the site of the defect[6]. A second option is an allograft, in which bone from a human cadaver is harvested and implanted in the patient. In both cases, the cancellous bone being transplanted is osteoconductive, being composed of collagen and hydroxyapatite, and contains stromal cells that can differentiate along the osteoblastic lineage; cortical bone has better mechanical properties, but is less osteoconductive[6]. However, there are several limitations with both approaches. Autografts are limited to how much bone can be harvested, and can result in complications with

donor site morbidity and pain. Allografts are limited by the number of donors available and the need for immune suppressants, which can lead to severe illness for the recipient. Alternatives are limited, but include a variety of bioceramics, such as bioinert ceramics (alumina and zirconia), bioactive ceramics (Bioglass and synthetic hydroxyapatite), and bioabsorbable ceramics (tricalcium phosphate and calcium carbonate)[7]. Therefore, there is significant need to create materials that could effectively fill bone defects, be fully resorbable, and encourage the remodeling and formation of new bone.

Alternatively, fractures and joint damage often require the used of orthopaedic implants. There are two categories of orthopaedic implants: fracture fixation devices (fracture plates, spinal fixation devices, pins, screws, etc.) and joint replacements (arthroplasties of the hip, knee, finger, etc.)[5]. Fracture fixation devices composed of bioinert materials have been fairly successful, but could be improved with the development of fully resorbing materials that would be replaced with natural tissue. Common ailments for patients with implanted fixation devices include sensitivity to temperature change and sometimes hypersensitivity to the materials used. Joint replacements have also been successful, but are subject to limited life spans due to several methods of failure. The primary issue is often loosening of the implant. Fixation is commonly achieved using PMMA-based bone cement[8], which is effective in terms of practical implantation, but results in implant loosening over time due to degradation and can cause damage to the host tissue due to the exothermic reaction associated with the setting of the PMMA. Consequently, several approaches to make porous coatings have been attempted to allow for direct tissue ingrowth, thereby fixing the implant in place. While this appears to be a better approach in the long term, a longer recovery time for the patient is required to allow for bone growth into the

implant. A second cause of implant loosening is the effect of stress-shielding. When a load is applied to an appendage, an implant material with a higher modulus will carry a higher portion of the load than the adjacent bone, which is more compliant. This so called stress-shielding phenomena results in bone resorption adjacent to the implant due to Wolff's law of bone remodeling[9]. Therefore, it would be desirable to create a material that would promote bone ingrowth for fixation and that would have a modulus much closer to that of the host tissue.

While the ideal requirements for materials for bone regeneration and orthopaedic implants appear to be significantly different, there is a surprising degree of overlap. In both cases we wish to fill space with a material that would direct cellular growth, encourage differentiation along the osteoblastic lineage, and promote mineralization towards bone regeneration. This is the aim of regenerative medicine and tissue engineering, which will be introduced later. The fundamental difference, however, lies in the mechanical function required. In the case of bone regeneration, external fixation could be used to meet these requirements. However, in the case of joint replacement, a functional load-bearing implant still appears to be necessary. To meet these structural requirements, the best choice remains metal alloys.

### 1.1.2 Biomedical Alloys for Orthopaedic Implants

Metals have been used as an orthopaedic implant material for many years due to their superior mechanical properties[10]. In contrast to polymers, which have low yield strengths and poor fatigue strengths, and ceramics, which are brittle and poor in tension, metals offers a excellent combination of yield strength, fatigue strength, and the ability to plastically deform prior to failure. When considering a material for a biomedical application, the biocompatibility of the alloy must also be taken into account. Consequently, three groups of alloys have been

used primarily in the twentieth century for implant fabrication. These are stainless steels (SS), cobalt chrome (CoCr) alloys, and titanium (Ti) alloys. Some important mechanical properties related to orthopaedic implant applications are shown in Table 1.1. The earliest implants were made from stainless steel for its known corrosion resistance and good mechanical properties in other applications. As an off-the-shelf material, it was a good starting place, and a number of SS alloys are still used today for a variety implants, including bone plates and screws, joint replacements, wires, and sutures, among others[10]. In the 1930's CoCr alloys began to be used as dental materials, and later as orthopaedic implants, due to their increased strength and corrosion resistance[10]. However, as the understanding of biocompatibility and the effect of stress-shielding developed, Ti and Ti-based alloys began to be used for many biomedical applications.

Titanium and its alloys appear to be the best metal for many implant applications due to its superior biocompatibility, lower modulus, and increased corrosion resistance compared to SS and CoCr alloys[10]. In addition, Ti has good fatigue strength and a high strength-to-weight ratio. Ti forms a spontaneous, very stable oxide film on its surface in oxygen-rich environments, including physiological fluids at body temperature. This means that even if an implant is nicked or scratched during a surgical procedure, the inert oxide film will re-grow *in situ*. Indeed, it is this $TiO_2$ oxide that makes Ti so biocompatible, passivating the material[8] and limiting diffusion of the metallic ions, allowing the formation of much thinner fibrous capsules, if any, around an implant[11]. This has led to the common use of commercially pure Ti and several alloys, including the stronger Ti-6Al-4V alloy, for many orthopaedic implants, such as the modular components of joint replacements and many long-term, permanent devices[10]. However, Ti and its alloys are not the best material for all applications, such as bone nails and the acetabular component of a hip

implant, due to its poor shear strength and its propensity to gall or seize in sliding contact with metals[8].

**Table 1.1 Mechanical properties of orthopaedic implant materials and cortical bone**

| Material | Young's Modulus (GPa) | Ultimate Tensile Strength (MPa) | Fracture Toughness (MPa √m) |
|---|---|---|---|
| Austenitic stainless steel[10] | 200 | 540-1000 | ~100 |
| Cobalt-chromium alloys[10] | 230 | 900-1540 | ~100 |
| Ti-6Al-4V[10] | 106 | 900 | ~80 |
| Ti-6Al-4V foam (~41-47% porous)[12, 13] | 23-39 | --- | --- |
| Austenitic Equimolar nickel-titanium alloy (NiTi)[10] | 83 | 895 | --- |
| NiTi foam (20, 16% porous)[14, 15] | 6-12, 15-25 | --- | --- |
| Cortical bone[10] | 7-30 | 50-150 | 2-12 |

More recently, nickel-titanium (NiTi) alloys have been studied and used for biomedical applications. First discovered by Buehler and Wiley at the U.S. Naval Ordinance Laboratory[16], equiatomic NiTi (Nitinol®) was observed to exhibit a unique shape memory effect (SME)[8, 17, 18]. Resulting from its diffusionless transition from austenitic to martensitic phases[8], the SME is manifested in several ways, including superelasticity, one-way shape memory, and two-way shape memory. This makes NiTi very attractive for implants such as stents, where the implant can be designed to expand to fit and maintain residual forces when placed in the artery, rather than relying on a balloon catheter to expand a typical SS stent. Additionally, NiTi has great potential as a material for bone plates, which can be made to shrink in length after warming up body temperature after implantation, creating a press-fit for a fracture that is not possible with

traditional metal plates. For hip and other joint replacements, the superelastic behaviour and lower modulus could help to increase the fatigue life and minimize the stress-shielding effect, respectively. Before NiTi was well known in the biomedical field, there was initial concern that nickel, an element with known toxicity, would leach out of the material and elicit a local and/or systemic cytotoxic effect. However, due to the spontaneous Ti-rich oxide that forms on NiTi surfaces, it has been shown to exhibit good biocompatibility, reported to be as good or better than SS and CoCr and comparable to titanium[19-24]. NiTi alloys also have lower moduli than these other metals (Table 1.1), and can be tougher and more resilient than SS or CoCr alloys[8]. Furthermore, NiTi exhibits other useful properties, such as a high damping coefficient, and good fatigue resistance.

### 1.1.3 Design Improvements in Orthopaedic Implants

Although there have been successful advancements in the design of orthopaedic implants, implant loosening due to stress-shielding and imperfect fixation remain a challenge. While the use of Ti alloys or NiTi will improve stress-shielding compared to SS or CoCr alloys, there still remains a considerable moduli mismatch compared with bone. Additionally, there is an inherent problem with bone cement fixation. A solution that addresses both of these concerns is a porous implant. A number of studies have been concerned with the design of metallic foams that have porosity throughout the entire structure, including Ti alloys[25-29] and NiTi alloys[30-34]. The advantage of this approach is the combined decrease in modulus associated with foam structures in addition to the ability for fixation via boney ingrowth. A variety of methods have been attempted, including variations of powder sintering[26, 27, 29], leaching of a space holding material[28], and expansion of gas that is entrapped within a densified powder[35]. This latter

technique was later improved by the Dunand group[36] to increase the kinetics of foaming and the total porosity by utilizing the superplasticity associated with the allotropic transformation of Ti and its alloys by using thermal cycling. Using this technique, their group has produced foams of commercially pure Ti[36-38] and Ti-6Al-4V[39-41] at porosities up to 45-50%. Similarly, but with the exception of not being able to use the superplasticity as with the Ti alloys, they have produced NiTi foam with porosity up to ~20% that maintains its shape memory properties[42]. The benefits of this approach include the purity of the resulting foam, the ability to increase porosity beyond that of conventional foaming techniques, and good mechanical properties, including a modulus that approximates that of bone (as shown in Table 1.1).

Given the beneficial properties of NiTi alloys and Ti/NiTi foams, it would be very beneficial to incorporate these materials into the design of orthopaedic implants. However, these materials remain bioinert at best, and while they *allow* for fixation via boney ingrowth, they do not *promote* boney ingrowth. A better approach would be to use these metals in conjunction with materials designed to *direct* cellular behaviour using regenerative medicine and tissue engineering strategies.

### 1.1.4 Regenerative Medicine & Tissue Engineering

The idealized concepts of tissue engineering and regenerative medicine combine the use of scaffolds/extracellular matrix (ECM), signaling molecules/bioactive factors, and cells together to regenerate normal and functional tissue[43]. The scaffold provides creates a 3D space for cells to migrate, proliferate, and differentiate into the desired tissue. Additionally, scaffolds can be used to present, deliver, and release bioactive factors[44]. The ideal scaffold for tissue engineering would include the following criteria: high volume, interconnected porosity for cell growth and

flow transport of nutrients and waste; biocompatible with controlled biodegradation to match tissue growth; surface chemistry suitable to direct cell attachment, proliferation, and differentiation; and mechanical properties matching those of the host tissue[45]. Numerous approaches have been investigated, including natural ECM or components of ECM (such as collagen, hyaluronic acid, alginate, etc.), non-ECM natural molecules (such as fibrinogen and thrombin), synthetic polymers (such as poly(L-lactic acid) (PLLA), poly(glycolic acid) (PGA), etc.), ceramics (such as hydroxyapatite, β-tricalcium phosphate, bioglass, etc.), and peptide-based hydrogels (synthetic molecules designed to self-assemble by non-covalent interactions). It should be noted that for bone applications, it is quite a difficult task to create a material that matches all the criteria mentioned above, particularly concerning the dual requirements of mechanical properties and resorption/degradation. Currently for bone filling applications, the few synthetic choices for surgeons typically involve these ceramics, so there is a lot of room for improvement. Ideally, a synthetic material would be made that mimics the structure of bone, a composite of organic fibers (mainly type I collagen) and mineral (hydroxyapatite). An additional consideration involves the method of implantation. A material that could form *in situ* would allow for much less invasive procedures to be developed, reducing risk of infection and minimizing pain and recovery time.

The second component is the use of bioactive factors that act as the signaling cues to direct cellular behaviour, and can include peptides/proteins, growth factors, drugs, hormones, and nucleic acid derivatives/nucleotides, among others[3, 46]. This body of knowledge has experienced a tremendous growth in recent years as biologists have developed new tools to better understand the myriad of cell signaling pathways and related molecules involved in their complex cellular

systems. When new families of receptors, proteins, and signaling mechanisms are discovered, engineers and scientists are quick to incorporate them into their tissue engineering strategies, and has been the catalyst for more strategic and eloquent systems for tissue engineering and regenerative medicine. For bone applications, bioactive factors commonly considered include various methods (protein or gene delivery) of growth factors (bone morphogenic proteins, transforming growth factor beta, etc.)[47] and cellular adhesion peptides and proteins (Arg-Gly-Asp "RGD" peptide). The latter approach has been widely studied because of the importance of cell attachment via integrin receptors for cell shape, cell function, cell differentiation, and tissue integrity[48-52].

The third component is the use of cells that respond to the bioactive cues and create the desired tissue[44]. For bone applications, the options include stem cells and all the cells along the osteoblastic lineage to mature osteoblasts. Pluripotent embryonic stem (ES) cells have the potential to differentiate into all lineages except those required for a fetus's development *in utero*[53], but are entangled in inherently deep moral issues. Alternatively, many believe that multipotent tissue stem (TS) cells derived from adults are sufficient for most applications, and are devoid of many of these issues. Indeed, these cells have been used medically since the 1950's, such as bone marrow transplants for leukemia[53]. TS cells are capable of self-replicating or differentiating along their system's function. There are some disadvantages to TS cells compared to ES cells, including their low concentration in the body, degenerated quality with age, and limited ability to proliferate with age. However, TS cells are favored over differentiated cells because they are indeed multipotential, they tend to be more prone to proliferating *ex vivo*, and can be harvested without donor site morbidity. For example, mature osteoblasts must be

harvested from a portion of the patient's bone, such as the iliac crest, whereas mesenchymal stem cells (MSC) could be harvested from the patient's bone marrow, which would be regenerated without damage. MSCs are capable of differentiating into bone, cartilage, tendon, muscle, and ligament lineages[54], and are used in portions of the work described herein.

However, a modified approach based on the practical implementation of bone tissue engineering is to eliminate the cells from the equation for *in vivo* applications. By doing so, the possibility to envision and create off-the-shelf products for surgical intervention becomes legitimate. In this case, scaffolds created from peptide-based systems, polymers, and hydrogels containing bioactive factors can be manufactured and prepared for storage, and be readily available for implantation in surgical rooms. This route avoids the lengthy processes required to harvest, purify, and culture a patients cells for re-implantation. For patients suffering unpredictable trauma, such as broken bones or spinal injury, such a wait for treatment is not an option, and an off-the-shelf treatment is highly desirable.

It has been one of the focuses of our laboratory to create novel scaffolds for tissue engineering and regenerative medicine applications, both with and without cells, in pursuit of new treatments for a variety of diseases and maladies for which a cure is not available or the current treatment is unsatisfactory. To this end, we use a system of peptide amphiphiles (PA) that self-assemble into nanofibers to create self-supporting gels at very low concentrations (~99% water).

### 1.1.5 Peptide Amphiphiles

The PA consists of three regions: a carbon tail that creates a hydrophobic end, a middle peptide segment that promotes β-sheet formation to give the assembled nanofiber rigidity, and a

hydrophilic end peptide segment that is displayed on the exterior of the assembled nanofibers[55, 56]. The PAs are water soluble and will self-assemble into nanofibers under the appropriate conditions to create a matrix that is self-supporting to as low as ~1 wt%. The PA structure and self-assembled nanofiber assembly are show schematically in Figure 1.1. Induction of self-assembly can be triggered by pH change, divalent ion addition, concentration effects[56], and mixing PAs of opposite charge[57]. This is important for bone and orthopaedic applications, since solutions of PA can be gelled by the addition of calcium, culture medium, or by injection into tissue. The end peptide segment can be modified to a great extent without disrupting the β-sheet secondary structure, allowing for a wide variety of epitopes to be incorporated into the PA architecture. Once self-assembly has been triggered, these epitopes are presented in very high density on the exterior of the nanofibers for presentation to the cells or tissue. The ability to tailor the PA for specific biological applications makes it possible to incorporate bioactive peptide sequences, and PAs have been demonstrated to control cellular adhesion via RGD epitope recognition[58], to promote blood vessel growth[59], or to template mineralization[55].

In terms of PA design, the strategy for this work has been to develop a new system of PAs for the regeneration of bone. In addition, strategies for integrating the PA with metallic structures to create orthopaedic implants capable of directing cellular behaviour were developed and tested. The experimental approach for using the PA in bone regeneration applications and orthopaedic implants is described below.

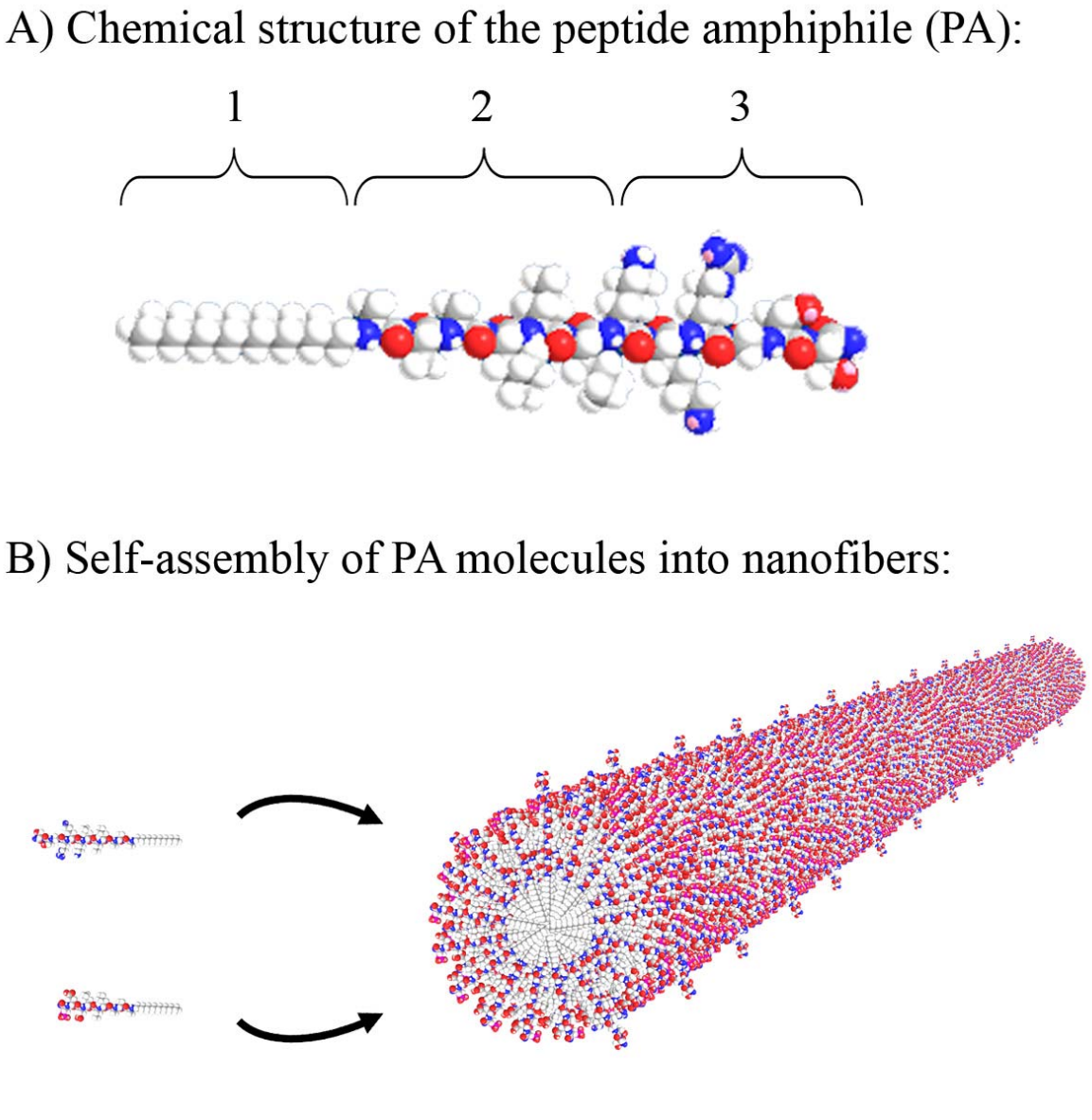


**Figure 1.1 Schematic of the general chemical structure of a peptide amphiphile (A) and the nanofibers formed by self-assembly in aqueous conditions (B). The PA is composed of 3 segments: a hydrophobic tail that drives self-assembly in water (1), a β-sheet forming peptide sequence that gives the self-assembled structure order (2), and a charged, hydrophilic segment that can be tailored for bioactivity (3). It is the latter portion of the PA (segment 3) that is presented on the exterior of the nanofiber when assembled, as shown in (B).**

## 1.2 Experimental Approach

This work attempts to shed light on several key factors regarding the potential for self-assembling peptide-based systems in bone regeneration and orthopaedic implant design, and is categorized into three areas: 1) creating an optimal PA system for bone formation, 2) developing effective methods to create robust, high density PA coatings on metal substrates, and 3) developing Ti foam – PA hybrids for orthopaedic implants.

First, a system of peptide amphiphiles for bone regeneration is developed. The original PA molecule used to demonstrate hydroxyapatite templated on the nanofibers[55] incorporated a phosphoserine (S(P)) residue to mimic the high number of S(P) residues in phosphophoryn, an abundant protein involved in the HA mineralization in dentin. However, it is not known what role the S(P) residue plays in the PA system, and whether the ability to template mineral is primarily influenced by charge or the interaction of calcium ions with the phosphates presented on the nanofiber surface. The strategy described herein evaluates the importance of S(P) in PA mineralization and probes the mineralization potential in a mixed PA system. This work is presented in Chapter 2.

Second, a method to create robust PA coatings for metallic substrates is developed. Previous work in our laboratory demonstrated a proof of concept that individual PA nanofibers could be covalently bound to silanized titanium[60]. However, for the creation of bioactive implants, it is desirable to create a general method that could be used for a variety of metal substrates and applications with improved coating quality. Consequently, there was significant room to improve the process by optimization of the metal preparation, silane coating process, and PA nanofiber coverage. This strategy involves the optimization of these parameters with NiTi to

facilitate covalent attachment of self-assembled PA nanofibers in high density. Materials characterization of these coatings and their biological performance are performed, and are presented in Chapter 3.

Third, a method to create Ti foam – PA nanofiber hybrids for orthopaedic applications is presented. There is a clear need for materials that would encourage bone ingrowth for implant fixation, as discussed above. There are very few examples of organic/metal hybrids for such applications, and consequently much of the work in this area is unexplored and novel. This strategy involves the development of a biocompatible method for the *in situ* self-assembly of PA within the Ti foams. Additionally, organic/metal hybrids introduce significant challenges in materials characterization and biological evaluation, and have required some ingenuity to develop methods for characterization that could not be accomplished by traditional techniques. Materials characterization and demonstration of the incorporation of cells for *ex vivo* culture are presented in Chapter 4. Additionally, a detailed *in vitro* assessment of the PA-Ti hybrids using pre-osteoblastic cells is presented in Chapter 5, and an *in vivo* assessment of the PA-Ti hybrids using a rat femoral model is presented in Chapter 6.

Each of these areas of work is related, yet they are scientifically independent. The overall experimental approach was to create materials systems for bone regeneration and orthopaedic implants, characterized from a Materials Science perspective and evaluated for their biological performance *in vitro* and/or *in vivo*.

### 1.2.1 Specific Aims

The specific aims for this work include:

1. Develop and characterize a mixed system of PAs to control cellular adhesion and template calcium phosphate mineral.
2. Develop an optimized method to create uniform, functionalized metal surfaces for the presentation of biologically relevant molecules.
3. Develop a method to create uniform, dense, and covalently bound PA nanofiber coatings.
4. Develop a method to fill the porosity of metallic foams with PA nanofiber matrix (PA-Ti hybrids).
5. Evaluate the potential of PA-Ti hybrids to facilitate and sustain cellular ingrowth and differentiation.
6. Evaluate the biocompatibility of PA-Ti hybrids and their ability to foster bone ingrowth.

### 1.2.2 Hypotheses

The hypotheses used in this work include:

1. A mixed system of PAs can be created that present RGDS adhesion epitopes and retain the ability to template calcium phosphate mineral.
2. Silane coatings on NiTi can be used to covalently bind a dense coating of PA nanofibers.
3. PA can be triggered to self-assemble within and throughout Ti foams by biocompatible methods, and cells can be encapsulated within the PA matrix.
4. PA-Ti hybrids are suitable for cellular ingrowth and differentiation, and allow for sufficient nutrient diffusion to maintain cell density.

5. PA-Ti hybrids are biocompatible, and promote improved bone ingrowth compared to bare Ti foams.

# CHAPTER 2: MINERALIZATION OF PEPTIDE AMPHIPHILES FOR BONE APPLICATIONS

## *2.1 Introduction*

Bone is a highly organized tissue, composed of organic matrix (primarily type I collagen) and inorganic mineral (hydroxyapatite)[61]. The current gold standard for bone replacement is the autologous bone graft, in which bone from another area of the patient, such as the iliac crest, is harvested and implanted at the site of the defect[6](pg 59). However, there are several limitations, including limitations in size, complications with donor site morbidity, and pain. Alternatives are limited, but include allografts and a variety of bioceramics[7](pg 446), and also have considerable limitations. Therefore, there is significant need to create materials that could effectively fill bone defects, be fully resorbable, and encourage the remodeling and formation of new bone.

Our efforts to replace bone include a biomimetic material that is biodegradable, bioactive by molecular design, and can facilitate the growth of biologically relevant mineral. One class of materials that meet these criteria are self-assembling peptide amphiphiles (PAs)[55]. These molecules are suitable for a variety of tissue engineering and regenerative medicine applications, including bone regeneration, because they can be tailored by molecular design[56]. Previous work by our laboratory[55] demonstrated the templated formation of hydroxyapatite on PA nanofibers bearing a phosphorylated serine (S(P)) to mimic the high occurrence of phosphoserine residues in phosphophoryn, an important protein in the formation of dentin[62]. However, the role and importance of the phosphoserine residue in calcium phosphate templating in these systems is not fully understood. There has also been interest in developing mixed systems of PAs, allowing for

the molecular control of epitopes presented on the exterior of the nanofiber surface. We wish to incorporate PAs bearing the adhesion epitope Arg-Gly-Asp-Ser (RGDS) at controlled concentrations in addition to templating calcium phosphate. Additionally, the cellular response to mineralized PA nanofibers has not been studied. Current tissue engineering strategies aim to create scaffolds with biological cues to direct the behavior of cells. This commonly entails the incorporation of stem cells, which have the ability to differentiate into a variety of lineages.

In this work, the role and importance of S(P) in calcium phosphate formation on PA nanofibers is investigated. Additionally the effect of mixing a small percentage of a net positively-charged RGDS-bearing PA on mineral formation is evaluated. PA nanofiber gels are incubated in cell medium under standard culture conditions to evaluate the mineral that would be formed during *in vitro* applications. Scanning electron microscopy (SEM), Fourier-transform infrared (FT-IR) spectroscopy, and transmission electron microscopy (TEM) are used to characterize the structure and evolution of mineral of PA nanofibers. Additionally, cell cultures with human mesenchymal stem cells (hMSCs) are used to probe any effect of PA nanofiber mineralization on cellular differentiation along the osteoblastic lineage. Quantitative real-time reverse transcription polymerase chain reaction (QRT-PCR) is used to assess the levels of two osteoblastic markers, alkaline phosphatase (ALP) and osteopontin (OP). ALP is a glycoprotein enzyme that is involved in bone mineralization, although the control of its expression is incompletely understood. Nevertheless, it is commonly used as an early indicator of osteoblastic differentiation[63](pg 197). OP, another glycoprotein originally found in bone matrix extracts, is expressed in high levels in the late stages of osteoblastic maturation, just prior to matrix mineralization[64](pg 160). Consequently, it is a good indicator of hMSC differentiation into

mature osteoblasts. To confirm that the genes probed are actually produced by the cells, immunohistochemistry of ALP and OP are also presented.

## *2.2 Materials and Methods*

All chemical reagents, unless otherwise noted, were purchased from Sigma-Aldrich (St. Louis, MO). Solvents were purchased from Fisher Scientific (Hanover Park, IL). Amino acids were purchased from EMD Biosciences (San Diego, CA). Human mesenchymal stem cells (hMSCs) and medium components were purchased from Lonza (Switzerland). Other cell culture supplies were purchased from VWR (West Chester, PA).

### 2.2.1 Synthesis and Preparation of Peptide Amphiphiles

Peptide amphiphiles (PA) were synthesized using solid phase peptide synthesis methods previously reported[65, 66], purified by prep-scale high performance liquid chromatography (HPLC), and characterized using electron spray ionization spectroscopy (ESI) and analytical HPLC. Three different PAs were made: a negatively charged phosphoserine-bearing PA (S(P) PA), a negatively charged serine-bearing PA (S PA), and a positively charged RGDS-bearing PA (RGDS PA). All three PAs were made with analogous designs containing either two lysines or two glutamic acids to promote mixing between the oppositely charged molecules. The structures of all three PAs are shown in Figure 2.1.

### 2.2.2 Cell Culture

Prior to experiments, human mesenchymal stem cells (hMSCs) were cultured under standard tissue culture conditions at 37 ˚C and 5% $CO_2$ in growth medium (Lonza). For experiments,

cells were cultured inside PA gels or on top of PA gels at 37 ˚C and 5% $CO_2$ in osteogenic medium (Lonza) supplemented with 20 mM $CaCl_2$, hereafter known as mineralization medium.

To create the PA gels, dry PA powder was reconstituted in 0.2 μm filtered $H_2O$ to 10 mM concentration and sterilized with UV light for 20 minutes. Then 50 μL of PA solution was placed in a 96-well plate, and 50 μL of mineralization medium was then added to trigger self-assembly of the PA molecules into nanofibers and form a gel. To create PA gels with encapsulated hMSCs, 50 000 cells were added to the 50 μL of mineralization medium prior to adding it to the PA solution. PA gels were incubated for 30 minutes to allow the gels to set, and then 200 μL of additional mineralization medium was added. Every three days, half the mineralization medium was exchanged with fresh mineralization medium. Pre-mineralized PA gels were cultured without cells for 2 weeks before adding 50 000 cells on top of the gels.

### 2.2.3 Biological Analysis

PA gels with cells were assayed by quantitative real-time polymerase chain reaction (QRT-PCR) and immunohistochemical (IHC) staining for two osteogenic markers, alkaline phosphatase (ALP) and osteopontin (OP). For QRT-PCR, samples were cultured for 2 or 4 weeks. Purified RNA was prepared and then reverse transcribed into cDNA using standard protocols. QRT-PCR was then run using a Bio-Rad iCycler Thermal Cycler (Hercules, CA) with Bio-Rad iQ5 software. For IHC staining, samples were cultured for 4 weeks. Samples were embedded in Tissue-Tek O.C.T. compound (Sakura Finetek USA,Torrance, CA), frozen to -80 ˚C, and cryo-sectioned using a Microm HM550 microtome. Sections cut to 5 μm thickness were mounted on glass slides and IHC stained using OP or ALP anti-human primary antibodies (R&D Systems, Minneapolis, MN), a streptavidin HRP mouse bioassay IHC kit with DAB chromagen

(US Biological, Swampscott, MA), and hematoxylin counter stain as per standard protocols. Control samples were prepared using the same protocol, without the addition of the primary antibody.

### 2.2.4 Mineral Characterization

PA gels for mineralization characterization were prepared as described above without cells and cultured for various times in mineralization medium at 37 ˚C and 5% $CO_2$, with 50% medium exchanges every 3 days. Mineralization of the PA gels was characterized by scanning electron microscopy (SEM), Fourier transform infrared spectroscopy (FT-IR), and transmission electron microscopy (TEM).

SEM samples were removed from culture and dehydrated in graded ethanol solutions up to 100% ethanol, followed by critical point drying. Samples were then coated with 3 nm Au-Pd and imaged on an FEI Quanta ESEM fitted with a Schottky thermal field emission gun and Oxford EDS at 10kV. A secondary electron detector was used for high-resolution imaging.

FT-IR samples were removed from media after 14 days of culture and gently rinsed with PBS and ultrapure water. They were dried in a desiccator under vacuum for at least 24 h. Samples non-mineralized, mineralized, and mineralized and burned in an oven for 5 h at 250 ˚C, 350 ˚C, 450 ˚C or 550 ˚C. Samples were prepared as a KBr-pellet and analyzed with a Thermo Nicolet, Nexus 870 FT-IR with the Tabletop Optics Module (TOM) over the range 4000-400 $cm^{-1}$ at 0.4 $cm^{-1}$ resolution averaging 128 scans.

TEM samples were prepared by two different methods. First, samples were removed from medium, rinsed in ultrapure $H_2O$, and burned at 350 ˚C. The remaining mineral was collected and placed onto a holey carbon coated Cu TEM grids. Images, diffraction patterns, and EDS

spectra were obtained using a JEOL JEM-2100F FAST TEM equipped with a high-brightness Schottky FEG emitter operated at 200kV. Alternatively, a second set of samples were removed from culture, fixed in 2% gluteraldehyde and 2% paraformaldehyde, rinsed in PBS, post-fixed in 1% $OsO_4$, and rinsed in PBS. Samples were then dehydrated in graded acetone and embedded in EmBed-812/DER 73 (Electron Microscopy Sciences) according to protocol. Briefly, samples were soaked in a 1:2 solution of EMbed-812/DER 73 and acetone, a 1:1 solution of EMbed-812/DER 73 and acetone, and then straight EMbed-812/DER 73 with several fresh exchanges. The resin was then cured for 24 hours at 60˚C. Samples were then section to approximately 70 nm thick using a glass knife, and floated onto a Cu TEM grid. Lastly, another subset of the samples was stained with uranyl acetate before imaging on a JEOL 1230 TEM equipped with a Hamamatsu ORCA camera and AMT imaging software at 100 kV.

### 2.2.5 Statistical Analysis

Statistics for biological analysis are shown using standard deviation error bars. Multivariate analysis was performed with JMP 6 software to determine significance values and power values. For individual comparisons, T-test with unknown variance was used to determine two-tailed P-values.

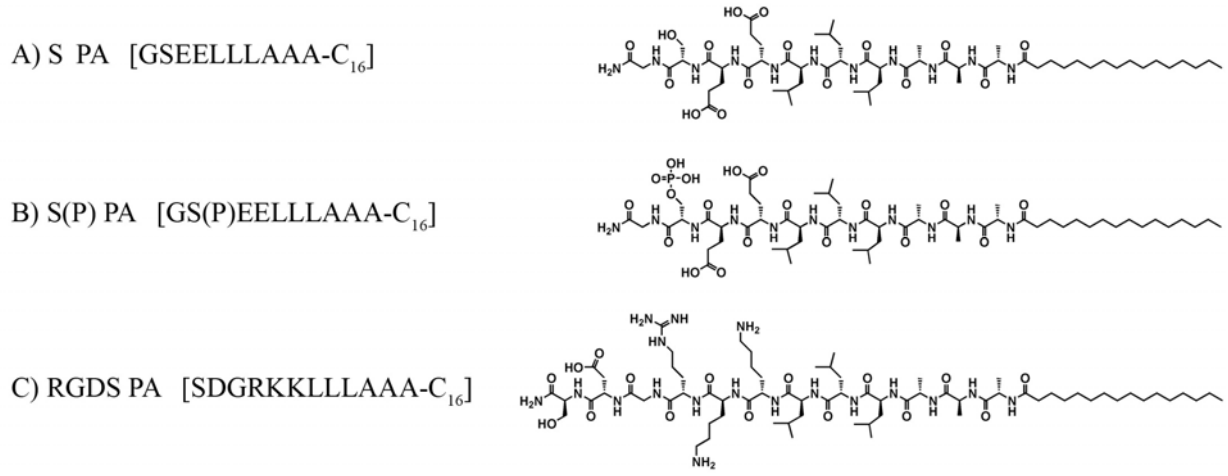


**Figure 2.1 Chemical structures of the 3 PAs used to create nanofiber gels: A) net negatively charged serine-bearing PA, B) net negatively charged phosphoserine-bearing PA, and C) net positively charged RGDS-bearing PA.**

## *2.3 Results and Discussion*

### 2.3.1 Mineralization of Peptide Amphiphile Nanofibers

Peptide amphiphile gels were made without cells and incubated with mineralization medium at 37 ˚C and 5% $CO_2$ to study the evolution of mineral growth. Four different 10 mM PA gel mixtures were characterized: 100% S PA, 95% S/5% RGDS PA, 100% S(P) PA, and 95% S(P)/5% RGDS PA. As shown in Figure 2.2, SEM imaging from day 3 shows the formation of spherical mineral that is associated only with the nanofibers for all samples. The mineral is spherical and typically measured 100 nm in diameter for all samples after 3 days of incubation in osteogenic medium. After 7 days of mineral growth, the spheres still typically measure 100 nm in diameter, but grow denser along the nanofibers with time. At higher magnification (Figure 2.3), it is clear that the mineral is associated with the nanofibers, indicating the mineral is templating from the PA and not a result of aqueous precipitation. Additionally, the high

resolution image confirms the mineral is spherical and not an agglomerate of nanocrystals. This morphological observation is important, and will be discussed after the mineral characterization is presented.

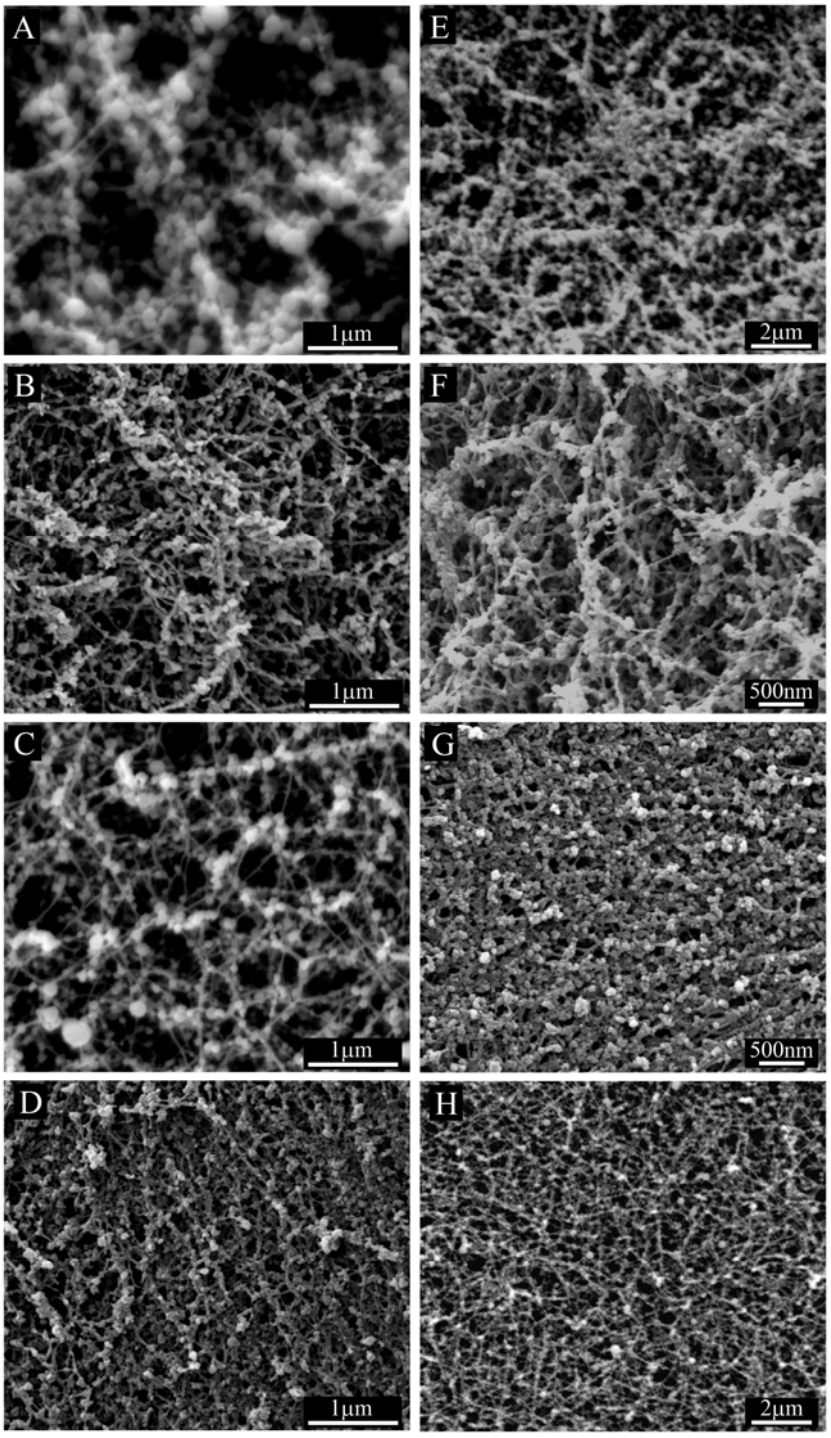


**Figure 2.2 SEM images of 10 mM PA gels mineralized for 3 days (left column) and 7 days (right column) in hMSC osteogenic medium supplemented with 20 mM $CaCl_2$ (mineralization medium). From top to bottom, 100% S PA (A, E), 95% S/5% RGDS PA (B, F), 100% S(P) PA (C, G), and 95% S(P)/5% RGDS PA (D, H). All PAs show the formation of spherical nodules of calcium phosphate mineral associated with the PA nanofibers.**

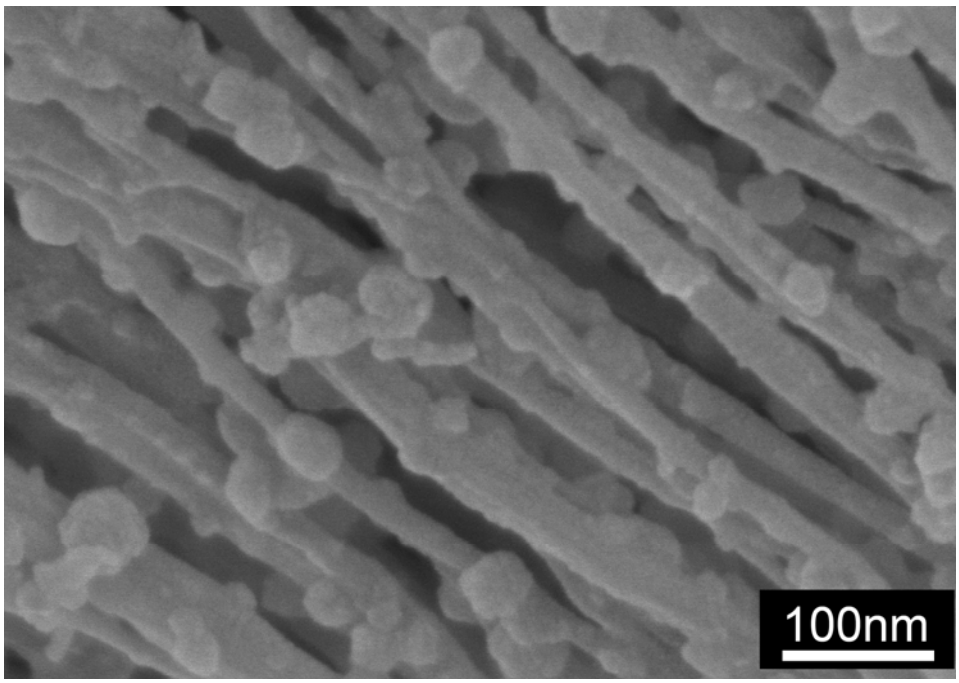


**Figure 2.3 High resolution SEM image of mineralized PA nanofibers. The PA has the amino acid sequence $C_{16}$-VVVAAAEES(P)G and was mineralized under the same conditions as the other PAs used here. The mineral can be clearly seen templated on the nanofibers. Furthermore, the mineral is spherical, not platelike or needlelike as is commonly observed in other systems. Image courtesy of Prof. Conrado Aparicio.**

To better characterize the mineral on the PA nanofibers, samples were prepared for analysis by FT-IR spectroscopy and TEM. Mineralized PA gels were first washed repeatedly with distilled $H_2O$ to remove residual medium components, including salts that might precipitate during sample preparation. PA gels were then burned at increasing temperatures to remove the organic (PA and medium) components. FT-IR spectra of mineralized S(P) and S PA gels before and after burning at increasing temperatures are shown in Figure 2.4. Spectra for both of the unburned PA samples show contributions from PA and mineral. Several bands are observed that correspond to the amines in the PA structure, including 1635-1670 $cm^{-1}$ (Amide I), 1545 $cm^{-1}$ (Amide II), and 1400 and 1445 $cm^{-1}$ (Amide III), respectively. The Amide I band is bimodal, and indicates the contribution of β-sheet confirmation (1635 $cm^{-1}$) and α-helix conformation

(1670 $cm^{-1}$) in the nanofiber structure[55]. Additional bands corresponding to the mineral, including $HPO_4^{2-}$ (1090-1100 $cm^{-1}$), $\upsilon_3$ $PO_4^{3-}$ (1045, 603, and 570 $cm^{-1}$), $\upsilon_1$ $PO_4^{3-}$ (960 $cm^{-1}$), and B-type $CO_3^{2-}$ (875-878 $cm^{-1}$). When the PA is burned at increasing temperatures, the bands contributed by the PA nanofibers are reduced, and are not present in the 350 ˚C spectrum. This indicates that the PA is being burned off, leaving the mineral behind. As the Amide III bands (1400 and 1445 $cm^{-1}$) disappear, a new bimodal band emerges (1420-1430 and 1470-1480 $cm^{-1}$), corresponding to B-type $CO_3^{2-}$. Combined, this indicates that the mineral formed on S(P) PA and S PA is the same, and is most likely a carbonated, slightly calcium-deficient, crystalline hydroxyapatite. Indeed, naturally occurring hydroxyapatite is typically non-homogenous, non-stoichiometric and contains impurities like carbonate[67]. B-type carbonated apatites have $CO_3^{2-}$-for-$PO_4^{3-}$ substitutions, and are the primary type found in normal enamel, dentin, and bone[67]. The FT-IR results also indicate that burning the mineralized PA gels at 350 ˚C is sufficient to remove the organic component, leaving only the mineral behind. While the phosphate adsorption bands are broad in the unburned samples, this can be explained by the interference of the PA signal and the effect of drying of the nano-sized mineral spheres[68]. Both of these factors would be expected to broaden the bands for the mineral. Additionally, amorphous calcium phosphate is stable beyond 500 ˚C, and will only begin to convert to poorly crystallized apatite at 600 ˚C[67]. The only other possible route of conversion, solution-mediated transformations[67], is not a factor in this instance. Therefore, we can conclude that the templated calcium phosphate is indeed crystalline apatite.

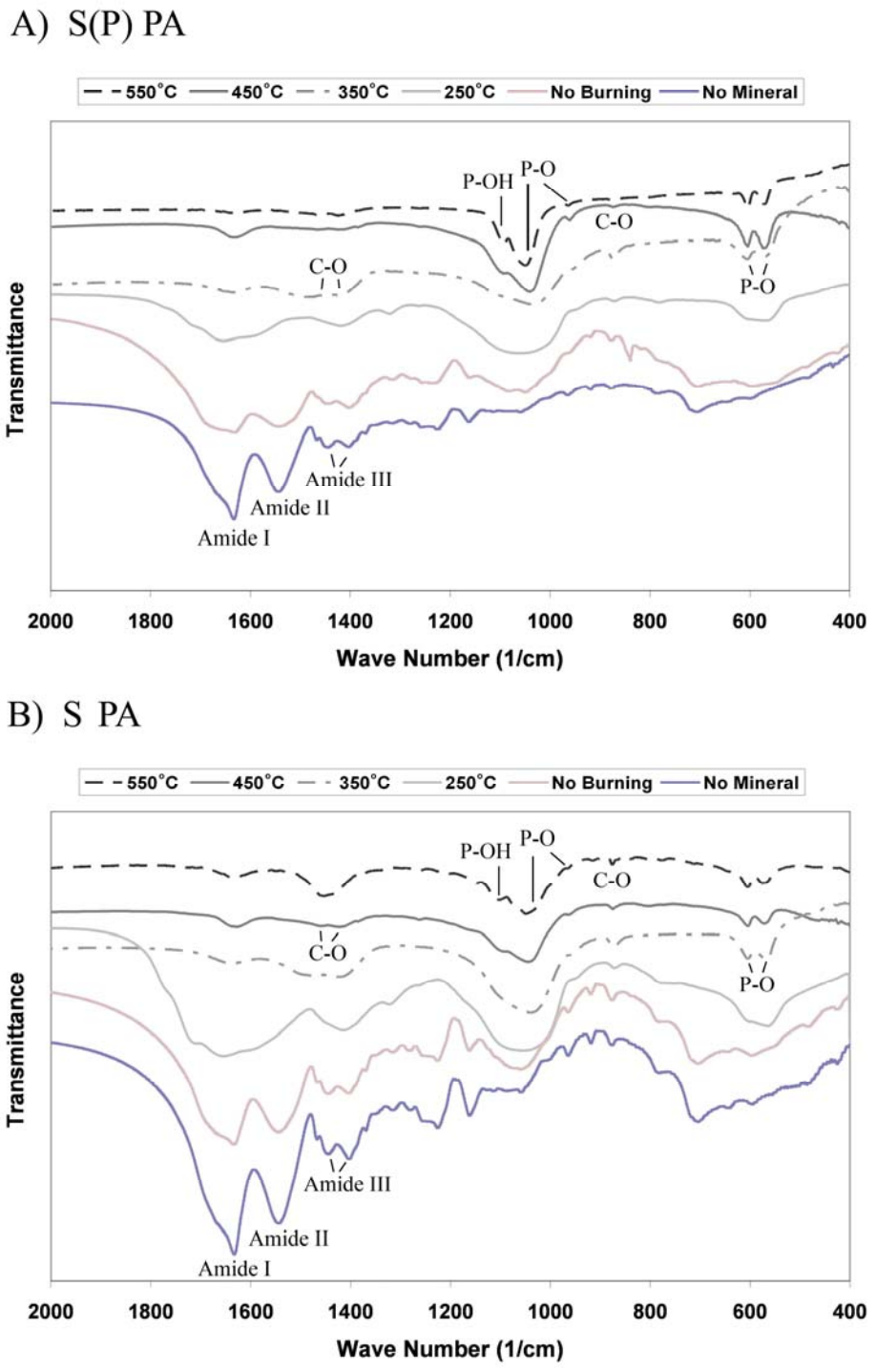


**Figure 2.4 FT-IR spectra of S(P) PA (A) and S PA (B) mineralized for 2 weeks in hMSC osteogenic medium supplemented with 20 mM $CaCl_2$ (culture medium). Mineralized PA gels were washed to remove medium components and then burned at various temperatures to remove the PA, leaving behind only mineral. Peaks that correspond to the PA (Amide I, II, III) and carbonated hydroxyapatite (C-O, P-O, and P-OH) are indicated.**

To verify the identity of the apatite, additional data was obtained by TEM. Mineralized PA gels were washed and burned at 350 ˚C, and then analyzed by TEM to obtain images and diffraction patterns, as seen in Figure 2.5. The TEM images show the agglomerated, unstained mineral formed on S(P) and S PA nanofibers, respectively. Consistent with the FT-IR results above, washing and burning of the PA gels at 350 ˚C removes the organic and salts components, leaving only the mineral formed on the PA nanofibers. EDS spectra from these samples show strong peaks for calcium, phosphorous, and oxygen, with only trace amounts of other elements. Diffraction patterns obtained were similar in different regions of the sample, and indexing confirms the formation of hydroxyapatite. This confirms the findings by FT-IR, and is consistent with previous mineralization experiments with other phosphoserine-bearing PA systems[55]. In both these works, hydroxyapatite is formed on the PA nanofibers, even though the chemical structures of the PA and the mineralization conditions were quite different, indicating a preference for this particular phase of calcium phosphate in these systems. In the mineralization of S(P)-bearing PA demonstrated by Hartgerink et al.[55], mineral was templated on a dried layer of PA nanofibers by immersion at the interface of two solutions containing calcium and phosphate ions, respectively. As a result, the two solutions mixed at the PA nanofiber coating interface in a very controlled manner. In comparison, the mineralization presented in the current study involves the bulk mineralization of 3D PA gels cultured in hMSC medium under standard culture conditions. Furthermore, hydroxyapatite is formed on the PA nanofibers with and without the phosphate group. It was previously hypothesized that the interaction of the calcium ions with the phosphate groups acted as a seed for mineral nucleation. Indeed, phosphoserine was incorporated into the molecular design of the PA to mimic the high concentration of

phosphorylated residues observed in phosphophoryn, a major component of dentin. This and other phosphoproteins found in bone are known to influence the mechanisms and type of calcium phosphate, in addition to the crystal size and morphology[69]. However, our findings suggest that phosphorylated serine is not necessary for PA nanofiber mineralization. For these PA nanofiber systems, it appears that calcium incorporated into the self-assembled structure in association with the negatively charged glutamic acids is sufficient to induce mineralization under the appropriate conditions. Furthermore, these PA molecules, with and without phosphorylated residues, self-assemble into nanostructures that inherently favor the formation of hydroxyapatite over other calcium phosphate phases. If this is true, then any net-negatively charged PA that presents negative moieties for calcium binding should lead to hydroxyapatite formation under similar mineralization conditions.

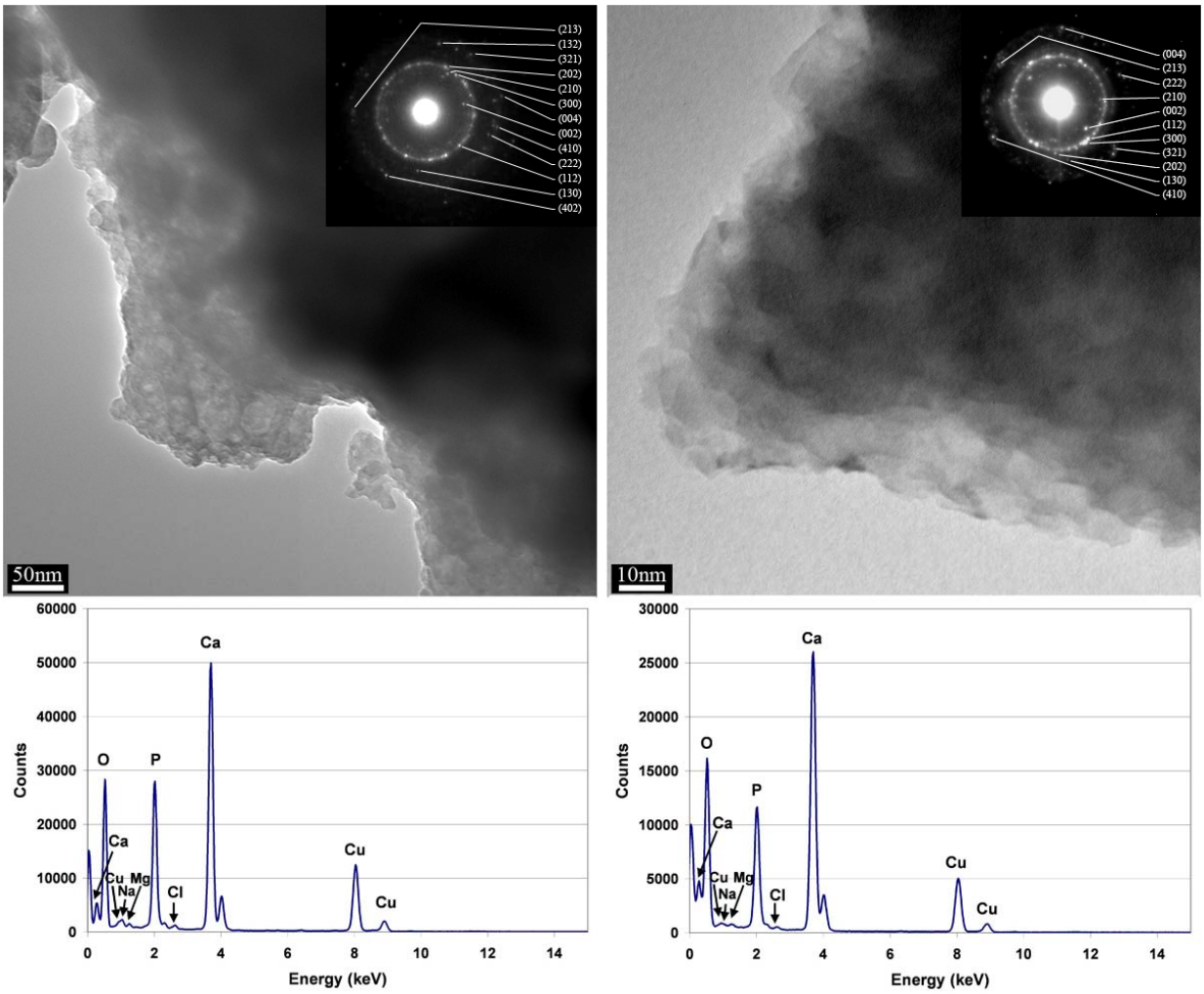


**Figure 2.5 TEM images, diffraction patterns, and EDS spectra from mineralized S(P) PA (left) and S PA (right) after washing and burning at 350˚C to remove residual medium components and the PA. The remaining mineral from both PAs each produce a diffraction pattern corresponding to hydroxyapatite.**

To better understand the nucleation of hydroxyapatite on the PA nanofibers, PA gels were embedded and cross-sectioned for imaging by TEM. Figure 2.6 shows S(P) PA after 24 hours of mineralization (A), and then stained with uranyl acetate (UA) after 24 hours (B) and 72 hours (C) mineralization. Comparing images 5A and 5B, it is clear that the contrast of the mineral associated with the PA nanofibers is not an artifact of the UA stain. It is also clear that the mineral is directly associated with the PA nanofibers, indicating nucleation growth from the

nanofibers and precluding precipitation of mineral from solution that could fall onto the PA nanofiber matrix. Figure 2.7 illustrates the templated mineral on each of the 4 PA gel mixtures mineralized for 24 hours (left) and 72 hours (right). It is clear from these images that nucleation of templated hydroxyapatite occurs on both S(P) and S PAs, with and without 5% RGDS PA mixed in. This confirms the findings by SEM, and shows that mineral is formed in the middle of the gel as well at the surface. Considering both the SEM and cross-sectional TEM images, it appears that while the mineral size and composition are similar, there may be an increase in the amount of mineral formed on the S(P)-bearing PA gels. However, in this particular PA system, the difference does not appear to be extremely large.

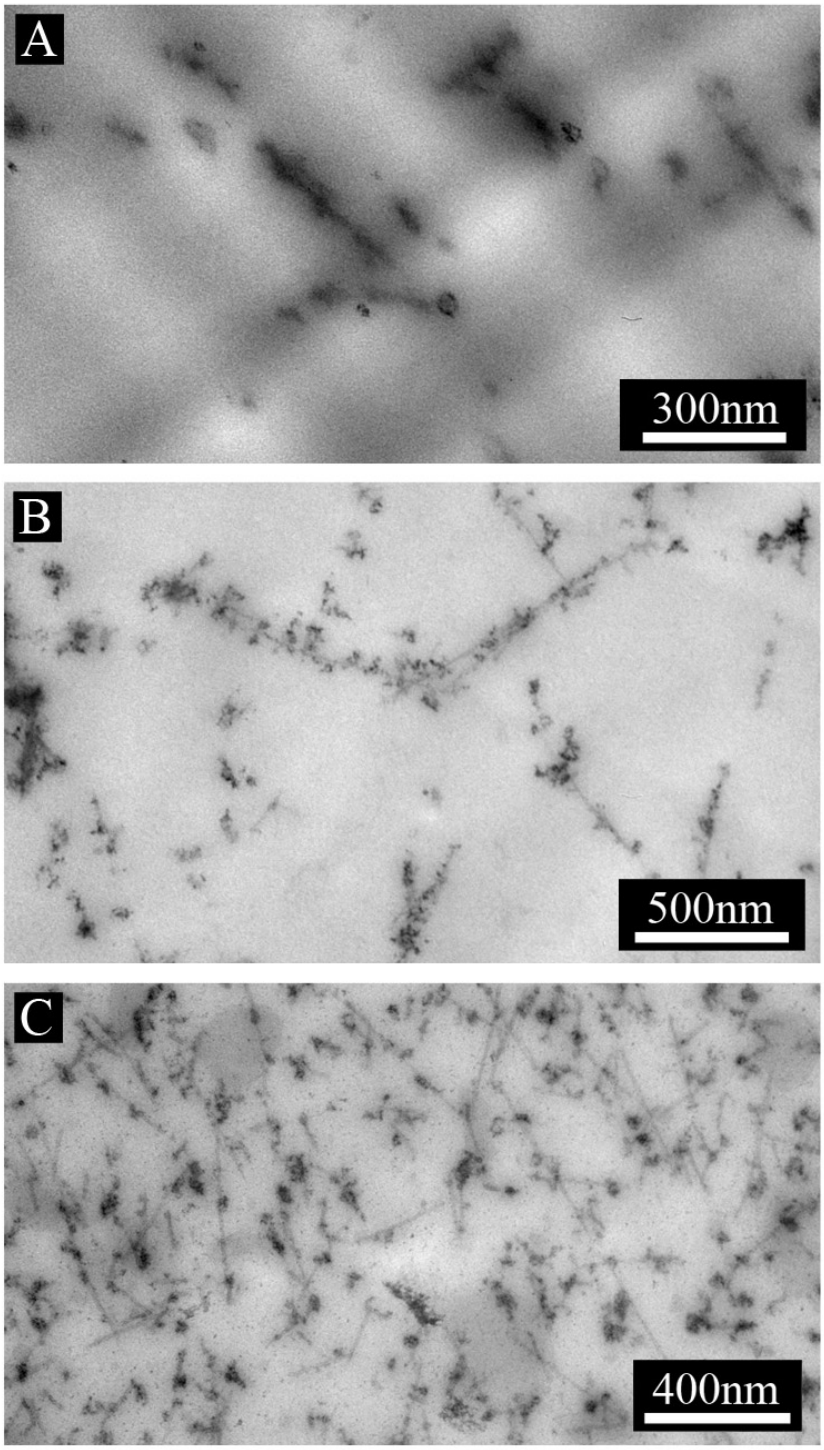


**Figure 2.6 TEM images of embedded and cross-sectioned 10 mM S(P) PA gels mineralized in hMSC osteogenic medium supplemented with 20 mM $CaCl_2$ (culture medium). From top to bottom: S(P) PA mineralized for 24 hours with no stain (A), S(P) PA mineralized for 24 hours with UA stain (B), and S(P) PA mineralized for 72 hours with UA stain (C).**

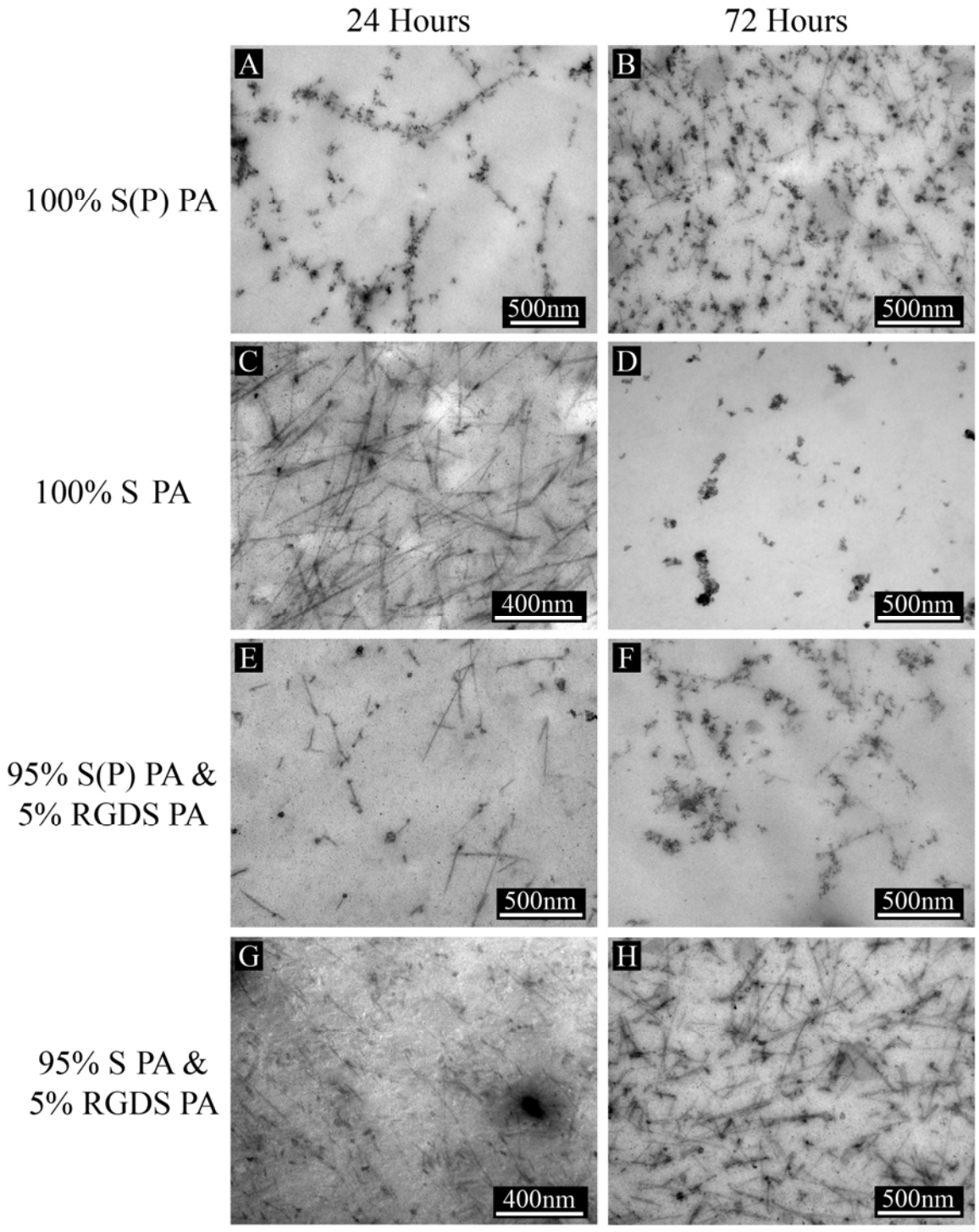


**Figure 2.7 TEM images of embedded and cross-sectioned 10 mM PA gels mineralized for 24 and 72 hours in hMSC osteogenic medium supplemented with 20 mM $CaCl_2$ (culture medium). All PAs show the formation of mineral along the nanofibers, but mineral formation appears to occur quicker on the S(P)-bearing PA nanofibers (A, E).**

Compiling the results from SEM, TEM, and FT-IR, we conclude that the PA nanofibers template carbonated hydroxyapatite in osteogenic medium supplemented with 20 mM $CaCl_2$ under standard culture conditions (37 ˚C, 5% $CO_2$). What is quite novel about this system is the observation that the mineral is *spherical* and nanoscale. Nano-scale, crystalline, spherical calcium phosphate powders have been produced by methods including aqueous precipitation with sintering[70] and by sol-gel methods with sintering[71], although, the latter work showed that the mineral was part crystalline prior to sintering. Alternatively, nano-scale calcium phosphate precipitates and plate-like structures have been templated on micron-scale 3D cellulose fabrics[72]. However, to the knowledge of the author, there is no precedent for templated, nanoscale, spherical hydroxyapatite (nor any form of calcium phosphate) on a nanofiber scaffold. In the PA nanofiber system, the spherical mineral formed does not exceed 100 nm in diameter, and is evenly dispersed along the nanofibers. This is on the same order of magnitude as bone, where carbonated, plate-like, apatite crystals templated on collagen fibrils measure approximately 50-100 nm x 25-50 nm x 2-4 nm[73, 74]. It is interesting, however, that the crystalline hydroxyapatite observed on the PA nanofibers is not platelike or needlelike, but rather spherical. This would imply that the mineral is forming as amorphous calcium phosphate nanospheres, which in turn crystallize *in situ* without heat treatment. These results also raise the question as to why the nanospheres do not exceed 100 nm. If fact, at earlier timepoints, the nanospheres are commonly observed to be approximately 20-30 nm in diameter. It is not clear why the spheres do not grow larger with time. Conversely, new nanospheres are formed instead, indicating that nucleation of new nanospheres is favored over the growth of pre-existing nanospheres once they reach some critical size. Two possibilities for this effect include protein interaction/absorption on the

mineral surface, which could limit growth, and the onset of crystallization of the amorphous mineral, which may do so in a way unfavorable for continued growth. Given the ability to design the PA on a molecular level, the PA nanofiber system presents itself as an excellent system for studying the evolution of biologically relevant calcium phosphate.

From a scientific aspect, this work raises interesting questions about the formation this calcium phosphate. Future experiments should be performed to study the evolution of crystalline mineral from the amorphous precursor, and to determine what limits the size of the spherical mineral. From a practical aspect, this system shows promise as a biodegradable scaffold for bone regeneration. While the morphology of the mineral and the organic matrix in the PA nanofiber system are different than the natural components they mimic, they could serve as a bioactive matrix to induce cellular differentiation along the osteoblastic lineage. Additionally, mineralized PA nanofibers could serve as a resource for cellular remodeling, akin to the natural remodeling process of non-lamellar bone into lamellar bone that occurs during bone development and fracture healing[61].

### 2.3.2 Differentiation of hMSCs in Mineralizing Peptide Amphiphile Gels

To determine the effect of PA mineralization on human mesenchymal stem cell (hMSC) osteoblastic differentiation, cells were cultured in mineralizing PA gels. The effect of the four PA mixtures, as well as the effect of the pre-mineralized of PA gels was evaluated. QRT-PCR was used to determine the gene expression of two osteogenic markers, alkaline phosphatase (ALP) and osteopontin (OP) after two and four weeks of culture. The results for cells cultured on the four PA mixtures are shown in Figure 2.8. The data demonstrate there is an overall effect

of PA type on ALP expression (P=0.0004), where the S(P)-containing PA mixtures are significantly higher than the S-containing PA mixtures (α=0.05). Given that the mineral formed on each PA gel is the same, this indicates that the phosphorylation of the PA has an inductive effect on ALP production. In addition, it appears that the addition of 5% RGDS PA does not inhibit this effect. The data for OP gene expression indicate there is an overall effect of PA type at week 4 (P=0.0002), but not at week 2. Given the expected late onset of OP expression, it is not surprising that there is no effect by week 2. By week 4, 100% S PA is statistically higher than the other three PA mixtures, but there is no statistical difference with other pairs. 100% S(P) PA at week 4 is higher, but not statistically (α =0.0599), than week 2, while 100% S PA at week 4 is statistically higher than week 2 (α =0.0440). This data indicates that the S PA increases the differentiation rate of the hMSCs towards the osteoblastic lineage compared to S(P) PA, but is inhibited by the addition of 5% RGDS PA. It is possible that the increased ALP production induced by the S(P) PA somehow inhibits the continued differentiation towards the mature osteoblastic state, unlike the S PA, which expresses less ALP but increased OP at week 4.

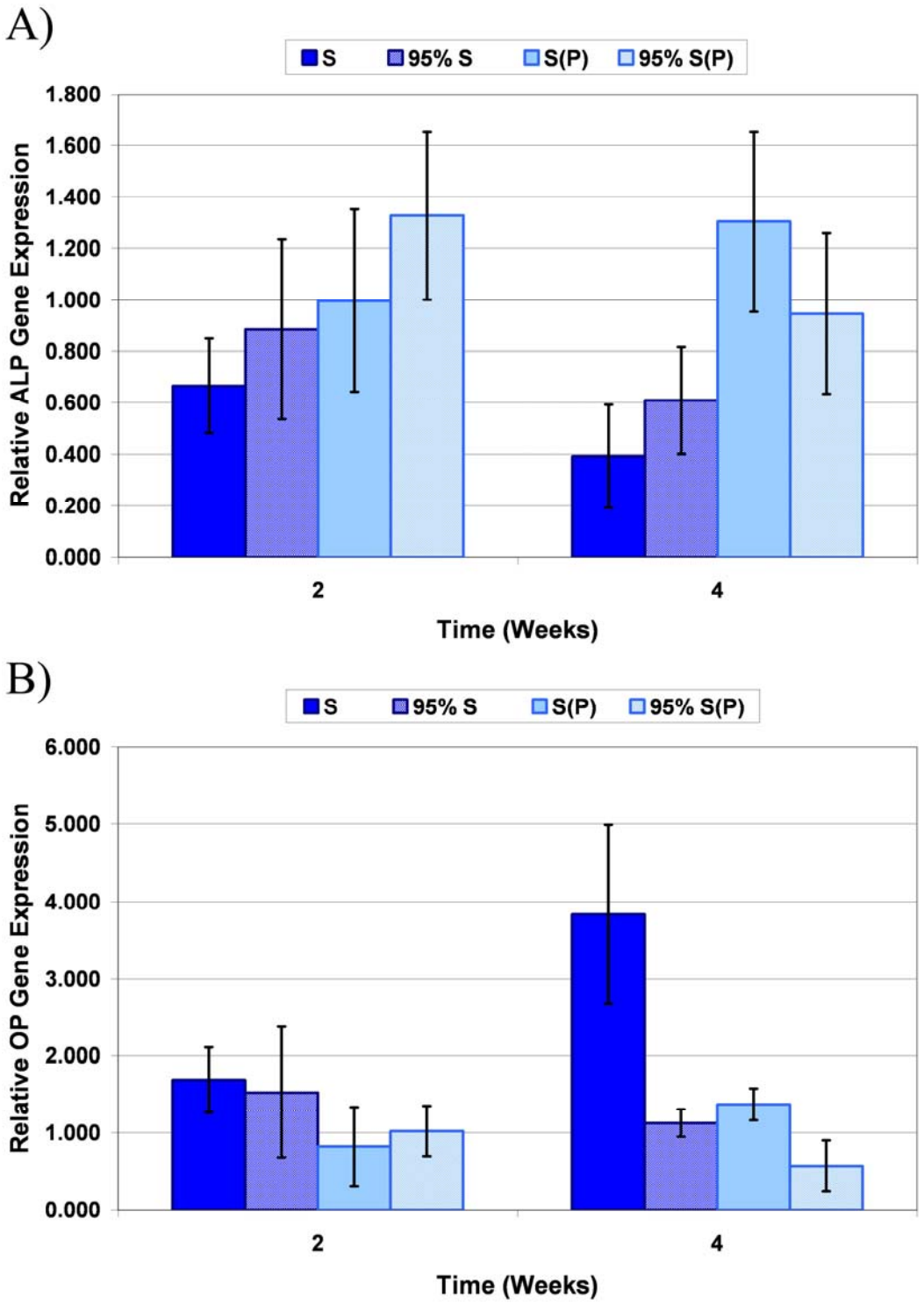


**Figure 2.8 QRT-PCR data for hMSCs cultured in 100% S PA, 95% S/5% RGDS PA, 100% S(P) PA, and 95% S(P)/5% RGDS PA. Samples were assayed for alkaline phosphatase (ALP) gene expression (A) and osteopontin (OP) gene expression (B).**

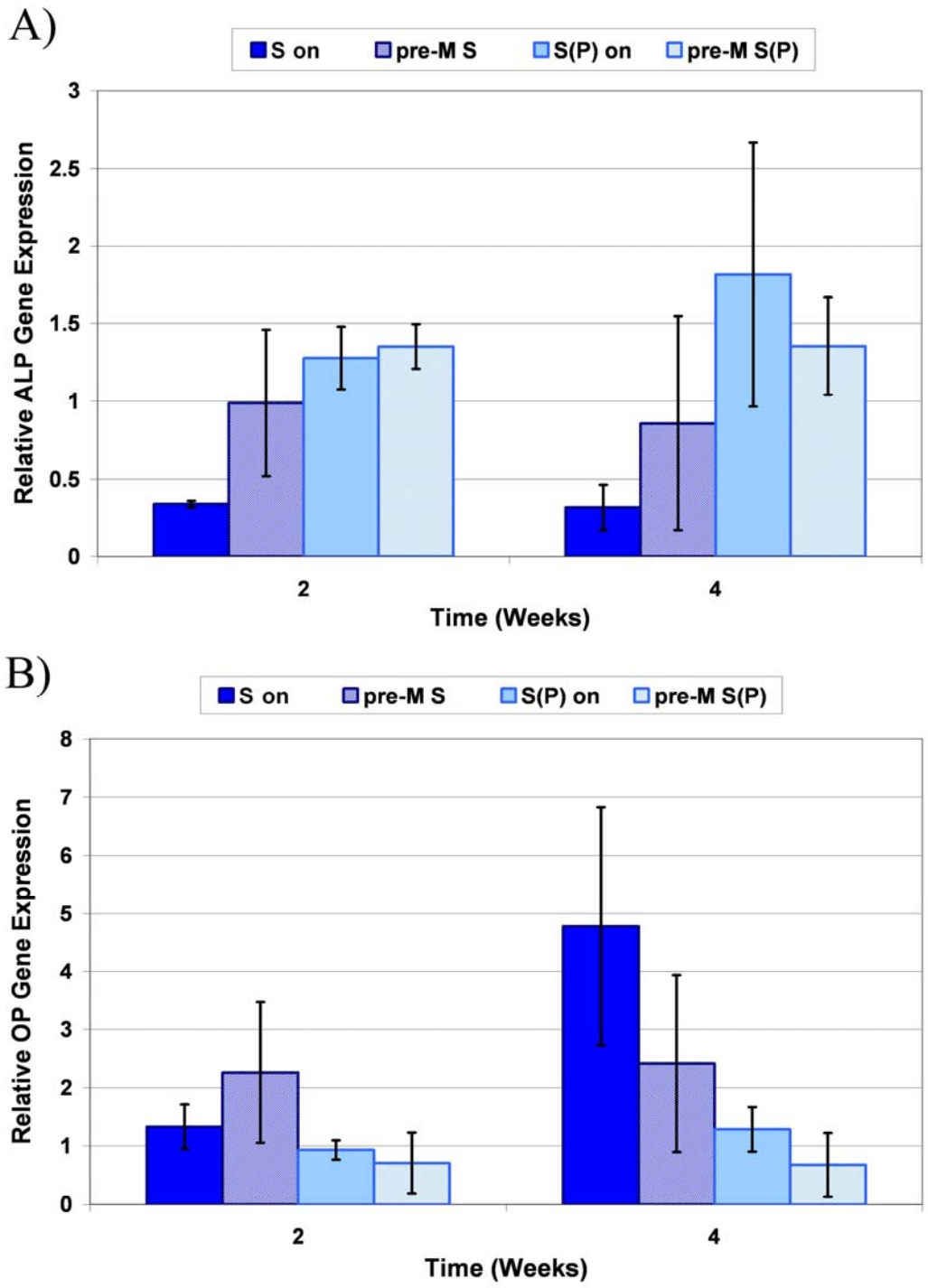


**Figure 2.9 QRT-PCR data for hMSCs cultured on 100% S PA or 100% S(P) PA gels that were pre-mineralized or not. Samples were assayed for alkaline phosphatase (ALP) gene expression (A) and osteopontin (OP) gene expression (B). The results indicate that there is no overall effect of pre-mineralization on ALP or OP gene expression.**

To determine the effect of pre-mineralizing the PA nanofiber gels, hMSCs were seeded on top of fresh PA gels (termed S-on and S(P)-on, respectively) and two week pre-mineralized PA gels (termed pre-M S and pre-M S(P), respectively). After two and four weeks of culture, the cells were harvested and the ALP and OP gene expression was quantified by QRT-PCR, as shown in Figure 2.9. The data show that there is no overall effect of pre-mineralization on ALP or OP gene expression. As before, however, there is an overall statistical difference on ALP gene expression, but not OP gene expression, between the PAs used (S vs. S(P)). Given the fast rate of mineral formation on the PA nanofibers (within 24 hours there is significant mineral) and relatively slow rate of differentiation of hMSCs in the PA gels (on the order of weeks for osteoblastic differentiation), the data indicates that the early influence of the mineral does not have a significant effect on the cells measured after two or four weeks.

Immunohistochemistry (IHC) was used to confirm that the genes for ALP and OP expressed resulted in protein production. Figure 2.10 shows representative images of cryo-sectioned PA gels containing hMSCs cultured for 4 weeks. The images clearly show the presence of both ALP (left panel) and OP (right panel). In addition to confirming the PCR data, the IHC validates the potential of these PA nanofiber systems for culturing hMSCs and inducing their differentiation along the osteoblastic lineage.

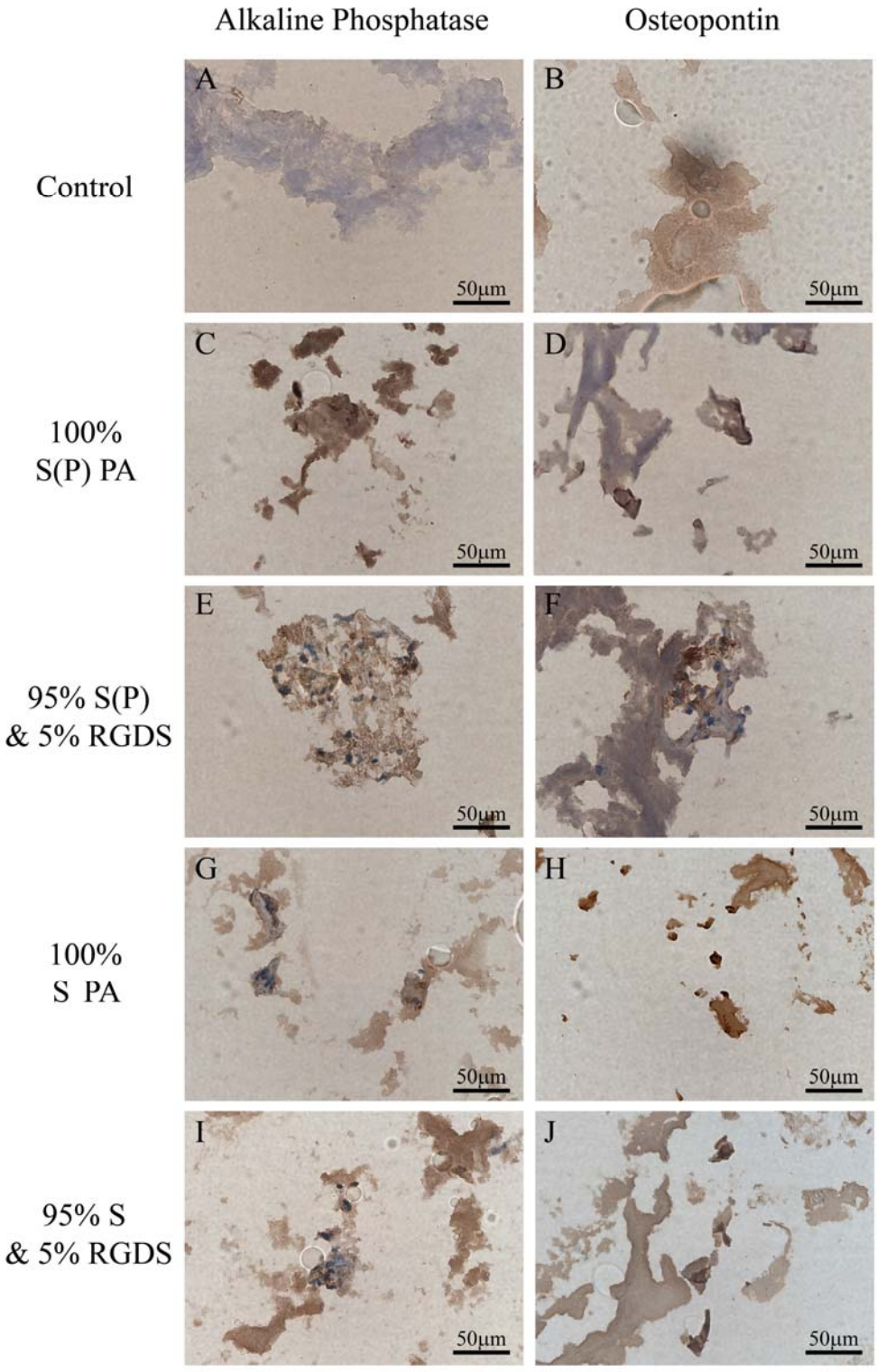


**Figure 2.10 Immunohistochemistry of ALP and OP on cryo-sectioned PA gels with hMSCs cultured for 4 weeks. Dark brown areas, illustrated with arrows, indicate the presence of ALP or OP, respectively. In confirmation of the PCR data, ALP and OP are produced by hMSCs in each of the PA nanofiber gels.**

## 2.4 Conclusions

This work demonstrates that PA nanofibers, with and without a phosphoserine residue, are capable of templating carbonated hydroxyapatite in culture medium at physiological temperatures. In addition, an RGDS-bearing PA can be mixed in at 5% without inhibiting mineral formation. SEM showed that the mineral forms in a *spherical* morphology less than 100 nm in diameter and with uniformity along the nanofibers. Longer mineralization times lead to increased mineral density along the nanofibers without increase in mineral diameter. FT-IR and TEM demonstrated that the mineral was a crystalline, carbonated hydroxyapatite, and that the mineral is only associated with the fibers. The spherical morphology of the nanomineral indicates that it is initial formed as amorphous hydroxyapatite, which then crystallizes *in situ*. QRT-PCR demonstrates the differentiation of hMSCs into the osteoblastic lineage when cultured in each of these mineralizing gels, and was confirmed by IHC. ALP gene expression was upregulated by S(P)-bearing PAs, but osteoblast maturation was enhanced by 100% S-bearing PA. These results show that self-assembling peptide amphiphiles have the potential to induce novel nanospherical hydroxyapatite, can direct the differentiation of hMSCs along the osteoblastic lineage, and could be used as a strategy for bone tissue engineering.

# CHAPTER 3: SURFACE MODIFICATION OF METALLIC IMPLANTS WITH PEPTIDE AMPHIPHILES

## *3.1 Introduction*

By incorporating recent advances in cellular biology into implant design, materials surfaces that are bioactive have been created to promote specific biological responses from host tissues[75-77]. Some important examples of surface biofunctionalization include apatite coatings for osteogenic applications[78, 79], immobilization of proteins and peptides for directed cellular response[80, 81], immobilization of gene vectors[82], and immobilization of antibodies for cellular adhesion[83].

Among the different functionalization techniques, covalent attachment of molecules on the surface of a substrate provides several distinct advantages. They include control of molecular orientation, minimization of non-specific interactions, and greater stability of the functional surface by preventing dissolution, desorption, and degradation of molecules[84, 85]. In order to covalently immobilize molecules on substrates, aminosilanes have been used commonly because of their ability to bind to hydroxyl groups on oxide surfaces[81, 86, 87], and the versatility of primary amine groups for subsequent coupling reactions[86, 88]. The aminosilanes have been typically deposited onto substrates using liquid[86, 88] and vapor[89, 90] deposition techniques. Vapor deposition offers several benefits over liquid deposition, including improved coating uniformity and thickness[91], improved ordering of overlayers[91], and typically simpler experimental setups[92].

The metals used currently as implants include stainless steels, cobalt-chrome (CoCr) alloys, titanium alloys, and nickel-titanium (NiTi) alloys, among others. Nearly equimolar NiTi alloys

are of particular interest for certain biomedical applications such as vascular stents, bone plates, and artificial joints, because of their inherent shape memory effect (SME) and resulting superelasticity[93-95]. For example, shape memory may facilitate improved fitting of bone plates and joint replacements, while the superelastic effect enables superior stent expansion at lower stresses, resulting in less damage to the arterial wall[96]. Due to an inert protective $TiO_2$ oxide layer on the surface, NiTi has demonstrated biocompatibility that is as good or better than stainless steel, and comparable to titanium implants[22, 24, 34, 97, 98]. Furthermore, NiTi has a fairly low elastic modulus, which can limit stress shielding in bone applications, as well as a high damping coefficient and good fatigue resistance[95, 96]. As NiTi offers several structural advantages over other metallic implants, it would be appealing to develop a versatile method to modulate its bioactivity through covalent attachment of biomolecules on its surface.

In this work, covalent attachment of self-assembled peptide amphiphile (PA) nanofibers to NiTi substrates is studied. Due to their well-documented bioactivity[55-57, 59, 99] PA nanofibers are interesting motifs for surface functionalization of implant materials. Using a model system of PA nanofibers containing the RGDS cellular adhesion sequence[51], the metallic oxide and vapor deposition of silane are optimized to create functional NiTi substrates capable of covalently binding PA nanofibers.

Initial studies were performed using aminopropyldimethylethoxysilane (APDMES) as a model molecule because of its inability to polymerize under the conditions used. With only one ethoxy group, it is capable of covalently binding solely to the hydroxyl group of the substrate or forming a dimer with another molecule, at which point it would be washed away during the cleaning procedure. Consequently, it is an ideal molecule for measuring the amount of silane

that will bind the substrate as a function of the oxide produced by the various treatments. Using APDMES, we have optimized the oxide preparation to maximize the bonding between a silane layer and the underlying NiTi surface. Once the optimal metal oxide treatment was selected, a vapor deposition technique was optimized for aminopropyltriethoxysilane (APTES). With three ethoxy groups, this molecule is capable of undergoing extensive polymerization, leading to thin coatings that are more resistant to degradation from hydrolysis because of the increased number of bonds.

Combining the optimized procedures, proof of concept for covalent binding of a PA nanofibers layer was performed, and the robustness of the coating evaluated. The functionalized substrates were characterized using XPS, SIMS, AFM, fluorimetry, and SEM techniques. Furthermore, we have performed microscopy and a cell quantification assay with pre-osteoblastic cells and pulmonary artery endothelial cells in order to biologically probe the modified substrates.

## *3.2 Materials and Methods*

All chemical reagents, unless otherwise noted, were purchased from Sigma-Aldrich (St. Louis, MO). Solvents were purchased from Fisher Scientific (Hanover Park, IL). Aminopropyltriethoxy silane (APTES) was purchased from Gelest Inc. (Morrisville, PA), and amino acids from EMD Biosciences (San Diego, CA). Nickel-titanium alloy (NiTi) strip was generously donated by Nitinol Devices & Components, Inc. (Fremont, CA). CyQuant Cell Proliferation Assay Kit was purchased from Molecular Probes (Carlsbad, CA) and other cell culture supplies from VWR (West Chester, PA). 8-well chamber slides were purchased from Nunc Lab-Tek II (Rochester, NY).

A 3 stage approach was taken to develop silane coatings on NiTi to covalently bind PA coatings for biomedical applications. First, an experiment was performed using APDMES to determine the optimum physical and chemical treatment for silane deposition. A second experiment was performed using the selected treatment to determine the optimum vapor deposition method for APTES deposition. Finally, the covalent attachment of PA nanofibers onto the optimized silane coated NiTi was developed, characterized, and evaluated with *in vitro* cell assays. To simplify the naming of the many samples evaluated, abbreviations were used to describe the various NiTi surfaces. A list of the nomenclature used is shown in Table 3.1.

**Table 3.1 Nomenclature used for NiTi samples**

| Nomenclature | Sample Description |
|---|---|
| **P** | Polished NiTi |
| **T** | **P** treated with HF, $HNO_3$ and boiling water |
| **SP** | **P** followed by silane vapor deposition |
| **ST** | **T** followed by silane vapor deposition |
| **ST+CA** | **ST** subjected to covalent attachment procedure w/out PA |
| **T+PA** | Drop-cast PA nanofiber layer on **T** samples |
| **DC-PA** | Drop-cast PA nanofiber layer on **ST** samples |
| **CA-PA** | Covalently attached PA nanofiber layer on **ST** samples |

### 3.2.1 Mechanical and Chemical Preparation of NiTi Substrates

NiTi with a composition of 55.8 wt % Ni, <0.05 wt % O, <0.02 wt % C, and balance Ti was used for this study (information obtained from the NDC). The cold-rolled NiTi had an austenitic transformation temperature of 5-10 ˚C, but was not heat treated to give superelasticity. Samples for spectroscopy were cut to dimensions of 8.50 mm × 8.50 mm × 1.60 mm, while samples for biological assay and fluorimetry measurements were cut to 8.70 mm × 10.65 mm × 1.60 mm. All NiTi samples were initially polished to remove the “bright” surface created during cold-

rolling and provide a consistent baseline for comparison of the treatments. Polishing was performed using silicon carbide coated papers up to 320 grit, followed by water-based diamond paste polishing up to 1 µm to produce a mirror-like finish. The samples were cleaned ultrasonically using dichloromethane, acetone, and deionized (DI) water for 3 × 5 minutes each, and dried under vacuum. To optimize the coating of NiTi with a silane layer, an array of physical and chemical treatments to modify the NiTi oxide layer were first evaluated. A number of selected treatments were tested, as shown in Table 3.2, because of their reported use in literature or industry to achieve one or more of the following: uniform oxide formation, decreased nickel content in the oxide surface, increased $TiO_2$ formation, and an increase in hydroxyl groups present on the surface. After treatment, samples were rinsed in $H_2O$, blown dry with $N_2$, and dried by desiccation. An additional sample with no treatment after polishing was also used.

**Table 3.2 Physical and chemical treatments for NiTi surface modification.**

| Plasma Treatment | Plasma Time (mins) | Acid Treatment | Acid Time (mins) | Acid Temp. (°C) |
|---|---|---|---|---|
| $O_2$ | 5 | $H_2SO_4$ & $H_2O_2$ | 5 | 21 |
| $O_2$ | 5 | $H_2SO_4$ & $H_2O_2$ | 30 | 21 |
| $O_2$ | 5 | $H_3PO_4$ | 30 | 75 |
| $H_2O$ | 1 | $H_2SO_4$ & $H_2O_2$ | 5 | 21 |
| $H_2O$ | 1 | $H_2SO_4$ & $H_2O_2$ | 30 | 21 |
| $H_2O$ | 1 | $H_3PO_4$ | 30 | 75 |
| $H_2O$ | 5 | $H_2SO_4$ & $H_2O_2$ | 5 | 21 |
| $H_2O$ | 5 | $H_2SO_4$ & $H_2O_2$ | 30 | 21 |
| $H_2O$ | 5 | $H_3PO_4$ | 30 | 75 |
| $O_2$ | 5 | --- | --- | --- |
| $H_2O$ | 5 | --- | --- | --- |
| **Acid Treatment** | **Acid Time (secs)** | **Treatment** | **Acid Time (mins)** | **Temp. (°C)** |
| $HF\&HNO_3$ | 10 seconds | $H_2O$ | 30 | 100 |
| $HF\&HNO_3$ | 10 seconds | $HNO_3$ | 30 | 21 |

### 3.2.2 Vapor Deposition of OrganoSilanes on NiTi Substrates

Initial experiments were performed using aminopropyldimethylethoxy silane (APDMES) to evaluate the best NiTi surface for silane bonding. Vapor deposition of the silane was performed in an airtight Teflon© container with a custom made Teflon© sample holder, shown in Figure 3.1. To do so, 2 mL of neat APDMES precursor was placed at the bottom of the vessel, following which, NiTi samples were exposed to APDMES vapors for a period of 24 hours at 50 °C. The samples were then removed from the vessel and heat treated at 75 °C for 24 hours. Subsequently, the silanized samples were cleaned ultrasonically with reagent grade acetone for 10 minutes, dried under nitrogen gas, and stored under vacuum (ca. 25 in. Hg) until further use.

After the optimum NiTi surface was determined, experiments were performed using APDMES and then aminopropyltriethoxy silane (APTES) to develop a vapor deposition technique to create uniform, polymerized silane coatings. The range of parameters studies for silane coating optimization are shown in Table 3.3. The final method, used for covalent attachment of PA nanofibers and cell assay is described as follows: 2 mL of neat precursor was placed at the bottom of the vessel, following which, NiTi samples were exposed to APTES vapors for the 24 hours at 50 ˚C. The samples were then removed from the vessel and heat treated at 50 °C for 12 hours and then at 75 °C for an additional 12 hours. Subsequently, the silanized samples were cleaned ultrasonically with reagent grade acetone for 10 minutes. After silane deposition was completed, the process was repeated. Samples were then dried under nitrogen gas and stored under vacuum (ca. 25 in. Hg) until further use.

**Figure 3.1 Image of the Teflon© air tight container and matching custom made sample holder used to vapor deposit silane onto NiTi.**

**Table 3.3 Parameters for silane coating optimization experiments**

| **APDMES Vapor Deposition** | |
|---|---|
| ***Temperature:*** | ***Time:*** |
| **25 °C (R.T.)** | **1 day** |
| **100 °C** | **1, 2, 4, 4x1 days** |
| **APTES Vapor Deposition** | |
| ***Temperature:*** | ***Time:*** |
| **50 °C** | **1, 3, 6, 24, 48, 3x24 hours** |

### 3.2.3 Synthesis of Peptide Amphiphiles

Peptide amphiphiles (PAs) were synthesized using solid phase peptide synthesis (SPPS) on a Rink amide MBHA resin, using standard 9-Fluorenylmethoxycarbonyl (Fmoc) protected amino acids in N,N-dimethylformamide (DMF) with diisopropylethylamine (DIEA) and 2-(1H-Benzotriazol-1-yl)-1,1,3,3-tetramethyluronium hexafluorophosphate (HBTU). To create the branched PA architecture, palmitic acid was first coupled to the ε-amine on a lysine to create a hydrophobic tail group. The peptide group was then synthesized using orthogonal protecting group chemistry. Selective deprotection of Fmoc, Boc, and 4-methyl trityl (Mtt) protecting groups allowed for control over the design of the PA. After its synthesis, the PA was cleaved from the resin using TFA, and purified by prep-scale high performance liquid chromatography (HPLC) using a Phenomenex column (purchased from Torrance, CA). The product was then analyzed by electrospray ionization mass spectrometry (ESI-MS) and analytical HPLC for product confirmation.

### 3.2.4 Covalent Attachment of Self-Assembled Peptide Amphiphile Nanofibers on Silanized NiTi Substrates

For all experiments, a 0.05 % solution by weight of the appropriate peptide amphiphile was prepared in distilled water and the pH adjusted to 7.4 with ammonium hydroxide. To create PA coatings, this solution was drop-cast onto NiTi before or after silanization (T or ST) and allowed to dry overnight to produce T+PA and DC-PA samples. Separately, silanized NiTi with or without PA (DC-PA and ST) were then subjected to the covalent attachment procedure to create CA-PA and ST+CA samples, respectively. This was achieved by immersing the samples in a solution of 0.1 M *N*-(3-Dimethylaminopropyl)-*N*'-ethylcarbodiimide (EDC) and 5 mM *N*-

hydroxysulfosuccinimide sodium salt (sulfo-NHS) in distilled water for 2 hours. Samples were then rinsed with fresh distilled water, and dried in a desiccator. Throughout the procedure, pyr-RGDS PA (shown in Figure 3.11C) was protected from light to prevent loss of fluorescence from pyrene.

### 3.2.5 X-ray Photoelectron Spectroscopy (XPS)

XPS analysis was performed on NiTi for both the APDMES and APTES studies before and after chemical treatment or silanization (P, T, SP, and ST samples) using an Omicron ESCA Probe equipped with an EA125 energy analyzer. Spectra were obtained using a monochromatized Al $K_{\alpha 1}$ radiation (1486.6 eV) at 10 kV with a current of 7.74 mA under UHV. EIS software (Omicron, Taunusstein, Germany) was used to collect and evaluate survey and high resolution scans with pass energies of 50 and 25 eV, respectively. The system was calibrated using the C1s peak at 284.8 eV. The data was quantified using the following formula:

$$C_i = \frac{I_i / S_i}{\sum_i I_i / S_i} \tag{1}$$

The intensity, $I_i$, for each element was obtained from the raw data using EIS software, and the sensitivity factor, $S_i$, (specific to the instrument) was used to calculate the concentrations of each element detected. Gaussian peak fitting was used to determine the peak locations for each element with Microcal Origin 6.0 software.

### 3.2.6 Time-of-Flight Secondary Ion Mass Spectroscopy (ToF-SIMS)

SIMS analysis was performed on NiTi for both the APDMES and APTES studies before and after chemical treatment or silanization (P, T, SP, and ST samples) using a PHI TRIFT III mass

spectrometer (Physical Electronics, Chanhassen, MN) in pulse mode at 15 kV using a Ga source at a pressure of $10^{-9}$ mbar. Samples were analyzed three times each in random locations to ensure homogeneous readings. WinCadence software was used to analyze the data and evaluate the ions detected. The system was calibrated in positive mode using $CH_3^+$, $C_2H_5^+$, and $C_3H_7^+$ hydrocarbons.

### 3.2.7 Atomic Force Microscopy (AFM)

AFM was performed on all NiTi surfaces in the APTES study (P, T, SP, ST, DC-PA, CA-PA, and ST+CA) using a Digital Instruments Multimode Scanning Probe Microscope in tapping mode with a Nanoprobe SPM tip. A scan size of 5 mm was used with a scan rate of 2 Hz. Images were collected with respect to height, amplitude, and phase for each sample. Line scans were performed to illustrate surface roughness, and 3D reconstructions were made using both height and amplitude information. Both the pyrene-PA (pyr-RGDS PA) and non-pyrene-PA ($C_{16}$-RGDS PA) were used to create nanofiber coatings for AFM.

### 3.2.8 Fluorimetric Analysis of PA Nanofibers Attached on Silanized NiTi

APTES deposited NiTi samples with PA coatings before and after covalent attachment (DC-PA and CA-PA) made with pyr-RGDS PA were subjected to controlled rinsing to evaluate the robustness of the PA nanofibers attached to the substrates. The samples were ultrasonically washed in 1X Hanks' balanced salt solution (HBSS) containing 1.26 mM $CaCl_2$ and 0.493 mM $MgCl_2$ for 20 minutes, followed by a quick rinse in ultrapure $H_2O$. Fluorescence measurements were made on the samples before PA coating, and before and after ultrasonic rinsing. While

performing this work, the samples were protected from light to prevent degradation of pyrene fluorescence.

Photoluminescence spectra were measured using a Horiba Jobin-Yvon (Edison, NJ) Nanolog-3 spectrofluorimeter with a double excitation-side and a single emission-side monochromator, both set to band pass slit widths of 2 nm. Photoluminescence was monitored using a room-temperature PMT detector. Xenon lamp excitation was incident normal to the sample surface on a spot size of ca. 0.5 cm x 0.2 cm, and photoluminescence was detected in front-face (reflectance) mode, at 22.5 deg. off the angle of incidence. Single-point excitation/emission measurements were collected until variation was less than 1%, up to 10 seconds. Full spectra for the same surface region of each sample were obtained with excitation at 346 nm and emission collection between 355 and 600 nm. A step size of 1 nm and less than 10 sec. integration time was used with the sample oriented at 0 and 180 degrees. Measured intensities were dark-count subtracted and normalized using a reference detector to account for lamp fluctuations.

### 3.2.9 Cell Quantification Assays on Modified NiTi substrates

To evaluate cell proliferation of two cell types on substrates, primary bovine pulmonary artery endothelial cells (CPAE) and a mouse calvarial pre-osteoblastic cell line (MC3T3-E1) were measured on all APTES and PA variations of chemically treated NiTi (T, ST, ST+CA, DC-PA, CA-PA, and T+PA) after 7 days in culture. The PA used for this experiment was the $C_{16}$-RGDS PA (Figure 3.1B). The proliferation assay was performed using a CyQuant Cell Proliferation Assay Kit as per protocol. Briefly, cells were cultured on sample substrates cut to fit an 8-well chamber slide. CPAE cells were cultured in Dulbecco's Modified Eagle's Medium

(DMEM) supplemented with 20% Fetal Bovine Serum (FBS), 1% Penicillin/Streptomycin (P/S), 1 mM sodium pyruvate, 3.6 mM L-glutamine, and 0.02 mM non-essential amino acids. MC3T3-E1 cells were cultured in Minimum Essential Medium α (MEMα) supplemented with 10% FBS, 1% P/S, 10 mM β-glycerophosphate, and 10 μg/ml L-ascorbic acid. Half the media was replaced every 2-3 days during culture. After 7 days of culture the media was removed from the wells and the entire substrate was frozen to –80 $^{o}$C. Samples were then thawed, subjected to CyQuant reagent for 5 minutes and transferred to a 96-well plate. The fluorescence was then measured using a multi-well plate reader. To quantify results, a standard curve was prepared using a known quantity of cells as per protocol. In a second experiment, the number of cells detaching during media exchange was evaluated for bare NiTi (T), and PA coated NiTi before or after covalent attachment (DC-PA or CA-PA). In order to do this, the same experiment mentioned above was performed, with the exception that media was fully exchanged at days 1, 3, and 5. The collected media was then transferred to a standard tissue culture plate and incubated for 5 hours to allow any viable cells to adhere. This media was then removed and plates were subjected to the CyQuant assay as described above.

### 3.2.10 Cell Morphology Assessment by Scanning Electron Microscopy (SEM)

SEM was used to evaluate the cell morphology on each sample type used in the proliferation assay at day 1, as well as T, CA-PA, and DC-PA samples at days 3 and 7. For SEM preparation, samples were removed from culture and rinsed with PBS, fixed with 10% formalin for 1 hour, dehydrated with graded ethanol, critical point dried, and coated with 3 nm Au-Pd layer using a spin coater. SEM was performed using a Hitachi S-4500 with a cold field emission electron gun

at 3 kV with a current of 20 mA. A secondary electron detector was used for high-resolution imaging.

### 3.2.11 Statistical Analysis

Statistics for XPS and CyQuant Assay are shown using 95% confidence error bars. T-test with unknown variance was used to determine two-tailed P-values.

## *3.3 Results and Discussion*

### 3.3.1 Optimization of NiTi Surfaces for Silane Coating

In order to create robust PA coatings, it is desirable to maximize the amount of covalent bonds between the substrate (NiTi) and coating (PA nanofibers). Consequently, it is desirable to maximize the number of bonds between the intermediary silane layer and NiTi. Due to the ability for APTES to polymerize, it is not possible to correlate silane density and bonding to the underlying substrate. Therefore, an analogous silane, APDMES, was used as a study molecule due to its inability to polymerize. APDMES has two methyl groups and only one ethoxy group, and hence it is only possible for the silane to bind to the NiTi oxide or form a dimer with itself under the conditions used. Therefore, it is an excellent silane to study the effect of NiTi surface modification on silane deposition.

The 13 plasma and chemical treatments listed in Table 3.2, as well as the polished sample (C&P), were coated with APDMES by vapor deposition and evaluated by XPS and SIMS. XPS data was obtained at three random areas for each sample to ensure accuracy of the results. For each method of treatment the samples were found to exhibit uniform analyses from measurement to measurement. Spectrums for each sample were similar in shape and showed peaks for Si, C,

N, O, Ti, and Ni as expected. Quantification of the XPS spectra, shown in Figure 3.2, illustrate the %Si (top) and Ni/Ti ratio (bottom) for the surface of each sample. Quantitative analysis of the results showed that the highest amounts of silane (indicated by Si) were present on the samples treated with $H_2SO_4$ & $H_2O_2$ acid preceded by 5 minutes of O2 plasma or followed by 5 minutes of H2O plasma treatment, the HF & $HNO_3$ acid and boiling $H_2O$ treatment, and the polished and cleaned sample with no further treatment. As a group, all the samples treated by oxygen plasma followed by an acid treatment also showed fairly good silane coverage, while the group of samples treated with acid followed by water vapor plasma exhibited varied results with a difference of over four-fold in Si percent. The two plasma treatments by themselves, however, resulted in the lowest amounts of silane coating on the NiTi substrates.

Because the silane coatings were submonolayer, XPS was also able to characterize the outer oxide layer of the NiTi substrate resulting from the various plasma and chemical treatments. Quantification of the surface ratio of Ni to Ti showed that the HF & $HNO_3$ acid and boiling $H_2O$ treatment resulted in extremely low amounts of Ni (<0.01). HF & $HNO_3$ acid followed by passivation with $HNO_3$ acid, and O2 plasma followed by $H_2SO_4$ & $H_2O_2$ acid also resulted in low levels of nickel at the surface approaching a ratio of 0.1. Additionally, the polished and cleaned sample with no further pretreatment also resulted in a low Ni/Ti ratio of approximately 0.15. Conversely, water vapor plasma alone, oxygen plasma alone, and the H3PO4 acid treatments resulted in high Ni/Ti ratios (>0.5). While the nickel content in the surface oxide layer does not affect the deposition of silane, it is an important effect when considering biocompatibility[96]. Consequently, it is desirable to choose a NiTi treatment that will result in both high silane deposition and low nickel content in the oxide layer.

Positive mode SIMS data was obtained for each type of sample preparation after silane deposition and for a polished and cleaned sample with no silane as a control. Each sample was analyzed three times in random areas to ensure accurate readings. The data was quantified, and the ratio of Si to the sum of Ni plus Ti was calculated for each sample. Several treatments resulted in relatively high levels of silane deposition, including HF & $HNO_3$ acid and boiling $H_2O$ treatment and the $H_2SO_4$ & $H_2O_2$ acid preceded by $O_2$ plasma or followed by $H_2O$ plasma. Interestingly, the largest amount of Si was detected on the sample that was polished and cleaned with no further treatment prior to silane deposition. Samples that were not exposed to silane deposition exhibited very low levels of Si. These results are shown graphically in Figure 3.3.

Combining the data from XPS and SIMS, the NiTi preparation treatments that resulted in the most silane deposition include HF & $HNO_3$ acid and boiling $H_2O$ treatment, $H_2SO_4$ & $H_2O_2$ acid preceded by $O_2$ plasma or followed by $H_2O$ plasma treatment, and the polished sample with no treatment. Because it is desirable to develop a treatment that will be applicable to a variety of implants, many of which cannot be polished (stents for example), the polished sample was eliminated from consideration. The second criterion, mentioned earlier, is the level of Ni in the surface oxide layer. The NiTi treatment consisting of HF & $HNO_3$ acid and boiling $H_2O$ resulted in a far lower level of Ni than that others, and hence it was chosen as the optimum treatment for silane deposition. For simplicity, NiTi treated with HF & $HNO_3$ acid and boiling $H_2O$ will hereafter be referred to as b$H_2O$-NiTi.

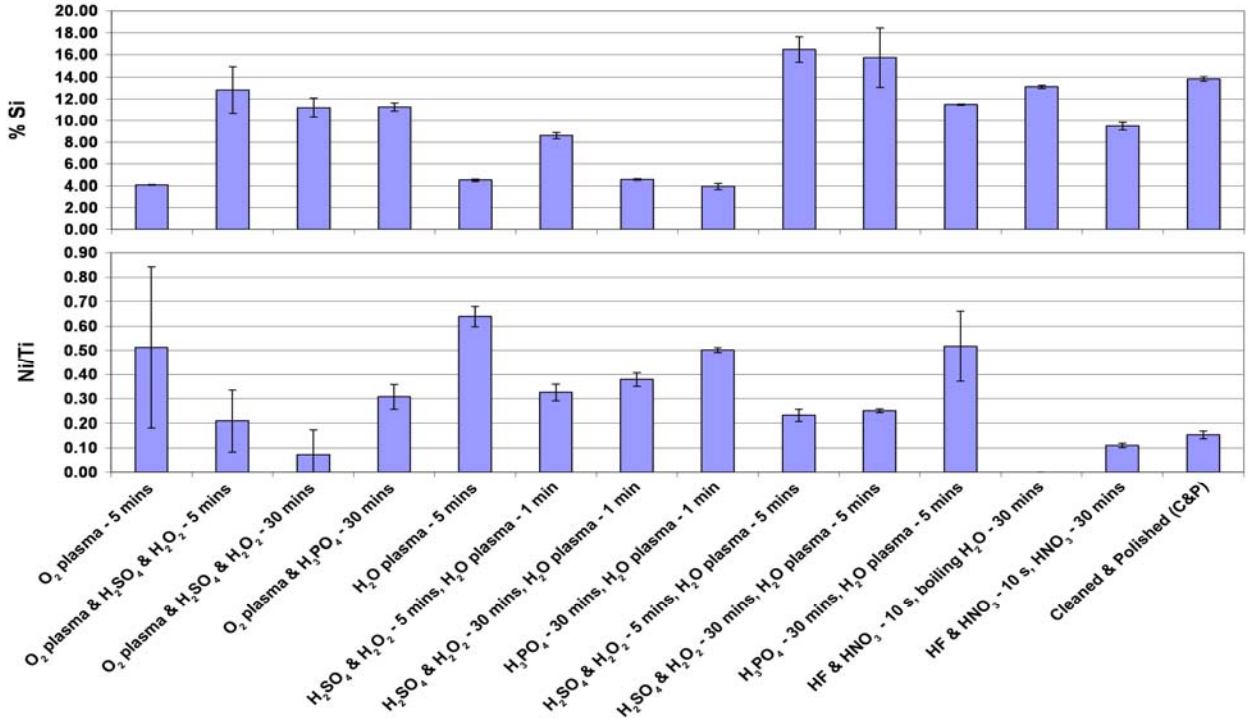


**Figure 3.2 Quantitative XPS data for the Si content (top) and Ni/Ti ratio (bottom) for NiTi subjected to various plasma and acid treatments, followed by vapor deposition of APDMES.**

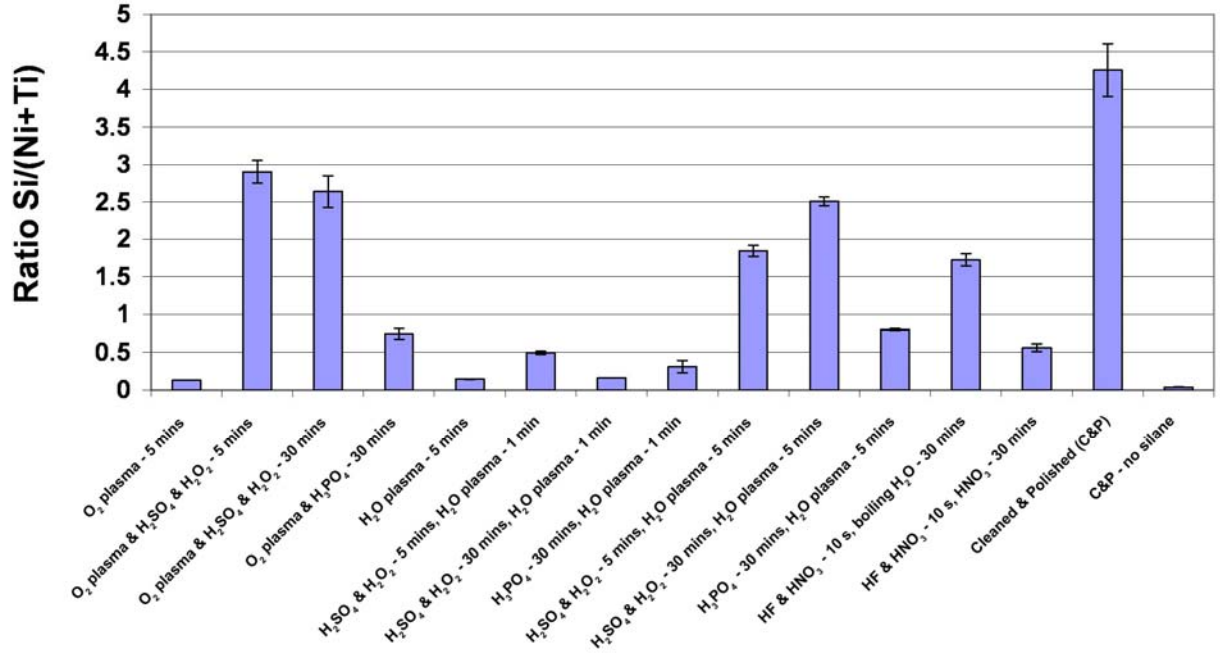


**Figure 3.3 Quantitative SIMS data for the Si peak, normalized to the Ti + Ni peaks, for NiTi subjected to various plasma and acid treatments, followed by vapor deposition of APDMES.**

### 3.3.2 Optimization and Characterization of Vapor Deposited APTES

The next step was to optimize the vapor deposition technique for APTES onto b$H_2O$-NiTi to create a thin, uniform silane layer. The criteria used to develop this method included resulting silane coating, time for coating, and temperature for vapor deposition. Ideally, the APTES would form a fully dense, polymerized monolayer film on the NiTi substrate, as depicted in Figure 3.4. Realistically, however, it is expected that APTES would polymerize in a less organized way, and a thin multi-layer coating is more likely to form if complete coverage is required. For practical reasons, it is also desirable to minimize the time required for silanization. Similarly, it is desirable to perform the vapor deposition at as low a temperature as possible, with a lower limit of room temperature.

Prior to using APTES, however, APDMES was used to evaluate the effect of time and temperature on the vapor deposition onto b$H_2O$ NiTi. Quantitative SIMS was used to determine the relative amount of silane deposited, as shown in Figure 3.5. The data indicates that the amount of silane deposited increases as a function of time. However, the amount of silane deposited at room temperature is minimal to the amount deposited at 100 ˚C. From visual observation, the silane coatings vapor deposited at room temperature were transparent, while the excessive silane had deposited at 100 ˚C, resulting in an opaque coating. Consequently, it was decided to set the temperature at 50 ˚C, which would increase the deposition rate but yield the ability to create thin coatings.

A second experiment was performed using APTES, with the time varying and setting the vapor deposition temperature at 50 ˚C. Quantitative SIMS was used again to determine the relative silane deposition, normalized to Ti + Ni, as shown in Figure 3.6. As with APDMES

deposition, APTES deposition increases with time. However, there is a ten-fold increase in the Si/Ti+Ni ratio between 24 and 48 hours vapor deposition. From the multiple deposition sample (3 x 24 hours), there was an increase in the Si/Ti+Ni ratio of approximately two orders of magnitude. It is important to recognize that because SIMS is a surface technique, the quantification does not translate to absolute volumes, ie. a 10-fold increase does not mean there is ten times more silane present. It does, however, signify an increase in surface coverage. Therefore, the data implies that there is significantly more PA deposited after 48 hours, and using repeated depositions appears to increase the surface area coverage. This can be understood by considering that as the silane molecules absorb onto the surface, there will be a variety of orientations that will be possible. The orientations that favor bond formation to the substrate or other silane molecules that are bound to the substrate will remain in place after washing. However, the molecules that aren't in a proper orientation are likely to be washed away. By repeating the vapor deposition step, fresh silane molecules are given the opportunity bind to the substrate or adjacent silane molecules in those spaces. Therefore, it was decided to use a 2 x 24 hour vapor deposition method. In between the depositions, it was decided to use a 12 hour 50 ˚C annealing step, followed by a 12 hour baking step. The reasoning is similar as before. It is proposed that the 50 ˚C annealing step would supply enough energy for those molecules that have not formed bonds to possibly orient into a position that would facilitate bond formation. Afterwards, the temperature is increased to supply additional energy to allow for these potential bonds to form. Washing removes any residual unbound silane, leaving a thin coating with free amines sufficient for further chemical reaction.

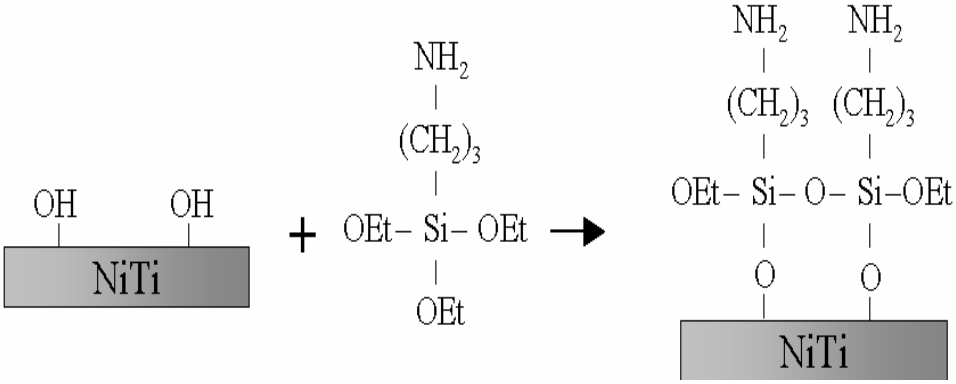


**Figure 3.4 Schematic of the reaction that occurs between the hydroxyl groups present in the NiTi surface oxide and the ethoxy groups on the silane. The advantage of using APTES is the reaction of adjacent molecules to create a polymerized network, making the coating more robust and decreasing the rate of hydrolysis at the NiTi interface.**

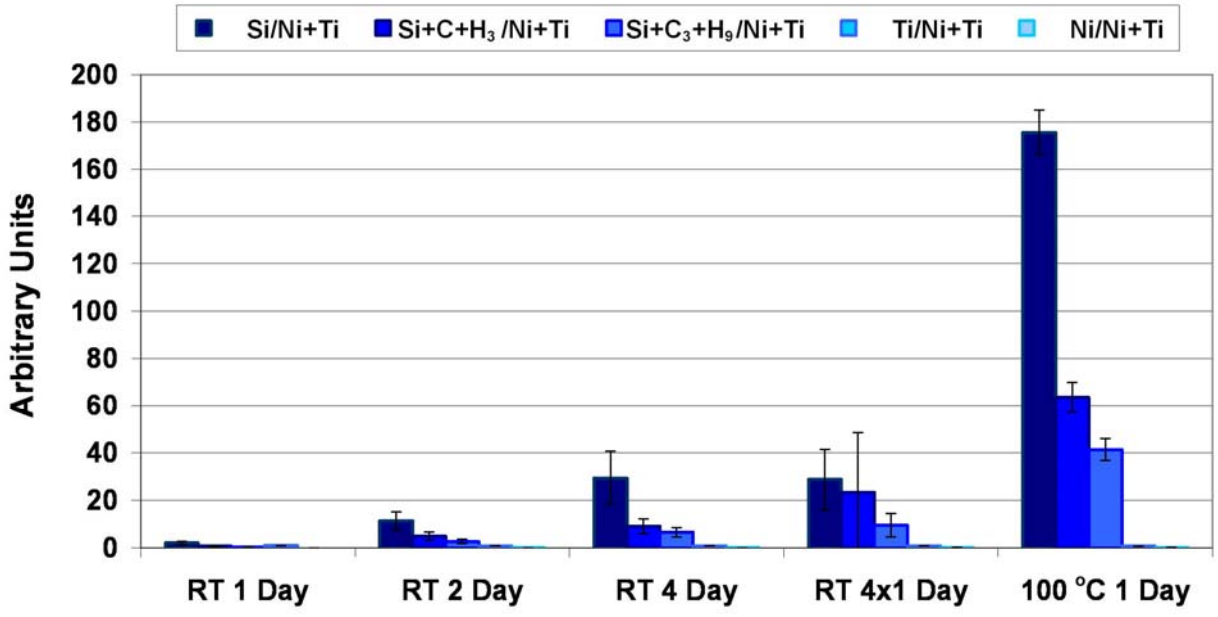


**Figure 3.5 Quantitative SIMS of $bH_2O$ treated NiTi subjected to vapor deposition of APDMES at varying times and temperatures.**

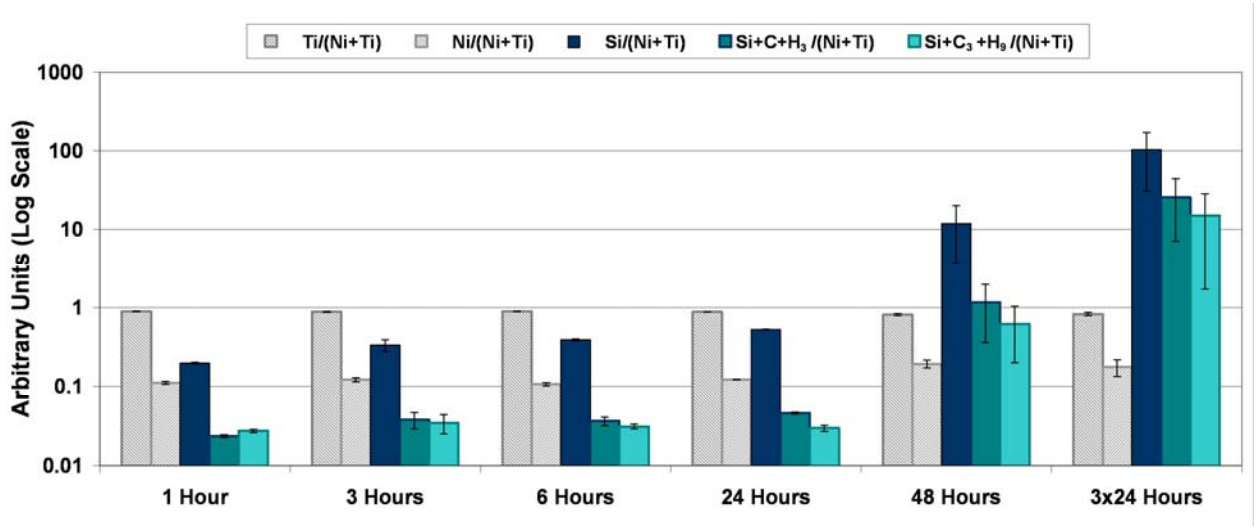


**Figure 3.6 Quantitative SIMS of APTES and b$H_2O$ NiTi fragments after vapor deposition of APTES onto b$H_2O$-treated NiTi for various times.**

### 3.3.3 Characterization of Optimized APTES Vapor Deposition

After the optimum method for APTES vapor deposition onto b$H_2O$-NiTi surfaces was determined, the silane coatings were characterized in more detail by XPS, SIMS and AFM. XPS data was obtained from two indiscriminate areas of each sample type (n = 4) in order to obtain representative results. The spectral curves for NiTi before and after chemical treatment (P and T samples) were similar and exhibited low standard deviation values. A similar trend was observed for the two silanized samples (SP and ST). Typical spectra for T and ST are shown in Figure 3.7. The quantitative compositional results for all sample types are shown in Table 3.4. Spectra for the bare NiTi samples (P and T) samples showed peaks for C, N, O, Ti, and Ni, while silanized samples (SP and ST) showed peaks for Si in addition to those observed for P and T samples. A Ti:Ni ratio of approximately 3:1 is observed for the P sample, while a ratio of 11:1 is observed for T samples, indicating a decrease in Ni content due to the chemical treatment procedure employed for the NiTi samples. The levels of C and O are comparable for both of

these sample types. Polished NiTi (P) samples showed greater traces of N than chemically treated NiTi (T) and neither sample showed the presence of Si as expected. For both P and T samples, all elements except for O were statistically different ($P<0.01$). Comparing the silanized samples SP and ST, only very low levels of Ti were observed, and Ni was undetectable. In addition to the Si peaks, C levels were found to increase and O levels were found to decrease as compared to bare NiTi samples, indicating the deposition of APTES layer on the NiTi surface. No significant difference was observed for any element between the two silanized sample types ($P<0.05$).

As shown in Table 3.5, XPS was also used to determine the oxidative state of each element. The single Ti 2p3/2 peak corresponding to $TiO_2$ was determined to be 458.8 eV for bare NiTi samples (P and T) and 458.2 for silanized samples (SP and ST)[81, 100, 101]. Multiple Ni 2p3/2 peaks were determined for P and T samples measured at 852.2 eV, 852.9 eV, and 855.8 eV. P had an additional peak at 857 eV. These peaks correspond to $Ni^0$ and $Ni^{2+}$, as well as their corresponding shake up satellite peaks[102, 103]. Ni peaks were not observed for both silanized samples, and three O 1s peaks were present for P, T, SP, and ST samples. For bare NiTi samples, two large peaks were located at 529.9 eV and 531.4 eV, with a smaller peak at 532.9 eV. These peaks are assigned to $TiO_2$, TiOH, and hydrated Ti or basic OH, respectively[81, 101, 104]. Silanized samples had one dominant peak at 532.2 eV, with two smaller peaks located at 529.6 eV and 530.8 eV. These peaks are assigned to Ti-O-Si, $TiO_2$, and TiOH, respectively[81, 101, 104]. Typical high resolution O 1s spectra for T and ST with deconvoluted peaks are shown in Figure 3.8. The average peak locations, their assignments, and the corresponding percentages for these three elements are shown in Table 3.5.

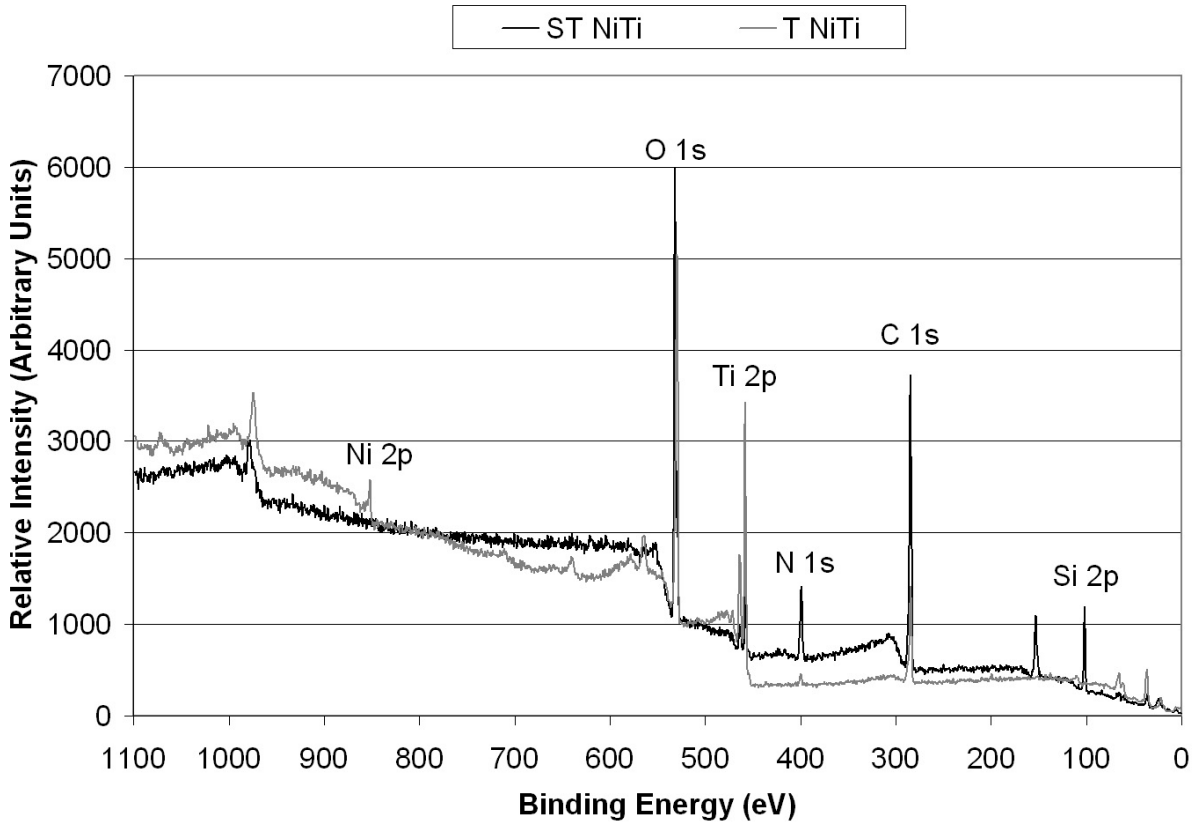


**Figure 3.7 Typical XPS survey spectra of T and ST NiTi surface showing observed elements.**

**Table 3.4 XPS characterizations of P and T NiTi, both before and after silanization (SP and ST). Numbers in brackets indicate 95% confidence interval.**

| Sample | C | N | Ni | O | Si | Ti |
|---|---|---|---|---|---|---|
| P NiTi | 34.1 (2.6) | 3.6 (0.4) | 3.8 (0.7) | 43.3 (2.2) | 0.0 (0.0) | 15.2 (1.0) |
| T NiTi | 35.9 (0.9) | 1.1 (0.3) | 1.4 (0.3) | 43.2 (0.8) | 0.0 (0.0) | 18.4 (0.4) |
| SP NiTi | 52.6 (2.4) | 7.9 (1.1) | 0.0 (0.0) | 24.6 (1.4) | 13.7 (1.7) | 1.3 (0.6) |
| ST NiTi | 51.7 (1.2) | 7.7 (0.9) | 0.0 (0.0) | 26.2 (1.3) | 12.8 (1.1) | 1.5 (0.5) |

**Table 3.5 Characteristic XPS binding energies of Ni, O, and Ti for P, T, SP, and ST NiTi surfaces, and the proposed assignments to surface functionalities. Numbers in brackets indicate standard deviation.**

| Sample | Ni $1s_{3/2}$ region<br>*BE (eV), %, assignments* | Ti $2p_{3/2}$ region<br>*BE (eV), %, assignments* | O 1s region<br>*BE (eV), %, assignments* |
|---|---|---|---|
| P | 852.3, (49), $Ni^0$<br>855.5, (51), $Ni^{2+}$ | 458.5, (100), $TiO_2$ | 529.9, (44), $TiO_2$<br>531.3, (49), TiOH<br>533.0, (7), hydrated Ti, basic OH |
| T | 852.3, (100), $Ni^0$ | 458.6, (100), $TiO_2$ | 530.0, (55), $TiO_2$<br>531.4, (39), TiOH<br>532.9, (5), hydrated Ti, basic OH |
| SP | ---* | 458.2, (100), $TiO_2$ | 529.6, (8), $TiO_2$<br>530.7, (4), TiOH<br>532.2, (88), Ti-O-Si |
| ST | ---* | 458.2, (100), $TiO_2$ | 529.6, (10), $TiO_2$<br>530.9, (7), TiOH<br>532.2, (83), Ti-O-Si |

*Indicates peak was undetectable.

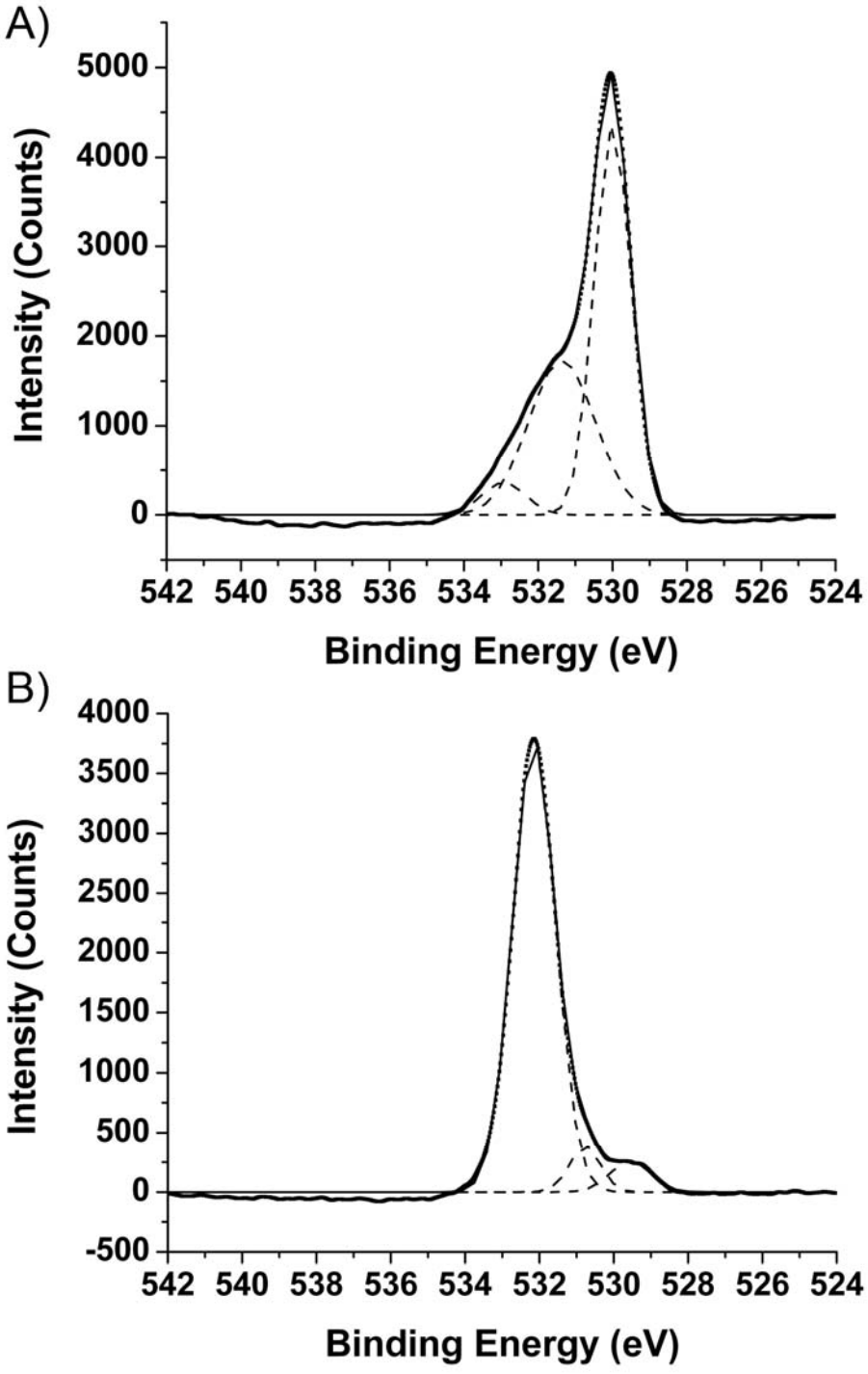


**Figure 3.8 High resolution XPS spectra for Oxygen 1s for T NiTi surface (left) and ST NiTi surface (right). Dotted lines indicate smoothed spectra, dashed lines indicate deconvoluted peaks, and solid lines indicate sum of deconvoluted peaks.**

SIMS was performed in conjunction with XPS to confirm the nature of the elements present. SIMS spectra obtained in positive mode for bare NiTi samples (P and T) showed peaks for Ti, Ni, TiO, and low levels of hydrocarbons. Peaks indicative of the presence of silane molecules were not observed. Spectra for silanized samples (SP and ST) showed peaks for the typical fragmented species for APTES, including Si, $SiCH_3$, and $SiC_3H_9$. Very small intensity peaks for Ti were present, and Ni was not detected at all. Typical spectra for chemically treated NiTi surfaces before and after silanization (T and ST) are shown in Figure 3.9.

The mechanical polishing and cleaning technique used herein (sample P) reduced the nickel content to low levels (<4%) and produced an oxide layer with a Ti to Ni ratio of 3:1. Acid-treatment of this surface with a mixture of HF and $HNO_3$, followed by exposure of the sample to boiling water, further reduced the nickel level to create a surface oxide that is primarily titanium oxide. These results correlate well to Shabalovskaya[95] who attributes the observed reduction in Ni content to Ni diffusion into water. For P samples, polishing was performed with water-based solutions. As the surface gets removed, the newly exposed Ni in metallic form is more susceptible to diffusion. The chemically treated samples (T) were obtained by treating polished samples (P) with acid followed by boiling water. The HF and $HNO_3$ mixture removes the existing oxide and preferentially leaches out Ni to help create a new Ti rich oxide grown during the boiling water treatment. The metallic Ni near the surface is susceptible to diffusion in the boiling water, leaving only a very small amount of Ni in the oxide layer[95]. In P samples, Ni is observed to be present in almost equal percentages in metallic and ionic forms, while for T samples, $Ni^{2+}$ is observed to be present in a greater quantity compared to $Ni^0$. This indicates oxidation of $Ni^0$ to $Ni^{2+}$, and an increased extent of diffusion of $Ni^0$ compared to $Ni^{2+}$. The

excess $Ni^{2+}$ has a lower diffusion rate and therefore might improve biocompatibility of T samples[105, 106]. The single peak at 485.5 eV for Ti indicates the presence of $TiO_2$, which is ideal for silane deposition. The $TiO_2$ layer is known to provide hydroxyl groups on the surface for the ethoxy groups of APTES to form a covalent bond as shown in Figure 3.4. In addition, our sample surfaces contain no other trace elements than C and N (attributed to hydrocarbon contamination in XPS), and in fact, seem comparable to those of Nanci *et al.*[107], who reported preparation of Ti substrates for silane deposition.

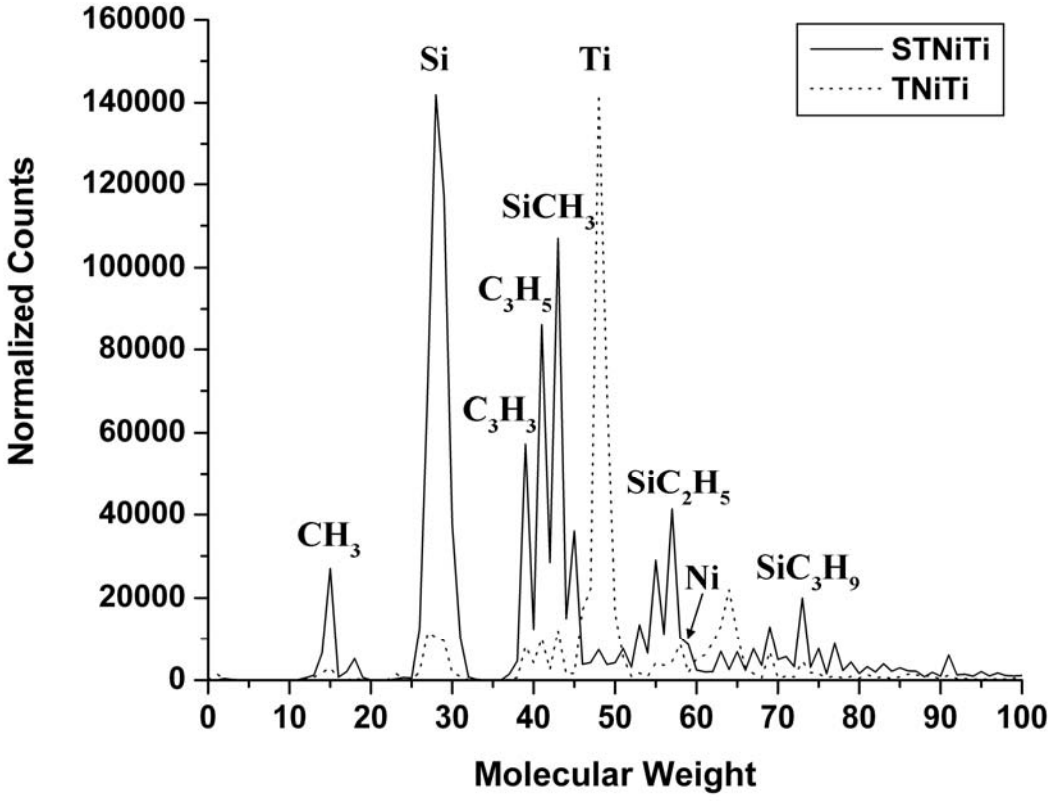


**Figure 3.9 SIMS spectra of T NiTi surface (dashed) and ST NiTi surface (solid) normalized so maximum counts are equal for comparison.**

To deposit the silane layer on NiTi, we have used a moderately low temperature condition and neat aminosilane precursor without any solvent as the starting solution. Previous work by Ek *et al.* have shown the importance of vapor deposition below 150 $^{o}$C[92] and the improvement in silane coating density with repeated depositions[108]. Our method uses a 50 $^{o}$C deposition temperature, followed by 50 $^{o}$C heat treatment to allow for molecular orientation, and then a 75 $^{o}$C curing temperature to crosslink the deposited silane molecules. The advantages of using neat precursor without any solvent are an increased density of aminosilane molecules on the substrate due to absence of solvent molecules, and also a shorter time to achieve desired coating thickness.

Characterization of aminosilane deposited NiTi samples (SP and ST) with XPS and SIMS confirmed the presence of a covalently attached silane layer on NiTi substrates. XPS showed increased levels of Si, N, and C, lower levels of Ti and O, and undetected Ni. The observed increase in Si, N, and C signals are expected, as they are components of the APTES molecule. We also expected to see a decrease in Ni and Ti as the NiTi surface would be covered with an aminosilane layer. The decrease in O can be explained by considering that the surface is changing from primarily $TiO_2$ (where O is theoretically 66% of the surface components) to a silane coating, where O is now a much smaller component (theoretically ~30% not including the $TiO_2$ substrate). This is more easily viewed in Figure 3.8 and the corresponding Table 3.5, where we see that the deconvoluted peaks corresponding to $TiO_2$ and TiOH are by far the largest in the O1s spectra for the chemically treated samples (T), whereas for the silanized samples (ST), the peak corresponding to Ti-O-Si is the major feature in the spectrum. Furthermore, this peak shows that the silane layer is covalently attached to the NiTi surface, and not just physically adsorbed. SIMS data confirms the coverage of NiTi by APTES after vapor deposition, as shown

in Figure 3.9. Chemically treated NiTi (T) shows peaks for Ti oxide, Ni oxide, Ti, Ni, O, and a small amount of hydrocarbons that were used to calibrate the system. After vapor deposition, we see these peaks greatly reduced, with larger peaks corresponding to fragments of APTES, including Si, $SiCH_3$, and $SiC_3H_9$.

AFM was used to determine the surface topography of bare (P and T) and silanized (ST) samples. Representative images are shown in Figure 3.10. A noticeable difference in surface topography between the P and T samples is observed, with the chemically treated sample (T) having an increased level of surface roughness. After APTES deposition (ST), the surface roughness is similar in topography to that of chemically treated NiTi (T), with slightly increased roughness. While this is simply an artifact of the procedure used to create the bioactive surface, texturing has been shown to influence cellular behavior in different ways. For example, several studies have shown increased endothelial cell (EC) proliferation, adhesion, and spreading on nano-textured substrates with identical surface chemistries[109-111]. However, Webster[112] has seen minimal effect of nanoscale texture on EC adhesion, while Xu[113] has found that EC proliferation *decreased* on surfaces with *micron*-scale roughness ($R_{ms}$ = 1557 nm) compared to "smooth" surfaces ($R_{ms}$ = 135 nm) . A similar trend has been observed by studies on the effect of surfaces with different roughness and topography on osteoblast cell (OC) behavior. Surfaces prepared with nanoscale roughness have been shown to correlate well with increased osteoblast adhesion, proliferation, and function[112, 114, 115], whereas studies with larger-scale roughness and texture have shown mixed results[116-119]. Since cellular adhesion occurs via serum proteins absorbed onto a synthetic substrate[109], it appears that the scale of surface roughness plays a significant role in determination of the type and conformation of absorbed proteins, and hence the cellular

response[112, 115]. Therefore, it would be expected that the acid treatment would be beneficial for tissue applications due to the resulting chemical composition *and* topographical features.

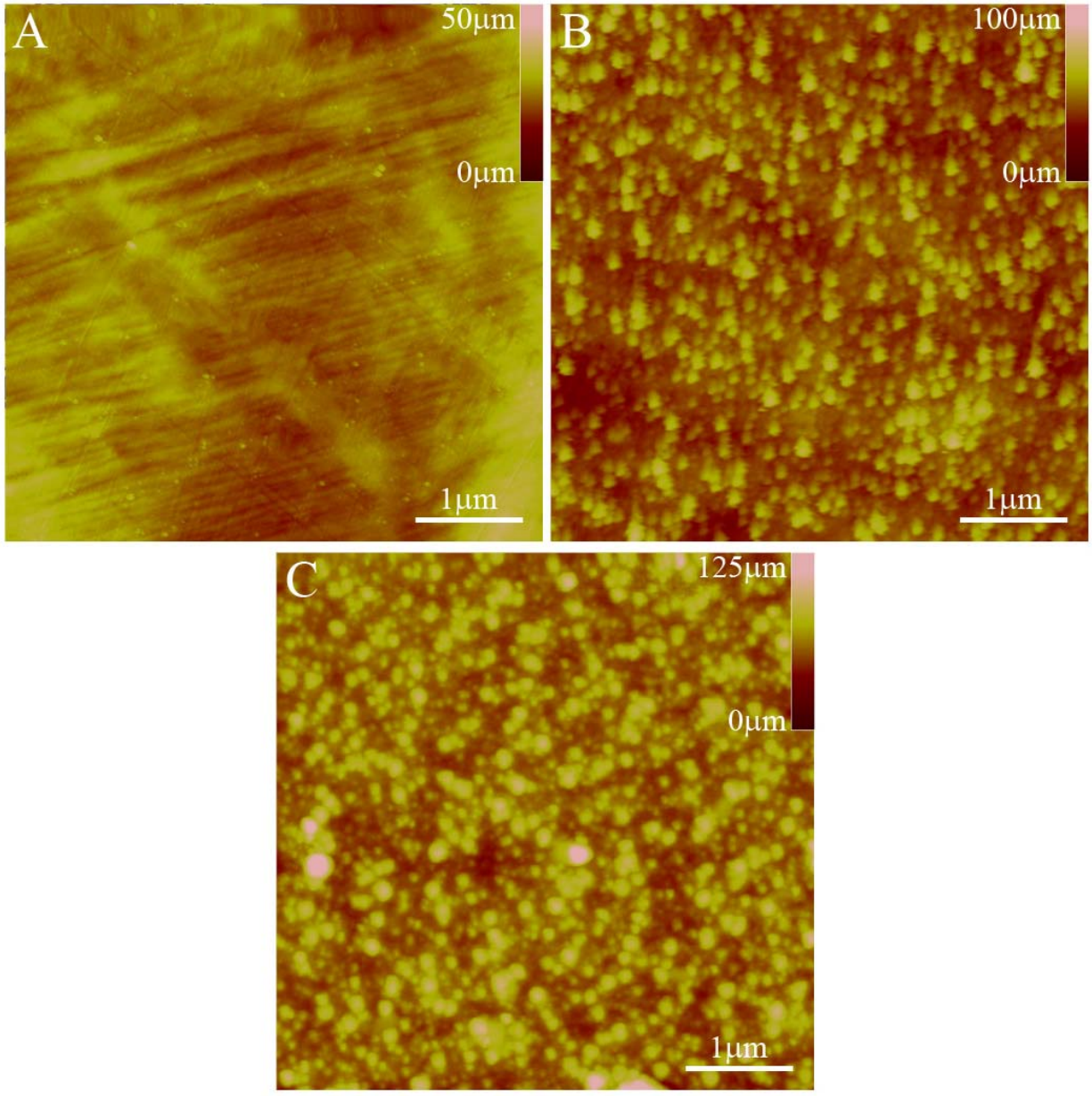


**Figure 3.10 AFM images of P NiTi surface (A), T NiTi (B), and ST NiTi surface (C) showing topography changes after acid treatment and then APTES vapor deposition.**

### 3.3.4 Covalent Attachment of Peptide Amphiphiles

The purpose of silanizing NiTi was to covalently attach biologically relevant moieties on the surface to facilitate adhesion and proliferation of cells and promote tissue integration of implants. Our interest in attaching PA nanofibers to such NiTi surfaces stems from the fact that PA nanofibers have demonstrated their versatility in eliciting cellular response[56, 99] and templating biomineralization[55]. By incorporating these PA nanofibers on a metallic surface, we hope to improve tissue integration and interfacial biocompatibility. In this case, we are using a model RGDS containing PA to evaluate a general strategy to create covalently bound nanofiber coatings on NiTi. A schematic representation of the PAs and surfaces described herein are shown in Figure 3.11. Fluorimetry and AFM techniques have been used to characterize these PA nanofiber coatings and demonstrate their covalent attachment to NiTi substrates.

AFM images were taken of PA coated NiTi before and after covalent attachment (DC-PA, and CA-PA), as well as the covalent attachment control (ST+CA) using both the $C_{16}$-RGDS PA and the pyr-RGDS PA, as shown in Figure 3.12. There is a marked difference between the silanized surface and the PA nanofiber coated surface, where bundles of fibers can be readily distinguished. After covalent attachment both coatings of PA remain assembled into nanofibers as shown in Figure 3.12 (B-C and E-F). When the covalent attachment process is performed on silanized NiTi without PA (ST+CA), the surface retains its topography and nanofibers are not observed (Figure 3.12D), indicating the reaction reagents are not assembling or remaining on the surface after rinsing.

Of the several methods investigated, drop-casting PA solution to form nanofibers on the surface followed by their covalent attachment to the substrate resulted in the most reproducible,

thin, homogeneous coatings of PA nanofibers on metallic surfaces. Other methods, such as covalently attaching pre-formed nanofibers in solution often result in vary sparse coatings, with individual fibers spaced far apart from one-another. Conversely, by using an appropriate concentration of PA molecules in solution, we were able to create a coating of nanofibers that covered the entire surface. This is clearly seen in AFM images shown in Figure 3.12, where similar structures are observed for both PAs. Here we see that the nanofibers, often aggregated in patches of aligned areas, cover the surface in a thin layer that masks the topography observed for a silanized NiTi (ST) surface. Furthermore, the self-assembled nanofibers, formed after drop-casting, retain their structural integrity after the covalent attachment procedure.

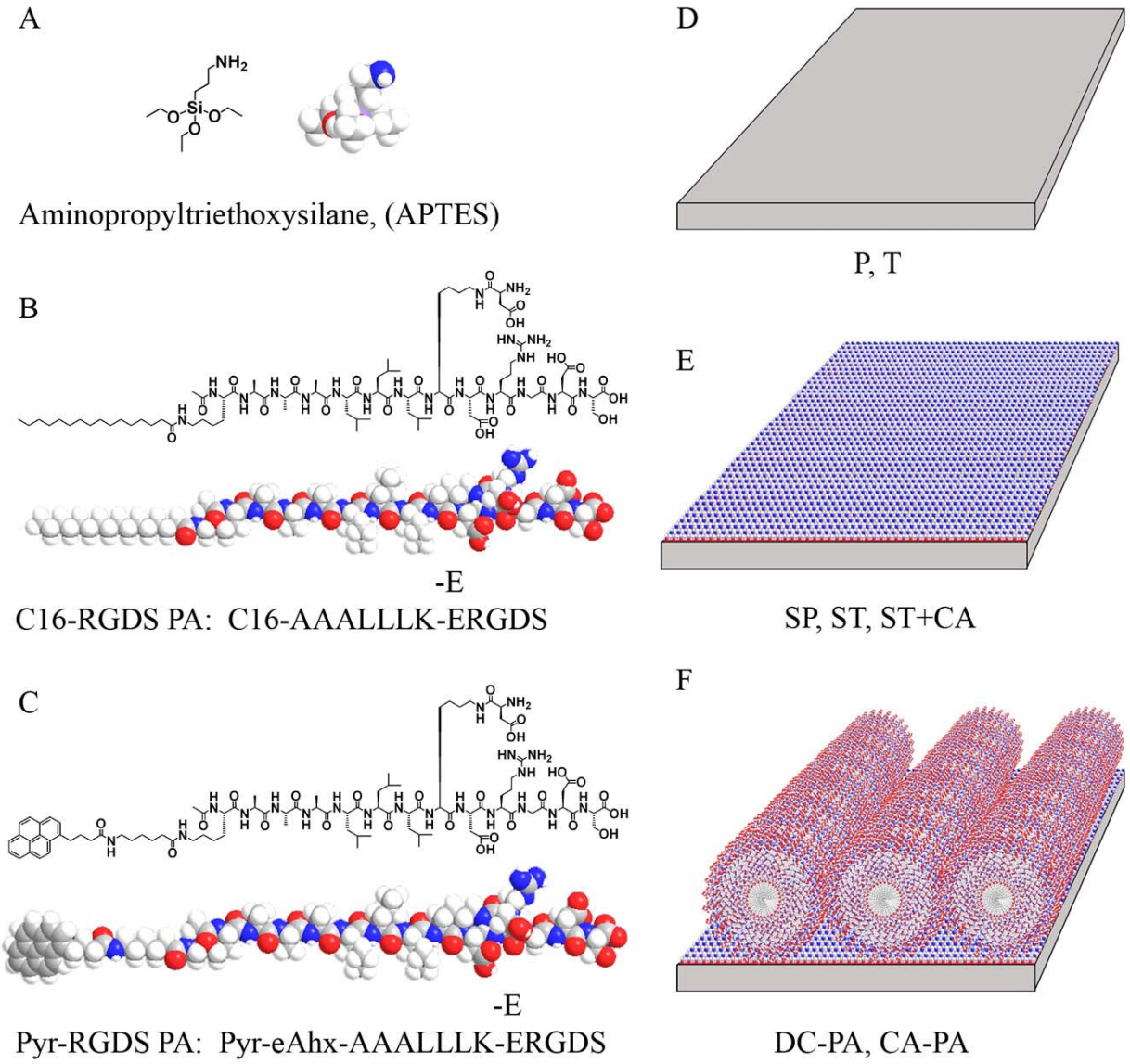


**Figure 3.11 Chemical structures of APTES (A), the peptide amphiphile (PA) used for AFM, SEM, and biological assays (B), the peptide amphiphile (pyr-PA) used for the fluorimetry assay and AFM (C), and schematics for the various NiTi surfaces obtained in the process to create covalently bound PA nanofibers substrates (D-F).**

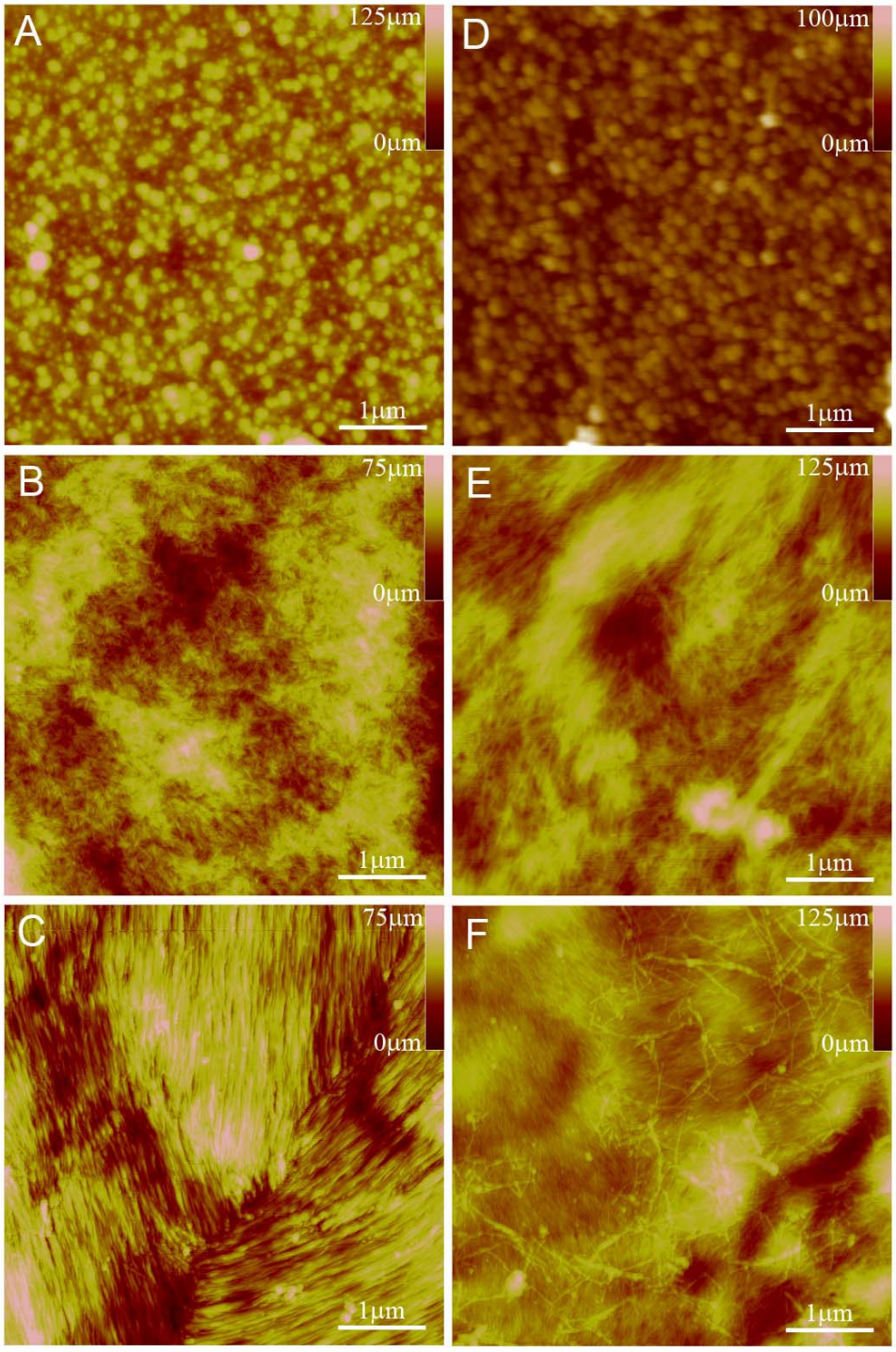


**Figure 3.12 AFM images of ST (A), C16-RGDS PA as DC-PA (B) and CA-PA (C), ST+CA (D), and pyr-RGDS PA as DC-PA (E) and CA-PA (F). B & C and E & F show that the PA nanofiber structure is maintained after covalent attachment. D is a control to show no change in topography due the covalent attachment process.**

The use of an aminosilane linker to covalently attach PA nanofibers does not allow us to confirm the formation of a peptide bond between the PA and aminosilane molecules. Due of the large number of peptide bonds present in the PA nanofiber, the signal from this additional linkage is undetectable by Fourier Transform infrared spectroscopy (FT-IR). Consequently, we designed a fluorescent PA molecule that enabled us to measure the fluorescence associated with the PA nanofiber coating. We then assessed the robustness of covalent attachment of PA nanofibers to NiTi substrates by measuring the fluorescence before and after rigorous washing. To be consistent with the rest of the work presented, a pyrene containing PA (Figure 3.11C) that is analogous to the $C_{16}$-RGDS PA (Figure 3.11B) was used to create these PA coatings (DC-PA and CA-PA samples). Fluorimetry spectra were obtained on silanized samples before PA drop-casting (ST), after drop-casting or covalent attachment, i.e. DC-PA and CA-PA samples respectively, and then after rigorous washing. A spectrum of 0.05 wt% pyr-RGDS PA solution was also measured to compare against the spectra obtained from the NiTi samples. Spectra of the pyrene solution and silanized NiTi before and after drop-cast PA (ST and DC-PA) are shown in Figure 3.13A, demonstrating the monomeric signal of the solution, the addition of the excimeric signal in the PA coating, and the lack of signal contributed by the silanized NiTi. A spectrum corresponding to the monomeric species has been shown previously with a similar PA design[120], when the PA self-assembly is not triggered in a solution state. When a PA solution is dried on a substrate and the self-assembly has been triggered by concentration effects, we also see the onset of excimeric emission. Comparing these spectra for PA coated NiTi before and after covalent attachment (DC-PA and CA-PA) before and after washing with HBSS (Figures 3.13B and C), we see that the signal has almost completely disappeared when the PA is not

covalently bound, while the covalently bound sample retains a slightly diminished signal for the excimer as compared to the sample before washing. This clearly demonstrates that PA is retained on the covalently bound PA samples and not on the drop-cast PA samples. Furthermore, the PA molecules are still observed to form excimers, indicating very close proximity of the pyrene moieties. While the PA nanofibers may not remain completely intact under such extreme and harsh conditions, the PA nanofiber coatings would be robust enough for most implant applications. For applications that would require a higher level of robustness, such as stent coatings, PA molecules that can be cross-linked within the nanofibers could be used to ensure the integrity of the PA nanofiber coating[55]. Usually, washing procedures with HBSS result in masking of the electrostatic interactions between the PA molecules and the substrate due to the presence of salts, and the weak physisorption is insufficient to retain any PA coating. This is an important point, and highlights the necessity for covalent attachment to create robust PA coatings for biological applications.

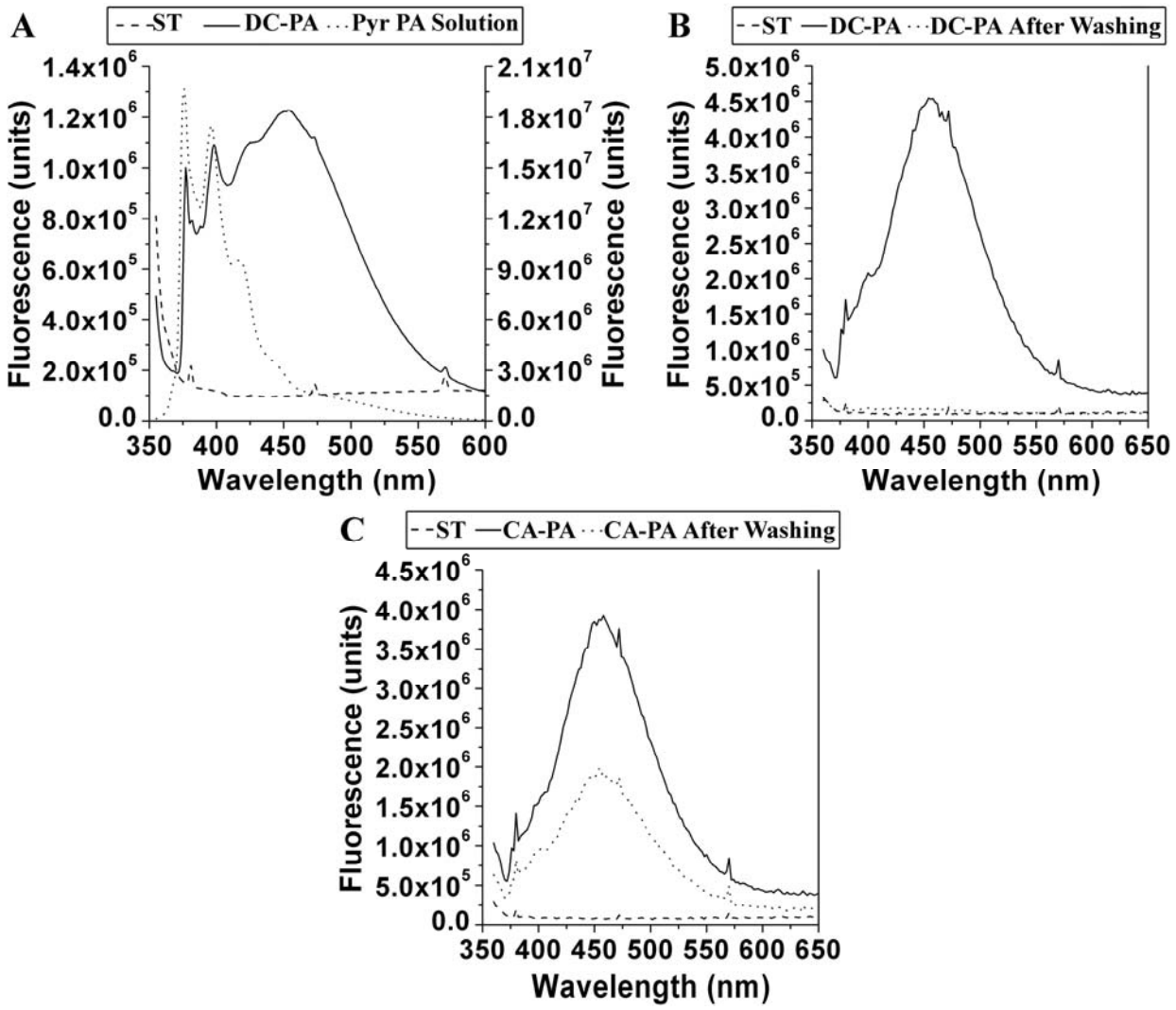


**Figure 3.13 Fluorimetry spectra of pyr-PA coatings on NiTi. Graph (A) shows the spectra for ST NiTi and a typical DC-PA NiTi sample (left scale bar), and the pyr-PA in solution (right scale bar). Upon self-assembly of the PA molecules when dried on the NiTi, an excimer signal is observed. Graph (B) shows the elimination of the characteristic pyr-PA signal after washing DC-PA, while graph (C) shows conservation of the pyr-PA excimer signal after washing CA-PA, indicating the covalent coupling reaction enabled the retention of assembled pyr-PA on the NiTi.**

### 3.3.5 Cellular Response to PA Coated NiTi Samples

When an implant with a covalently bound coating is placed *in situ*, the surface of the substrate undoubtedly changes over time. In the present case, the adjacent tissue will initially come in contact with the PA nanofibers, which are designed to elicit an initial response, such as

cellular adhesion. As the cells respond to this surface, they will attach to the surface and begin to secrete a host of proteins that will eventually become ECM. The cells will also start to resorb the biodegradable PA nanofibers, and eventually come into contact with the underlying silane layer and NiTi substrate. Consequently, it is of great interest to assess the biological response of relevant cells to these materials *in vitro*. To evaluate these factors, we used a 7 day cell quantification assay (CyQuant) and SEM imaging to assess any potential negative biological response to the model RGDS containing PA ($C_{16}$-RGDS PA) and other materials used to create covalently bound PA coatings on silanized NiTi.

For cell quantification, the samples assayed included the various stages between chemically treated NiTi and NiTi with covalently bound PA (T, ST, ST+CA, CA-PA, DC-PA, and T+PA). The results of the proliferation assay are shown in Figure 3.14A. All samples demonstrated cell proliferation from the initial seeding density, indicated by the dashed horizontal line. Chemically treated NiTi before and after silanization (T, ST), with covalently bound PA (CA-PA), and the covalent attachment control (ST+CA) showed no statistical difference in cell number at day 7. However, samples with drop-cast PA on bare or silanized NiTi (T+PA and DC-PA) had significantly ($P<0.01$) lower cell numbers than the other sample types, and significantly different ($P<0.05$) from one another. To understand the cause of diminished cell proliferation on the non-covalently bound PA samples, the number of viable cells removed during media exchanges was evaluated for chemically treated NiTi (T), and PA coated NiTi before and after covalent attachment (DC-PA and CA-PA), as shown in Figure 3.14B. There is a statistically significant increase in the number of viable cells removed from the non-covalently bound PA samples (DC-PA) compared to bare NiTi or covalently bound PA samples (T and CA-

PA) at 1 day ($P<0.05$) and 3 days ($P<0.01$). There was no significant difference at 5 days between the sample types because most of the cells on the DC-PA samples were already removed.

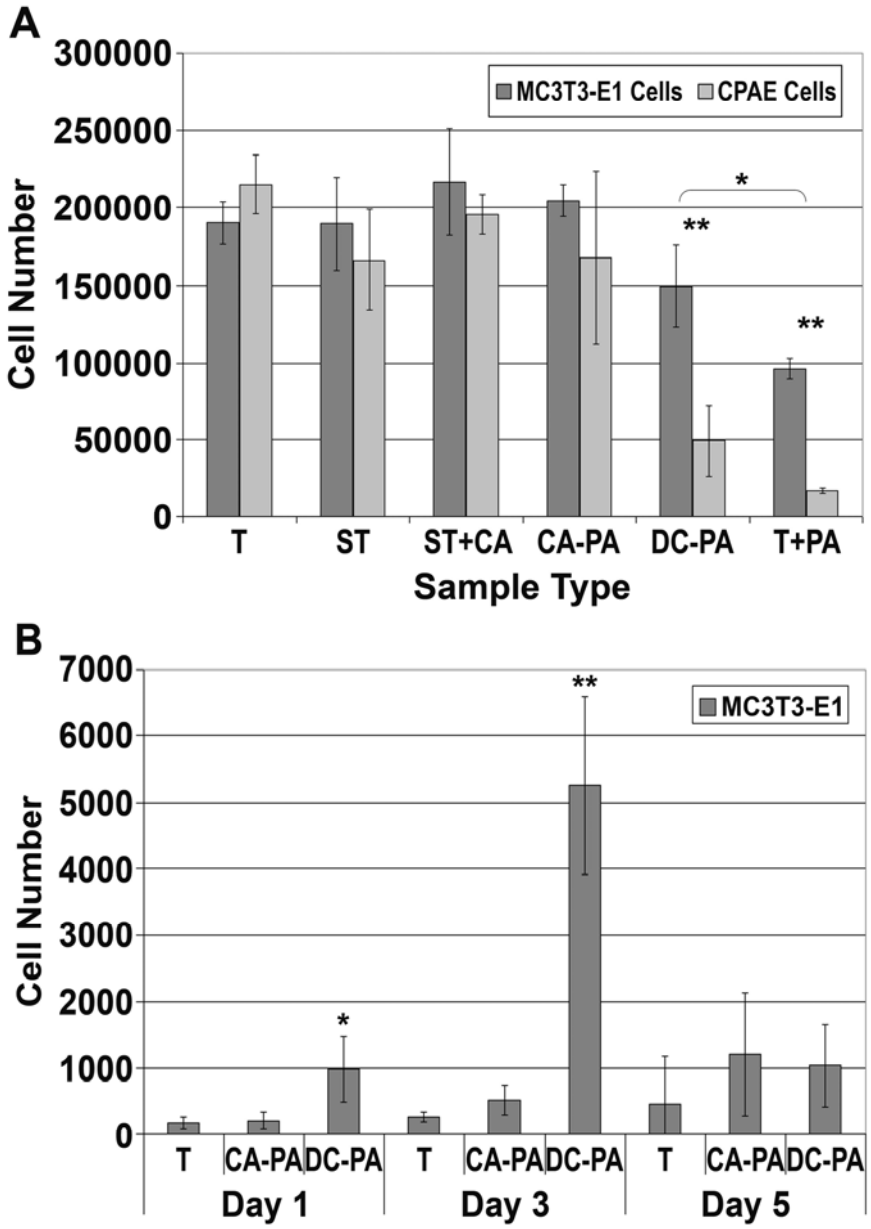


**Figure 3.14 7-day CyQuant® proliferation assay results for MC3T3-E1 and CPAE cells on various modified NiTi substrates (A) and quantification by CyQuant® assay for the number of cells detached during medium changing (B). In (A), DC-PA and T+PA are both significantly different from T, ST, ST+CA, and CA-PA ($P<0.01$). T+PA is also significantly different from DC-PA ($P<0.05$). In (B), DC-PA is significantly different from T and CA-PA at day 1 ($P<0.05$) and day 3 ($P<0.01$).**

SEM images of MC3T3-E1 and CPAE cells cultured for 1 day on the same samples used for cell quantification (T, ST, DC-PA, CA-PA, and ST+CA), except for PA coated NiTi without silane (T+PA), are shown in Figure 3.15. Both cells types adhere to and spread on each sample type. The cell morphology indicates normal cellular behavior; rounded cells that would indicate necrosis were not observed. Images were also taken for both cell types on bare NiTi (T) and PA coated NiTi before and after covalent attachment (CA-PA and DC-PA) at days 3 and 7, as shown in Figure 3.16. At day 3, both cell types have proliferated significantly and cover a majority of bare NiTi and covalently bound PA NiTi samples, while only a few small colonies of cells were observed on the drop-cast PA NiTi samples. By day 7, both cell types were observed to have grown to confluency on bare NiTi (not shown) and covalently bound PA samples, while the drop-cast PA samples (not shown) still resembled the day 3 samples.

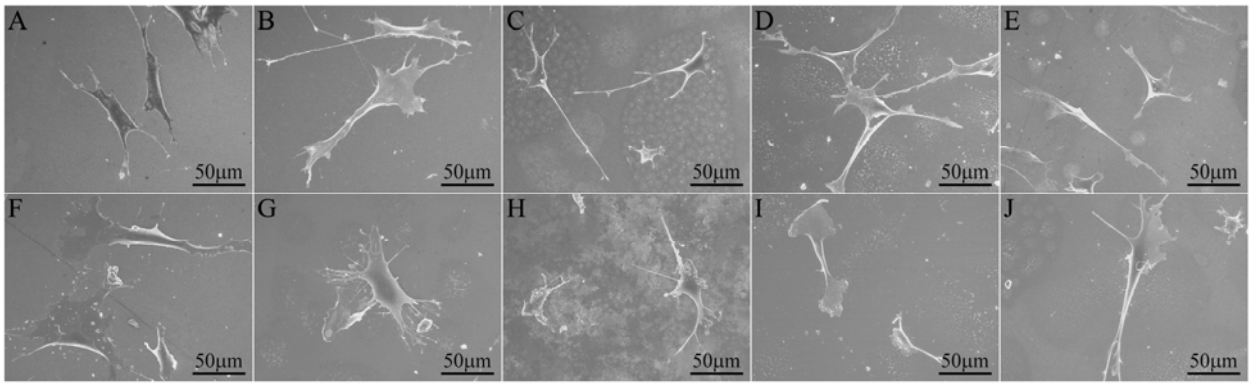


**Figure 3.15 SEM images of MC3T3-E1 cells (top row) and CPAE cells (bottom row) on NiTi: (A, F) T; (B, G) ST; (C, H) DC-PA; (D, I) CA-PA, and (E, J) ST+CA, all showing initial attachment and spreading after cell seeding.**

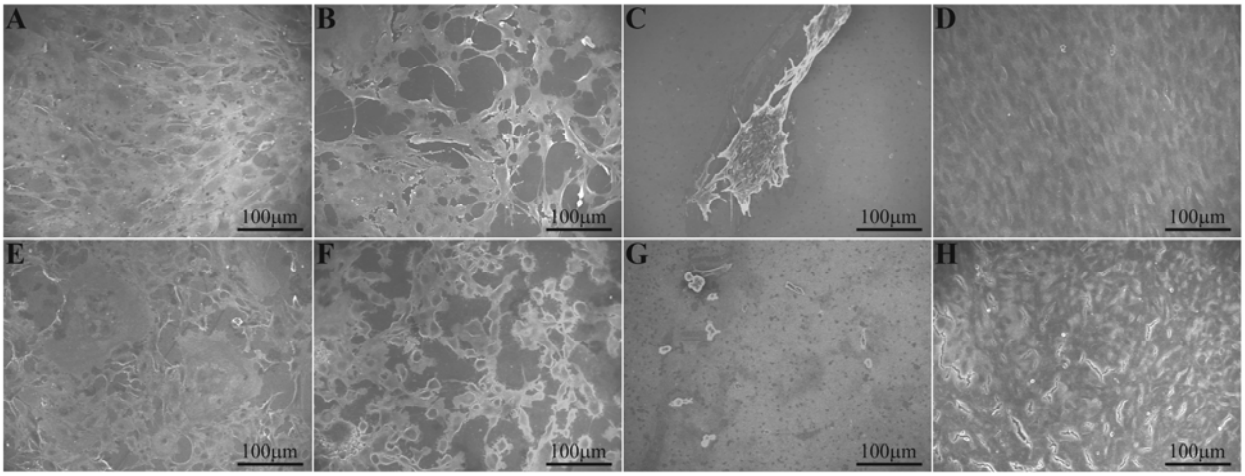


**Figure 3.16 SEM images of MC3T3-E1 (top row) and CPAE (bottom row) cells on NiTi: (A, E) T, Day 3; (B, F) CA-PA, Day 3; (C, G) DC-PA, Day 3; (D, H) CA-PA, Day 7. There is a drastic reduction in cell attachment when the PA nanofibers are not covalently bound to the silanized NiTi (DC-PA), whereas cells attach and grow to confluency on the CA-PA surfaces.**

Several interesting findings can be concluded from these experiments. First, the cell quantification at day 7 was statistically the same for each chemically treated NiTi before and after silanization (T and ST), with covalently bound PA (CA-PA), and for the covalent attachment control (ST+CA). At first, this appears to imply no preference between any of these surfaces; however, upon viewing the day 7 SEM images it is clear that the cells have reached confluency on each of these surfaces. Therefore, the lack of statistical difference is simply due to the fact that both cell types have proliferated to confluency on each of these surfaces, and hence no negative effect on cell viability can be attributed to the NiTi, silane, or the PA molecules. This is also confirmed by the SEM images in Figure 3.16, which shows the cells to be adhered and spreading to all surfaces, as is typical of healthy cells. In fact, there is no obvious difference of cell morphology among the different substrates. Secondly, we see that there was a decreased number of cells on silanized NiTi with drop-cast PA, and even less on bare NiTi with drop-cast PA. This effect cannot be attributed to the PA itself because the surface exposed to the

cells is effectively identical to the covalently bound PA samples. However, there is a difference in the interaction between the PA nanofibers and the underlying substrate. For the covalently bound PA samples, the PA is bound very strongly to the silane layer; for silanized NiTi with drop-cast PA, there is electrostatic interaction between the negatively charged PA molecule and the positively charged free amines of the silane layer; and for the bare NiTi with drop-cast PA, there are Van der Waals attractive forces but repulsive electrostatic forces between the negatively charged PA and oxide layer. Consequently, it is quite possible that the cells do in fact like the PA, so much so that they might be binding the RGDS epitopes via integrin receptors[58] and pulling the nanofibers from the surface, thereby inhibiting cell spreading and motility, and even possibly detaching from the substrate altogether. Given the complete coverage of nanofibers on the surface, there is sufficient PA for this to occur. To test this hypothesis, chemically treated NiTi (T) and PA coated NiTi before and after covalent attachment (DC-PA and CA-PA) were cultured and the exchanged media was collected and incubated to allow for viable cells to re-plate in a culture dish. The quantitative results shown in Figure 3.14B confirm this hypothesis. There is a significant increase in the number of cells detaching from the drop-cast PA samples compared to the covalently bound PA samples and bare NiTi samples, while the latter two are not statistically different. This indicates that viable cells are detaching from the substrate when the PA is not strongly bound to the NiTi. This is confirmed by the SEM images in Figure 3.16, showing good cell proliferation and spreading at day 3 in both the bare NiTi and covalently bound PA samples, with very few cells surviving the media exchange and SEM sample preparation on the drop-cast PA samples. Therefore we can conclude that the cells prefer the PA over the silane or NiTi, as evident by their propensity to bind the PA and detach

rather than adhere to the underlying silane or NiTi. Furthermore, it is interesting that the detached cells do not undergo apoptosis after detaching. This may indicate that the detachment is occurring during or media exchange, or possibly that the interaction of the cells with the PA is leading to the release of soluble mediators that cause the inhibition of apoptosis[121]. Third, the results confirm that there is no cytotoxic effect from any residual reagents used for covalent attachment. When the silanized samples underwent the covalent attachment reaction in the absence of PA nanofibers (ST+CA), there was no effect on cell viability as compared to the silanized samples from any residual chemical reagents.

## *3.4 Conclusions*

A method to covalently attach self-assembled PA nanofibers on pre-treated NiTi substrates has been demonstrated using an intermediary aminosilane layer. Using APDMES as a model organosilane, a chemical modification treatment was selected on the basis of maximized silane coverage and a resulting NiTi surface oxide that contains very low nickel and significantly higher $TiO_2$ levels. A novel vapor deposition method was then developed to create a homogenous, more robust coating of APTES molecules on NiTi substrates. Covalent attachment of PA nanofibers to the intermediary silane layer does not cause disassembly of the nanofiber architecture and leads to retention of the PA nanofibers on the surface under harsh washing conditions at physiological salt concentrations. Biological assay results showed no toxic effect on endothelial and pre-osteoblast cells by any of the materials or reagents used. Furthermore, we have demonstrated the importance of covalently binding the PA nanofibers to the substrate to create robust coatings, leading to a confluent cell monolayer within 7 days. We have developed a general strategy to create modified NiTi surfaces that can be used as biomedical implants with

enhanced capabilities to facilitate cell adhesion, proliferation, and potentially a variety of implant-specific cellular responses.

# CHAPTER 4: THE DEVELOPMENT OF PEPTIDE AMPHIPHILE – TITANIUM FOAM (PA-Ti) HYBRIDS FOR BONE APPLICATIONS

## *4.1 Introduction*

The lifetime of orthopaedic implants is limited primarily by implant loosening, a result of interfacial breakdown and stress shielding[122]. In past clinical practice, fixation of implants has primarily been achieved via screws and bone cements[123]. While initial stability is adequately realized, cement degradation over time or screw loosening eventually lead to implant instability and required surgical revision. Furthermore, implant materials that are much stiffer than bone, e.g., titanium, stainless steel, and cobalt alloys, often lead to stress shielding and subsequent resorption of surrounding bone[124, 125]. The current approach of creating porous surfaces on implants attempts to improve fixation, but does not solve the issue of stiffness mismatch. A strategy addressing both problems is to use a porous metallic implant, which allows for the ingrowth of bone to achieve improved fixation and also reduces the Young's modulus of the implant material to better match that of bone[32, 126-130].

Prior work has shown that metallic scaffolds with pores that are either isolated (closed to the surface) or interconnected (usually open to the surface) can be fabricated with biomedical alloys, including commercially-pure titanium (CP-Ti)[36], the alloy Ti-6Al-4V[13, 131, 132], and near-equiatomic nickel-titanium alloy (NiTi)[15, 133]. Commonly used for bone implants, the Ti-6Al-4V alloy can be foamed by solid-state expansion of argon to a fully open porosity of approximately 50%[134]. This allows for tissue ingrowth as well as considerable elastic modulus reduction, reducing risks of bone resorption due to stiffness mismatch. However, these CP-Ti and Ti-6Al-

4V foams remain bioinert at best, without direct capacity to influence cell behavior or encourage bone formation.

There has been recent interest on the design of surfaces on the nanoscale for cell signaling[120, 135-137]. The Stupp laboratory has developed a system of peptide amphiphile molecules (PAs) that self-assemble in aqueous solutions under the appropriate conditions to create high aspect ratio nanofibers that can form a self-supporting gel at low molar percent (10 mM)[55, 56]. Self-assembly can be triggered by charge screening via changes in pH or the addition of multi-valent ion or charged molecules. Our PAs are designed such that when self-assembly occurs, a bioactive epitope can be presented in high density on the periphery of the nanofiber. This portion of the PA can be designed with a variety of biologically-relevant epitopes without disrupting the self-assembling properties, allowing for the creation of nanofibers that can present an array of epitopes for cellular attachment, signaling, or biomolecule binding[55, 65, 99]. As a result, we are able to create an artificial matrix with the advantage of being able to signal host tissue.

In this work, the development of a bioactive hybrid bone implant consisting of a Ti-6Al-4V foam filled with a PA nanofiber matrix produced by in-situ self-assembly within the foam is reported. A new method for cell encapsulation within these hybrids is also described, which may be desirable to enhance the post-operative recovery associated with cement-free skeletal implants, by increasing cellular proliferation and mineralization, both within the implant and at the implant-tissue interface.

## *4.2 Materials and Methods*

All chemical reagents, unless otherwise noted, were purchased from Sigma-Aldrich (St. Louis, MO). Solvents were purchased from Fisher Scientific (Hanover Park, IL). Amino acids

were purchased from EMD Biosciences (San Diego, CA). Cellular medium components were purchased from Invitrogen (Carlsbad, CA) and other cell culture supplies from VWR (West Chester, PA). pEGFP-N1 vector was generously provided by Dr. Earl Cheng (Children's Memorial Hospital, Chicago, IL).

### 4.2.1 Ti-6Al-4V Foam Processing

Procedures established previously for superplastic foaming of CP-Ti and Ti-6Al-4V were followed[12, 36-38, 138]. Pre-alloyed Ti-6Al-4V powders (Starmet Corporation) with a particle size range of 149-177 μm were poured in a mild-steel can which was weld-sealed after being evacuated and backfilled with 330 kPa of 99.999% pure argon gas. The can containing the gas and powders was then densified in a hot isostatic press (HIP) for 4 hours at 950˚C and at a pressure of 100 MPa. The steel can was then removed and the Ti-6Al-4V billet (10 mm diameter and 10 mm height) was annealed for 180 hours in a high-vacuum furnace (residual gas pressure: $10^{-5}$ mTorr) to let the entrapped argon, present as small, isolated spherical pores, expand within the solid Ti-6Al-4V matrix. Temperature was continuously cycled between 890 and 1030˚C with an 8 minute period, so as to induce transformation superplasticity within the Ti-6Al-4V matrix, which has been previously demonstrated to enhance the foaming rate as compared to isothermal annealing[12, 36-38]. The total porosity of the foamed billet was determined by the water-displacement Archimedes method and the closed porosity by helium pycnometry.

The foamed Ti-6Al-4V billet was cut into 1-2 x 4 x 4 $mm^3$ samples using a diamond saw with oil lubrication, which were ultrasonically cleaned with dichloromethane, acetone, and water for 15 minutes each. To remove metal smearing into the external pores from cutting, the samples were exposed to an aqueous solution of 0.25% HF and 2.5% $HNO_3$ for 45 minutes. After

repassivation with 40% $HNO_3$ for 30 minutes, samples were repeatedly rinsed in ultrapure water and dried in a desiccator.

### 4.2.2 Peptide Amphiphile Synthesis and Preparation

Peptide amphiphiles (PA) were synthesized using methods previously described[65, 66]. Solid phase peptide synthesis (SPPS) was performed using Rink amide MBHA resin with standard 9-Fluorenylmethoxycarbonyl (Fmoc) protected amino acids in N,N-dimethylformamide (DMF), diisopropylethylamine (DIEA) and 2-(1H-Benzotriazol-1-yl)-1,1,3,3-tetramethyluronium hexafluorophosphate (HBTU). To create the branched PA architecture, palmitic acid was first coupled to the ε-amine on a lysine to create a hydrophobic tail group. The peptide sequence was then synthesized using orthogonal protecting group chemistry. Selective deprotection of Fmoc, Boc, and 4-methyl trityl (Mtt) protecting groups allowed for control over the design of the PA. After synthesis, the PA was cleaved from the resin using TFA:Triisopropyl silane (TIS): water (95:2.5:2.5), precipitated with ice-cold ether, solubilized in water, and dried by lyopholization. The product was then characterized using MALDI-TOF and analytical HPLC.

### 4.2.3 Cell Culture Experiments

Mouse calvarial pre-osteoblastic (MC3T3-E1) cells were cultured under standard tissue culture conditions at 37˚C and 5% $CO_2$ in Minimum Essential Medium α (MEMα) medium supplemented with 10% fetal bovine serum (FBS), 100 units/mL penicillin and streptomycin, 10 mM β-glycerophosphate, 50 μg/mL ascorbic acid. For confocal imaging, it was desirable to transfect a population of MC3T3-E1 cells with a green fluorescent protein vector to enable fluorescent imaging. This was achieved by plating cells at greater than 90% confluency in

antibiotic-free MEMα medium, adding 1μg pEGFP-N1 vector and 2.3 μL Lipofectamine™ 2000 transfection reagent (Invitrogen) in antibiotic-free MEMα medium without serum, mixing gently and incubating for 24 hours at 37˚C. Cells were then passaged and cultured in MEMα medium for one day, followed by medium exchange with selection medium consisting of penicillin/streptomycin-free MEMα medium containing 600 μg/mL Geneticin® selective antibiotic (Invitrogen). Cells were cultured in selection medium for 14 days, followed by culturing in maintenance medium, consisting of penicillin/streptomycin-free MEMα medium containing 300 μg/mL Geneticin® selective antibiotic. Cells were then sorted by flow cytometry to obtain a homogeneous population for cell experiments hereon termed GFP-MC3T3-E1 cells. All experiments with GFP-MC3T3-E1 cells were performed using the maintenance medium.

### 4.2.4 PA-Ti Hybrid Preparation

To create PA gels within the Ti-6Al-4V foams, lyophilized PA powder was solubilized in ultrapure water to 2 wt %, pH adjusted to approximately 7, and further diluted to 1 wt % with Dulbecco's phosphate buffered saline (PBS). For the biotinylated PA, FITC-labeled avidin was added in at 1:400 molar ratio. Meanwhile, Ti-6Al-4V foams were autoclave sterilized, and pre-wet via graded soakings starting with 100% ethanol and ending with 100% ultrapure water. The pre-wet Ti-6Al-4V foam samples were then placed in the PA, and agitated on a plate shaker at low speed for 30 minutes. RGDS PA or S(P) & RGDS PA mixtures were gelled with the addition of 7 μL of 1 M $CaCl_2$ to each sample solution (~85mM $CaCl_2$ final concentration), while the biotinylated PA was gelled by subjecting the samples to ammonium hydroxide ($NH_4OH$) vapor to bring the pH up to ~8.5. Following gelation, samples were annealed by incubation at 37˚C and 5% $CO_2$ for 1.5 hours. For cellular assays and *in vivo* experiments, the

excess PA was scraped aseptically from the exterior. These PA nanofiber / Ti-6Al-4V foam hybrids are termed PA-Ti hybrids in the following. For *in vitro* mineralization, PA-Ti hybrids were incubated at 37˚C and 5% $CO_2$ in human mesenchymal stem cell osteogenic medium (Lonza) supplemented with 20mM $CaCl_2$ for 7 days. As described below, PA-Ti hybrid samples were characterized by SEM and/or confocal microscopy.

### 4.2.5 Cell Encapsulation

To encapsulate cells within the PA-Ti hybrid a similar procedure was used. Cells were detached from culture plates by trypsinization, counted, and resuspended in PBS without calcium or magnesium at twice the final cell concentration. Lyophilized PA powder was solubilized in 0.1 M ammonium hydroxide to 4 weight percent, diluted to 2 weight percent with PBS, and pH adjusted to ~7 with 0.1 M HCl. The PA solution was then sterilized by UV radiation for 30 minutes. Equal volumes of the PA solution and cell suspension were then mixed and aliquoted into a half-area 96-well plate. The pre-wet Ti-6Al-4V foams were again placed in the PA and cell solution, shaken for 30 minutes, gelled with $CaCl_2$, and annealed for 1.5 hours at 37˚C and 5% $CO_2$. Samples for SEM and confocal microscopy were then cultured overnight in maintenance medium.

### 4.2.6 Biological Analysis

For cell quantification, PA-Ti hybrid samples were extracted and frozen in liquid nitrogen, lyophilized, and digested in a papain solution[139]. Briefly, samples were incubated in 0.125 mg/mL papain activated with 1.76 mg/mL cysteine in phosphate buffer with EDTA (0.1M $Na_2HPO_4$, 0.01M $Na_2EDTA$, pH adjusted with 1N NaOH) for 16 hours at 60˚C. Samples were

then assayed for dsDNA content using a Quant-iT PicoGreen dsDNA Assay Kit (Molecular Probes) as per protocol. A 5 μL aliquot of digestion solution was incubated with 95 μL of 1X TE and 100 μL of PicoGreen Working Reagent for 5 minutes and fluorescence was read on a Gemini EM fluorescence/chemiluminescence plate reader with ex/em of 480/520 nm. A standard curve made with calf thymus DNA was used to convert fluorescence to cell number assuming 7.7 pg DNA/cell[140].

PA-Ti hybrid samples with and without cells for SEM and confocal microscopy were extracted and pre-fixed with 1% gluteraldehyde in MEMα on ice for one hour. Samples were rinsed in PBS for 20 minutes, and fixed in 2% formaldehyde, 2% gluteraldehyde in 0.1 M cacodylate buffer for 3 hours at room temperature and then overnight at 4˚C. Samples were then rinsed in cacodylate buffer for 20 minutes and dehydrated using a graded series of ethanol. Mineralized PA-Ti hybrid samples for SEM were removed from media and dehydrated in graded ethanol. At this point, all SEM samples were critical point dried, coated with 3nm Au-Pd, and imaged using a Hitachi S-4500 (Schaumburg, IL) with a cold field emission electron gun at 3 kV with a current of 20 mA or an FEI Quanta ESEM fitted with a Schottky thermal field emission gun and Oxford EDS at 10kV. A secondary electron detector was used for high-resolution imaging. Alternatively, samples for confocal microscopy were embedded in EmBed-812/ DER 73 (Electron Microscopy Sciences) according to protocol. Briefly, samples were rinsed in propylene oxide for 20 minutes, followed by 50:50 solution of EMbed-812/ DER 73:propylene oxide overnight, and then straight EMbed-812/ DER 73 with several fresh exchanges. The resin was then cured for 24 hours each at 40˚C, 60˚C, and 70˚C. Embedded samples were then sectioned using a diamond saw and mounted on glass slides. Imaging was performed on a Leica

Confocal Laser Scanning System inverted microscope (Bannockburn, IL) using an argon laser and driven with Leica Confocal Software.

## *4.3 Results and Discussion*

### 4.3.1 Ti-6Al-4V Foam Processing

The foamed billet had a total porosity of 52.5% after 180 hours of thermal cycle foaming (8 minutes per cycle from 890-1030˚C). A 1 cm cube sample cut from the billet had a total porosity of 52.5% with 14.2% closed porosity. When the pores expand, they merge with each other forming networks which, as they connect to the billet surface, allow for the gas to escape, thus eliminating the driving force for foaming and leading to open porosity. The porosity of 52.5% achieved here is higher than any other value reported in the literature for Ti-6Al-4V foams produced by solid-state expansion at constant temperature: 32% for Kearns *et al.* after 46 hours at 1240˚C[35, 141] (or 40% for several days at 1250˚C[35]), 23% for Queheillalt *et al.* after 10 hours at 920˚C[132] and 35-40% for Schwartz *et al.* after 24 hours at 920˚C[142]. The higher porosity achieved here illustrates that transformation superplasticity, produced by thermal cycling conditions, delays pore merging due to fracture of pore walls (leading to the formation of a pore network and eventual escape of gas from the sample), as compared to isothermal, non-superplastic foaming conditions used in the previous studies. It is noteworthy that even though the foams in the latter two studies were faced with dense Ti-6Al-4V sheets (thus preventing escape of gas on two sides of the foam), their porosity remained below that achieved here under superplastic condition. Based on their porosity of 52.5%, the present foam stiffness is calculated as 25 GPa (using a Young's modulus of 110 GPa for Ti-6Al-4V and standard equations linking

stiffness with the square of porosity[143]), close to the range of dense cortical bone (wet at low strain rate, 15.2 GPa; wet at high strain rate, 40.7 GPa[1]).

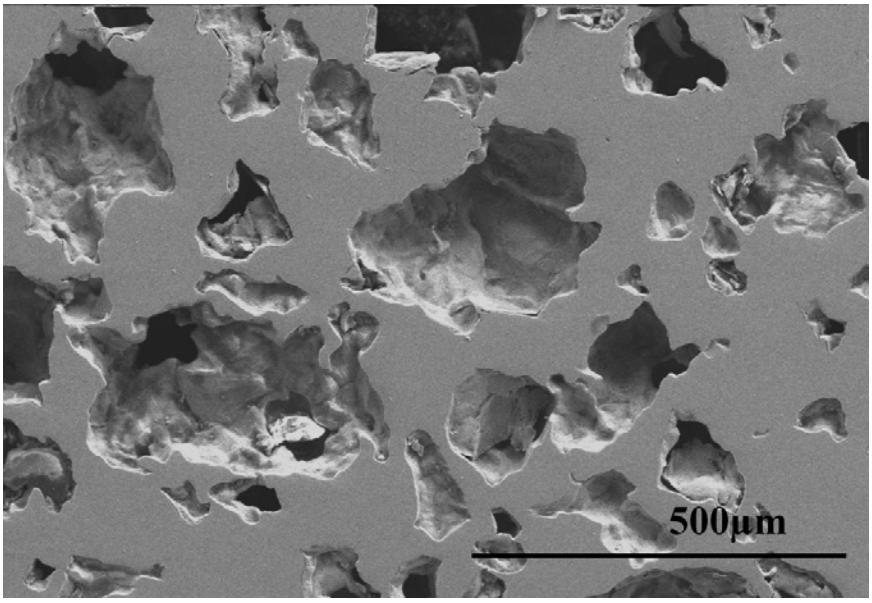


**Figure 4.1 SEM micrograph of polished, bare Ti-6Al-4V foam in cross-section. The mean line intercept was 110 µm, corresponding to a pore diameter of 165 µm. The pores are irregular in shape and equiaxed, showing no preferential orientation.**

Figure 4.1 shows an SEM micrograph of a polished cross-section of the foam. The mean line intercept is 110 µm, corresponding to a pore diameter of 165 µm, under the assumption that pores are spherical, monosized and unconnected (real pore size differs from this value, given that these assumptions are not fulfilled). It is generally accepted that the optimum pore diameter for bone ingrowth is 150-400 µm[32], although it has been shown that bone can grow into pores as small as 60 µm[144]. The pores in Figure 4.1 are jagged and equiaxed, as also observed in previous studies of CP-Ti foams with similar high porosity[12, 37], where it was shown that protrusions within the large pores are remnants of the fractured pores walls initially separating small pores that have merged.

### 4.3.2 Preparation of the PA-Ti Hybrid

Two complementary microscopic techniques were used to characterize the structure of the PA-Ti hybrids. First, SEM was utilized to image the exterior surfaces and the PA nanostructure. Second, confocal microscopy of cross-sectioned samples was performed to characterize study the interior of the PA-Ti hybrids.

SEM images were taken of the bare exterior surface of the Ti-6Al-4 foams (after acid treatment and repassivation) and the PA-Ti hybrids, as shown in Figure 4.2. A low magnification image (Figure 4.2(B)) shows the irregular shape of pores in the foam, also visible in the cross-section image in Figure 4.3. When the hybrid is created by triggering self-assembly of the PA solution contained within the Ti-6Al-4V foam, the external pores are completely filled with the PA nanofiber matrix, as shown in Figure 4.2(C and E). Higher magnification images (Figure 4.2D and E) reveal very high aspect ratio, self-assembled PA nanofibers forming a complex tangled matrix not only within the larger macroscopic porosity of the Ti-6Al-4V foam, but also as a thin layer on the outer surfaces of the Ti-6Al-4V foam. This may allow implants to have a bioactive matrix within the larger scale pores of the Ti-6Al-4V, but also on their exterior surfaces that come in direct contact with host tissues.

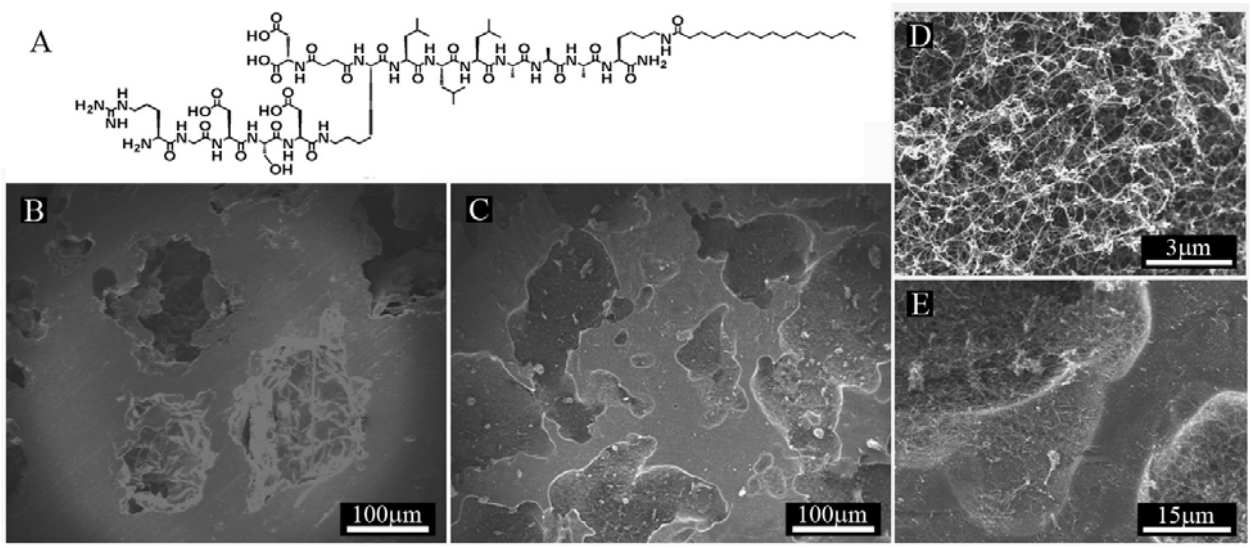


**Figure 4.2 (A) Chemical structure of the peptide amphiphile (PA) used to infiltrate and fill the pores of the Ti-6Al-4V foam. Scanning electron microscopy (SEM) images of (B) the bare Ti-6Al-4V foam; (C) Ti-6Al-4V foam filled with PA gel; (D) higher magnification of the self-assembled PA nanofibers forming a three dimensional matrix within the pores; and (E) higher magnification of the PA coating the Ti-6Al-4V foam surface and filling the pores.**

Confocal microscopy images were taken of sectioned Ti-6Al-4V foams to evaluate the effectiveness of the PA to self-assemble into a gel matrix within the metallic foam. To be able to image the PA, a biotinylated version of the PA used for SEM and the cell experiments was used in conjunction with FITC-labeled avidin. Given the well known strong interactions between avidin and biotin[145-147], previous work in the Stupp laboratory has shown this to be a useful method to fluorescently tag PA using FITC-labeled avidin[66]. Figure 4.3 shows the chemical structure of the biotinylated PA (A) and the resulting confocal images (B-D). The images shown in Figure 4.3(B-D) are composites of multiple dual-channel overlaid images in order to show the full cross-section of the sample. The first channel measured reflectance (grey) while the second channel measured GFP fluorescence (green). Figure 4.3(B) shows Ti-6Al-4V foam that has been impregnated with a biotinylated PA and FITC-labeled avidin; Figure 4.3(C) shows Ti-6Al-4V foam that has been impregnated with only biotinylated PA; and Figure 4.3(D) shows bare Ti-

6Al-4V foam without PA that was embedded with acrylic. All samples were imaged under identical conditions. As expected, there is no observed fluorescence from either the biotinylated PA itself (Figure 4.3C) or the foam embedded in acrylic (Figure 4.3D). Meanwhile, the FITC-labeled avidin that is bound to the biotinylated PA is clearly visible throughout the entire cross-section, confirming the ability of the PA to penetrate the interconnected porosity of the Ti-6Al-4V foam. Furthermore, since PA was retained within the pores after the five solution exchanges during the embedding procedure, it is very likely that self-assembly of the PA molecules into an entangled matrix had occurred due to successful diffusion of the $CaCl_2$ throughout the thickness of the sample. If the PA would have remained in the unassembled state, the PA would be expected to have been removed during the multiple solution exchanges. While the PA is shown to be present in the entire cross-section, there are several reasons why PA may not be visible in all of the pores. As mentioned earlier, not all the pores are interconnected. Secondly, incomplete infiltration of the resin may have led to PA removal during the sectioning process. Finally, reflectance from the metal made fluorescent imaging difficult. Consequently, it was not possible to obtain a single image that captured the fluorescence of all the pores. To better illustrate the true infiltration, we combined two images to create the composite image shown in Figure 4.3(B). The presence of the PA covering the exterior (top and bottom) surfaces of the foams is also apparent in the confocal images as previously demonstrated in the SEM images.

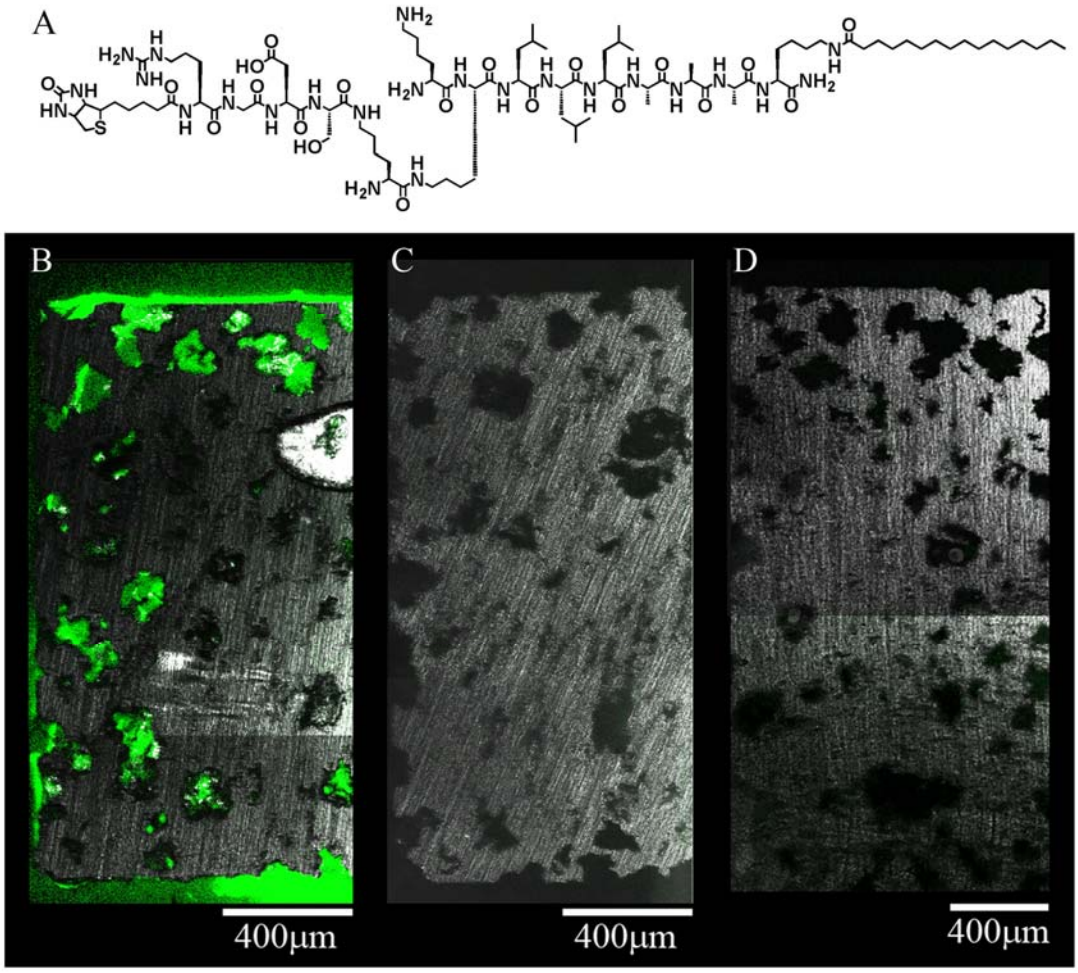


**Figure 4.3 Chemical structure of the biotinylated PA used for the confocal microscopy without cells (A), and the resulting confocal microscopy images of the biotinylated PA-Ti hybrids embedded in acrylic and cross-sectioned, showing (B) the fluorescence of avidin-FITC bound to biotinylated PA gelled throughout the cross-section of Ti-6Al-4V foam, (C) no fluorescence from a control sample of Ti-6Al-4V foam and biotin-PA without avidin-FITC, and (D) no fluorescence from a second control of Ti-6Al-4V in acrylic without PA.**

### 4.3.3 Mineralization of the PA Matrix in PA-Ti Hybrids

As described in Chapter 2, the PAs used to create the PA-Ti hybrids are capable of templating hydroxyapatite under culture conditions. To confirm that this remains true for the PA-Ti hybrids, samples were made with a mixed PA system consisting of 95 mol % phosphoserine-bearing PA (S(P) PA) and 5 mol % RGDS-bearing PA (RGDS PA). The

chemical structures of these molecules are shown in Figure 4.4A, B). After incubation of the PA-Ti hybrids for 7 days in medium, samples were evaluated for mineral formation by SEM. As seen in Figure 4.4(C-E), small spherical structures are observed to have nucleated and grown all along the PA nanofibers. High resolution imaging reveals that these spherical structures are fairly homogeneous in size and dispersion. Furthermore, due to their location along the fibers, and not in clusters or caught between the nanofibers, it is clear that these are not simply precipitates that have adsorbed onto the nanofibers, but rather they have originated from the nanofibers themselves. Analysis by EDS shows peaks for both calcium and phosphate, and quantification yields a Ca:P ratio of 1.71 +/- 0.18. This value is similar to that associated with hydroxyapatite (1.67) based on the formula $Ca_{10}(PO_4)_6(OH)_2$, and is anticipated based on the work described in Chapter 2 and by Hartgerink et al.[55].

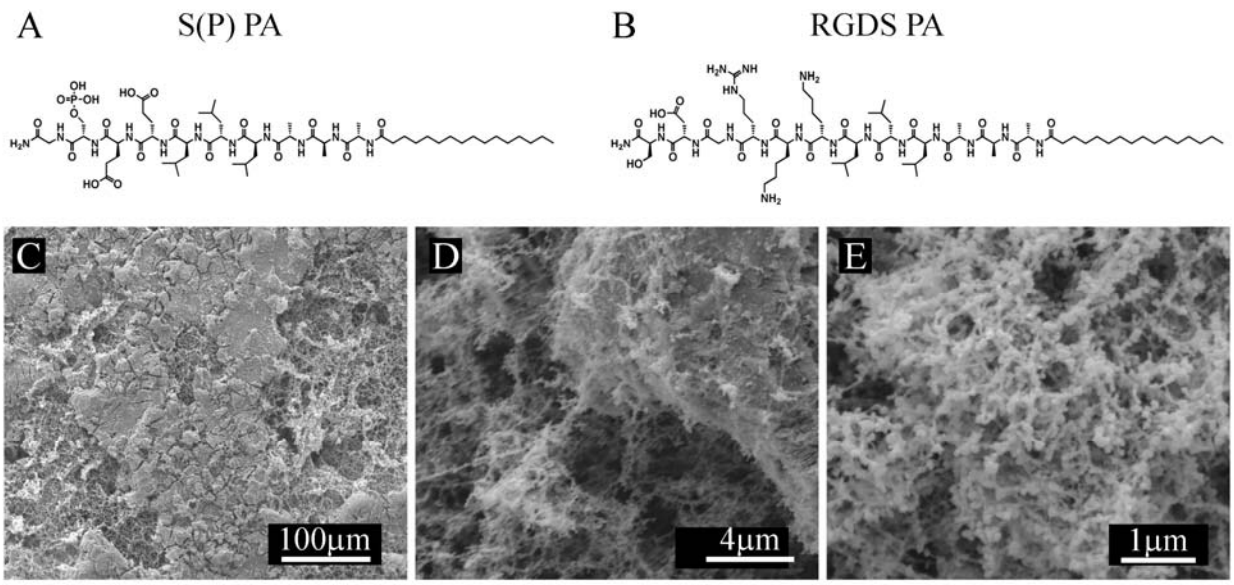


**Figure 4.4 Chemical structures of the S(P) PA and RGDS PA used to create PA-Ti Hybrids for mineralization (A, B). SEM images (C-E) show nanoscale bead-like mineral formation on the PA nanofibers. High magnification images (D-E) show the mineral formation only on the nanofibers, and not on the metal surface, indicating templating by the PA nanofibers. EDS quantification reveals a Ca:P ratio for the mineral as 1.71+/-0.18, in line with hydroxyapatite.**

### 4.3.4 *In vitro* Assessment of Potential PA Cytotoxicity

To assess any potential cytotoxicity of the PA, a live/dead assay was performed on non-GFP transfected MC3T3-E1 cells encapsulated in just the self-assembled RGDS PA gel. After five days of culture, fluorescent optical microscopy was used to qualitatively evaluate the number and morphology of live cells with calcein AM (green) and dead cells with ethidium homodimer (red). As shown in Figure 4.5, the vast majority of cells was alive and spread throughout the entire gel, indicating that there was no significant cytotoxic effect. In fact, the cells appeared to survive well in this environment, spreading in the PA nanofiber matrix and not migrating out of the gel. Live/dead was not performed on the PA-Ti hybrids due to the difficulties associated with fluorescent imaging of the opaque foams.

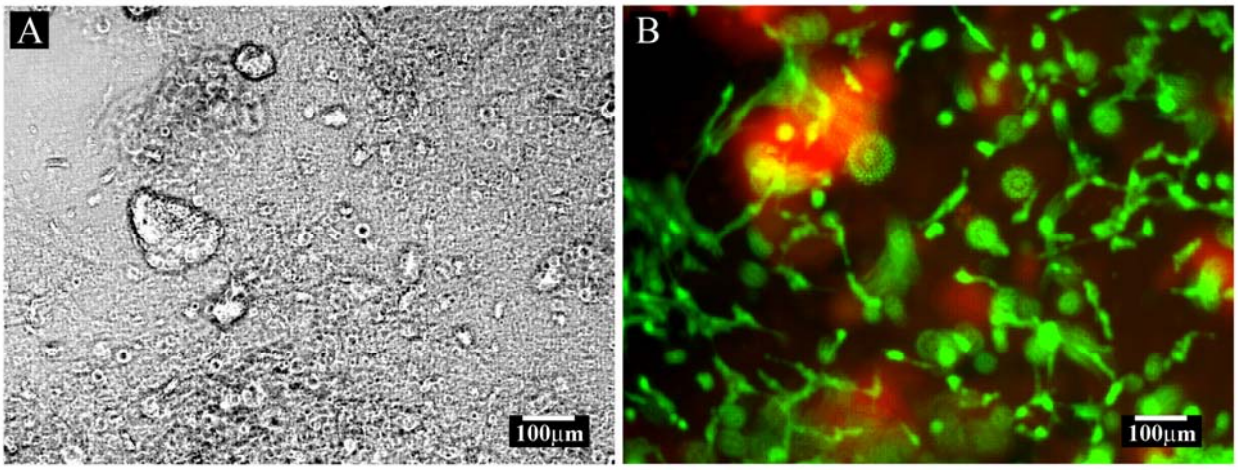


**Figure 4.5 Optical (A) and fluorescence (B) microscopy images of non-transfected MC3T3-E1 cells encapsulated within the nanofiber matrix of the PA shown in Figure 2(A). Almost all cells fluoresced green due to the conversion of calcein AM to calcein, indicative of live cells. The hazy red areas are background fluorescence due to the interaction of the PA with EthD-1.**

### 4.3.5 Encapsulation of Cells within Nanofiber Matrix of PA-Ti hybrid

Confirmation of the presence of cells encapsulated within the self-assembled PA nanofibers was determined by several approaches. First, a PicoGreen dsDNA assay was utilized to determine the number of cells associated with the PA-Ti hybrid. Secondly, qualitative observation of cells within the hybrids was achieved by confocal microscopy of cross-sectioned samples and SEM imaging of the exterior of the samples. Finally, a live/dead assay was performed to confirm the biocompatibility of the PA gel.

Quantification of the number of cells encapsulated in the PA-Ti hybrids was achieved by utilizing a Quant-iT PicoGreen dsDNA assay kit after 1.5 hours of incubation. Cell-encapsulated PA-Ti hybrids were created using PA solutions containing three different cell seeding densities. Five samplings from three to five foams were measured for each seeding density of $5 \times 10^5$, $1 \times 10^6$, and $5 \times 10^6$ cells/mL PA solutions. The samplings were averaged for each foam to determine the cell seeding, and error was set as the standard deviation of these averages. As shown in Figure 4.6, the resulting cell population encapsulated within the Ti-6Al-4V foams showed a general increase with increasing initial cell seeding concentrations. A correlation analysis demonstrated a good linear fit ($R^2 = 0.992$) between the initial cell seeding concentration and the resulting number of cells encapsulated within the Ti-6Al-4V foams. This demonstrates that cells can indeed be encapsulated within the PA-Ti hybrids, and that this can be done in a controlled manner.

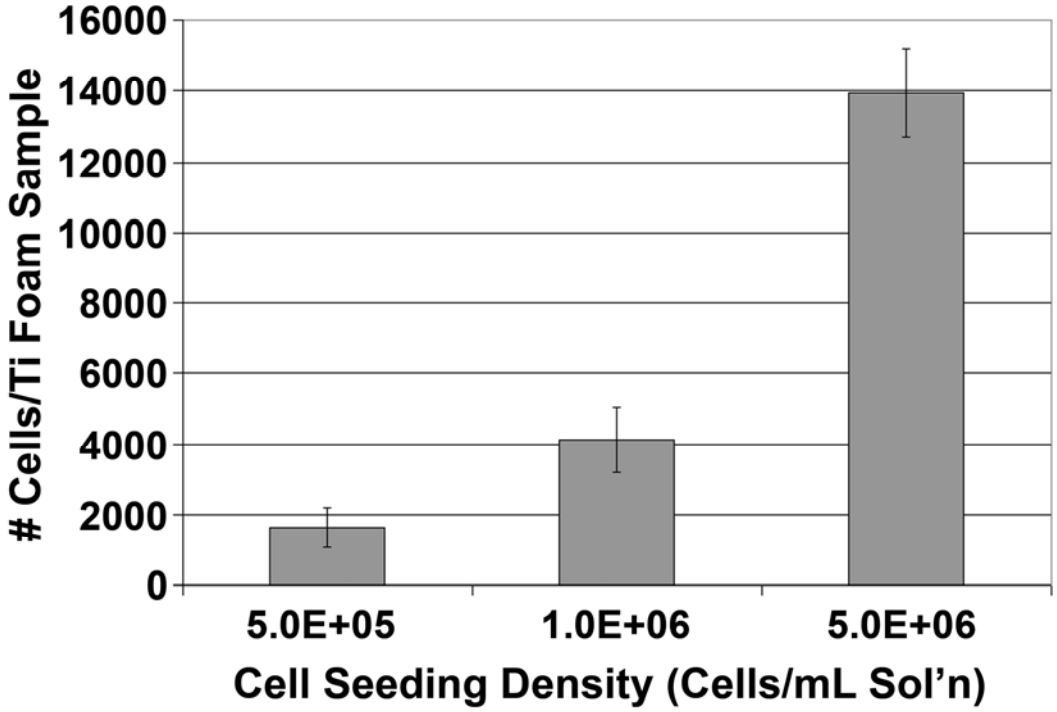


**Figure 4.6 Quantification of cells encapsulated within PA-Ti hybrids at different seeding densities, showing a direct correlation between seeding density and encapsulated cell number.**

Scanning electron microscopy (SEM) offered a qualitative method to observe cells encapsulated near the surface of the PA-Ti hybrids. As shown in Figure 4.7, encapsulated GFP-MC3T3-E1 cells can be seen within 100 μm from the surface of the sample, attaching and spreading in the PA nanofiber matrix that fills the Ti-6Al-4V foams. Culturing the samples for ~16 hours provided enough time for the cells to start to exhibit a reaction to their surrounding environment, yet not enough time for proliferation to distort the qualitative observations of the cellular location within the samples. The cells appear stretched in shape with extended processes, and more importantly, we did not observe rounded shapes that may be indicative of apoptosis. The experiments confirmed the presence of cells within the PA-Ti hybrids and their interaction with the surrounding PA matrix.

Fluorescent confocal microscopy was used to qualitatively confirm the presence the cells within the interior PA nanofiber matrix of the PA-Ti hybrids after 1.5 hours incubation. Fixed samples were embedded in acrylic and cross-sectioned for observation as described earlier. Figure 4.8 shows the two channels measured, reflectance in grey (A) and GFP fluorescence in green (B). Due to the particular angle of the sample and z-depth of the cells imaged, reflectance of the metal was also detected by the detector, giving a false fluorescence for the metal. Therefore, the true fluorescence is given by the subtraction of the (A) from (B). It is apparent from these images that the cells are indeed encapsulated within the PA nanofiber matrix as several are observed within the Ti-6Al-4V pore, as indicated with arrows in Figure 4.8(A, B). Because of the sharp z-depth resolution of the confocal microscope, it was determined that the cells are not attached to the pore surface above or below the plane of view, and they are also clearly not in contact with the pore surface within the imaging plane. Therefore, we can conclude that they are suspended within the PA nanofiber matrix. Furthermore, we expect to see individual cells spaced apart because the cells dispersed in solution were effectively entrapped as self-assembly of the nanofiber matrix occurred, minimal time was allowed for cell proliferation or migration, and also because out of plane cells are not visible due to the sharp z-depth imaged by confocal microscopy. Together with the SEM images, we can also conclude that the cells measured in the quantification assay are indeed encapsulated throughout the PA-Ti hybrid and not merely adhering to the exterior foam surface.

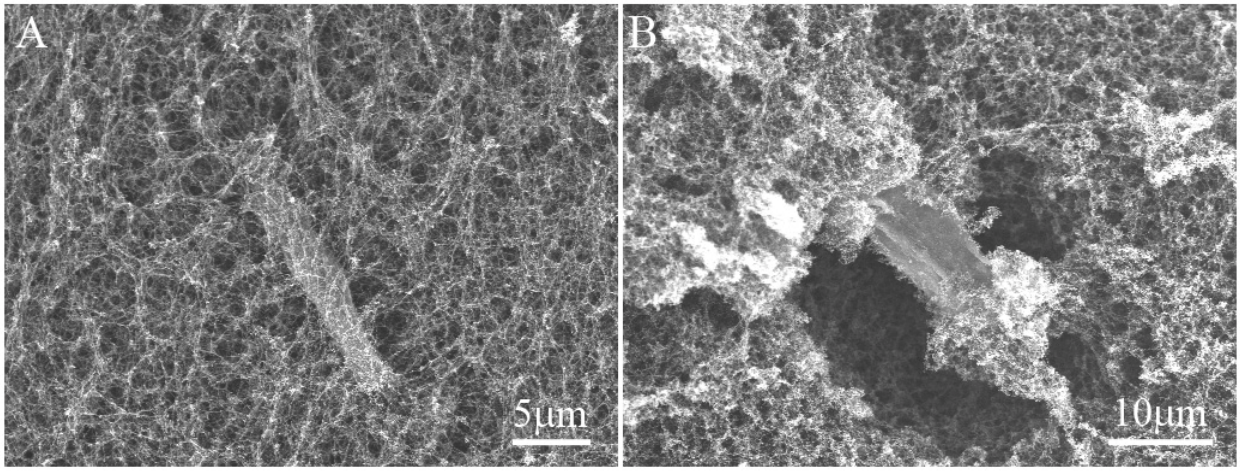


**Figure 4.7 SEM of GFP-transfected MC3T3-E1 cells encapsulated within PA-Ti hybrids. Cells encapsulated near the surface of the PA gel can be visualized spreading and pulling on the nanofibers presenting the RGDS cellular adhesion motif.**

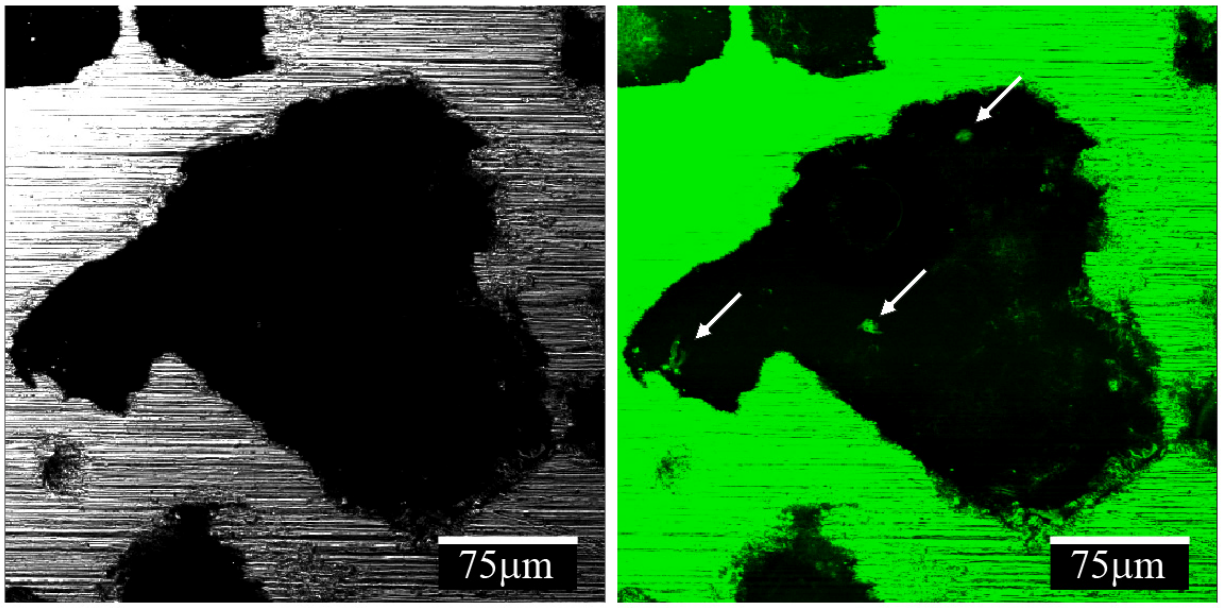


**Figure 4.8 Confocal microscopy of GFP-transfected MC3T3-E1 cells encapsulated within PA-Ti hybrids (cross-section). Left image is reflectance mode, while right image is fluorescence, showing cell suspended in an interior pore. The metal shows artificial fluorescence due to reflectance at the wavelength collected. The difference between the images is the true fluorescence of the cells, indicated by the arrows.**

## 4.4 Conclusions

This work demonstrates that Ti-6Al-4V foams with 52.5% porosity can be filled with a self-assembling peptide amphiphile to create a bioconductive hybrid. SEM showed that the structure of the PA nanofiber matrix is retained when filling the pores of the foam, while confocal microscopy showed that the PA infiltrates the entire thickness. The PA matrix has been shown to mineralize with calcium phosphate, is not cytotoxic, and can be used to encapsulate cells in the PA-Ti hybrids in a controlled manner. Self-assembly of peptide amphiphile nanofibers within pores of metallic foams have potential to induce mineralization and direct a cellular response from the host tissue at its interfaces with an implant.

# CHAPTER 5: *IN VITRO* ASSESSMENT OF PA-Ti HYBRIDS USING A ROTATING BIOREACTOR

## *5.1 Introduction*

Titanium and its alloys remain the optimum material for many biomedical implants, such as joint replacements and dental prostheses, due to the combination of excellent mechanical properties and an inert oxide surface layer. Compared with other biomedical alloys, such as stainless steels and cobalt-chrome (CoCr) alloys, titanium alloys have lower moduli, enhanced corrosion resistance, and good fatigue strength[124]. Additionally, the surface oxide layer provides good biocompatibility *in vivo*[148]. In recent years there has been significant work on the development of porous metals for biomedical implants to provide fixation via bone ingrowth, while also reducing the material's elastic modulus to minimize bone resorption due to stress shielding[13, 15, 149].

However, these materials lack any specific bioactivity for bone tissue formation, leading to extensive research on titanium surface treatments and coatings[150]. Early efforts were directed towards the modification of surface topography[119, 151], and later to ceramic coatings, including various calcium phosphates[152, 153] and apatites[154, 155]. More recently, efforts have been directed towards surface modification with peptides and other biological molecules[156]. Yet given the development of porous metallics for biomedical applications, a better approach than merely coating the metal's surface might be to *fill* the open, interconnected porosity with a bioactive scaffold and thus direct cellular response. To this end, Ti-6Al-4V foams filled with a self-

assembled, peptide amphiphile (PA) nanofiber matrix (PA-Ti hybrids) have been developed, as described in Chapter 4[157].

There are several advantages to this approach. First, an organic scaffold is provided within which cells can migrate, remodel, and lay down their own extracellular matrix. Second, the PA's molecular design affords a unique ability to tailor the bioactivity of the resulting matrix by controlling the orientation and density of bioactive peptide epitopes[58]. Recently our group has shown the concentration of the peptide sequence Arg-Gly-Asp-Ser (RGDS) within PA nanofibers modulates cellular adhesion, with a maxima observed when an RGDS-bearing PA is mixed with a non-specific control PA at varying ratios[58]. However, the influence of RGDS epitope presentation on more complex/important biological processes like cellular proliferation, colonization, and differentiation has not been previously examined with the PA nanofiber system within a three-dimensional context. Here, the effect of RGDS epitope presentation in PA-Ti hybrids on the proliferation, ingrowth into the hybrid (colonization), and differentiation of pre-osteoblastic mouse calvarial cells (MC3T3-E1) *in vitro* is evaluated.

## *5.2 Materials and Methods*

All chemical reagents, unless otherwise noted, were purchased from Sigma-Aldrich (St. Louis, MO). Solvents were purchased from Fisher Scientific (Hanover Park, IL). Amino acids were purchased from EMD Biosciences (San Diego, CA). Cellular medium components were purchased from Invitrogen (Carlsbad, CA) and other cell culture supplies from VWR (West Chester, PA). pEGFP-N1 vector was generously provided by Dr. Earl Cheng (Children's Memorial Hospital, Chicago, IL).

### 5.2.1 PA-Ti Hybrid Preparation

PA-Ti hybrids were made as described in Chapter 4[157]. Briefly, peptide amphiphiles (PA) were synthesized using solid-phase peptide synthesis methods previously described[65, 66] and characterized using MALDI-TOF and analytical HPLC. Meanwhile, Ti-6Al-4V foams were created by procedures established previously for superplastic foaming[12, 36-38, 138]. The foamed Ti-6Al-4V billet was cut into $1 \times 4 \times 4$ mm$^3$ samples using a diamond saw with oil lubrication, which were ultrasonically cleaned with dichloromethane, acetone, and water for 15 minutes each. To remove metal smearing into the external pores from cutting, the samples were exposed to an aqueous solution of 0.25% HF and 2.5% $HNO_3$ for 45 minutes. After repassivation with 40% $HNO_3$ for 30 minutes, samples were repeatedly rinsed in ultrapure water and dried in a desiccator.

PA-Ti hybrids were then prepared with different ratios of a phosphoserine-bearing PA (S(P) PA) and an Arg-Gly-Asp-Ser containing PA (RGDS PA), as shown in Figure 5.1. Three ratios were used: 0.5 mol% RGDS PA with 99.5 mol% S(P) PA; 5 mol% RGDS PA with 95 mol% S(P) PA; and 15 mol% RGDS PA with 85 mol% S(P) PA. These samples will hereafter be referred to as 0.5% RGDS, 5% RGDS, and 15% RGDS hybrids, respectively. Lyophilized PA powders were solubilized at 10 mM in ultrapure water, adjusted to pH 7, and UV-sterilized for 25 minutes. S(P) PA and RGDS PA were mixed at the appropriate ratios and ultra-sonicated for 20 minutes at 50 ˚C to encourage mixing. Meanwhile, Ti foams were autoclave sterilized and pre-wet via graded soakings starting with 100% ethanol and ending with 100% ultrapure water. Pre-wet Ti foam samples were then placed in 75 μL of the appropriate mixed PA solutions, and agitated on a plate shaker at low speed for 30 minutes. The PA solutions containing the Ti foams

were then gelled with the addition of 5 μL of 1 M $CaCl_2$ each, resulting in a final $CaCl_2$ concentration of 62.5 mM. Following gelation, samples were annealed by incubation at 37 ˚C and 5% $CO_2$ for 1.5 hours.

### 5.2.2 Transfection and Culture of GFP-MC3T3-E1 Cells

Mouse calvarial pre-osteoblastic (MC3T3-E1) cells were cultured under standard tissue culture conditions at 37 ˚C and 5% $CO_2$ in Minimum Essential Medium α (MEMα) medium supplemented with 10% fetal bovine serum (FBS), 100 units/mL penicillin and streptomycin, 10 mM β-glycerophosphate, and 50 μg/mL ascorbic acid, hereafter referred to as 'growth medium'. To enable fluorescence confocal imaging, MC3T3-E1 cells were transfected with a vector for green fluorescent protein (GFP). This was achieved by plating cells at greater than 90% confluency in antibiotic-free growth medium without serum, adding 1 μg pEGFP-N1 vector and 2.3 μL Lipofectamine™ 2000 transfection reagent (Invitrogen), mixing gently and incubating for 24 hours at 37 ˚C. Cells were then passaged and cultured in growth medium for one day, followed by medium exchange with a 'selection medium', consisting of penicillin/streptomycin-free growth medium with the addition of 600 μg/mL Geneticin® selective antibiotic (Invitrogen). Cells were cultured in the selection medium for 14 days, followed by culturing in a 'maintenance medium', consisting of penicillin/streptomycin-free growth medium with the addition of 300 μg/mL Geneticin® selective antibiotic. Cells were then sorted by flow cytometry to obtain a homogeneous population for cell experiments, hereafter termed 'GFP-MC3T3-E1' cells. All experiments were performed using GFP-MC3T3-E1 cells in maintenance medium.

### 5.2.3 Rotating Bioreactor Experiments

The PA-Ti hybrids were cultured in a rotating bioreactor as described by Speorke[158]. Briefly, samples with 1 mm holes drilled in the middle were placed on steel skewers with Teflon spacers and a Teflon plug at the end, and inserted into a pre-conditioned rotating 110 mL STLV bioreactor culture vessel (Synthecon, Houston, TX) at 37 ˚C and 5% $CO_2$. To begin culture, $10^7$ GFP-MC3T3-E1 cells were added in 110 mL maintenance medium for 16 hours to allow cells to adhere to the samples. Medium was then replaced with fresh maintenance medium (designated as time 0) and again every 3 days. Samples were harvested at days 1, 7, 14, 21, and 28, with the exception of samples for alkaline phosphatase (ALP) analysis, osteocalcin (OC), and calcium analysis, which were harvested at days 1, 6, 13, 20, and 27, and cultured for 1 more day in a 96-well plate under the same conditions.

### 5.2.4 Additional Culture Experiments

Cells were also cultured in PA gels without Ti foams to determine the effect of S(P) on proliferation by mixing with a non-specific PA, shown in Figure 5.2 A and B, respectively. For comparison with the PA-Ti hybrids, PA gels made with 0.5 mol% S PA and 99.5 mol% S(P) PA, 5 mol% S PA and 95 mol% S(P) PA, and 15 mol% S PA and 85 mol% S(P) PA. Cells were encapsulated in 10 mM PA gels by mixing a cell suspension in mineralization medium 1:1 with 20 mM PA solution, triggering self-assembly of the PA. The cells were then cultured in well plates at 37 ˚C and 5% $CO_2$ for 14 days.

### 5.2.5 Cell Quantification

For cell quantification, PA-Ti hybrid samples and PA gel samples were extracted and frozen in liquid nitrogen, lyophilized, and digested in a papain solution[139]. Briefly, samples were incubated in 0.125 mg/mL papain activated with 1.76 mg/mL cysteine in phosphate buffer with EDTA (0.1 M $Na_2HPO_4$, 0.01 M $Na_2EDTA$, pH adjusted with 1 N NaOH) for 16 hours at 60 ˚C. Samples were then assayed for dsDNA content using a Quant-iT PicoGreen dsDNA Assay Kit (Molecular Probes) as per the manufacturer's protocol. A 5 μL aliquot of digestion solution was incubated with 95 μL of 1X TE and 100 μL of PicoGreen Working Reagent for 5 minutes and fluorescence was measured on a Gemini EM fluorescence/chemiluminescence plate reader with excitation/emission of 480/520 nm. A standard curve was prepared using a known number of cells and used to determine the sample values.

### 5.2.6 PA-Ti Hybrid Imaging

PA-Ti hybrid samples for SEM and confocal microscopy were extracted and pre-fixed with 1% gluteraldehyde in MEMα on ice for one hour. Samples were rinsed in PBS for 20 minutes, and fixed in 2% formaldehyde, 2% gluteraldehyde in 0.1 M cacodylate buffer for 3 hours at room temperature and then overnight at 4 ˚C. Samples were then rinsed in cacodylate buffer for 20 minutes and dehydrated using a graded series of increasing ethanol concentration. SEM samples were critical-point dried, coated with 3 nm Au-Pd, and imaged using a Hitachi S-4500 with a cold field emission electron gun at 3 kV with a current of 20 mA. A secondary electron detector was used for high-resolution imaging. Alternatively, samples for confocal microscopy were embedded in EmBed-812/DER 73 (Electron Microscopy Sciences) according to the manufacturer's protocol. Briefly, samples were soaked in propylene oxide for 20 minutes,

followed by 50:50 solution of EMbed-812/ DER 73 and propylene oxide overnight, and then straight EMbed-812/DER 73, with several fresh exchanges. The resin was then cured for 24 hours each at 40 ˚C, 60 ˚C, and 70 ˚C. Embedded samples were then sectioned using a diamond saw and mounted on glass slides. Imaging was performed on a Leica Confocal Laser Scanning System inverted microscope using an argon laser and driven with Leica Confocal Software.

### 5.2.7 Determination of Cell Differentiation

PA-Ti hybrids for ALP, OC, and calcium assays were removed from the bioreactor and placed into a 96-well plate with 75 μL fresh maintenance medium for 24 hours at 37 ˚C and 5% $CO_2$. For the ALP and OC assays, the medium was collected from each sample and frozen at -20 ˚C for 1 day, and then at -70 ˚C until the assay was performed. For the calcium assay, the PA-Ti hybrid was removed and rinsed twice for 10 minutes in PBS, and then placed in 200 μL 0.5 N HCl. Samples were then frozen at -20 ˚C for 1 day, then at -70 ˚C until the assay was performed. ALP was assayed using an ALP Liquicolor kit (No. 2900) from Stanbio, as per protocol, and data were normalized relative to a maintenance medium control. OC was assayed using a Mouse Osteocalcin ELISA kit (BT-470) from Biomedical Technologies, Inc., as per protocol. Calcium content was assayed using a Stanbio Total Calcium Liquicolor kit as per protocol.

### 5.2.8 Statistical Analysis

Statistics for biological analysis are shown using standard deviation error bars. Multivariate analysis was performed with JMP 6 software to determine significance values and power values. For individual comparisons, T-test with unknown variance was used to determine two-tailed P-values.

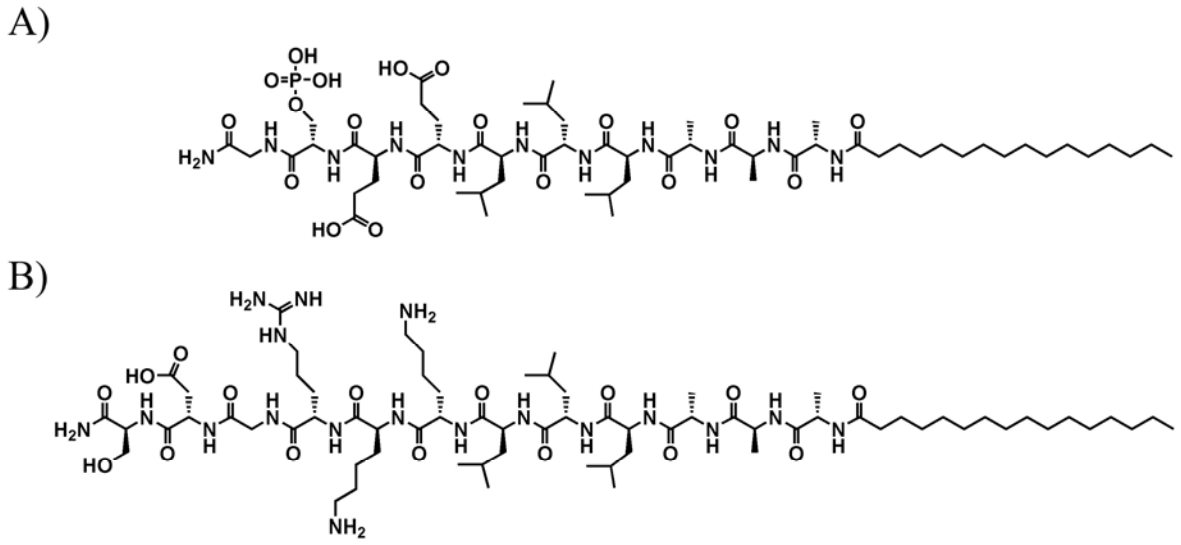


**Figure 5.1 Structure of the peptide amphiphiles used to create the hybrid bone implant materials. Top: a phosphoserine-bearing PA used as a "filler" PA. Bottom: an RGDS-bearing PA for cellular adhesion.**

## *5.3 Results and Discussion*

### 5.3.1 Cellular Proliferation

In order to evaluate the ability for cells to grow on the PA-Ti hybrid and into the pores filled with PA matrix, a cell quantification assay was performed on three different PA-Ti hybrids cultured in a rotating bioreactor for up to 28 days. The results, shown in Figure 5.2, indicate a significant effect of time on cell proliferation for all sample types ($\alpha$=0.05, P=1.00). There is not a significant effect on cell number between the sample types at any time point, with the exception of day 14, when 15% RGDS PA-Ti hybrids were significantly higher than the other two hybrid types. Furthermore, there appears to be a critical cell density that is reached by day 21 for all sample types. This plateau is maintained at day 28, with a mean cell density of $3.6 \times 10^5$ cells per sample. A similar plateau effect was observed for MC3T3-E1 proliferation on bare

titanium foam scaffolds by St-Pierre[159]. In that system, cell proliferation ceased after 9 days and the cell density was maintained until day 17. For the PA-Ti hybrids, this indicates that in the range of RGDS epitope density studied for these PA-Ti hybrids, there is not a correlation between the average concentration of RGDS epitopes and either initial cell seeding or ultimate cell proliferation. However, increased RGDS epitope concentration may cause the PA-Ti hybrids to reach their ultimate cell density faster than lower RGDS epitope concentrations, which is important in the context of tissue engineering and regenerative medicine for both *ex vivo* cell seeding of scaffolds and *in vivo* tissue ingrowth after orthopaedic implantation.

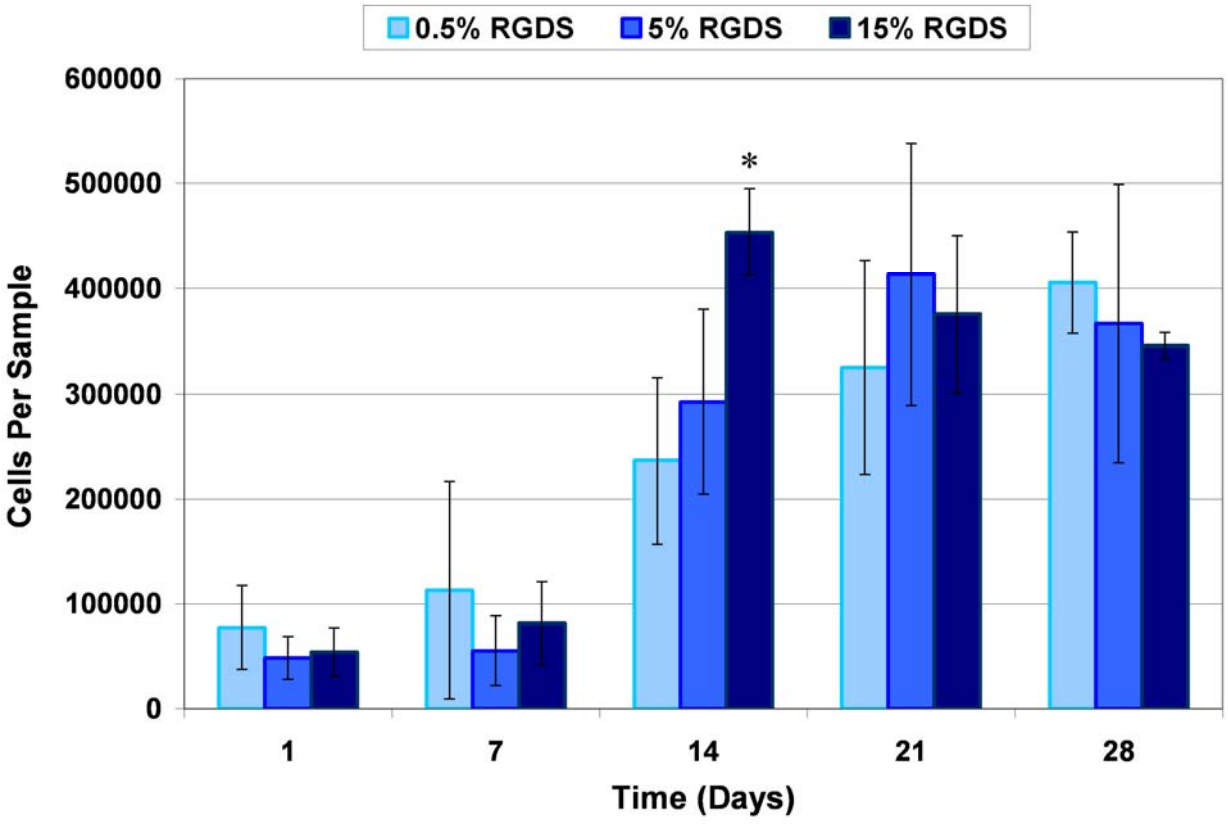


**Figure 5.2 Cell quantification as a function of days cultured on PA-Ti hybrids in a rotating bioreactor, n=8. There is a statistical effect of time on cell number (α=0.05, P=1.00). At particular time points, significant differences are indicated by asterisks (α=0.05). There appears to be a critical cell density that is reached between 2 and 3 weeks, with a mean value of 3.6 x $10^5$ cells at day 28.**

This result is also interesting in the context of previous works on the role of RGD ligands on cell adhesion and motility. Several studies have shown that in controlled experiments with serum-free medium, the concentration and clustering of RGD-containing ligands lead to controllable cellular adhesion[58, 136, 160]. However, in normal culture conditions containing serum, the adsorbed proteins may mask this effect, which is what we appear to observe in this system. However, during the exponential growth stage observed between days 7 and 14, there is a significant increase in proliferation for the 15% RGDS hybrids. By day 21, all samples are statistically similar, displaying typical sigmoidal growth behaviour and reaching a plateau[159]. Therefore, in this system under serum-containing culture conditions, variation in the ligand density appears to modulate the exponential growth phase of the sigmoidal growth profile, but not the initial cell adhesion or final cell density.

To confirm that the observed effect of increased proliferation was due to the variation in RGDS concentration and not the variation in S(P) concentration, a proliferation assay without the RGDS epitopes was performed. This was accomplished using the same S(P) concentrations, but instead mixed with a non-specific PA at 0.5%, 5%, and 15% as before. The PA chemical structures and the results of the cell quantification assay are shown in Figure 5.3. The results demonstrate that the S(P) epitope does not affect the proliferation of the cells during the period of exponential growth, confirming that the RGDS epitopes are responsible for the increased proliferation observed for the PA-Ti hybrids. Consequently, the 15% RGDS PA-Ti hybrid will be used for all of the experiments that follow.

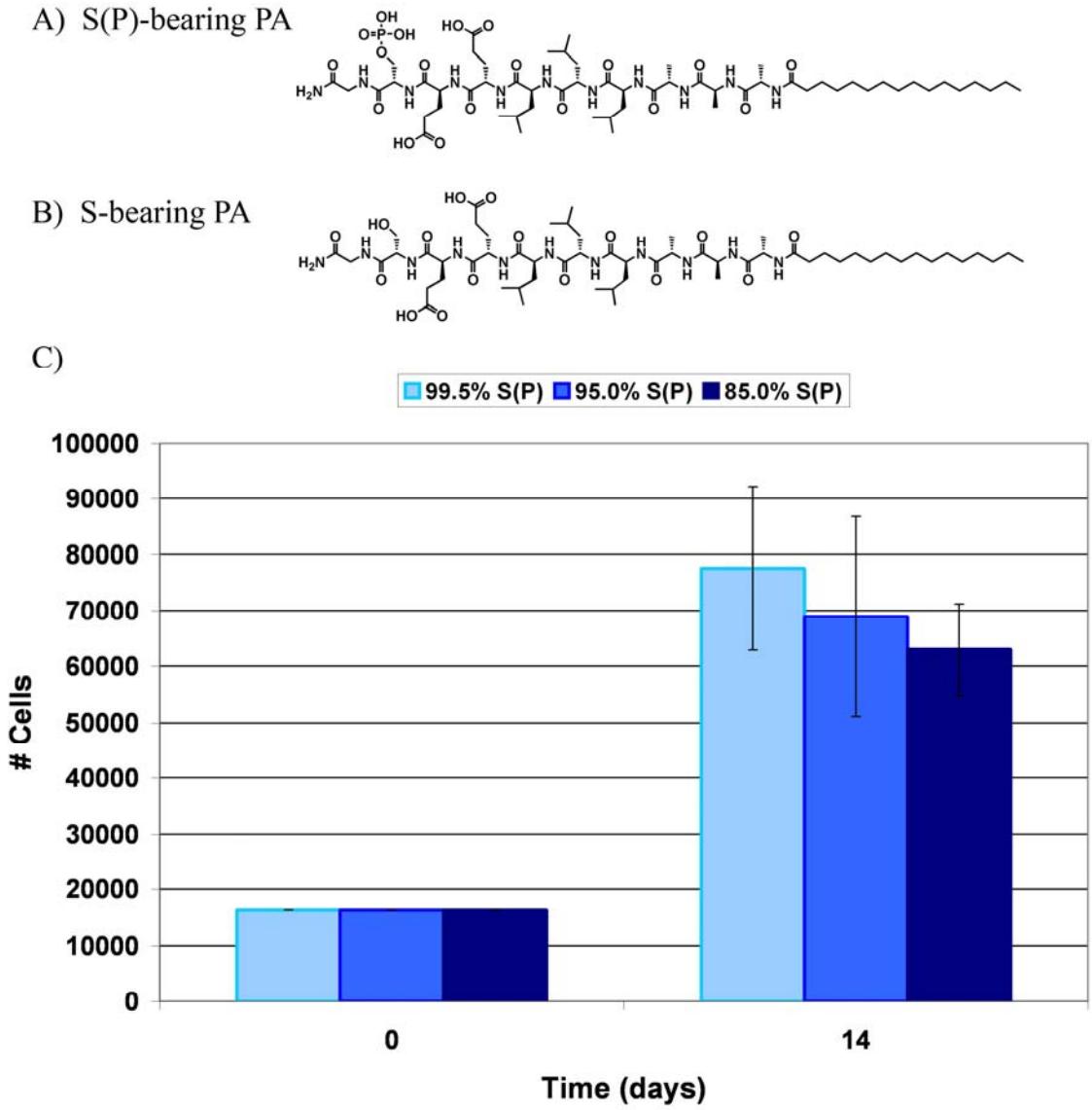


**Figure 5.3 Cell quantification assay of MC3T3-E1 cells cultured in PA gels without RGDS epitopes. The assay was performed using the same concentrations of S(P) PA (A) as in Figure 2, but instead mixed with a PA with a non-specific epitope (B). The non-statistically different results at day 14 confirm that the increase in cell proliferation in the PA-Ti hybrids is due to the RGDS epitope presentation, and is not a function of the S(P) residues.**

### 5.3.2 Cellular Colonization of Hybrid

To better understand the way in which these PA-Ti hybrids are colonized by the pre-osteoblastic cells, samples were imaged by SEM and in cross-section by confocal microscopy. PA-Ti hybrids were imaged by SEM at each time-point, and were observed to be similar for each sample group at a given time. Figure 5.4 shows representative SEM images of 15% RGDS PA-Ti hybrids at day 1 with cells observed to be adherent and spread on the surface of the hybrid. There is a clear interaction between the cells and the underlying PA nanofibers, with the cells extending filopodia to bind the matrix. Figure 5.5 shows SEM images of 15% RGDS PA-Ti hybrids at days 1, 7, and 21, demonstrating the surface colonization of the cells. At day one, much of the hybrid is still visible, with cells adherent to portions of the exterior at low confluency. By day 7, less of the hybrid exterior is visible, with cells having proliferated to cover a significant amount of the exterior and beginning to form cell-cell contacts. By day 21, the underlying hybrid is completely covered with a confluent cell layer, and the hybrid is only visible in areas where the cell layer has cracked from the processing of the samples for SEM imaging. Figure 5.6 illustrates the cellular interaction with the PA matrix and the cellular migration into the hybrid at day 7 on 15% RGDS PA-Ti hybrids. In image A, a cell is seen stretching across a gap and extending filopodia to adhere to PA nanofibers, indicated by arrows. In image B, cells are seen lining the rim of a pore, and cells are observed to be migrating into the interior (arrow) of the hybrid by pulling on the PA matrix and Ti substrate. This clearly demonstrates the preference of the cells for the PA matrix, including their ability to adhere specifically to the PA nanofibers and migrate into the hybrid.

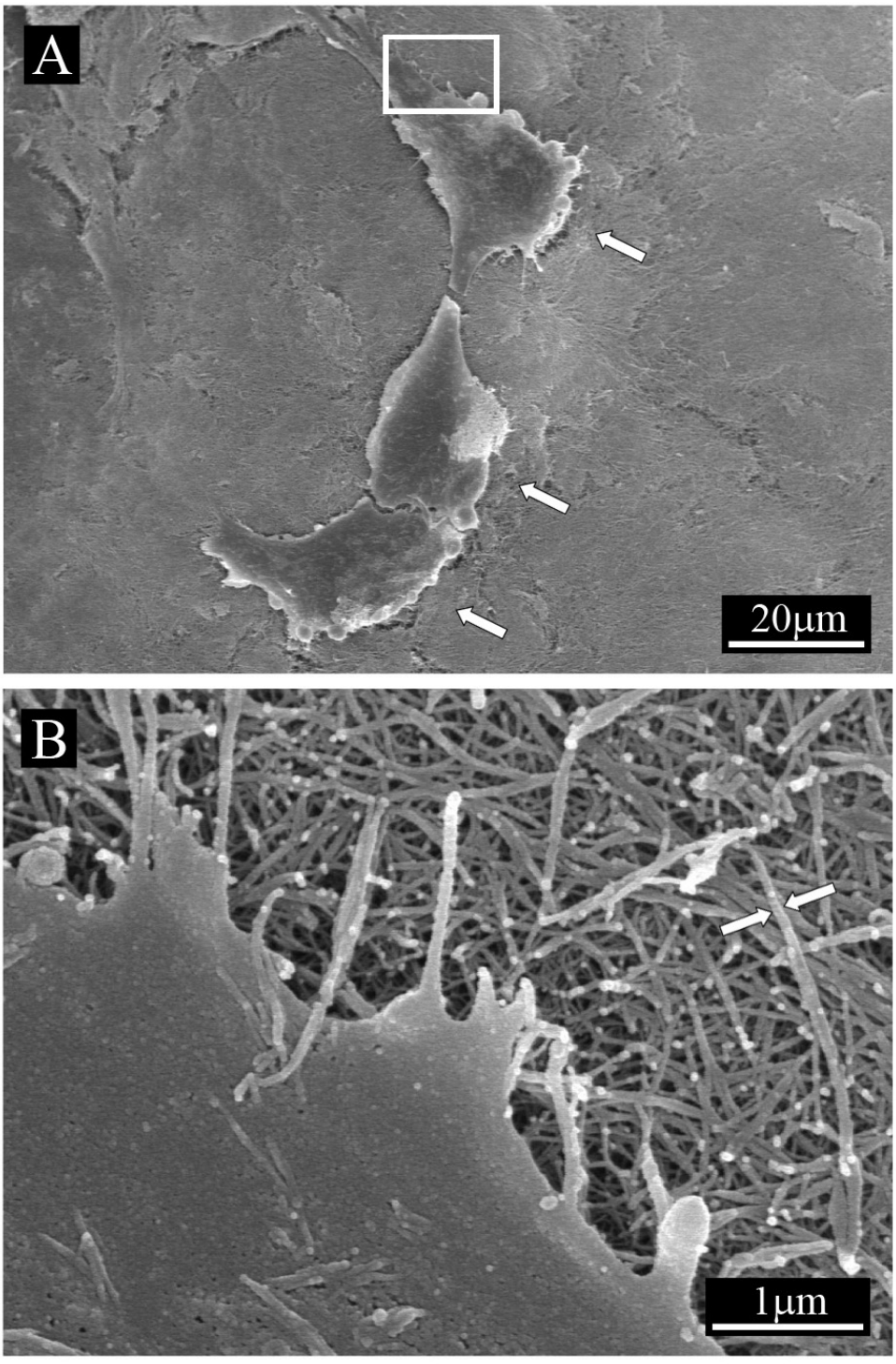


**Figure 5.4 SEM images of MC3T3-E1 pre-osteoblastic cells cultured for 1 day on 15% RGDS PA-Ti hybrids in a rotating bioreactor. Image A shows cells, indicated by arrows, spread on the exterior of the hybrid. Image B shows a high magnification of the boxed area in image A, illustrating the filopodia of the cell reaching out to the underlying PA nanofibers.**

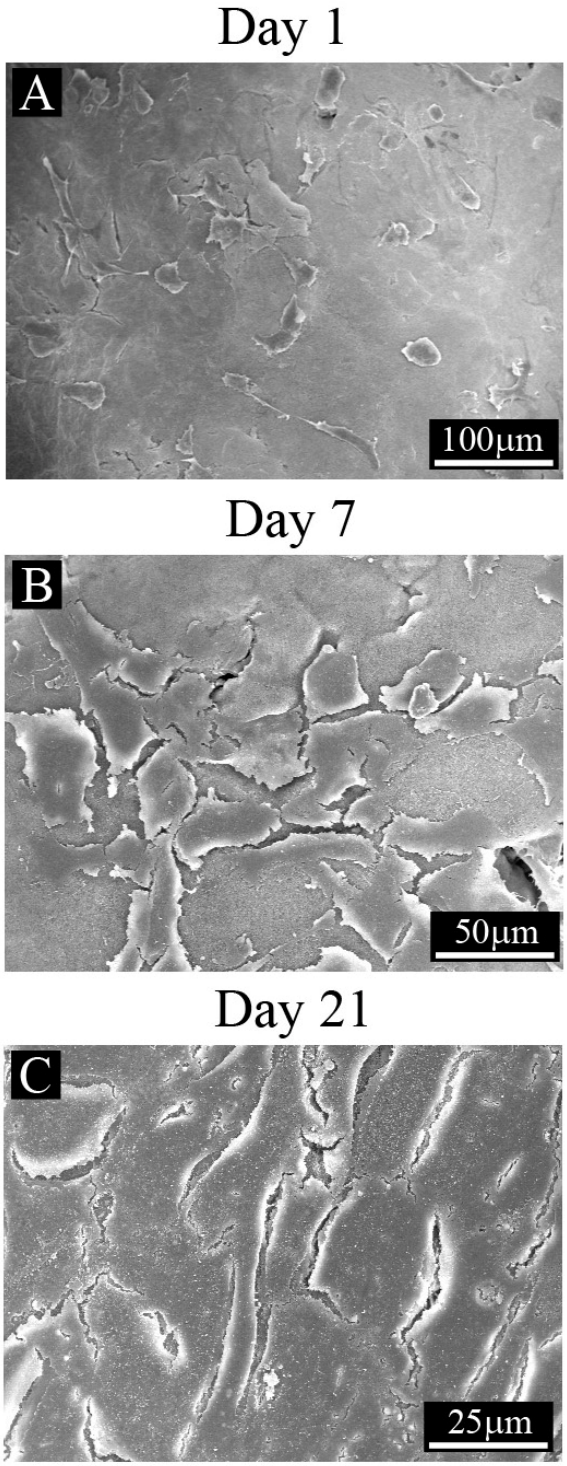


**Figure 5.5 SEM images of 15% RGDS PA-Ti hybrids cultured for 1 (A), 7 (B) and 21 (C) days. After 1 day of culture, cells have adhered and begin to spread on the exterior of the hybrids (A). By day 7, the cells have covered a significant amount of the hybrid exterior (B). By day 21, the exterior of the implant is completely covered with cells (C).**

Confocal images of cross-sectioned samples were also taken to determine the extent of migration and proliferation into the core of the hybrids. Representative images at days 1, 7, and 28 are shown of a 15% RGDS PA-Ti hybrid in Figure 5.7. The GFP-transfected MC3T3-E1 pre-osteoblastic cells fluoresce green, reflection from the top surface of the Ti foam appears white, and the PA nanofiber matrix is not visible. By day 1 the cells are seen to be adherent and spread on portions of the exterior of the implant, and by day 7 the cells have covered most of the exterior surface, in agreement with the SEM images. Furthermore, the confocal image at day 7 additionally shows that cells have begun to migrate into the hybrid (indicated with arrows), confirming the observation indicated by the SEM image in Figure 5.6(B). By day 28, cells have migrated throughout the entire thickness of the hybrid via the PA matrix-filled interconnected porosity. Cells are shown both lining the rims of some pores and in the middle of the PA matrix of others. This indicates that the hybrids show an excellent capacity to facilitate ingrowth and maintain cellular viability in the core of the hybrid. Furthermore, the transfection of the cells is not expected to be absolutely complete, and may diminish slightly with time, so the fluorescence observed gives a lower bound of the potential cells that are actually present. Also, deposited ECM matrix, mineral, or remodeled PA matrix will not fluoresce, so areas that appear absent of cells may indeed be filled by one of these components. This implies that the dimensions of the pores and interconnects are sufficient for nutrient diffusion, even when the exterior of the hybrid is fully covered in a confluent cell layer. The 165 μm average pore size of these PA-Ti hybrids[157] also corresponds with the generally well-accepted ideal pore size of approximately 150-400 μm for bone ingrowth and vascularization[32, 126, 161].

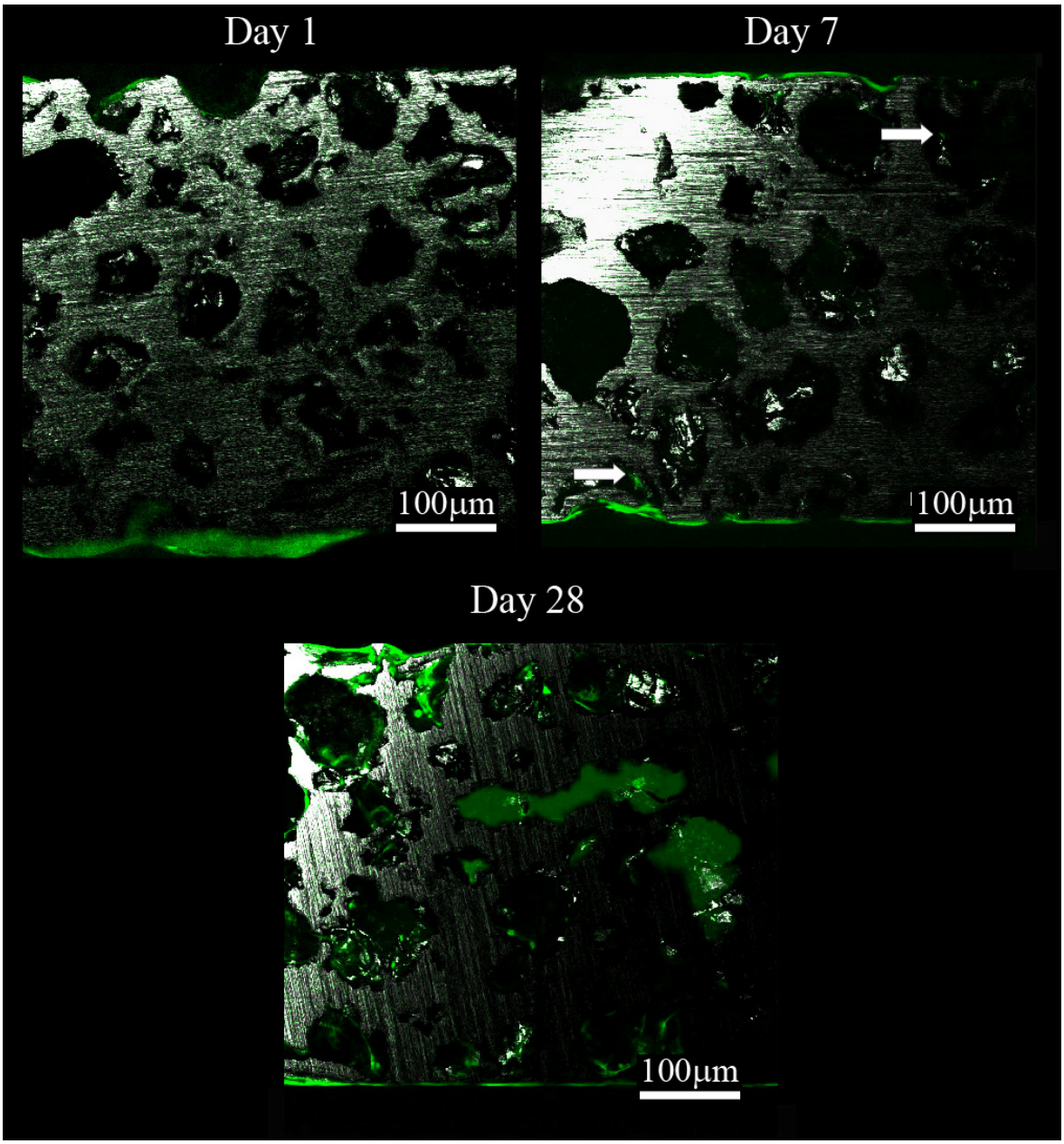


**Figure 5.6 SEM images of MC3T3-E1 pre-osteoblastic cells cultured for 7 days on 15% RGDS PA-Ti hybrids in a rotating bioreactor. Image A shows a cell that is stretched across a gap and adhering to the PA matrix, indicated with arrows. Image B shows a cell that is migrating into the PA matrix-filled porosity of the PA-Ti hybrid (arrow).**

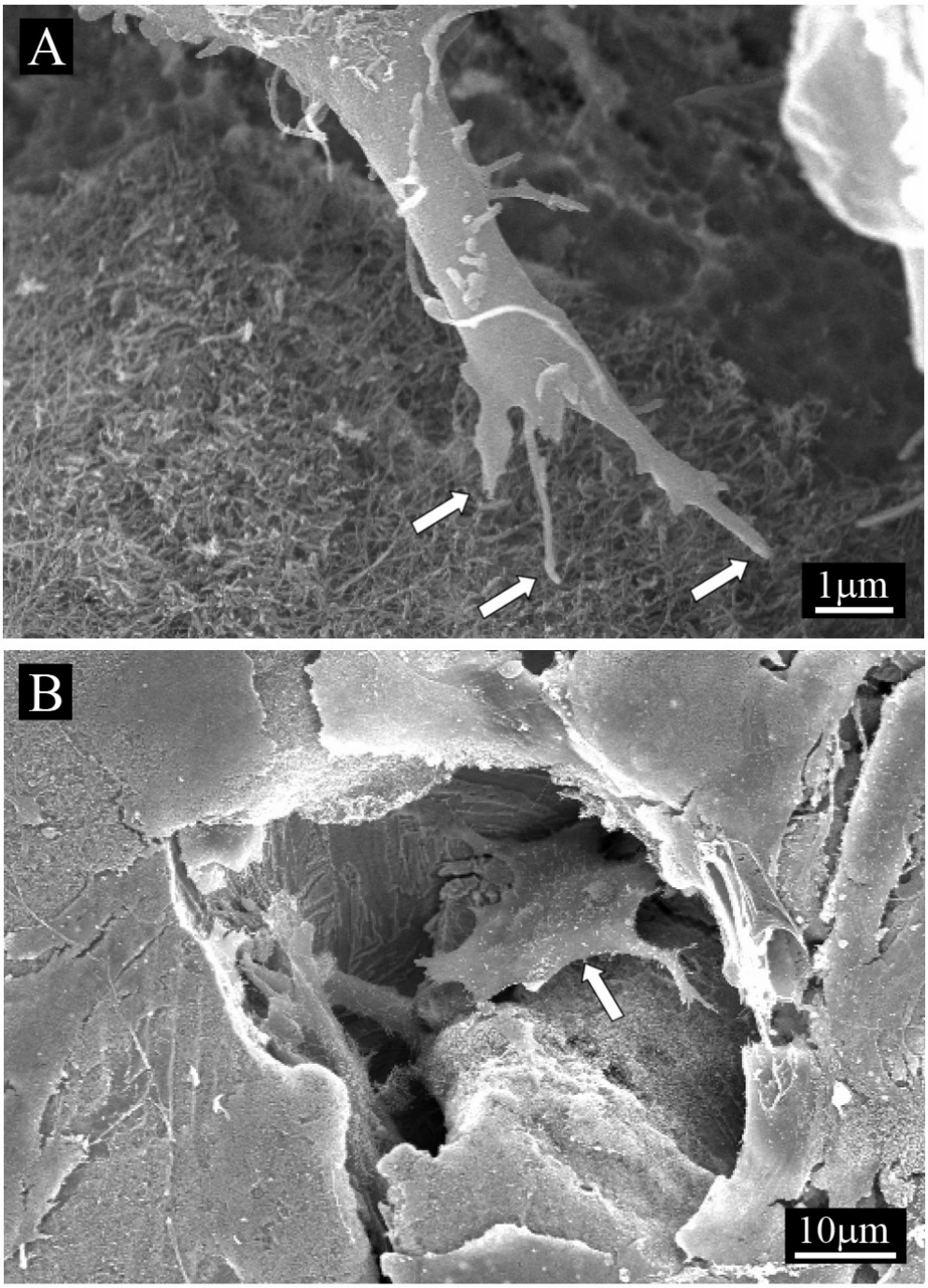


**Figure 5.7 Confocal fluorescent images of cross-sectioned 15% RGDS PA-Ti hybrids at days 1, 7, and 28 showing GFP-transfected MC3T3-E1 pre-osteoblastic cellular ingrowth and proliferation. The cells are shown in green, with the top surface of the metal reflecting white, and the PA matrix not visible. As seen at day 1 (shown left), cells adhere to the exterior of the implant and proceed to migrate and proliferate into the core of the PA-Ti hybrid up to 28 days (shown right), where cells are observed both adjacent to the pore wall as well as in the PA matrix in the center of the pores.**

### 5.3.3 Cellular Differentiation

To assess the progression of differentiation of the pre-osteoblastic cells, two markers for the osteoblastic lineage were assayed: alkaline phosphatase (ALP) for early pre-osteoblastic and osteoblastic stages of differentiation, and osteocalcin (OC) for later osteoblastic and osteocytic stages of differentiation[162]. As the pre-osteoblasts differentiate into osteoblasts and then osteocytes, we would expect a decrease in ALP production and an increase in OC production. ALP and OC were assayed for at each time point and normalized to the cell number from the DNA quantification assay. As seen in Figure 5.8, ALP production shows a statistically significant decrease with time for each of the hybrid types ($\alpha$=0.05, P=0.9719). In contrast, OC production shows a statistically significant increase as a function of time in culture ($\alpha$=0.05, P=1.00). Combining the ALP and OC data, there is clear evidence for differentiation along the osteoblastic lineage with time for the PA-Ti hybrids. Based on the compilation of differentiation data by Aubin et al.[162], these MC3T3-E1 cells have matured to osteoblasts by 14 days, and may have begun to mature to osteocytes by day 21 or 28. Traditionally, osteoblast differentiation follows three stages: proliferation, matrix synthesis and maturation, and then mineralization[162-164]. This was observed by St. Pierre et al.[159], who studied MC3T3-E1 colonization of bare titanium foam and measured an increase in ALP production when the proliferation plateaus. However, they observe a concurrent increase in OC at the same time as ALP, and both decrease shortly thereafter. This does not correspond with the linear progression of pre-osteoblastic cells[162-164], and was attributed by St-Pierre to the cells responding to different mechanisms that may be influenced by TGF-$\beta$ interaction with the titanium scaffold. In this work, the ALP expression from cells in the PA-Ti hybrids is elevated during the first week while the

proliferation rate is low. It is postulated that as the cells initially adhere and begin to migrate into the PA-Ti hybrid, the cell density is low and proliferation is minimal, allowing the cells to secrete ALP, the marker expected at their pre-osteoblastic stage of differentiation. Once the cells start to grow into the implant and the proliferation rate increases during week 2, the ALP expression level drops off. Indeed, we observed cells migrating into the PA-Ti hybrids by day 7, as shown in Figures 5.6(B) and 5.7. After 14 days, the samples approach their cell density plateau and OC expression increases, signaling their maturation into osteoblasts and the onset of mineralization of their ECM. Therefore, this data demonstrates that PA-Ti hybrids facilitate the differentiation of pre-osteoblastic cells along the osteoblastic lineage.

Previously, Ti foam materials were coated with a bioactive organoapatite coating and cultured under similar conditions by Spoerke et al.[158]. The key differences between Spoerke's system and that presented in this chapter are that Spoerke's system had less porosity (22% compared to 52.5%) and the nature of the hybrid (2D coating compared to 3D filling matrix). The similarities include the cell line, the sample size, and the bioreactor culture system used. For the organoapatite coated (OA) Ti foams, the cells are shown to bind and proliferate, but increase in number up to 28 days. This is contrast to the sigmoidal growth curve observed for the PA-Ti hybrids, where a maximum cell density is achieved after 14-21 days. In addition, for the OA Ti foams the ALP enzyme production per cell increases an order of magnitude over 28 days. This suggests that the pre-osteoblasts on the OA Ti foams have not differentiated into mature osteoblasts by 28 days, which may in part be due the cells continuing to proliferate at long time points. Conversely, for the PA-Ti hybrids the maximum cell density is reached much earlier and the onset of osteoblastic maturation is observed earlier than for the OA Ti foams. This is

particularly interesting given that there is more than twice the porosity in the Ti foam used for the PA-Ti hybrids compared to the Ti foam used for the OA Ti foams, and that samples were prepared at exactly the same size. Using the sample size, porosity, and density of Ti, the OA samples are approximately 56 mg in weight each. Converting the proliferation data on the OA Ti hybrids, the maximum cell density achieved at 28 days corresponds to approximately 112,000 cells per sample. This is more than 3-fold fewer cells than obtained on the PA-Ti hybrids, which might be due to the decreased surface area, leading to lower seeding densities (approximately 10 times higher on the PA-Ti hybrids). However, for the OA Ti foams the cells increase approximately 4-fold over 14 days of culture, compared to an increase of approximately 10-fold for the 15% RGDS PA-Ti hybrid. This suggests that the PA enhances the proliferation and maturation of pre-osteoblasts compared to OA coated Ti foams.

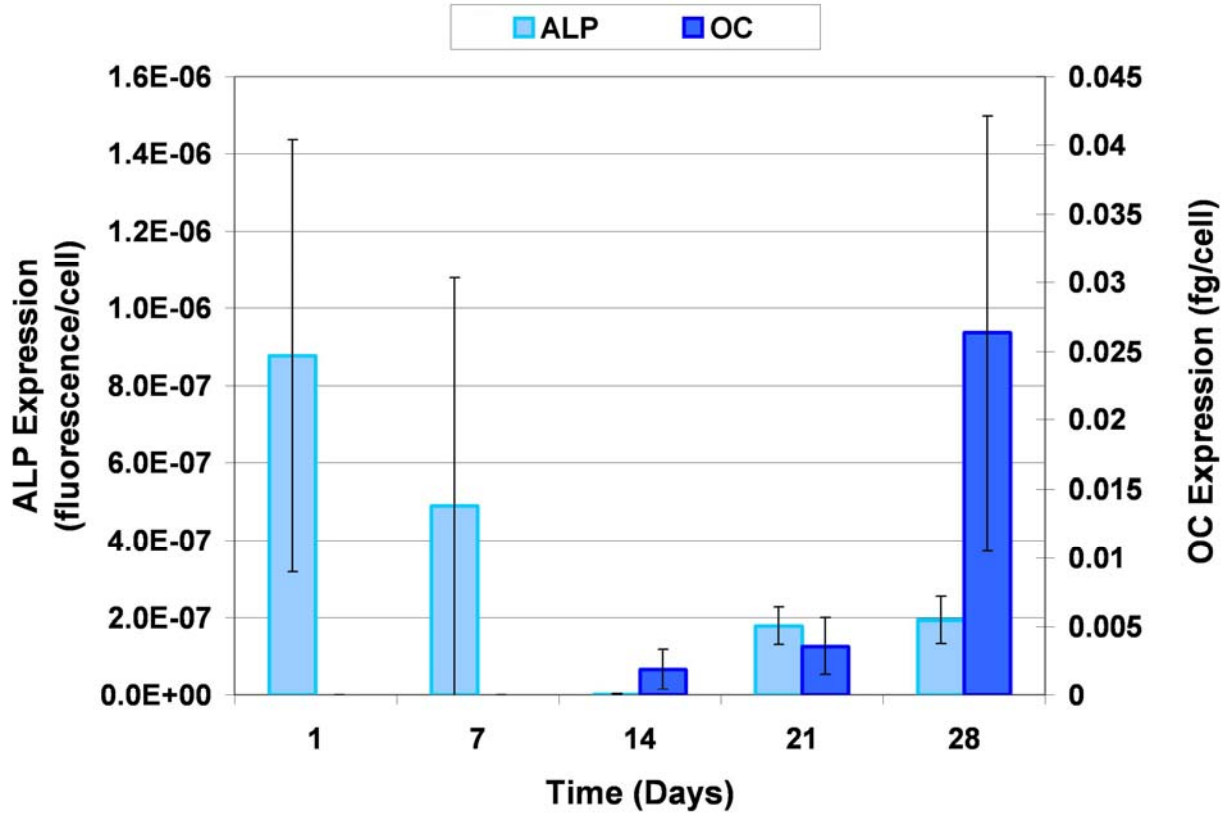


**Figure 5.8 Alkaline phosphatase (ALP) and osteocalcin (OC) expression as a function of days cultured in a bioreactor, n=4. There is a significant effect of time on both ALP production (α=0.05, P=0.9719) and OC production (α=0.05, P=1.00). The data indicates the maturation of the pre-osteoblasts into mature osteoblasts as evident by the decrease in ALP expression and increase in OC expression.**

## *5.4 Conclusions*

A bioactive hybrid material consisting of a peptide amphiphile nanofiber matrix filling the pores of porous titanium foam has been developed that could be used for orthopaedic implants. These PA-Ti hybrids, containing mixed RGDS and phosphoserine peptides at 10 mM concentration, were evaluated for cell proliferation, ingrowth, differentiation, and interaction with the substrate. SEM microscopy showed GFP-MC3T3-E1 cells spreading on and extending processes to the PA matrix, and migrating into the interior of the hybrids. Cross-sectional

confocal microscopy demonstrated ingrowth and proliferation in all samples investigated. Cell quantification confirmed this proliferation and demonstrated sigmoidal growth that reached a plateau density fastest for the 15% RGDS PA-Ti hybrids. Biochemical assays for ALP and OC demonstrate that the pre-osteoblastic cells matured along the osteoblastic lineage, differentiating into osteoblasts by day 14 in concurrence with the onset of the cell density plateau. Together, the data demonstrates the effectiveness of the PA-Ti hybrids to facilitate colonization and differentiation by pre-osteoblastic cells, which may be important for future orthopaedic implant design.

# CHAPTER 6: *IN VIVO* ASSESSMENT OF PA-Ti HYBRIDS USING A RAT FEMUR MODEL

## *6.1 Introduction*

Globally, orthopaedic sales reached approximately $14 billion in 2002 with an expected annual growth rate of 7-9%[5], representing approximately 700 000 hip and 700 000 knee replacement surgeries[5]. Titanium and its alloys appear to be the best metal for many implant applications due to its superior biocompatibility, lower modulus, and increased corrosion resistance compared to SS and CoCr alloys[10]. Indeed, it is this $TiO_2$ oxide that makes Ti so biocompatible, passivating the material[8] limiting diffusion of the metallic ions, and allowing the formation of much thinner fibrous capsules, if any, around an implant[11]. However, there remain significant problems that have yet to be fully addressed, including fixation of these devices and long-term implant loosening.

Implant fixation is commonly achieved using PMMA-based bone cement[8], which can damage the host tissue due to its exothermic reaction, and can lead to implant loosening as a result of degradation. Implant loosening is also caused by stress-shielding, a consequence of the mismatched moduli, and hence load-bearing, between the implant material and adjacent bone[124, 125]. Therefore, it would be desirable to create a material that would promote bone ingrowth for fixation and that would have a modulus much closer to that of the host tissue.

A solution that addresses both of these concerns is a porous implant. By creating a foamed structure from Ti, the modulus is decreased and boney ingrowth can provide fixation of the implant. A variety of methods to create Ti foams have been developed, including variations of

powder sintering[26, 27, 29], leaching of a space holding material[28], and expansion of gas that is entrapped within a densified powder[35]. This latter technique was improved by the Dunand group[36] to increase the kinetics of foaming and the total porosity by utilizing the superplasticity associated with the allotropic transformation of Ti and its alloys using thermal cycling. With this technique, their group has produced foams of commercially pure Ti[36-38] and Ti-6Al-4V[39-41] at porosities up to 45-50%. Consequently, it is of great interest to assess these novel Ti foams for their potential as an orthopaedic implant material.

Additionally, an improved strategy might be to use these metal foams in conjunction with materials designed to *direct* cellular behavior. To address this, a hybrid material composed of Ti foams filled with a bioactive, peptide amphiphile (PA) nanofiber matrix was developed[157], as described in Chapter 4, and tested *in vitro*, as described in Chapter 5. In this work, the potential of Ti foams and PA-Ti hybrids as orthopaedic implant materials are evaluated *in vivo* using a rat femoral defect model. Accordingly, biocompatibility of the materials, osteointegration, and tissue ingrowth are evaluated by histology and electron microscopy.

## *6.2 Materials and Methods*

All chemical reagents, unless otherwise noted, were purchased from Sigma-Aldrich (St. Louis, MO). Solvents were purchased from Fisher Scientific (Hanover Park, IL). Amino acids were purchased from EMD Biosciences (San Diego, CA). Medical supplies were purchased from VWR (West Chester, PA).

### 6.2.1 PA-Ti Hybrid Preparation

PA-Ti hybrids were made as previously reported in Chapter 4[157]. Briefly, peptide amphiphiles (PA) were synthesized by solid-phase peptide synthesis methods that have been previously described[65, 66]. Purification was performed using preparative scale HPLC, and the final product was characterized using MALDI-TOF and analytical HPLC. Ti-6Al-4V foams were produced by superplastic foaming methods previously described[12, 36-38, 138]. The foamed Ti-6Al-4V billet was cut into cylindrical samples measuring 3 mm high and 2 mm in diameter. The samples were ultrasonically cleaned with dichloromethane, acetone, and water for 15 minutes each, and then etched in an aqueous solution of 0.25% HF and 2.5% $HNO_3$ for 45 minutes to remove metal smearing over the external pores. The samples were then repassivated with 40% $HNO_3$ for 30 minutes, and repeatedly rinsed in ultrapure water and dried in a desiccator.

Two types of PA-Ti hybrids were prepared using two different PA mixtures. One set of hybrids was created with a mixture of 95 mol% phosphoserine-bearing PA (S(P) PA) and 5 mol % Arg-Gly-Asp-Ser containing PA (RGDS PA). The second set of hybrids was created with a mixture of 95 mol% serine-bearing PA (S PA) and 5 mol% RGDS PA. The chemical structures of the PA molecules used are shown in Figure 1. Lyophilized PA powders were solubilized at 10 mM in ultrapure water, adjusted to pH 7, and UV-sterilized for 25 minutes. The PAs were mixed at the appropriate ratios and ultra-sonicated for 20 minutes at 50 ˚C to encourage mixing. Meanwhile, Ti foams were autoclave sterilized and pre-wet via graded soakings starting with 100% ethanol and ending with 100% ultrapure water. Pre-wet Ti foam samples were then placed in 75 μL each of the appropriate PA solutions, and agitated on a plate shaker at low speed for 30 minutes to encourage diffusion. Self-assembly of the PA solutions within the Ti foam pores was

triggered by the addition of 5 μL of 1 M $CaCl_2$, resulting in a final $CaCl_2$ concentration of 62.5 mM. Following gelation, samples were annealed by incubation at 37 ˚C and 5% $CO_2$ for 0.5 hours prior to implantation.

### 6.2.2 Rat Femur Model and Surgical Technique

*In vivo* performance of the PA-Ti hybrids was assessed using a rat femoral model. 3 different materials were evaluated: S(P)/RGDS PA-Ti hybrids, S/RGDS PA-Ti hybrids, and bare Ti foams. The study utilized 13 animals containing 2 implants in each hind limb. Surgical procedures and animal care were approved by Northwestern University's Animal Care and Use Committee. The Ti foams (bare and hybrids) were implanted into 40 week old Sprague Dawley rats obtained from Harlan *(Indianapolis, IN)* with preoperative weights of approximately 450-500 g. The animals were anesthetized by intraperitoneal injection of Ketamine (100 mg/Kg) and Xylazine (5 mg/Kg). The femoral diaphysis was approached through a lateral incision in the skin and circumferential stripping of the muscle. Two 2 mm diameter holes were drilled on the diaphysis of the femur through the first cortex. The implants were press fit into the holes, which were sufficiently tight to provide adequate fixation of the implants. The muscle and skin were each sutured to close the wound. After 2 or 4 weeks, the animals were sacrificed and implants retrieved for histological and SEM analysis.

### 6.2.3 Sample Preparation for Histology

Implants were harvested and prepared for histochemical analysis. After sacrifice, sections of each femur containing the implants were retrieved, fixed in 10% formalin, and embedded in plastic. Cross-sections of the implant and surrounding bone were prepared using Exakt cutting

and grinding equipment (Oklahoma City, OK). Histological samples were mounted on slides and stained with either Goldner's Trichrome or methylene blue and basic fuchsin, and imaged by light microscopy.

### 6.2.4 Sample Preparation for SEM

Implants were also harvested and prepared for SEM analysis. Sections of each femur containing the implants were retrieved, and a portion of the remaining bone was cut to expose one side of the implant, as shown schematically in Figure 6.2. Samples were fixed in 10% formalin, dehydrated in graded ethanol, critical point dried, and coated with 3 nm Au-Pd. Sectioned femurs containing the implants were then imaged on an FEI Quanta ESEM fitted with a Schottky thermal field emission gun and Oxford EDS at 10kV. A secondary electron detector was used for high-resolution imaging.

### 6.2.5 Statistical Analysis

Tissue ingrowth into the implants and tissue growth adjacent to the exterior of the implants was quantified for each sample using ImageJ software. To do so, histological images were converted to gray scale and thresholds were set to determine the area filled with tissue and the area devoid of tissue. For tissue ingrowth, the results are displayed as the average percentage of tissue filled area over the total porosity. For tissue growth adjacent to the implant exterior, results are presented as the percent of new tissue formed in the region immediately adjacent to the exterior of the implant in regions close to cortical bone. This was normalized by the area measured to give an accurate representation of the percentage of induced bone formation from the cortical bone. All quantification was performed blinded by a second party.

Statistics for biological analysis are shown using 95% confidence error bars. Multivariate analysis was performed with JMP 6 software to determine significance values and power values. For individual comparisons, T-test with unknown variance was used to determine two-tailed P-values.

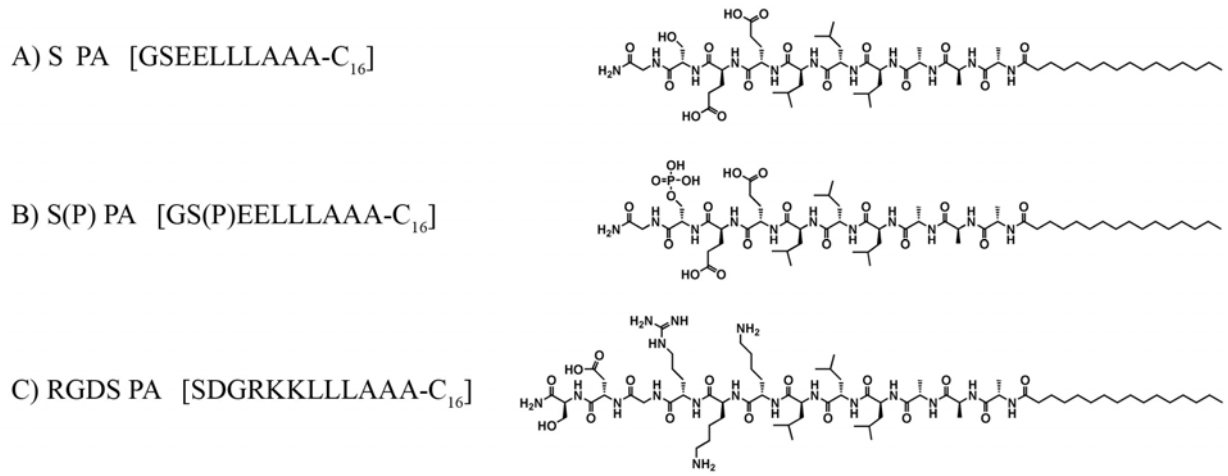


**Figure 6.1 Chemical structures of the 3 PAs used to create PA-Ti hybrids for the *in vivo* rat femur model. Two hybrids were used: 1) 95% S(P) PA with 5% RGDS PA, and 2) 95% S PA with 5% RGDS PA.**

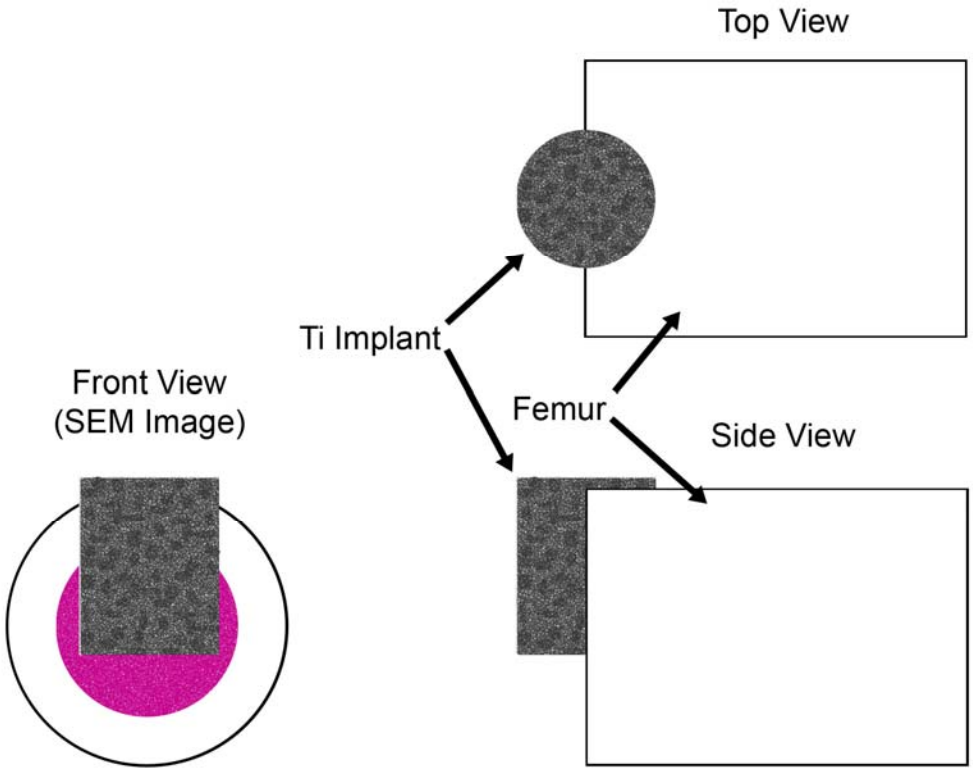


**Figure 6.2 Schematic illustrating the sample preparation for imaging by SEM of the intact Ti foams and hybrids with cross-sectioned femur. SEM images are taken from the "Front View".**

## *6.3 Results and Discussion*

The *in vivo* performance of Ti foams and PA-Ti hybrids was evaluated using a rat femoral model, illustrated in Figure 6.3. Two versions of the PA-Ti hybrids were tested, one type containing 95% S(P) PA with 5% RGDS PA, and a second type containing 95% S PA with 5% RGDS. These were compared to the bare Ti foam as an orthopaedic implant material, which has not been previously evaluated *in vivo*. Consequently, we wish to determine the biocompatibility of the Ti foam and the PA-Ti hybrids. Additionally, we wish to evaluate the ability for the Ti foam to be integrated into the host bone, and determine any beneficial effect the PA may have on this process. To achieve this, implants were retrieved at 2 and 4 weeks after implantation and evaluated by histology and SEM.

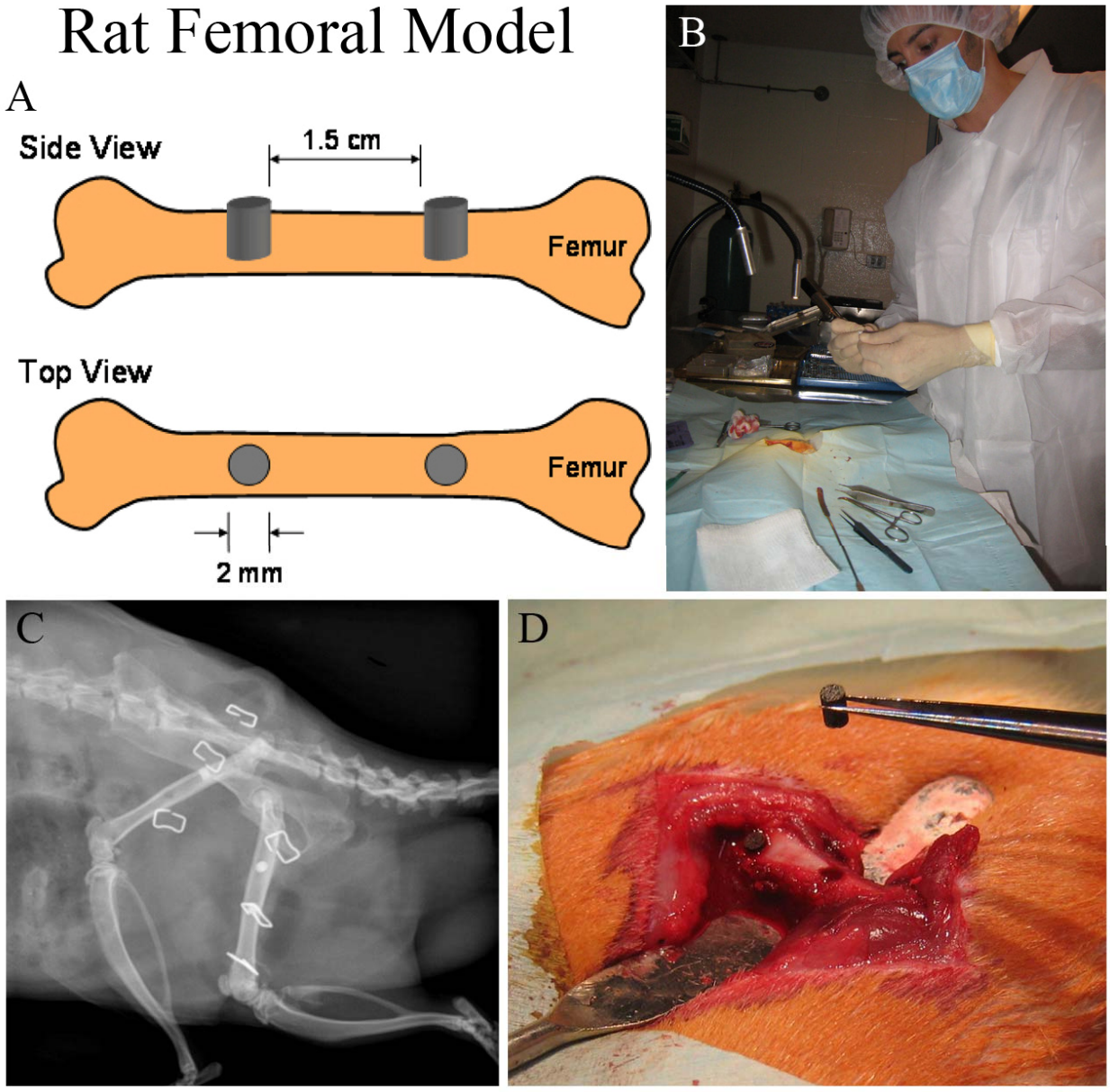


**Figure 6.3 Schematic of the site of implantation (left) and an image of the actual surgical site (right). Ti foam and hybrid implants were positioned inside 2 mm diameter holes that were ~ 1.5 cm apart.**

### 6.3.1 SEM Analysis

SEM samples were prepared from the harvested bare Ti foams and the PA-Ti hybrids after 2 and 4 weeks. The bone was cross-section at the site of placement of the implants, revealing half of the implant still intact in the bone. At both 2 and 4 weeks, all implant materials demonstrated good incorporation into the surrounding bone, and were covered with adherent cells, ECM products, and blood cells. Figure 6.4 shows an SEM image of bare Ti foam implanted in a rat femur. Bone marrow can be seen in the core of the femur with bright contrast due to charging. At the top of the implant on the exterior of the femur is a layer of soft tissue, which has adhered to both the femur and Ti foam. Figure 6.5 shows higher magnification images of a S(P)/RGDS PA-Ti hybrid, illustrating the attachment and migration of cells to the implant, and the deposition of ECM and proteins on the surface. Figure 6.5(A) shows the implant/cortical bone interface (right side) and the soft tissue covering the top of the implant (top side). Figure 6.5(B) shows many cells adhering and spreading on the implant surface, and Figure 6.5(C) shows cells migrating into the porosity of the implant (center). This confirms the ability for cells to penetrate the PA-Ti hybrids, as demonstrated *in vitro* in Chapter 5. All samples were similar in appearance, and no obvious negative effects were observed.

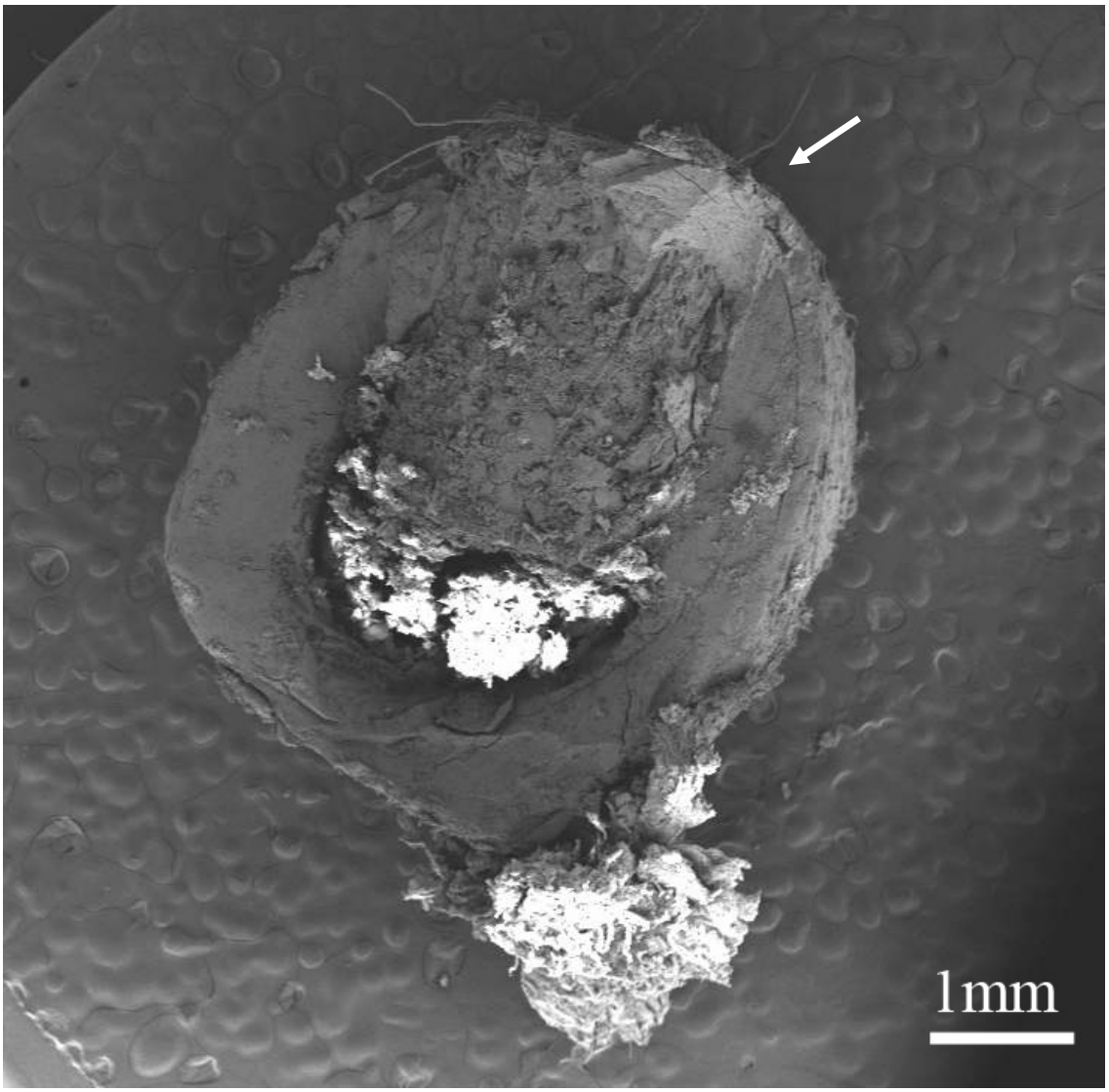


**Figure 6.4 SEM image of a sectioned bare Ti foam implanted in a rat femur, demonstrating the placement of the implant. Bone marrow can be seen (bright contrast) in the core of the diaphysis, and soft tissue can be seen at the top of the implant on the exterior of the bone (arrow).**

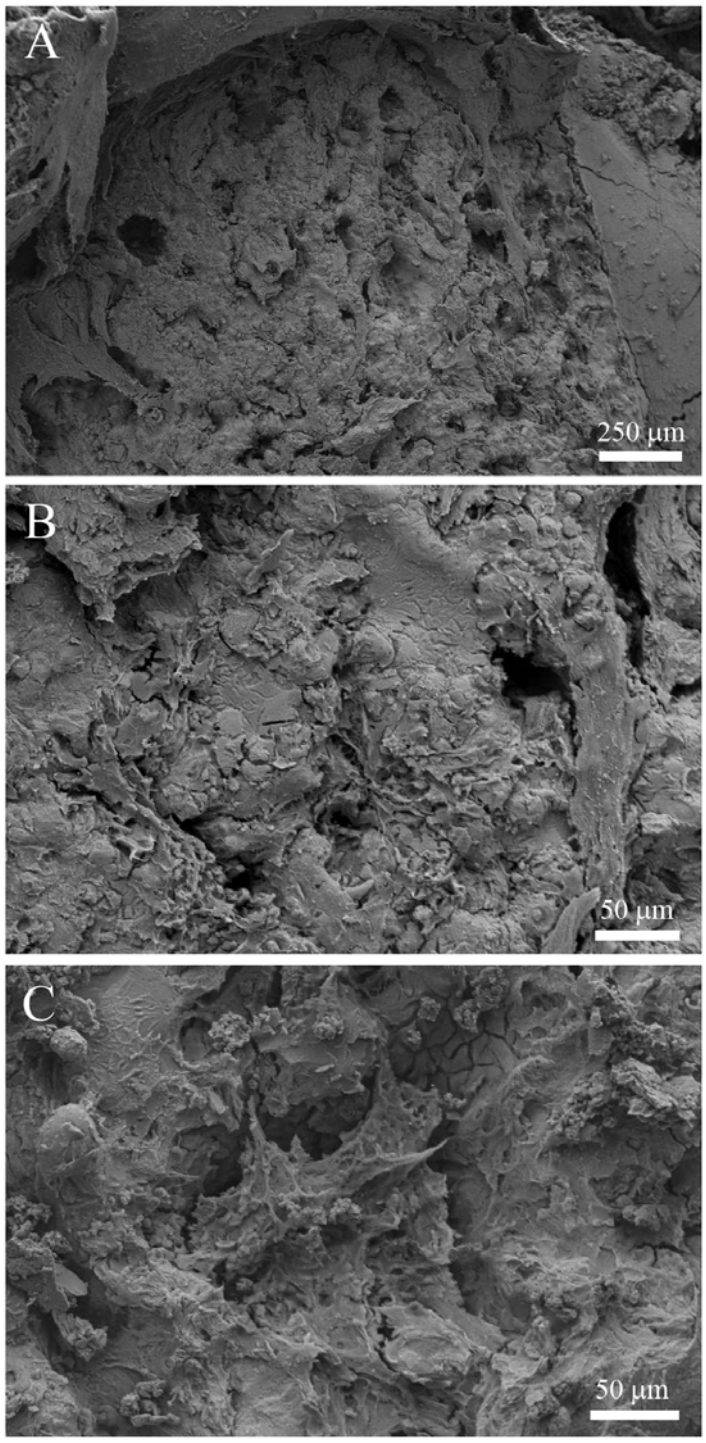


**Figure 6.5 SEM images of S(P)/RGDS PA-Ti hybrid illustrating the attachment and migration of cells to the implant, and the deposition of ECM and proteins on the surface. Image A shows the implant positioned adjacent to cortical bone (right side) and the soft tissue attached to the outer surface (top side). Image B show many cells adhering and spreading on the implant surface. Image C shows cells migrating into the porosity of the implant (center).**

### 6.3.2 Histological Analysis

Histological samples were prepared for the bare Ti foams and the PA-Ti hybrids. Images of the bare Ti foams implanted for 2 and 4 weeks are shown in Figure 6.6. The implants did not exhibit any signs of toxicity, and appear to integrate well with the host bone tissue. As shown in Figure 6.6A, *de novo* bone is observed to grow from the adjacent cortical bone towards the implant. This bone is highly mineralized and has the same structure as the cortical bone with lacunae. In places the bone grows directly onto and into the implant porosity. In other locations the bone is seen to form a rim around the implant. Closer inspection of the histological specimens indicates the presence of a collagenous area in between the implant and the rim. This offers evidence for a growth front into the implant, with bone that is being calcified on the outer layer and newer, less dense mineral on the inner layer.

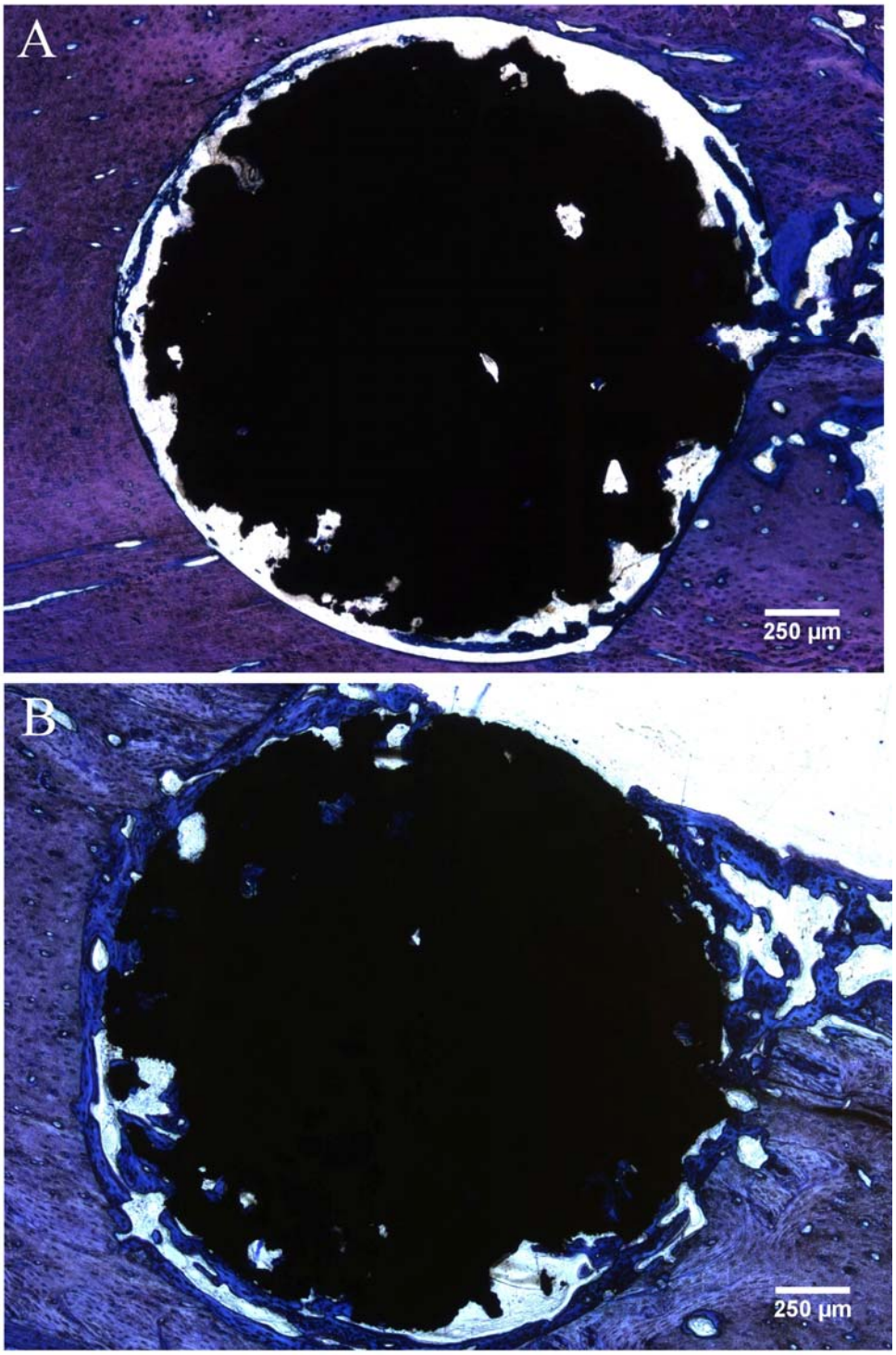


**Figure 6.6 Histological images of bare Ti foams implanted into a rat femur for 2 (A) and 4 (B) weeks. The plastic embedded sections are stained with methylene blue and basic fuchsin. The images show *de novo* bone growing from the adjacent cortical bone towards the implant, making direct contact with the Ti foam and also forming a rim around the implant.**

A similar positive host tissue response is observed with the PA-Ti hybrids. Figures 6.7 and 6.7 show a S(P)/RGDS PA-Ti hybrid implanted for 4 weeks. In Figure 6.7, the hybrid implant is stained with Goldner's Trichrome, which stains highly mineralized bone green and newly formed (immature) bone red. Bone can be seen forming inside the pores of the implant, even near the center (Figure 6.7A). It is not possible to distinguish between mineralized PA and mineralized matrix deposited by osteoblasts. However, due to the results of the *in vitro* mineralization, it is reasonable to expect that the PA would begin to mineralize when implanted. Furthermore, as with the bare Ti foams, the extent of bone formation into the implant demonstrates that the pores are sufficiently interconnected to allow for cellular migration between pores and nutrient diffusion. As shown in Figure 6.7(B), bone has grown directly against the PA-Ti implant surface. Furthermore, we see evidence of neo-vascularization around the implant, including the artery shown with red blood cells in the lumen. In Figure 6.8, the hybrid implant is shown stained with methylene blue and basic fuchsin. Figure 6.8(A) illustrates that bone has filled a majority of the porosity. Figure 6.8(B) shows bone spicules being formed adjacent to the implant in the bone marrow, offering evidence for osteoconduction. The spicule demonstrates a growth front into the PA-Ti hybrid, with collagenous fiber formation and early deposition of bone adjacent to the implant exterior, and bone that is being calcified on the outer layer. The wedge formation at the top of the spicule growing into the pore indicates cellular infiltration by the osteoblasts. The bone marrow appears healthy with intact and viable hematopoietic cells and areas of adipose tissue, and there is no evidence of cytotoxic effects based on the absence of neutrophils.

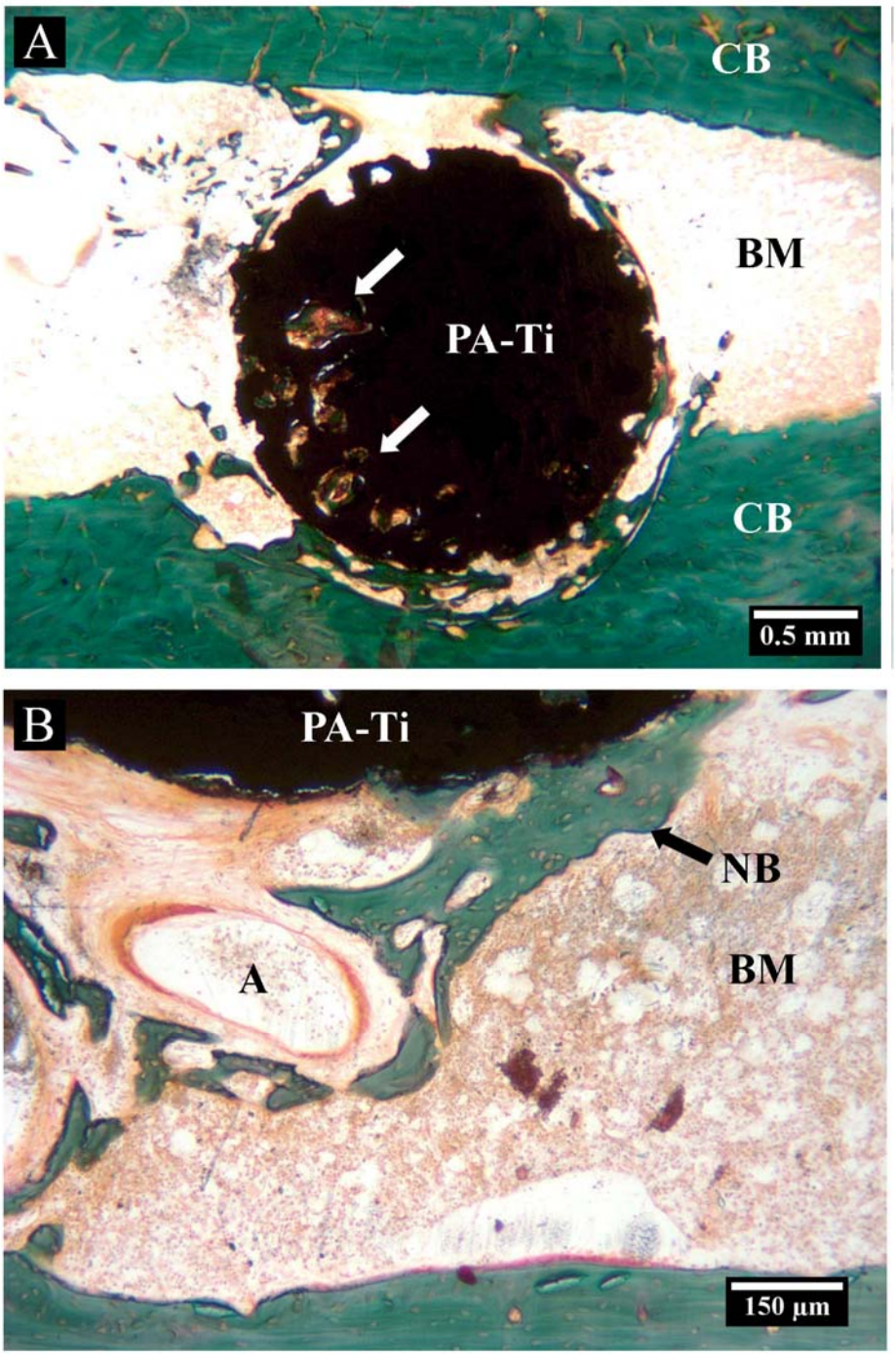


**Figure 6.7 Images of histological sections of a S(P)/RGDS PA-Ti hybrid implanted in a rat femur after 4 weeks. Non-decalcified, plastic embedded samples were stained with Goldner's Trichrome. When staining bone, green indicates highly mineralized bone; red indicates newly formed, immature bone. As seen in Image A, new, mineralized bone is seen growing from the cortical bone (CM) towards the PA-Ti hybrid in the bone marrow (BM), and infiltrating the open porosity (arrows). Image B shows newly formed, fully mineralized bone adherent to the PA-Ti hybrid exterior. An artery (A) is observed adjacent to the implant, indicating neo-vascularization around the PA-Ti hybrid.**

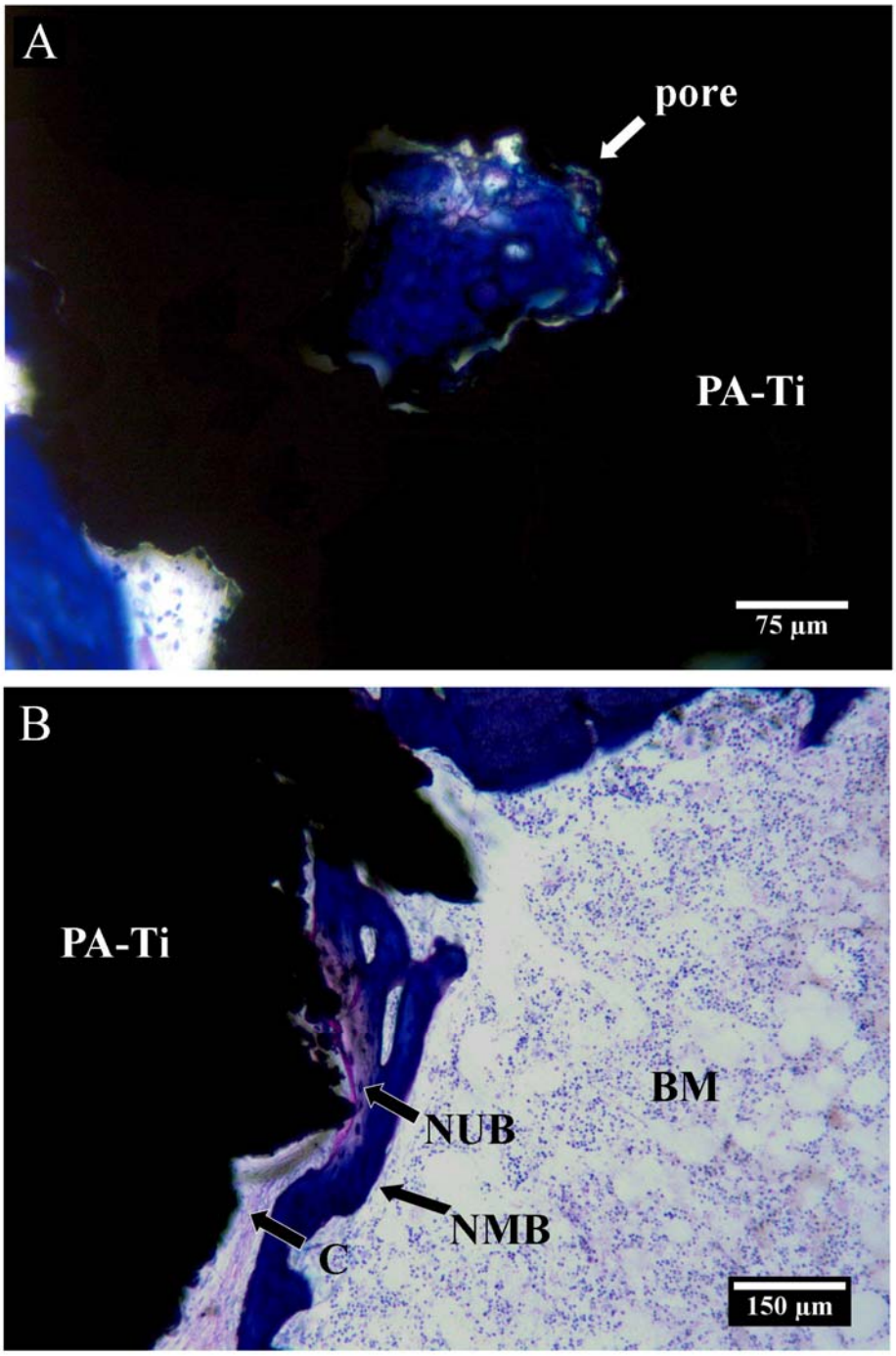


**Figure 6.8 Images of histological sections of a S(P)/RGDS PA-Ti hybrid implanted in a rat femur after 4 weeks. Non-decalcified, plastic embedded samples were stained with methylene blue and basic fuchsin. Image A shows mineralized bone formation (blue) within an interior pore of the PA-Ti hybrid. Image B shows new bone formation adjacent to and into the PA-Ti hybrid. The location and formation of these bone spicules are evidence of osteoconduction, with new mineralized bone (NMB, deep blue) on the exterior, new unmineralized bone (NUB, pink) in the middle, and collagenous fibers (C) against the PA-Ti hybrid.**

Figure 6.9 illustrates the *de novo* bone formation often seen in larger amounts in the hybrid foams as compared to the bare Ti foams. As shown in Figure 6.9(A), there is a significant amount of new, highly mineralized bone with morphology similar to that of the cortical bone around what appears to be residual PA matrix. It is not clear if the PA has been pulled out of the hybrid by cells, or if it is a result of the fluids or surgical procedure. However, there is clearly an osteoinductive effect. The holes seen in the *de novo* bone formed in the bone marrow are the remnants of adipocytes, seen throughout the rest of the bone marrow. Figure 6.9(B) shows additional evidence for the direct adhesion and ingrowth of cortical bone into the hybrid implants.

Comparisons between the bare Ti foam and the PA-Ti hybrids were done qualitatively and quantitatively. As shown in Figure 6.10, there is a positive response from the host bone tissue towards all three samples. However, there appears to be a difference between the samples in terms of *de novo* bone formation. While all 3 implant materials had bone grow around them, in direct contact with them, and into their porosity, qualitatively there appears to be more *de novo* bone formed around the hybrid implants. This was particularly apparent with regard to *de novo* bone formation in the bone marrow cavity, which was often greatly increased for the two hybrids. Additionally, the rim formed around the implant appears to make direct contact more often with the hybrid implants compared to the bare Ti foam. This suggests an osteoconductive and possibly an osteoinductive effect from the PA. Certainly, considering the work presented in Chapter 2, this would not be unexpected.

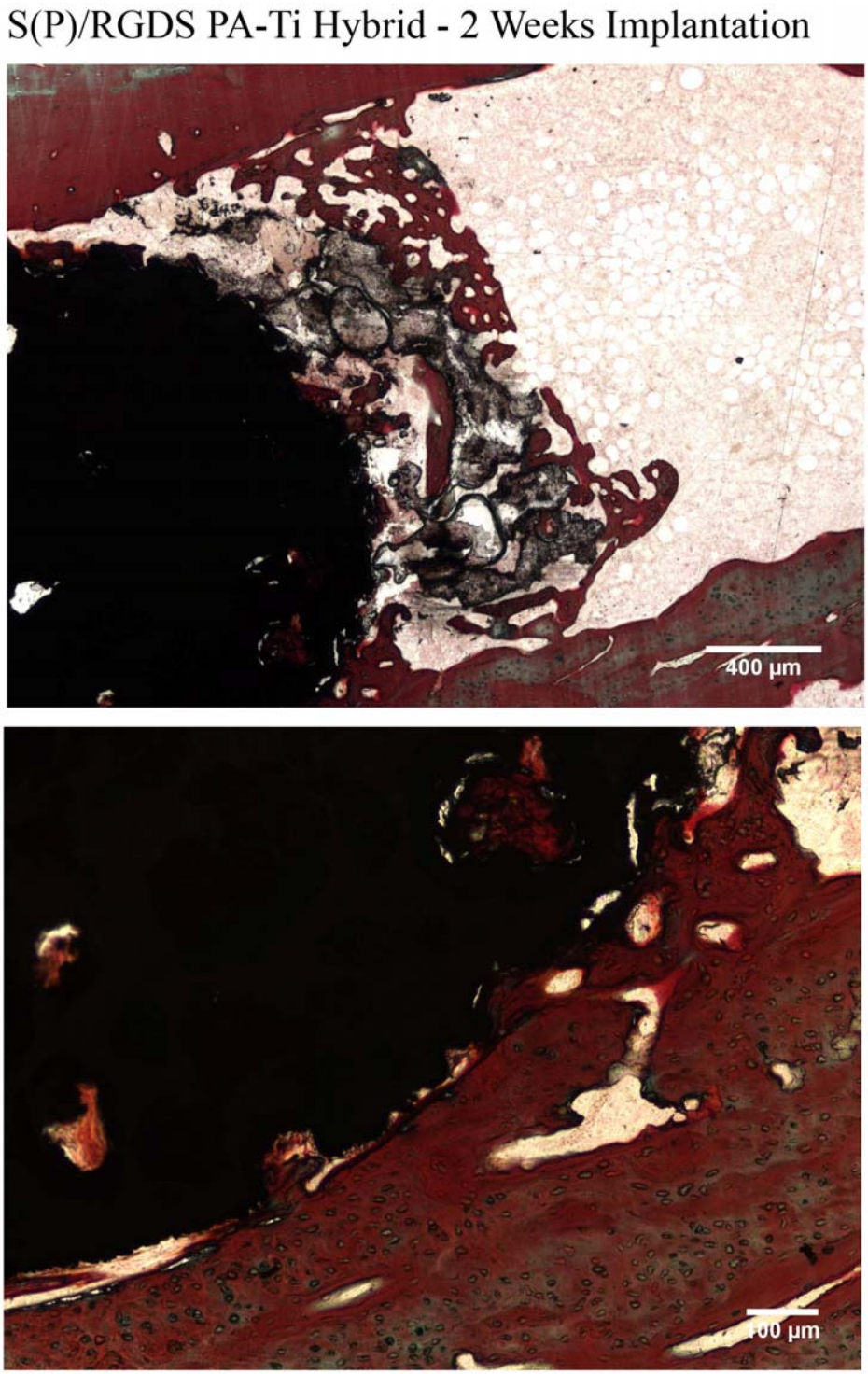


**Figure 6.9 Histological image of S(P)/RGDS PA-Ti hybrid after 2 weeks implantation. Goldner's Trichrome stain demonstrates the *de novo* bone formation commonly observed in the bone marrow in association with PA matrix (left). The cortical bone has grown into direct with the hybrid implant, and infiltrates the PA filled porosity (right).**

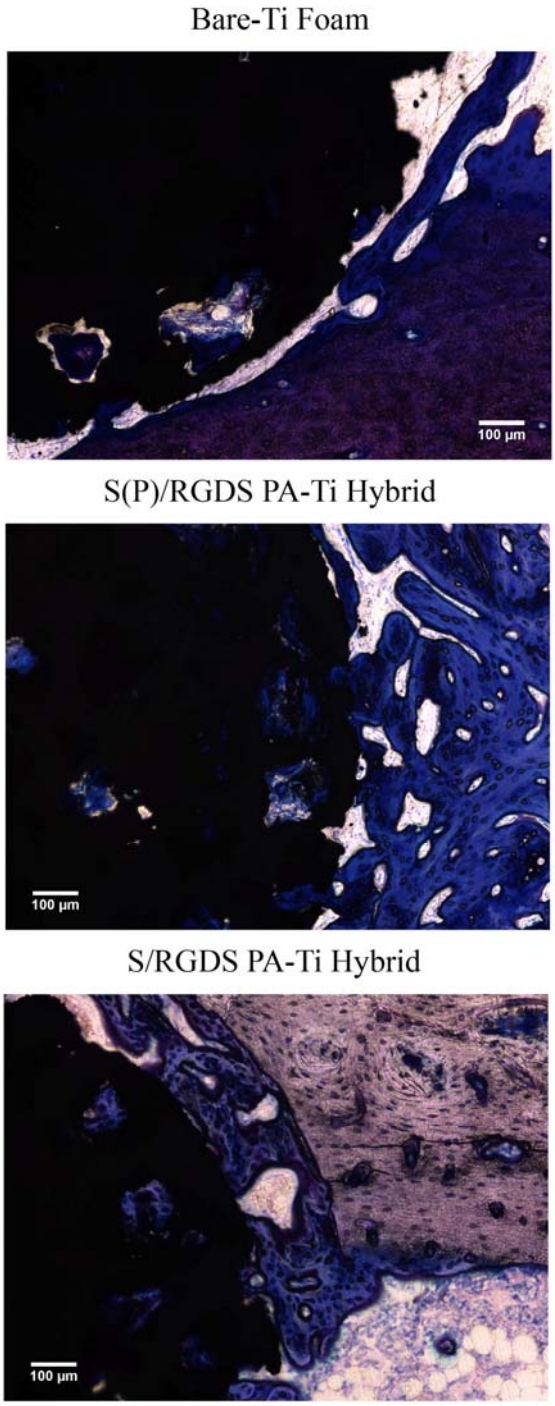


**Figure 6.10 Histological image of each sample after 4 weeks of implantation. New bone formation is observed to form around the implants, both adjacent to the cortical bone and often in the bone marrow. The *de novo* bone makes direct contact with the bare Ti foam, but often is observed to be separated by collagenous tissue (left). More often with the hybrid implants (middle and right), the *de novo* bone makes increased direct contact with the implant, infiltrating the porous implant.**

To attempt to quantify this effect, three sets of measurements were made on images of the sectioned implants. First, the amount of tissue ingrowth was calculated as a percentage of the 2D porous area. Second, the amount of *de novo* bone rimming the implant was calculated. However, to account for the differing positions in the implant that sections were collected from, only bone adjacent to cortical bone was counted, and the data was normalized to the area measured. Third, the total *de novo* bone formation within the region of the images was calculated. The data resulting from these calculations are shown in Figures 6.11, 6.12, and 6.13, respectively. As shown in Figure 6.11, quantification of the new tissue formed within the pores of the implants demonstrates that S/RGDS PA-Ti hybrids had significantly more tissue ingrowth than the S(P)/RGDS PA-Ti hybrid and the bare Ti foam after 2 weeks implantation. However, by 4 weeks of implantation, there is no significant difference between the different implants. Quantification of the new tissue formed adjacent to the exterior of the implants from the cortical bone, shown in Figure 6.12, demonstrates that S/RGDS PA-Ti hybrids had significantly higher new tissue rimming the implant compared to the bare Ti foam. Again, by 4 weeks of implantation, there is no significant difference between the different implants. Quantification of the total *de novo* bone formation, including within the pores of the foam, around the foam, and in the bone marrow cavity adjacent to the implant, is shown in Figure 6.13. After 2 weeks of implantation, the S/RGDS PA-Ti hybrids lead to increased *de novo* bone formation. This effect is not seen after 4 weeks, with all the samples being statistically equal. It should be noted, however, that the implant with the highest level of *de novo* bone formation was a S(P)/RGDS PA-Ti hybrid. A somewhat surprising find is that there is less *de novo* bone formation after 4 weeks compared to 2 weeks. However, upon examining the histology slides, it is apparent that

the cause of the reduced bone quantification is due to a reduction in the bone marrow cavity. The bone formed immediately adjacent to and within the foam implants does not appear to reduce. This indicates that the implants are both osteoconductive and gives evidence for the osteoinductive properties of the PA, which lead to increased bone formation in the marrow cavity. After extended time, the bone (and PA) in the marrow that is not under loading is presumably resorbed by osteoclasts according to Wolff's law. Combined, this data seems to suggest an increase effect on osteoconduction by the hybrids at early time points *in vivo*, particularly serine-containing PA-Ti hybrids. Considering the results of Chapter 2, which showed that both PA mixtures formed the same mineral, the reason behind this effect is not immediately clear. Presumably the mineral formed on the PA nanofibers is the same *in vitro* as *in vivo*, which would indicate that it is not an effect of mineralization since both PAs template the same mineral. In that case, the data suggests there is something concerning the chemistry of the PAs that is resulting in a biological effect. Examining the difference between the two PA-containing hybrids, the data suggests there may be a beneficial effect of using serine versus phosphoserine. Considering the difference between the bare Ti foams and the PA-Ti hybrids, there appears to be a beneficial effect of the PA matrix. This is likely due to the osteoinductive properties of the PA presented in Chapters 2 and 5.

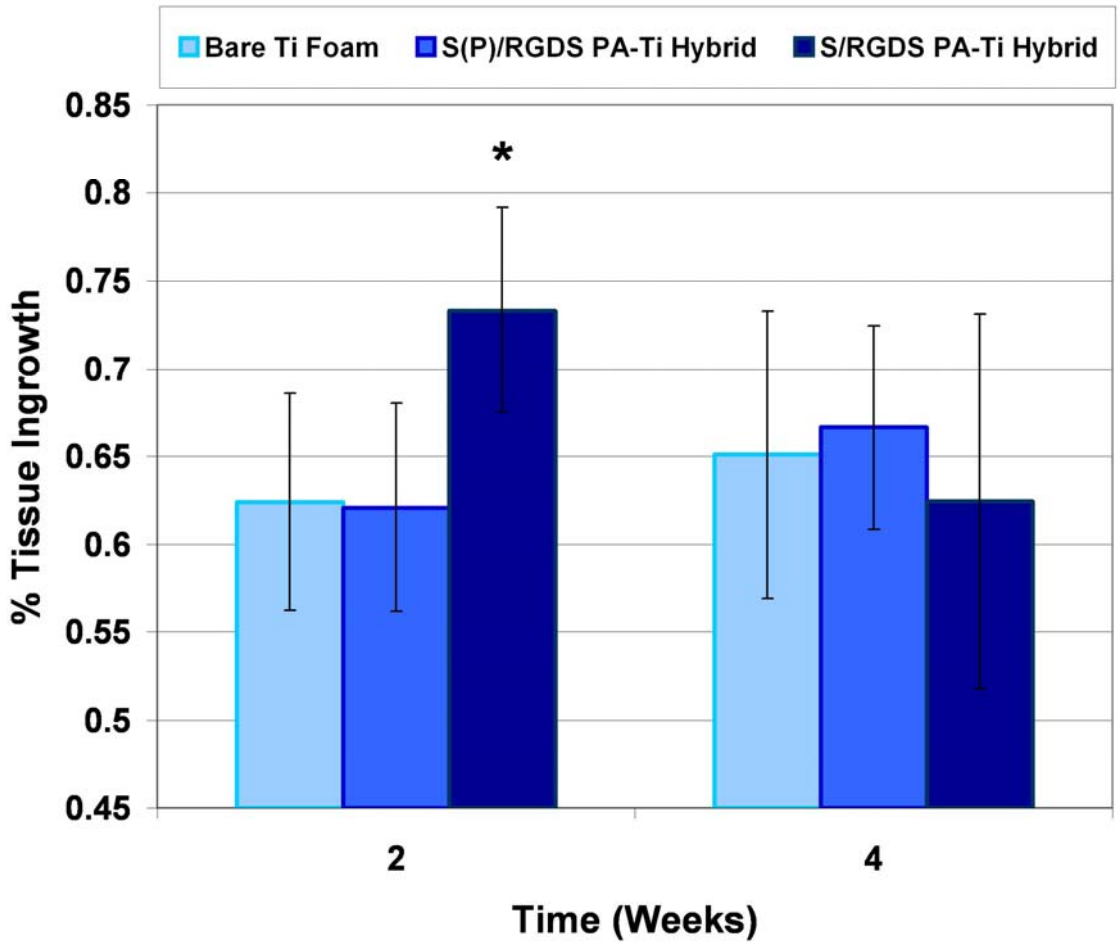


**Figure 6.11 Quantification of the new tissue formed within the porosity of the implants. After 2 weeks of implantation, the S/RGDS PA-Ti hybrid had significantly more tissue ingrowth than the S(P)/RGDS PA-Ti hybrid and the bare Ti foam. By 4 weeks of implantation, there is no significant difference between the different implants.**

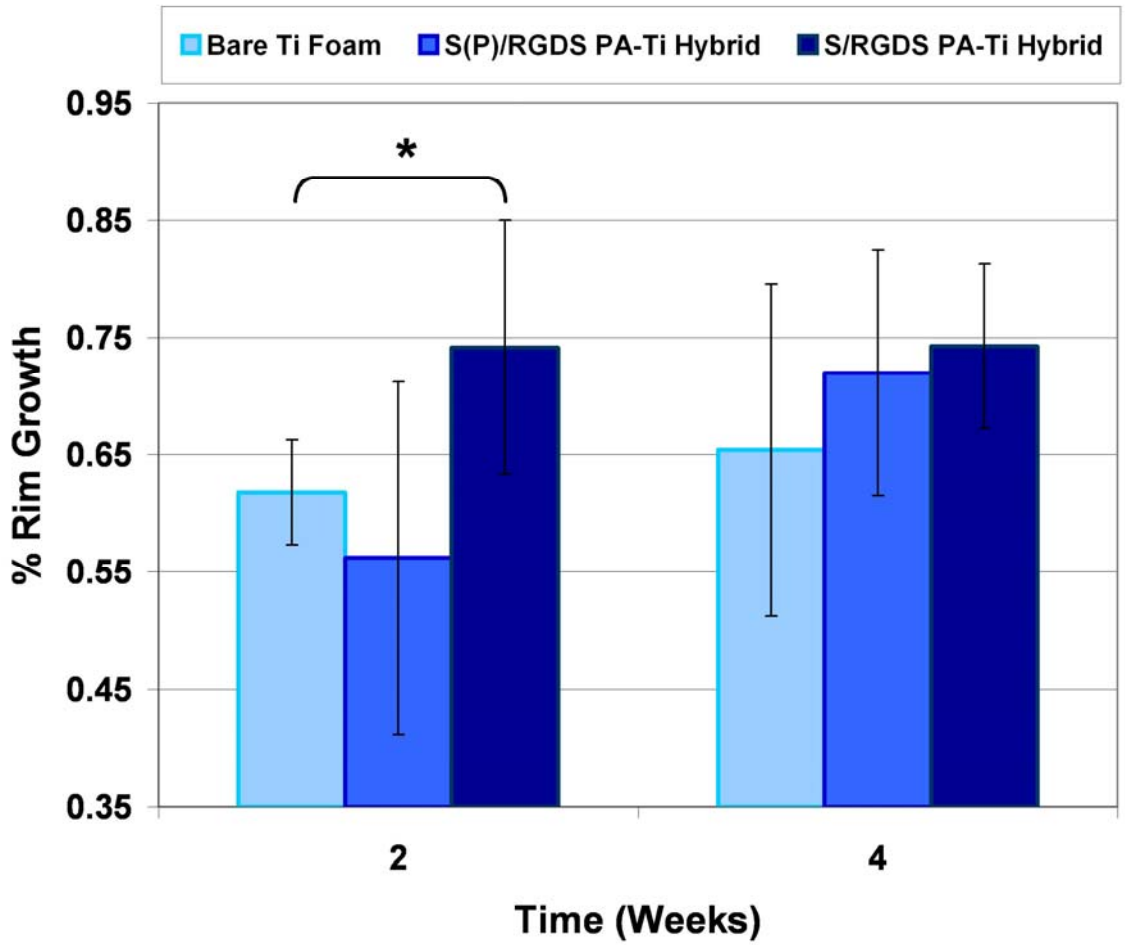


**Figure 6.12 Quantification of the new tissue formed adjacent to the exterior of the implants from the cortical bone. After 2 weeks of implantation, the S/RGDS PA-Ti hybrid had significantly higher new tissue rimming the implant compared to the bare Ti foam. By 4 weeks of implantation, there is no significant difference between the different implants.**

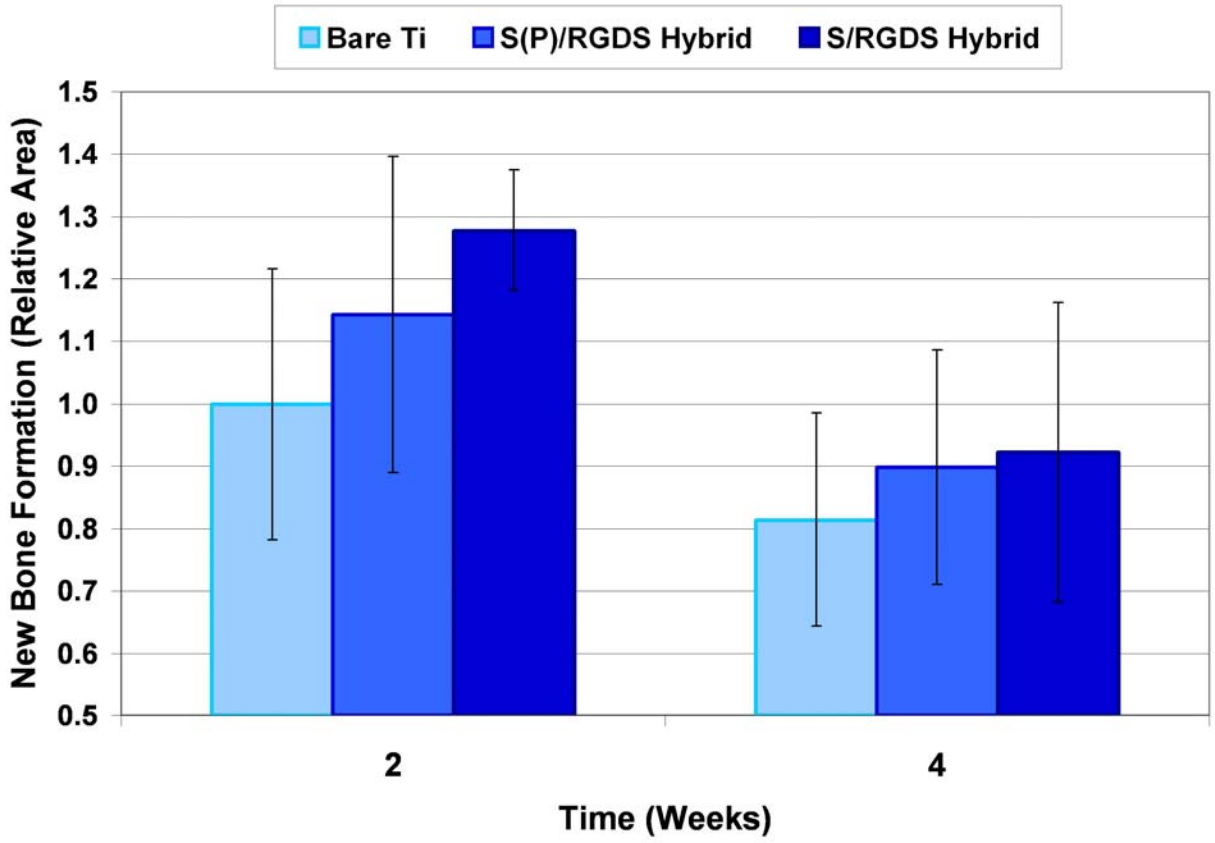


**Figure 6.13 Quantification of the total new bone formed in and around the implants, including in the bone marrow. The numbers represent the average of the best histological image for each sample, normalized to the bare Ti foams at week 2 (n=5-6). Error bars represent 95% confidence interval (α=0.05).**

There has been considerable work in recent years in the development of porous titanium scaffolds for biomedical applications, which has been nicely reviewed from a processing standpoint by Dunand[13] and more recently Ryan et al.[123]. However, nearly all work with metallic foams remains focused on the *in vitro* and *in vivo* evaluation of Ti foam parameters. Frosch et al. have evaluated the *in vitro* response of human osteoblast-like cells in porous Ti materials with varying channel diameters[165, 166]. Their work showed an optimum pore diameter range of 300 – 600 μm, corresponding to the widely regarded range of 150 – 400 μm[32]. This is not a limiting range, however, as bone has been shown to grow into pores smaller than 100 μm in diameter[144].

Using *in vivo* models, Otsuki et al.[167] have shown that not only is pore diameter important, but pore throat size as well. Their data indicate that the pore throat size can be correlated to predict the extent of tissue ingrowth. St-Pierre et al. have evaluated the *in vitro* response of mouse pre-osteoblasts to novel Ti foams with varying pore diameters compared to a solid Ti control. The porous Ti demonstrates the capacity to be colonized by the cells, which differentiate towards mature osteoblasts. However, all of these works are focused on bioinert scaffolds, regardless of geometry. There has been significant work on the modification of *solid* titanium surfaces, including coatings of collagen[168], attachment of peptides and ECM proteins[150], morphological modification of the surface oxide[169], and calcium phosphate-derived coatings[101, 153]. Recently, a few of these techniques have been applied to Ti foams. Kon et al. have created porous Ti foams modified with calcium ions by hydrothermal treatment to create calcium phosphate coatings after immersion in simulated body fluid (SBF)[26]. Similarly, Chunming et al. have created Ti foams with calcium phosphate coating by immersion in a supersaturated calcium phosphate solution[170]. However, in both cases, no biological evaluation was completed. One example of a bioactive modification of Ti foam is the organoapatite coated foams demonstrated by Spoerke et al.[60]. Using an organically-modified apatite layer on porous Ti, *in vitro* assays were performed to demonstrate directed cell adhesion and differentiation. Alternatively, titanium has been used in conjunction with biphasic calcium phosphate to create a composite, leading to increased ectopic bone formation compared to the titanium control in a goat model[171]. There are very few examples, however, of Ti foam being modified to create bioactive materials suitable for orthopaedic applications. Moreover, to the knowledge of the author, the use of a bioactive matrix to fill the porosity of Ti (or any other biomedical alloy) foams to create a composite

material has not been demonstrated prior to that described in Chapters 4, 5, and 6 and published by the author[157].

This work has important clinical relevance as well. For implants created from porous materials, the long-term goal is to obtain good osteointegration around and into the implant to provide secure fixation. A fully-infiltrated porous implant should also have better mechanical properties due to the effect of pore filling, thereby creating a composite as opposed to an empty porous material. However, it is also important for this osteointegration and bone ingrowth to occur as quickly as possible to shorten the healing period for the patient. Ultimately this is the main impetus for using the PA to create a hybrid. The preliminary results presented here seem to indicate that the PA-Ti hybrids have a beneficial effect on *de novo* bone formation, a key parameter for implant stabilization. Consequently, this work is of great interest, and the promising results necessitate future studies. In particular, it is postulated that increasing the size of the implant in a larger animal model might lead to a better understanding of the role of the PA in *de novo* bone formation and mineralized tissue ingrowth. The current study clearly demonstrates *de novo* bone formation and the direct apposition of bone to the implant surface. It is difficult to determine, however, if ingrowth would be limited in a larger diameter implant or if the PA would play a more predominant role in such a case. Perhaps in the bare Ti foam control, ingrowth to the exterior would be different than the core due to limited blood and fluid penetration during the time of implantation. There may also be a critical depth to which mineralized tissue may form which would not be apparent in a small model as used in this study. The versatility of the PA matrix by molecular design also provides many variables, such as the incorporation of sequences for cell-specific adhesion, biomolecule presentation, and improved

mechanical properties. For all of these reasons, there is much to pursue with this novel hybrid system for orthopaedic implants applications.

## 6.4 Conclusions

The *in vivo* potential of bare Ti foams and PA-Ti hybrids as orthopaedic materials was evaluated using a rat femoral implant model. Histological examination indicates that the bare Ti foams demonstrate good osteointegration up to 4 weeks from implantation and do not show signs of cytotoxicity. Bone is observed to grow from the cortical bone in direct contact with the Ti foam and into the open, interconnected porosity as early as 2 weeks. PA-Ti hybrids show similar positive osteointegration and lack of cytotoxic response. Quantification of the histological images indicates that there may be an increased osteoinductive response resulting from the PA nanofiber matrix in the hybrids. In particular, the serine-bearing PA appears to lead to increased *de novo* bone formation immediately adjacent to the implant exterior, and increased bone ingrowth. This appears to correlate with the *in vitro* data from Chapter 2, in which hMSCs were observed to more rapidly differentiate in serine-bearing PAs compared to phosphoserine-bearing PAs. SEM microscopy showed good integration of all implant materials with the host bone, with cells attaching, spreading, and migrating into the porous implants. This is the first *in vivo* demonstration of Ti foams filled with a bioactive matrix, and the data suggests that these novel Ti foams and PA-Ti hybrids may be suitable materials for orthopaedic implants.

# FUTURE WORK

As with most research, the pursuit of answering hypotheses invariably leads to new questions and new hypotheses; this work is no exception. In addition, new and alternative ideas are thought of during the process of experimentation. The sections that follow introduce possible routes for the continued development of the work presented in this thesis. The first concept is the use of a compressive bioreactor that can apply compressive strains to the metallic foams and their PA-modified hybrids, currently being developed by collaborators in the Brinson group at Northwestern University. The second section describes possible routes for *in vivo* studies of new PA-Ti hybrids. The third section involves next generation PA-Ti hybrids using novel NiTi foams developed by collaborators in the Dunand group at Northwestern University. The fourth section describes some possible directions for novel PA scaffolds for bone regeneration. Lastly, the fifth section introduces some alternative applications for some of the technologies discussed in this thesis.

## *Compressive Force Modified Rotating Bioreactor Culture Vessel*

Bone is a highly active tissue, continually being remodeled according to the stresses and resulting strains applied according to Wolff's law[9]. Mechanotransduction plays a crucial role in bone resorption and formation *in vivo*, but strain must be cyclic to result in new bone formation[172]. Tensile cyclic strain has been shown to affect the morphology, directionality, and proliferation of soft tissue cells[173, 174], and the biological activity of bone cells *in vitro*[175, 176]. Experiments *in vivo* have also demonstrated stimulated bone growth[177]. However, to the knowledge of the authors, a system to apply cyclic compressive strains to orthopaedic materials

has not yet been created. Traditional orthopaedic materials have all had very high moduli, making such an apparatus difficult to conceptualize. However, the recent development of novel, superelastic NiTi foams offers an orthopaedic material with a modulus on the order of bone and recoverable strains unattainable with other metals. An *in vitro* method to assess the cellular response to these materials under cyclic compressive strain is therefore plausible and necessary. It would also be beneficial to incorporate this into a culture system such as a rotating bioreactor due to its improved culture conditions. Consequently, the author originated the concept of a rotating bioreactor that could provide cyclic compressive strains. In collaboration with the Brinson and Dunand groups at Northwestern University, a prototype is being developed, which will be used to evaluate the biological response to NiTi foams.

## *Larger animal model studies of PA-Ti Hybrids*

As discussed in Chapter 6, there are many possibilities for this work to move forward. With so few others working on bioactive hybrids or composites containing metallic foams, there is great opportunity to advance this particular area of science and engineering. Studies need to be performed in larger animal models to evaluate the materials at their true scale and in more physiologically accurate implantation sites. The PA could be changed to incorporate alternative bioactive sequences, such as cell-specific adhesion sequences, or to deliver biomolecules and growth factors, such as BMPs. An alternative approach might include PAs to promote vascularization, which is essential for bone ingrowth to remain viable.

### *NiTi foams modified with Peptide Amphiphile Nanofibers*

With the development of NiTi foams exhibiting shape memory behavior (SME) and/or superelasticity, a number of improvements to orthopaedic implants becomes possible, including improved fitting of shaft components inside the long bone (by temperature dependent SME expansion) and reduced stress-shielding (due to decreased moduli). As with Ti foams, the incorporation of bioactive materials can be used to create orthopaedic implants capable of directing bone formation *in vivo*. The PA-Ti hybrids presented in Chapters 4-6 are but one possibility. Coating the metallic foams with 2D PA coatings present another strategy, which might be improved by covalent attachment, as demonstrated in Chapter 3. The materials developed would need to be tested *in vitro*, such as with the compressive bioreactor described above in Chapter 7.1, and ultimately in an animal model to determine the true biofunctionality.

### *New PAs for bone regeneration*

The strategy described in this thesis for bone regeneration involved the phosphoserine residue and its importance in PA nanofiber regeneration. Additionally, RGDS epitopes for cellular adhesion were used. However, a large number of peptides and growth factors have been discovered in recent years that play important roles in the complex formation of bone[156, 178, 179]. There are a variety of directions this work could go, but it is often a good strategy to incorporate something that is already FDA approved when clinical work is the ultimate goal. There is also more to be learned about the role of the chemical structure in hydroxyapatite mineralization and to better understand the process that leads to the specific morphology observed in the system described in Chapter 2.

### *Other applications of PA coatings on NiTi and Ti*

The modification of common metallic implants and novel metallic materials, such as NiTi and Ti-6Al-4V in solid and foam forms, with bioactive peptide amphiphile nanofibers lends itself well to orthopaedic implant applications. However, the concept of modifying metals with a bioactive surface could be applied to a variety of other implant applications. One implant that has received a great deal of media attention in recent years is the cardiovascular stent, used to prop open the arterial wall after balloon angioplasty for the treatment of artherosclerosis. The main problem with stent implantation is restenosis, whereby the smooth muscle cells (SMCs) in the tunica media migrate into the lumen of the artery. This occurs in part because the endothelial cells (ECs) that form the tunica intima are damaged, exposing the SMCs to blood. While drug-eluting stents have been made recently in an attempt to prevent SMC proliferation, it is likely that this will only temporarily prevent the inevitable. A better strategy might be to create coatings for the stent that promote the attachment and proliferation of endothelial cells to regrow the tunica intima and thereby prevent restenosis. A strategy that was developed during the course of this thesis, but not completed, involved the design and creation of a series of PA coatings for stents. Using PA nanofibers that incorporate peptides or biomolecules that encourage endothelial cell adhesion and proliferation, but not that of SMCs, could be very promising as a stent coating.

# FINAL CONCLUSIONS

The overall goal of the work presented in this thesis was to develop novel materials for bone regeneration and orthopaedic implants by the rational design of peptide amphiphiles to create scaffolds, coatings on biomedical alloys, and composite materials with metallic foams. The materials were characterized and evaluated for their biological response *in vitro* and/or *in vivo*. In the process of developing these systems, an attempt was made to better understand the fundamental aspects of their design on their resulting functionality and bioactivity. This chapter summarizes the significant findings in the experiments presented and describes how the conclusions address the aforementioned hypotheses.

Chapter 2 presents experiments aimed to assess the factors that mediate biologically relevant mineral templating on PA nanofibers. This includes the importance of the phosphate incorporated into the design of the original molecule discovered to template hydroxyapatite, and the effect of mixing a secondary epitope on mineralizing. Additionally, experiments were performed to assess the potential for these materials to induce stem cell differentiation along the osteoblastic lineage. The results of these studies show that:

- Net negatively-charged PAs, presenting either a serine or phosphoserine residue, self-assemble into nanofibers and template carbonated hydroxyapatite in culture medium at physiological temperatures.
- Net positively-charged RGDS-bearing PA can be mixed in at 5% without inhibiting mineral formation.

- Crystalline, carbonated hydroxyapatite forms on the nanofiber in a spherical morphology with diameters less than 100 nm, indicating that the mineral initially forms as amorphous calcium phosphate and crystallizes *in situ*. Longer mineralization times lead to increased mineral density along the nanofibers without increase in mineral diameter.
- hMSCs cultured in these PA gels differentiate along the osteoblastic lineage. S(P)-bearing PA upregulates ALP production, but S-bearing PA leads to quicker osteoblast maturation.

*These results support the hypothesis that a mixed system of PAs can be created that present RGDS adhesion epitopes and retain the ability to template calcium phosphate mineral. Additionally, the results demonstrate that phosphorylation is not required for hydroxyapatite mineral templating of PA nanofibers.*

Chapter 3 presents experiments aimed to develop, optimize, and characterize a method to create robust PA nanofiber coatings on biomedical alloys using an intermediary silane layer. Factors of importance in this system include the composition of the metal oxide layer, the silane deposition conditions, and the method of PA coating and subsequent covalent attachment. In addition to characterization of these coatings, experiments were performed to assess the biological potential and confirm there are no cytotoxic components. The results of these studies show that:

- Optimization of the chemical modification of NiTi results in a surface oxide that maximized the bonding with a model silane molecule and contains very low nickel and significantly higher $TiO_2$.

- A novel vapor deposition method was developed to create a homogenous, more robust coating of APTES molecules on NiTi substrates
- Covalent attachment results in a dense coating of self-assembled PA nanofibers on pre-treated NiTi substrates that is retained under harsh washing conditions at physiological salt concentrations
- Covalent attachment of PA nanofibers prevents detachment of cultured cells
- Biological assay results showed no toxic effect on endothelial and pre-osteoblast cells by any of the materials or reagents used

*These results support the hypothesis that silane coatings on NiTi can be used to covalently bind a dense coating of PA nanofiber, and that the resulting materials are not cytotoxic.*

Chapter 4 presents experiments aimed to develop and characterize a method to create composite materials for orthopaedic applications by combining self-assembling PA nanofibers with porous Ti alloy. Factors of importance in this system include the development of a biocompatible method to trigger self-assembly within the interconnected porosity of the foam that could be also used to encapsulate cells within the PA matrix. Characterization of these PA-Ti hybrids also proved to be a challenge in order to assess the incorporation of the PA and cells in the core of the Ti foam. The results of these studies show that:

- Self-assembly of PA solution can be triggered *in situ* within porous Ti foams by the addition of concentrated calcium.
- The PA infiltrates the entire thickness of the foam.
- The PA matrix retains its ability to mineralize within the Ti foam

- Cells can be encapsulated within the PA-Ti hybrids in a controlled manner

*These results support the hypothesis that PA can be triggered to self-assemble within and throughout Ti foams by biocompatible methods, and cells can be encapsulated within the PA matrix.*

Chapter 5 presents experiments aimed to assess the *in vitro* response of PA-Ti hybrids using GFP-transfected pre-osteoblastic cells. The experiments are designed to determine the capability of the PA-Ti hybrids to support cellular adhesion, proliferation, migration into the material, and differentiation into mature osteoblasts at times up to 4 weeks. The results of these studies show that:

- Cells adhered to and proliferated on the PA-Ti hybrids, and demonstrated sigmoidal growth that reached a plateau.
- Cells migrated into the core of the hybrids through the PA matrix and along the PA-coated Ti foam pore walls.
- Pre-osteoblastic cells matured along the osteoblastic lineage, differentiating into osteoblasts by day 14.
- The PA-Ti hybrids have sufficient nutrient diffusion to support cellular viability.

*These results support the hypothesis that PA-Ti hybrids are suitable for cellular ingrowth and differentiation, and allow for sufficient nutrient diffusion to maintain cell density*

Chapter 6 presents the results of an animal model used to evaluate the *in vivo* potential of bare Ti foam and PA-Ti hybrids as orthopaedic implant materials. The experiment was designed

to determine the biocompatibility and osteointegration of the Ti foams and PA-Ti hybrids with cortical bone. The results of these studies show that:

- Bare Ti foams demonstrate good osteointegration up to 4 weeks of implantation and do not shows signs of cytotoxicity.
- Bone is observed to grow from the cortical bone in direct contact with the Ti foam and into the open, interconnected porosity as early as 2 weeks.
- PA-Ti hybrids show similar positive osteointegration and lack of cytotoxic response.
- There may be an increased osteoinductive response resulting from the PA nanofiber matrix in the hybrids.
- Serine-bearing PA appears to lead to increased *de novo* bone formation immediately adjacent to the implant exterior, and increased bone ingrowth. This also correlates with the *in vitro* findings from Chapter 2 in which S-bearing PA increased the rate of osteoblast maturation.

*These results support the hypothesis that both Ti foams and PA-Ti hybrids are biocompatible, and PA-Ti hybrids might promote improved bone ingrowth and osteointegration compared to bare Ti foams.*

# REFERENCES

1. Ratner, B. D., A History of Biomaterials. In *Biomaterials science : an introduction to materials in medicine*, 2nd ed.; Ratner, B. D.; Hoffman, A. S.; Schoen, F. J.; Lemons, J. E., Eds. Elsevier Academic Press: Amsterdam ; Boston, 2004; pp xii, 851.

2. Schoen, F. J., Tissue Engineering. In *Biomaterials science : an introduction to materials in medicine*, 2nd ed.; Ratner, B. D.; Hoffman, A. S.; Schoen, F. J.; Lemons, J. E., Eds. Elsevier Academic Press: Amsterdam ; Boston, 2004; pp xii, 851.

3. Temenoff, J. S.; Steinbis, E. S.; Mikos, A. G., Biodegradable Scaffolds. In *Orthopedic tissue engineering : basic science and practice*, Caplan, A. I.; Goldberg, V. M., Eds. Basel : Marcel Dekker: New York ;, 2004; pp xv, 338.

4. Nather, A.; Aziz, Z., Role of Bone Allografts in Orthopaedic Surgery. In *Bone grafts and bone substitutes : basic science and clinical applications*, Nather, A., Ed. World Scientific: Hackensack, N.J., 2005; pp xvii, 592.

5. Hallab, N. J.; Jacobs, J. J.; Katz, J. L., Orthopaedic Applications. In *Biomaterials science : an introduction to materials in medicine*, 2nd ed.; Ratner, B. D.; Hoffman, A. S.; Schoen, F. J.; Lemons, J. E., Eds. Elsevier Academic Press: Amsterdam ; Boston, 2004; pp xii, 851.

6. Long, P. K.; Ibrahim, S., Autogenous Bone Grafting in Orthopaedic Surgery. In *Bone grafts and bone substitutes : basic science and clinical applications*, Nather, A., Ed. World Scientific: Hackensack, N.J., 2005; pp xvii, 592.

7. Vikram, D.; Nather, A.; Khalid, K. A., Role of Ceramics as Bone Graft Substitutes. In *Bone grafts and bone substitutes : basic science and clinical applications*, Nather, A., Ed. World Scientific: Hackensack, N.J., 2005; pp xvii, 592.

8. Park, J. B.; Lakes, R. S., *Biomaterials : an introduction*. 2nd ed.; Plenum Press: New York, 1992; p xiii, 394.

9. Einhorn, T. A., Biomechanics of Bone. In *Principles of Bone Biology*, Bilezikian, J. P.; Raisz, L. G.; Rodan, G. A., Eds. Academic Press: San Diego, 1996; pp xx, 1398.

10. Davis, J. R.; ASM International., *Handbook of Materials for Medical Devices*. ASM International: Materials Park, OH, 2003; p viii, 341.

11. Kanagaraja, S.; Wennerberg, A.; Eriksson, C.; Nygren, H., Cellular reactions and bone apposition to titanium surfaces with different surface roughness and oxide thickness cleaned by oxidation. *Biomaterials* 2001, 22, (13), 1809-1818.

12. Murray, N. G. D.; Dunand, D. C., Effect of initial preform porosity on solid-state foaming of titanium. *J Mater Res* 2006, 21, (5), 1175-1188.

13. Dunand, D. C., Processing of titanium foams. *Adv Eng Mater* 2004, 6, (6), 369-376.

14. Bansiddhi, A.; Dunand, D. C., Shape-memory NiTi foams produced by solid-state replication with NaF. *Intermetallics* 2007, 15, 1612-1622.

15. Greiner, C.; Oppenheimer, S. M.; Dunand, D. C., High strength, low stiffness, porous NiTi with superelastic properties. *Acta Biomater* 2005, 1, (6), 705-716.

16. Buehler, W. J.; Wiley, R. C.; Gilfrich, J. V., Effect of Low-Temperature Phase Changes on Mechanical Properties of Alloys near Composition Tini. *Journal of Applied Physics* 1963, 34, (5), 1475-&.

17. Hodgson, D.; Wu, M.; Biermann, R., Shape Memory Alloys. In *Metals Handbook*, Tenth Edition ed.; Vol. Vol. 2.

18. Schetky, L. M., Shape-Memory Alloys. *Scientific American* 1979, 241, (5), 74-82.

19. Gil, F. J.; Planell, J. A., Properties and Clinical Applications of Shape Memory Alloys. In *Biomaterials and Bioengineering Handbook*, Wise, D. L., Ed. 2000.

20. Park, J. B.; Kim, Y. K., Metallic Biomaterials. In *The Biomedical Engineering Handbook*, Second ed.; Bronzino, J. D., Ed. 2000; Vol. I.

21. Thierry, B.; Tabrizian, M.; Trepanier, C.; Savadogo, O.; Yahia, L. H., Effect of surface treatment and sterilization processes on the corrosion behavior of NiTi shape memory alloy. *J Biomed Mater Res* 2000, 51, (4), 685-693.

22. Thierry, B.; Merhi, Y.; Bilodeau, L.; Trepanier, C.; Tabrizian, M., Nitinol versus stainless steel stents: acute thrombogenicity study in an ex vivo porcine model. *Biomaterials* 2002, 23, (14), 2997-3005.

23. Bogdanski, D.; Koller, M.; Muller, D.; Muhr, G.; Bram, M.; Buchkremer, H. P.; Stover, D.; Choi, J.; Epple, M., Easy assessment of the biocompatibility of Ni-Ti alloys by in vitro cell culture experiments on a functionally graded Ni-NiTi-Ti material. *Biomaterials* 2002, 23, (23), 4549-4555.

24. Ryhanen, J.; Kallioinen, M.; Tuukkanen, J.; Junila, J.; Niemela, E.; Sandvik, P.; Serlo, W., In vivo biocompatibility evaluation of nickel-titanium shape memory metal alloy: Muscle and perineural tissue responses and encapsule membrane thickness. *J Biomed Mater Res* 1998, 41, (3), 481-488.

25. Nilles, J. L.; Karagian.Mt; Wheeler, K. R., Porous Titanium-Alloy for Fixation of Knee Prostheses. *J Biomed Mater Res* 1974, 8, (4), 319-328.

26. Kon, M.; Hirakata, L. M.; Asaoka, K., Porous Ti-6Al-4V alloy fabricated by spark plasma sintering for biornimetic surface modification. *J Biomed Mater Res Part B-Applied Biomaterials* 2004, 68B, (1), 88-93.

27. Oh, I. H.; Nomura, N.; Masahashi, N.; Hanada, S., Mechanical properties of porous titanium compacts prepared by powder sintering. *Scr Mater* 2003, 49, (12), 1197-1202.

28. Wen, C. E.; Yamada, Y.; Shimojima, K.; Chino, Y.; Asahina, T.; Mabuchi, M., Processing and mechanical properties of autogenous titanium implant materials. *J Mater Sci Mater Med* 2002, 13, (4), 397-401.

29. Yang, S. H.; Kim, W. Y.; Kim, M. S., Fabrication of unidirectional porous TiAl-Mn intermetallic compounds by reactive sintering using extruded powder mixtures. *Intermetallics* 2003, 11, (8), 849-855.

30. Rhalmi, S.; Odin, M.; Assad, M.; Tabrizian, M.; Rivard, C. H.; Yahia, L. H., Hard, soft tissue and in vitro cell response to porous nickel-titanium: a biocompatibility evaluation. *Bio-Medical Materials and Engineering* 1999, 9, (3), 151-162.

31. Kujala, S.; Ryhanen, J.; Danilov, A.; Tuukkanen, J., Effect of porosity on the osteointegration and bone ingrowth of a weight-bearing nickel-titanium bone graft substitute. *Biomaterials* 2003, 24, (25), 4691-4697.

32. Ayers, R. A.; Simske, S. J.; Bateman, T. A.; Petkus, A.; Sachdeva, R. L. C.; Gyunter, V. E., Effect of nitinol implant porosity on cranial bone ingrowth and apposition after 6 weeks. *J Biomed Mater Res* 1999, 45, (1), 42-47.

33. Assad, M.; Chernyshov, A. V.; Jarzem, P.; Leroux, M. A.; Coillard, C.; Charette, S.; Rivard, C. H., Porous titanium-nickel for intervertebral fusion in a sheep model: Part 2. Surface analysis and nickel release assessment. *J Biomed Mater Res Part B-Applied Biomaterials* 2003, 64B, (2), 121-129.

34. Assad, M.; Jarzem, P.; Leroux, M. A.; Coillard, C.; Chernyshov, A. V.; Charette, S.; Rivard, C. H., Porous titanium-nickel for intervertebral fusion in a sheep model: Part 1. Histomorphometric and radiological analysis. *J Biomed Mater Res Part B-Applied Biomaterials* 2003, 64B, (2), 107-120.

35. Kearns, M. W.; Blenkinsop, P. A.; Barber, A. C.; Farthing, T. W., Manufacture of a Novel Porous Metal. *International Journal of Powder Metallurgy* 1988, 24, (1), 59-64.

36. Davis, N. G.; Teisen, J.; Schuh, C.; Dunand, D. C., Solid-state foaming of titanium by superplastic expansion of argon-filled pores. *J Mater Res* 2001, 16, (5), 1508-1519.

37. Murray, N. G. D.; Dunand, D. C., Microstructure evolution during solid-state foaming of titanium. *Composites Sci Technol* 2003, 63, (16), 2311-2316.

38. Murray, N. G. D.; Schuh, C. A.; Dunand, D. C., Solid-state foaming of titanium by hydrogen-induced internal-stress superplasticity. *Scr Mater* 2003, 49, (9), 879-883.

39. Frary, M.; Schuh, C.; Dunand, D. C., Kinetics of biaxial dome formation by transformation superplasticity of titanium alloys and composites. *Metallurgical and Materials Transactions a-Physical Metallurgy and Materials Science* 2002, 33, (6), 1669-1680.

40. Schuh, C.; Dunand, D. C., Tensile fracture during transformation superplasticity of Ti-6Al-4V. *J Mater Res* 2001, 16, (3), 865-875.

41. Schuh, C.; Dunand, D. C., Non-isothermal transformation-mismatch plasticity: Modeling and experiments on Ti-6Al-4V. *Acta Mater* 2001, 49, (2), 199-210.

42. Oppenheimer, S. M.; J.G., O. D.; D.C., D., Porous, Superelastic NiTi Produced by Powder-Metallurgy. *TMS Letters* 2004, 1, (5), 93-94.

43. Goldberg, V. M.; Caplan, A. I., Principles of Tissue Engineering and Regeneration of Skeletal Tissues. In *Orthopedic tissue engineering : basic science and practice*, Caplan, A. I.; Goldberg, V. M., Eds. Basel : Marcel Dekker: New York ;, 2004; pp xv, 338.

44. Caterson, E. J.; Tuan, R. S.; Bruder, S. P., Cell-Based Approaches to Orthopaedic Tissue Engineering. In *Orthopedic tissue engineering : basic science and practice*, Caplan, A. I.; Goldberg, V. M., Eds. Basel : Marcel Dekker: New York ;, 2004; pp xv, 338.

45. Nather, A.; Aziz, S., Scaffolds in Bone Tissue Engineering. In *Bone grafts and bone substitutes : basic science and clinical applications*, Nather, A., Ed. World Scientific: Hackensack, N.J., 2005; pp xvii, 592.

46. Hoffman, A. S.; Hubbell, J. A., Surface-Immobilized Biomolecules. In *Biomaterials science : an introduction to materials in medicine*, 2nd ed.; Ratner, B. D.; Hoffman, A. S.; Schoen, F. J.; Lemons, J. E., Eds. Elsevier Academic Press: Amsterdam ; Boston, 2004; pp xii, 851.

47. Nather, A.; Dutton, A. Q., The Role of Bone Morphogenic Proteins in Bone Incorporation. In *Bone grafts and bone substitutes : basic science and clinical applications*, Nather, A., Ed. World Scientific: Hackensack, N.J., 2005; pp xvii, 592.

48. Fussell, G. W.; Cooper, S. L., Endothelial cell adhesion on RGD-containing methacrylate terpolymers. *J Biomed Mater Res* 2004, 70A, (2), 265-273.

49. Lin, H. B.; Garciaecheverria, C.; Asakura, S.; Sun, W.; Mosher, D. F.; Cooper, S. L., Endothelial-Cell Adhesion on Polyurethanes Containing Covalently Attached Rgd-Peptides. *Biomaterials* 1992, 13, (13), 905-914.

50. Ruoslahti, E., RGD and other recognition sequences for integrins. *Annual Review of Cell and Developmental Biology* 1996, 12, 697-715.

51. Ruoslahti, E.; Pierschbacher, M. D., New Perspectives in Cell-Adhesion - Rgd and Integrins. *Science* 1987, 238, (4826), 491-497.

52. Grant, R. P.; Spitzfaden, C.; Altroff, H.; Campbell, I. D.; Mardon, H. J., Structural requirements for biological activity of the ninth and tenth FIII domains of human fibronectin. *Journal of Biological Chemistry* 1997, 272, (10), 6159-6166.

53. Rauff, S.; Oakley, R. E., Stem Cell Technology and its Commercial Potential. In *Bone grafts and bone substitutes : basic science and clinical applications*, Nather, A., Ed. World Scientific: Hackensack, N.J., 2005; pp xvii, 592.

54. Nather, A.; De, S. D.; Wei, L. C., Culturing Mesenchymal Stem Cells from Bone Marrow. In *Bone grafts and bone substitutes : basic science and clinical applications*, Nather, A., Ed. World Scientific: Hackensack, N.J., 2005; pp xvii, 592.

55. Hartgerink, J. D.; Beniash, E.; Stupp, S. I., Self-assembly and mineralization of peptide-amphiphile nanofibers. *Science* 2001, 294, (5547), 1684-1688.

56. Hartgerink, J. D.; Beniash, E.; Stupp, S. I., Peptide-amphiphile nanofibers: a versatile scaffold for the preparation of self-assembling materials. *Proc Natl Acad Sci U S A* 2002, 99, (8), 5133-8.

57. Niece, K. L.; Hartgerink, J. D.; Donners, J. J. J. M.; Stupp, S. I., Self-assembly combining two bioactive peptide-amphiphile molecules into nanofibers by electrostatic attraction. *Journal of the American Chemical Society* 2003, 125, (24), 7146-7147.

58. Storrie, H.; Guler, M. O.; Abu-Amara, S. N.; Volberg, T.; Rao, M.; Geiger, B.; Stupp, S. I., Supramolecular crafting of cell adhesion. *Biomaterials* 2007, 28, (31), 4608-4618.

59. Rajangam, K.; Behanna, H. A.; Hui, M. J.; Han, X. Q.; Hulvat, J. F.; Lomasney, J. W.; Stupp, S. I., Heparin binding nanostructures to promote growth of blood vessels. *Nano Lett* 2006, 6, (9), 2086-2090.

60. Spoerke, E. D. Biomaterial systems for orthopedic tissue engineering. Northwestern University, Evanston, 2003.

61. Nather, A.; Ong, H. J. C.; Aziz, Z., Structure of Bone. In *Bone grafts and bone substitutes : basic science and clinical applications*, Nather, A., Ed. World Scientific: Hackensack, N.J., 2005; pp xvii, 592.

62. Lees, S., Some characteristics of mineralised collagen. In *Calcified tissue*, Hukins, D. W. L., Ed. CRC Press: Boca Raton, Fla., 1989; pp [xi], 250.

63. Henthorn, P. S., Alkaline Phosphatase. In *Principles of bone biology*, Bilezikian, J. P.; Raisz, L. G.; Rodan, G. A., Eds. Academic Press: San Diego, 1996; pp xx, 1398.

64. Robey, P. G., Bone Matrix Proteoglycans and Glycoproteins. In *Principles of bone biology*, Bilezikian, J. P.; Raisz, L. G.; Rodan, G. A., Eds. Academic Press: San Diego, 1996; pp xx, 1398.

65. Guler, M. O.; Hsu, L.; Soukasene, S.; Harrington, D. A.; Hulvat, J. F.; Stupp, S. I., Presentation of RGDS epitopes on self-assembled nanofibers of branched peptide amphiphiles. *Biomacromolecules* 2006, 7, (6), 1855-1863.

66. Guler, M. O.; Soukasene, S.; Hulvat, J. F.; Stupp, S. I., Presentation and recognition of biotin on nanofibers formed by branched peptide amphiphiles. *Nano Lett* 2005, 5, (2), 249-252.

67. LeGeros, R. Z., *Calcium phosphates in oral biology and medicine*. Karger: Basel New York, 1991; p [ix], 201.

68. Rey, C.; Combes, C.; Drouet, C.; Sfihi, H.; Barroug, A., Physico-chemical properties of nanocrystalline apatites: Implications for biominerals and biomaterials. *Materials Science & Engineering C-Biomimetic and Supramolecular Systems* 2007, 27, (2), 198-205.

69. Holt, C.; van Kemenade, M. J. J. M., The Interaction of Phosphoproteins with Calcium Phosphate. In *Calcified Tissue*, Hukins, D. W. L., Ed. CRC Press: Boca Raton, Fla., 1989; p 175.

70. Zhao, Y.; Zhang, Y.; Ning, F.; Guo, D.; Xu, Z., Synthesis and cellular biocompatibility of two kinds of HAP with different nanocrystal morphology. *Journal of Biomedical Materials Research Part B-Applied Biomaterials* 2007, 83B, (1), 121-126.

71. Fathi, M. H.; Hanifi, A., Evaluation and characterization of nanostructure hydroxyapatite powder prepared by simple sol-gel method. *Materials Letters* 2007, 61, (18), 3978-3983.

72. Cromme, P.; Zollfrank, C.; Muller, L.; Muller, F. A.; Greil, P., Biomimetic mineralisation of apatites on Ca2+ activated cellulose templates. *Materials Science and Engineering C* 2007, 27, 1-7.

73. Weiner, S.; Addadi, L., Design strategies in mineralized biological materials. *Journal of Materials Chemistry* 1997, 7, (5), 689-702.

74. Liao, S.; Watari, F.; Xu, G. F.; Ngiam, M.; Ramakrishna, S.; Chan, C. K., Morphological effects of variant carbonates in biomimetic hydroxyapatite. *Materials Letters* 2007, 61, (17), 3624-3628.

75. Albrektsson, T.; Johansson, C., Osteoinduction, osteoconduction and osseointegration. *European Spine Journal* 2001, 10, S96-S101.

76. Langer, R.; Vacanti, J. P., Tissue Engineering. *Science* 1993, 260, (5110), 920-926.

77. Vasita, R.; Katti, D. S., Growth factor-delivery systems for tissue engineering: a materials perspective. *Expert Review of Medical Devices* 2006, 3, (1), 29-47.

78. Stupp, S. I.; Ciegler, G. W., Organoapatites - Materials for Artificial Bone .1. Synthesis and Microstructure. *J Biomed Mater Res* 1992, 26, (2), 169-183.

79. Chou, Y. F.; Huang, W. B.; Dunn, J. C. Y.; Miller, T. A.; Wu, B. M., The effect of biomimetic apatite structure on osteoblast viability, proliferation, and gene expression. *Biomaterials* 2005, 26, (3), 285-295.

80. El-Ghannam, A. R.; Ducheyne, P.; Risbud, M.; Adams, C. S.; Shapiro, I. M.; Castner, D.; Golledge, S.; Composto, R. J., Model surfaces engineered with nanoscale roughness and RGD tripeptides promote osteoblast activity. *J Biomed Mater Res* 2004, 68A, (4), 615-627.

81. Xiao, S. J.; Textor, M.; Spencer, N. D.; Sigrist, H., Covalent attachment of cell-adhesive, (Arg-Gly-Asp)-containing peptides to titanium surfaces. *Langmuir* 1998, 14, (19), 5507-5516.

82. Fishbein, I.; Alferiev, I. S.; Nyanguile, O.; Gaster, R.; Vohs, J. M.; Wong, G. S.; Felderman, H.; Chen, I. W.; Choi, H.; Wilensky, R. L.; Levy, R. J., Bisphosphonate-mediated gene vector delivery from the metal surfaces ot stents. *Proceedings of the National Academy of Sciences of the United States of America* 2006, 103, (1), 159-164.

83. Aoki, J.; Serruys, P. W.; van Beusekom, H.; Ong, A. T. L.; McFadden, E. P.; Sianos, G.; van der Giessen, W. J.; Regar, E.; de Feyter, P. J.; Davis, H. R.; Rowland, S.; Kutryk, M. J. B., Endothelial progenitor cell capture by stents coated with antibody against CD34 - The HEALING-FIM (healthy endothelial accelerated lining inhibits neointimal growth-first in man) registry. *Journal of the American College of Cardiology* 2005, 45, (10), 1574-1579.

84. Heise, C.; Bier, F. F., Immobilization of DNA on microarrays. *Top Curr Chem* 2006, 261, 1-25.

85. Thakkar, H.; Davey, C. L.; Medcalf, E. A.; Skingle, L.; Craig, A. R.; Newman, D. J.; Price, C. P., Stabilization of Turbidimetric Immunoassay by Covalent Coupling of Antibody to Latex-Particles. *Clinical Chemistry* 1991, 37, (7), 1248-1251.

86. Zhang, F. X.; Srinivasan, M. P., Self-assembled molecular films of aminosilanes and their immobilization capacities. *Langmuir* 2004, 20, (6), 2309-2314.

87. Puleo, D. A., Activity of Enzyme Immobilized on Silanized Co-Cr-Mo. *J Biomed Mater Res* 1995, 29, (8), 951-957.

88. Moon, J. H.; Shin, J. W.; Kim, S. Y.; Park, J. W., Formation of uniform aminosilane thin layers: An imine formation to measure relative surface density of the amine group. *Langmuir* 1996, 12, (20), 4621-4624.

89. White, L. D.; Tripp, C. P., Reaction of (3-aminopropyl)dimethylethoxysilane with amine catalysts on silica surfaces. *Journal of Colloid and Interface Science* 2000, 232, (2), 400-407.

90. Petri, D. F. S.; Wenz, G.; Schunk, P.; Schimmel, T., An improved method for the assembly of amino-terminated monolayers on SiO2 and the vapor deposition of gold layers. *Langmuir* 1999, 15, (13), 4520-4523.

91. Ek, S.; Iiskola, E. I.; Niinisto, L., Gas-phase deposition of aminopropylalkoxysilanes on porous silica. *Langmuir* 2003, 19, (8), 3461-3471.

92. Ek, S.; Iiskola, E. I.; Niinisto, L.; Pakkanen, T. T.; Root, A., New bonding modes of gas-phase deposited gamma-aminopropyltriethoxysilane on silica studied by Si-29 CP/MAS NMR. *Chemical Communications* 2003, (16), 2032-2033.

93. Trepanier, C.; Leung, T. K.; Tabrizian, M.; Yahia, L.; Bienvenu, J. G.; Tanguay, J. F.; Piron, D. L.; Bilodeau, L., Preliminary investigation of the effects of surface treatments on biological response to shape memory NiTi stents. *J Biomed Mater Res* 1999, 48, (2), 165-171.

94. Trepanier, C.; Tabrizian, M.; Yahia, L.; Bilodeau, L.; Piron, D. L., Effect of modification of oxide layer on NiTi stent corrosion resistance. *J Biomed Mater Res* 1998, 43, (4), 433-440.

95. Shabalovskaya, S. A., Surface, corrosion and biocompatibility aspects of Nitinol as an implant material. *Bio-Medical Materials and Engineering* 2002, 12, (1), 69-109.

96. Shabalovskaya, S. A., On the nature of the biocompatibility and on medical applications of NiTi shape memory and superelastic alloys. *Bio-Medical Materials and Engineering* 1996, 6, (4), 267-289.

97. Rocher, P.; El Medawar, L.; Hornez, J. C.; Traisnel, M.; Breme, J.; Hildebrand, H. F., Biocorrosion and cytocompatibility assessment of NiTi shape memory alloys. *Scr Mater* 2004, 50, (2), 255-260.

98. Rhalmi, S.; Charette, S.; Assad, M.; Coillard, C.; Rivard, C. H., The spinal cord dura mater reaction to nitinol and titanium alloy particles: a 1-year study in rabbits. *European Spine Journal* 2007, 16, (7), 1063-1072.

99. Silva, G. A.; Czeisler, C.; Niece, K. L.; Beniash, E.; Harrington, D. A.; Kessler, J. A.; Stupp, S. I., Selective differentiation of neural progenitor cells by high-epitope density nanofibers. *Science* 2004, 303, (5662), 1352-1355.

100. Carley, A. F.; Roberts, J. C.; Roberts, M. W., Dissociative Chemisorption and Localized Oxidation-States at Titanium Surfaces. *Surface Science* 1990, 225, (3), L39-L41.

101. Viornery, C.; Chevolot, Y.; Leonard, D.; Aronsson, B. O.; Pechy, P.; Mathieu, H. J.; Descouts, P.; Gratzel, M., Surface modification of titanium with phosphonic acid to improve bone bonding: Characterization by XPS and ToF-SIMS. *Langmuir* 2002, 18, (7), 2582-2589.

102. Endo, K., Chemical modification of metallic implant surfaces with biofunctional proteins (Part 1). Molecular structure and biological activity of a modified NiTi alloy surface. *Dent Mater J* 1995, 14, (2), 185-98.

103. Gu, Y. W.; Tay, B. Y.; Lim, C. S.; Yong, M. S., Characterization of bioactive surface oxidation layer on NiTi alloy. *Applied Surface Science* 2005, 252, (5), 2038-2049.

104. Smith, N. A.; Antoun, G. G.; Ellis, A. B.; Crone, W. C., Improved adhesion between nickel-titanium shape memory alloy and a polymer matrix via silane coupling agents. *Composites Part a-Applied Science and Manufacturing* 2004, 35, (11), 1307-1312.

105. Armitage, D. A.; Parker, T. L.; Grant, D. M., Biocompatibility and hemocompatibility of surface-modified NiTi alloys. *J Biomed Mater Res* 2003, 66A, (1), 129-137.

106. Shabalovskaya, S. A., Biological aspects of TiNi alloy surfaces. *Journal De Physique Iv* 1995, 5, (C8), 1199-1204.

107. Nanci, A.; Wuest, J. D.; Peru, L.; Brunet, P.; Sharma, V.; Zalzal, S.; McKee, M. D., Chemical modification of titanium surfaces for covalent attachment of biological molecules. *J Biomed Mater Res* 1998, 40, (2), 324-335.

108. Ek, S.; Iiskola, E. I.; Niinisto, L.; Vaittinen, J.; Pakkanen, T. T.; Keranen, J.; Auroux, A., Atomic layer deposition of a high-density aminopropylsiloxane network on silica through sequential reactions of gamma-aminopropyltrialkoxysilanes and water. *Langmuir* 2003, 19, (25), 10601-10609.

109. Miller, D. C.; Thapa, A.; Haberstroh, K. M.; Webster, T. J., Endothelial and vascular smooth muscle cell function on poly(lactic-co-glycolic acid) with nano-structured surface features. *Biomaterials* 2004, 25, (1), 53-61.

110. Chung, T. W.; Liu, D. Z.; Wang, S. Y.; Wang, S. S., Enhancement of the growth of human endothelial cells by surface roughness at nanometer scale. *Biomaterials* 2003, 24, (25), 4655-4661.

111. Dalby, M. J.; Riehle, M. O.; Johnstone, H.; Affrossman, S.; Curtis, A. S. G., In vitro reaction of endothelial cells to polymer demixed nanotopography. *Biomaterials* 2002, 23, (14), 2945-2954.

112. Webster, T. J.; Ergun, C.; Doremus, R. H.; Siegel, R. W.; Bizios, R., Specific proteins mediate enhanced osteoblast adhesion on nanophase ceramics. *J Biomed Mater Res* 2000, 51, (3), 475-483.

113. Xu, C. Y.; Yang, F.; Wang, S.; Ramakrishna, S., In vitro study of human vascular endothelial cell function on materials with various surface roughness. *J Biomed Mater Res* 2004, 71A, (1), 154-161.

114. Balasundaram, G.; Sato, M.; Webster, T. J., Using hydroxyapatite nanoparticles and decreased crystallinity to promote osteoblast adhesion similar to functionalizing with RGD. *Biomaterials* 2006, 27, (14), 2798-2805.

115. Webster, T. J.; Ergun, C.; Doremus, R. H.; Siegel, R. W.; Bizios, R., Enhanced functions of osteoblasts on nanophase ceramics. *Biomaterials* 2000, 21, (17), 1803-1810.

116. Boyan, B. D.; Hummert, T. W.; Dean, D. D.; Schwartz, Z., Role of material surfaces in regulating bone and cartilage cell response. *Biomaterials* 1996, 17, (2), 137-146.

117. Schwartz, Z.; Lohmann, C. H.; Vocke, A. K.; Sylvia, V. L.; Cochran, D. L.; Dean, D. D.; Boyan, B. D., Osteoblast response to titanium surface roughness and 1 alpha,25-(OH)(2)D-3 is mediated through the mitogen-activated protein kinase (MAPK) pathway. *J Biomed Mater Res* 2001, 56, (3), 417-426.

118. Deligianni, D. D.; Katsala, N. D.; Koutsoukos, P. G.; Missirlis, Y. F., Effect of surface roughness of hydroxyapatite on human bone marrow cell adhesion, proliferation, differentiation and detachment strength. *Biomaterials* 2001, 22, (1), 87-96.

119. Martin, J. Y.; Schwartz, Z.; Hummert, T. W.; Schraub, D. M.; Simpson, J.; Lankford, J.; Dean, D. D.; Cochran, D. L.; Boyan, B. D., Effect of Titanium Surface-Roughness on Proliferation, Differentiation, and Protein-Synthesis of Human Osteoblast-Like Cells (Mg63). *J Biomed Mater Res* 1995, 29, (3), 389-401.

120. Harrington, D. A.; Cheng, E. Y.; Guler, M. O.; Lee, L. K.; Donovan, J. L.; Claussen, R. C.; Stupp, S. I., Branched peptide-amphiphiles as self-assembling coatings for tissue engineering scaffolds. *J Biomed Mater Res* 2006, 78A, (1), 157-167.

121. Bogdanski, D.; Esenwein, S. A.; Prymak, O.; Epple, M.; Muhr, G.; Koller, M., Inhibition of PMN apoptosis after adherence to dip-coated calcium phosphate surfaces on a NiTi shape memory alloy. *Biomaterials* 2004, 25, (19), 4627-4632.

122. Sargeant, A.; Goswami, T., Hip implants: Paper V. Physiological effects. *Materials & Design* 2006, 27, (4), 287-307.

123. Ryan, G.; Pandit, A.; Apatsidis, D. P., Fabrication methods of porous metals for use in orthopaedic applications. *Biomaterials* 2006, 27, (13), 2651-2670.

124. Long, M.; Rack, H. J., Titanium alloys in total joint replacement - a materials science perspective. *Biomaterials* 1998, 19, (18), 1621-1639.

125. Mcnamara, B. P.; Toni, A.; Tayor, D., Effects of Implant Material Properties and Implant-Bone Bonding on Stress Shielding in Cementless Total Hip-Arthroplasty. *Adv Eng Mater* 1995, 99-1, 309-314.

126. Wen, C. E.; Mabuchi, M.; Yamada, Y.; Shimojima, K.; Chino, Y.; Asahina, T., Processing of biocompatible porous Ti and Mg. *Scr Mater* 2001, 45, (10), 1147-1153.

127. Zardiackas, L. D.; Parsell, D. E.; Dillon, L. D.; Mitchell, D. W.; Nunnery, L. A.; Poggie, R., Structure, metallurgy, and mechanical properties of a porous tantalum foam. *J Biomed Mater Res* 2001, 58, (2), 180-187.

128. Li, H. L.; Oppenheimer, S. M.; Stupp, S. I.; Dunand, D. C.; Brinson, L. C., Effects of pore morphology and bone ingrowth on mechanical properties of microporous titanium as an orthopaedic implant material. *Materials Transactions* 2004, 45, (4), 1124-1131.

129. Shen, H.; Brinson, L. C., Finite element modeling of porous titanium. *International Journal of Solids and Structures* 2007, 44, (1), 320-335.

130. Thelen, S.; Barthelat, F.; Brinson, L. C., Mechanics considerations for microporous titanium as an orthopedic implant material. *J Biomed Mater Res* 2004, 69A, (4), 601-610.

131. Li, J. P.; de Wijn, J. R.; Van Blitterswijk, C. A.; de Groot, K., Porous Ti6Al4V scaffold directly fabricating by rapid prototyping: Preparation and in vitro experiment. *Biomaterials* 2006, 27, (8), 1223-1235.

132. Queheillalt, D. T.; Choi, B. W.; Schwartz, D. S.; Wadley, H. N. G., Creep expansion of porous Ti-6Al-4V sandwich structures. *Metallurgical and Materials Transactions a-Physical Metallurgy and Materials Science* 2000, 31, (1), 261-273.

133. Lagoudas, D. C.; Vandygriff, E. L., Processing and characterization of NiTi porous SMA by elevated pressure sintering. *Journal of Intelligent Material Systems and Structures* 2002, 13, (12), 837-850.

134. Elzey, D. M.; Wadley, H. N. G., The limits of solid state foaming. *Acta Mater* 2001, 49, (5), 849-859.

135. Spoerke, E. D.; Stupp, S. I., Synthesis of a poly (L-lysine)-calcium phosphate hybrid on titanium surfaces for enhanced bioactivity. *Biomaterials* 2005, 26, (25), 5120-5129.

136. Li, J.; Yun, H.; Gong, Y. D.; Zhao, N. M.; Zhang, X. F., Investigation of MC3T3-E1 cell behavior on the surface of GRGDS-coupled chitosan. *Biomacromolecules* 2006, 7, (4), 1112-1123.

137. Porte-Durrieu, M. C.; Guillemot, F.; Pallu, S.; Labrugere, C.; Brouillaud, B.; Bareille, R.; Amedee, J.; Barthe, N.; Dard, M.; Baquey, C., Cyclo-(DfKRG) peptide grafting onto Ti-6Al-4V: physical characterization and interest towards human osteoprogenitor cells adhesion. *Biomaterials* 2004, 25, (19), 4837-4846.

138. Murray, N. G. D.; Dunand, D. C., Effect of thermal history on the superplastic expansion of argon-filled pores in titanium: Part I kinetics and microstructure. *Acta Mater* 2004, 52, (8), 2269-2278.

139. Allen, R.; Eisenberg, S.; Gray, M., *Tissue engineering methods and protocols*. Humana Press: Totowa, NJ, USA, 1999; p xvi, 629.

140. Kim, Y. J.; Sah, R. L. Y.; Doong, J. Y. H.; Grodzinsky, A. J., Fluorometric Assay of DNA in Cartilage Explants Using Hoechst-33258. *Analytical Biochemistry* 1988, 174, (1), 168-176.

141. Kearns, M.; Blenkinsop, P.; Barber, A.; Farthing, T., *Metals and Materials* 1987, 3, (2), 85.

142. Schwartz, D. S.; Shih, D. S.; Lederich, R. J.; Martin, R. L.; Deuser, D. A., Development and Sacle-up of the low density core process for Ti-64. *Mat. Res. Soc. Symp. Proc.* 1998, 521, 225-230.

143. Gibson, L. J.; Ashby, M. F., *Cellular solids*. 2nd edition ed.; Cambridge University Press: Cambridge, 1997; p 429-450.

144. Itala, A. I.; Ylanen, H. O.; Ekholm, C.; Karlsson, K. H.; Aro, H. T., Pore diameter of more than 100 mu m is not requisite for bone ingrowth in rabbits. *J Biomed Mater Res* 2001, 58, (6), 679-683.

145. Emans, N.; Biwersi, J.; Verkman, A. S., Imaging of Endosome Fusion in Bhk Fibroblasts Based on a Novel Fluorometric Avidin-Biotin Binding Assay. *Biophysical Journal* 1995, 69, (2), 716-728.

146. Green, N. M., Avidin. *Adv Protein Chem* 1975, 29, 85-133.

147. Nicol, F.; Nir, S.; Szoka, F. C., Orientation of the pore-forming peptide GALA in POPC vesicles determined by a BODIPY-avidin/biotin binding assay. *Biophysical Journal* 1999, 76, (4), 2121-2141.

148. Singh, R.; Dahotre, N. B., Corrosion degradation and prevention by surface modification of biometallic materials. *J Mater Sci Mater Med* 2007, 18, (5), 725-751.

149. Kienapfel, H.; Sprey, C.; Wilke, A.; Griss, P., Implant fixation by bone ingrowth. *J Arthroplasty* 1999, 14, (3), 355-368.

150. Morra, M., Biochemical modification of titanium surfaces: peptides and ECM proteins. *Eur Cell Mater* 2006, 12, 1-15.

151. Boyan, B. D.; Lohmann, C. H.; Dean, D. D.; Sylvia, V. L.; Cochran, D. L.; Schwartz, Z., Mechanisms involved in osteoblast response to implant surface morphology. *Annu Rev Mater Res* 2001, 31, 357-371.

152. Toworfe, G. K.; Composto, R. J.; Shapiro, I. M.; Ducheyne, P., Nucleation and growth of calcium phosphate on amine-, carboxyl- and hydroxyl-silane self-assembled monolayers. *Biomaterials* 2006, 27, (4), 631-642.

153. Campbell, A. A.; Fryxell, G. E.; Linehan, J. C.; Graff, G. L., Surface-induced mineralization: A new method for producing calcium phosphate coatings. *J Biomed Mater Res* 1996, 32, (1), 111-118.

154. Spoerke, E. D.; Stupp, S. I., Colonization of organoapatite-titanium mesh by preosteoblastic cells. *J Biomed Mater Res A* 2003, 67, (3), 960-9.

155. Ong, J. L.; Chan, D. C., Hydroxyapatite and their use as coatings in dental implants: a review. *Crit Rev Biomed Eng* 2000, 28, (5-6), 667-707.

156. Garcia, A. J., Get a grip: integrins in cell-biomaterial interactions. *Biomaterials* 2005, 26, (36), 7525-7529.

157. Sargeant, T. D.; Guler, M. O.; Oppenheimer, S. M.; Mata, A.; Satcher, R. L.; Dunand, D. C.; Stupp, S. I., Hybrid bone implants: Self-assembly of peptide amphiphile nanofibers within porous titanium. *Biomaterials* 2008, 29, (2), 161-71.

158. Spoerke, E. D.; Murray, N. G.; Li, H.; Brinson, L. C.; Dunand, D. C.; Stupp, S. I., A bioactive titanium foam scaffold for bone repair. *Acta Biomater* 2005, 1, (5), 523-33.

159. St-Pierre, J. P.; Gauthier, M.; Lefebvre, L. P.; Tabrizian, M., Three-dimensional growth of differentiating MC3T3-E1 pre-osteoblasts on porous titanium scaffolds. *Biomaterials* 2005, 26, (35), 7319-7328.

160. Maheshwari, G.; Brown, G.; Lauffenburger, D. A.; Wells, A.; Griffith, L. G., Cell adhesion and motility depend on nanoscale RGD clustering. *J Cell Sci* 2000, 113, (10), 1677-1686.

161. Bobyn, J. D.; Pilliar, R. M.; Cameron, H. U.; Weatherly, G. C., The Optimum Pore-Size for the Fixation of Porous-Surfaced Metal Implants by the Ingrowth of Bone. *Clin Orthop Relat Res* 1980, (150), 263-270.

162. Aubin, J. E.; Liu, F.; Malaval, L.; Gupta, A. K., Osteoblast and Chondroblast Differentiation. *Bone* 1995, 17, (2), S77-S83.

163. Lian, J. B.; Stein, G. S., Concepts of Osteoblast Growth and Differentiation - Basis for Modulation of Bone Cell-Development and Tissue Formation. *Crit Rev Oral Biol Med* 1992, 3, (3), 269-305.

164. Liu, F.; Malaval, L.; Gupta, A. K.; Aubin, J. E., Simultaneous Detection of Multiple Bone-Related Messenger-Rnas and Protein Expression During Osteoblast Differentiation - Polymerase Chain-Reaction and Immunocytochemical Studies at the Single-Cell Level. *Dev Biol* 1994, 166, (1), 220-234.

165. Frosch, K. H.; Barvencik, F.; Lohmann, C. H.; Viereck, V.; Siggelkow, H.; Breme, J.; Dresing, K.; Sturmer, K. M., Migration, matrix production and lamellar bone formation of human osteoblast-like cells in porous titanium implants. *Cells Tissues Organs* 2002, 170, (4), 214-227.

166. Frosch, K. H.; Barvencik, F.; Viereck, V.; Lohmann, C. H.; Dresing, K.; Breme, J.; Brunner, E.; Sturmer, K. M., Growth behavior, matrix production, and gene expression of human osteoblasts in defined cylindrical titanium channels. *J Biomed Mater Res* 2004, 68A, (2), 325-334.

167. Otsuki, B.; Takemoto, M.; Fujibayashi, S.; Neo, M.; Kokubo, T.; Nakamura, T., Pore throat size and connectivity determine bone and tissue ingrowth into porous implants: Three-dimensional micro-CT based structural analyses of porous bioactive titanium implants. *Biomaterials* 2006, 27, (35), 5892-5900.

168. Morra, M.; Cassinelli, C.; Cascardo, G.; Mazzucco, L.; Borzini, P.; Fini, M.; Giavaresi, G.; Giardino, R., Collagen I-coated titanium surfaces: mesenchymal cell adhesion and in vivo evaluation in trabecular bone implants. *Journal of Biomedical Materials Research Part A* 2006, 78A, (3), 449-458.

169. Yi, J. H.; Bernard, C.; Variola, F.; Zalzal, S. F.; Wuest, J. D.; Rosei, F.; Nanci, A., Characterization of a bioactive nanotextured surface created by controlled chemical oxidation of titanium. *Surface Science* 2006, 600, (19), 4613-4621.

170. Chunming, Z.; Erlin, Z.; Songyan, Z., Porous titanium by fiber sintering and its biomimetic Ca-P coating. *Rare Metal Materials and Engineering* 2007, 36, (8), 1394-1397.

171. Li, J. P.; Habibovic, P.; Yuan, H. P.; van den Doel, M.; Wilson, C. E.; de Wijn, J. R.; van Blitterswijk, C. A.; de Groot, K., Biological performance in goats of a porous titanium alloy-biphasic calcium phosphate composite. *Biomaterials* 2007, 28, (29), 4209-4218.

172. Duncan, R. L.; Turner, C. H., Mechanotransduction and the Functional-Response of Bone to Mechanical Strain. *Calcified Tissue International* 1995, 57, (5), 344-358.

173. Kim, B. S.; Nikolovski, J.; Bonadio, J.; Mooney, D. J., Cyclic mechanical strain regulates the development of engineered smooth muscle tissue. *Nature Biotechnology* 1999, 17, (10), 979-983.

174. Matsumoto, T.; Yung, Y. C.; Fischbach, C.; Kong, H. J.; Nakaoka, R.; Mooney, D. J., Mechanical strain regulates endothelial cell patterning in vitro. *Tissue Engineering* 2007, 13, (1), 207-217.

175. Singh, S. P.; Chang, E. I.; Gossain, A. K.; Mehara, B. J.; Galiano, R. D.; Jensen, J.; Longaker, M. T.; Gurtner, G. C.; Saadeh, P. B., Cyclic mechanical strain increases production of regulators of bone healing in cultured murine osteoblasts. *Journal of the American College of Surgeons* 2007, 204, (3), 426-434.

176. Sumanasinghe, R. D.; Bernacki, S. H.; Loboa, E. G., Osteogenic differentiation of human mesenchymal stem cells in collagen matrices: Effect of uniaxial cyclic tensile strain on bone morphogenetic protein (BMP-2) mRNA expression. *Tissue Engineering* 2006, 12, (12), 3459-3465.

177. De Smet, E.; Jaecques, S. V. N.; Jansen, J. J.; Walboomers, F.; Sloten, J. V.; Naert, I. E., Effect of constant strain rate, composed of varying amplitude and frequency, of early loading on peri-implant bone (re)modelling. *Journal of Clinical Periodontology* 2007, 34, (7), 618-624.

178. Frenkel, S.; Singh, I. J., The Effects of Fibroblast Growth Factor on Osteogenesis in the Chick Embryo. In *Fundamentals of bone growth : methodology and applications : proceedings of the third international conference, held at the University of California Center for Health Sciences, Los Angeles, California, January 3-5, 1990*, Dixon, A. D.; Sarnat, B. G.; Hoyte, D. A. N., Eds. CRC Press: Boca Raton, 1991; pp xxiv, 626.

179. Horton, M. A.; Townsend, P.; Nesbitt, S., Cell Surface Attachment Molecules in Bone. In *Principles of bone biology*, Bilezikian, J. P.; Raisz, L. G.; Rodan, G. A., Eds. Academic Press: San Diego, 1996; pp xx, 1398.

# APPENDIX A: PROTOCOLS FOR BIOLOGICAL ASSAYS

There are many procedures, protocols, and techniques that are ubiquitous throughout given areas of science, and yet the particulars of a given method are commonly quite different. This is in part due to the fact that there is often some room for variation without affecting the results, and in part because they are optimized for a given application or system. Concerning the latter, scientific protocols often become more of an art. However, as this is the realm of science, we desire to establish experiments that lead to reproducible results. Consequently, the author has included some of the more elaborate or detailed protocols used in this thesis that were successfully used in the work described herein.

**List of Protocols:**

A.1 Making PA Bubble Gels with Cells ..... 201
A.2 PicoGreen Cell Quantification Assay ..... 202
A.3 PA Gel and Cell Preparation for SEM ..... 203
A.4 Immunohistochemical Staining ..... 204
A.5 Purification of RNA and Reverse Transcription for QRT-PCR ..... 205

## *A.1 Making PA Bubble Gels with Cells*

Several methods to create bubble gels with encapsulated cells have been shown to work well. The following is the preferred method of the author:

1. Make Sterile PA Solution in Hood
   - Solubilize PA with nanopure $H_2O$ at slightly greater than twice final desired concentration (ie. >20 mM)
   - Adjust pH ~ neutral with 1 M NaOH (usually a few μLs)
   - Top up with nanopure $H_2O$ to twice final concentration (ie 20 mM)
   - Sterilize PA solution with UV light (in hood, 20-25 minutes)
   - Mix PAs accordingly (if necessary)
2. Prepare Cells
   (Note: in order to trigger self-assembly, medium must contain sufficient multivalent ions. For net negatively charged PAs, I use 20 mM $CaCl_2$ supplement)
   - Trypsinize cells
   - Add medium to stop activity of trypsin
   - Spin down and remove supernatant
   - Resuspend cells in small amount (1 mL) of medium and count a sample
   - Figure out how many mLs needed to give # of cells desired
   - Take this amount of cells and add medium to give twice final concentration of cells
3. Make Bubble Gels
   - Aliquot 50 μL PA solution into each well of round bottom 96-well plate
   - Aliquot 50 μL cell suspension into the PA solution, slowly expelling PA as you swirl upwards, finishing at the top center of the bubble
   - Place in incubator to complete gelation (30-60 minutes)
   - Add 200 μL medium to each well and return to incubator for culture

Note: if no cells are to be encapsulated, the same procedure can be used with the exception of using medium without cells. Alternatively, sterile PA solution slightly above final concentration can be made and gelled with the addition of concentrated $CaCl_2$ (say 6 μL 1 M $CaCl_2$).

## *A.2 PicoGreen Cell Quantification Assay*

The following cell digestion protocol is based on work by Allen et al.[139].

Harvest samples:

- Scoop out PA gel with cells and place in a screw-top cryovial
- Put cryovial in -20˚C freezer until assay is to be performed
- When ready to do PicoGreen Assay, lyophilize day before

**Day 1**

- Make digestion solution
  - PBE solution (1L)
    - 14.20g $Na_2HPO_4$ (0.100M)
    - 3.36g $Na_2EDTA$ (0.010M)
    - Add to 1.0L demineralized water
    - Adjust pH to 6.5 with 1N NaOH
    - Autoclave-sterilize
    - Store at 2-6˚C
  - Digestion solution (100mL)
    - 176mg cysteine
    - Dissolve in small volume of PBE (1-10% final vol.)
    - Sterilize through 0.22µm syringe filter
    - Bring up volume to 100mL with PBE
    - Add room temperature papain to 0.125mg/mL (Sigma is 25mg/mL, so add 0.5mL)
- Add 150µL digestion solution per sample in eppindorf tube
- Place in water bath for 16 hours overnight, *vortexing periodically* at 60˚C

**Day 2**

- Make solutions before digestion completed
  - 1X TE solution (20mL)
    - Add 1mL 20X TE to 19mL milliQ water
  - Working solution (20mL final volume, made right before assay)
    - Add 75µL Quant-iT PG dsDNA reagent to 14.925ml TE *in plastic* container out of light
  - 2µg/mL stock solution of dsDNA in TE
    - Add 16µL 100µg/mL lambda DNA to 784µL TE for 2µg/mL stock
    - Take 5µL 2µg/mL stock into 195µL TE for 50ng/mL stock
    - Prepare standards
- Perform assaying according to PicoGreen Kit protocol
- Read on plate reader (ex. 480nm, em. 520nm)

## *A.3 PA Gel and Cell Preparation for SEM*

**Day 1**

*Prefixation:*

- Add cold (4°C) fixative (1% glutaraldehyde in MEM-α w/o FBS) to samples on ice for 1 hour
- Remove prefixative and wash once with PBS for 20 minutes

*Fixation:*

- Add Karnovsky fixative (2% formaldehyde, 2% glutaraldehyde in Cacodilate buffer) at room temperature for a few hours and then overnight in fridge
    - For 10ml, take 2.5ml 8% glut., 5ml 0.2M Caco., and 0.8g paraform. in 2.5ml milliQ $H_2O$, heating paraform. Up to 60-70°C to dissolve and letting cool to room temperature before mixing with other ingredients.

**Estimated Time:** 2 hours, then a few minutes after 3 more hours

**Day 2**

- Wash with Caco buffer twice for 20 minutes

*Staining*

- Stain w/ 1% $OsO_4$ in Caco @ room temp. 1 hour
- Wash with caco buffer 10 mins. and 2x10 mins. $H_2O$

*Dehydrating*

- Dehydrate w/ EtOH 20, 50, 70 (***can store 1 week here***), 95, 100% 2x10 mins.
- Critical point dry
- Coat w/ 3nm Au-Pd

**Estimated Time:** 4.5 hours if stopping at 70% EtOH, 40 more plus CPD and Au-Pd coating after that.

## *A.4 Immunohistochemical Staining*

Solutions To Make:

- Washing Buffer: 0.1% BSA in PBS
- Peroxidase blocking solution: 1 part 30% hydrogen peroxidase, 9 parts methanol.

*Start with crysectioned samples on glass slides*

***Before staining, air dry slides at room temperature for 30 minutes and fix in ice-cold acetone for 5 minutes. Air-dry another 30 minutes.***

1. Rinse sections in 2 changes of **washing buffer**, 2 minutes each
2. **Peroxidase Blocking:** incubate sections in **peroxidase blocking solution** for 10 minutes to block endogenous peroxidase activity.
3. Rinse sections in 2 changes of **washing buffer**, 2 minutes each
4. **Serum Blocking**: incubate sections with **serum block solution (Reagent A)** for 10 minutes to block non-specific binding of immunoglobulin. DO NOT RINSE.
5. **Primary Antibody:** incubate sections with Mouse anti-OP or –ALP overnight.
   a. Mouse anti-OP (1:50)
   b. Mouse anti-ALP (1:50)
6. Rinse in **washing buffer** for 2 x 2 mins.
7. **Secondary antibody:** incubate sections with biotinylated anti-mouse secondary antibody **(Reagent B)** for 10 minutes at room temperature.
8. Rinse in **washing buffer** for 3 x 2 mins.
9. **Detection:** incubate sections with HRP-Streptavidin diluted in HRP-streptavidin dilution buffer **(Reagent C)** for 30 minutes at room temperature.
10. Rinse in washing buffer for 3 x 2 mins.
11. **Chromogen/Substrate:** incubate sections in DAB peroxidase substrate solution for 5-10 minutes.
12. Rinse in distilled water briefly.
13. **Counterstain** with Gill's hematoxylin solution or Mayer's hematoxylin solution if desired.
14. Rinse in running tap water for 5 minutes.
15. Dehydrate in 95% ethanol for 2 minutes, 100% ethanol 2 x 3 minutes
16. Clear in xylene for 2 x 3 mins.
17. Coverslip with permanent mounting medium.

## *A.5 Purification of RNA and Reverse Transcription for QRT-PCR*

***Purification of RNA from cells in PA gels:***

- Spin down cells and PA in eppendorf tube (500 x g, 5min at 2500 rpm on microcentrifuge)
- Remove as much supernatant as possible
- Vortex, add 1 mL Trizol, incubate at RT for 5 min.
- Vortex, incubate 5 min
- Add 200 µL chloroform, shake 15 seconds by hand
- Spin at 12,000 x g (13,200 rpm (max.) on microcentrifuge) for 15 min. at 4 ˚C
- Remove supernatant/aqueous phase into a new eppendorf tube *with secure top* (~500 µL/ tube)—Be very careful not to disturb the interphase (white opaque film between the clear upper aqueous phase and the pink phenol phase)
- Add equal volume of isopropanol (500 µL) and 2 µL glycogen per tube, mix, incubate at RT for 10 min.
- Spin at 12,000 x g (13,200 rpm (max.) on microcentrifuge) for 10 min. at 4 ˚C
- Wash pellet once with 200 µL 75% EtOH
- Spin at 12,000 x g (13,200 rpm (max.) on microcentrifuge) for 5 min. at 4 ˚C
- Remove all liquid
- Dry the RNA pellet until pellet turns clear (not completely dry), add 20 µL of DEPC-water to dissolve the RNA pellet
- Store the isolated RNA at -80 ˚C
- For long term storage: add 20 µL of 3 M NaOAc (pH = 5.2) and 500 µL of 100% EtOH, then store at -80 ˚C

***Reverse Transcription—Formation of cDNA:***

To the 20 µL of resuspended RNA (from above):

- Add 2.5 µL dNTP (10mM) and 2.5 µL Hexamer (50 ng/µL)
- 65 ˚C for 5 minutes
- 0 ˚C for 1 minute, mix, centrifuge
- Add:
    - 5 µL 10xRT buffer,
    - 10 µL 25mM $MgCl_2$
    - 5 µL 0.1M DTT
    - 2.5 µL RNase Out

    Can mix these first 4 solutions and add 22.5 µL of mix per tube before adding Superscript

    - 2.5 µL Superscript
- 10 minutes at 25 ˚C
- 50 minutes at 50 ˚C
- 5 minutes at 85 ˚C
- 2.5 µL RNase H at 37 ˚C for 20 minutes

Samples are ready for PCR

# APPENDIX B: RAW DATA FROM *IN VIVO* STUDIES

Due to the large variations associated with biological data, the raw data from the histological quantification of the bare Ti foam and PA-Ti hybrid *in vivo* samples are included in this appendix. All data are quantification of grey-scaled images using ImageJ to set thresholds.

**Table B.1 Total new bone formation**

| | 2 Weeks Top 2 | | | | 4 Weeks Top 2 | | |
|---|---|---|---|---|---|---|---|
| | Bare Ti | S/RGDS Hybrid | S(P)/RGDS Hybrid | | Bare Ti | S/RGDS Hybrid | S(P)/RGDS Hybrid |
| | 772,765 | 1,076,986 | 879,120 | | 699,708 | 524,095 | 936,953 |
| | 632,180 | 917,466 | 979,827 | | 734,444 | 921,373 | 828,793 |
| | 887,022 | 1,078,799 | 791,631 | | 633,860 | 770,935 | 803,145 |
| | 621,237 | 994,503 | 623,458 | | 486,994 | 711,855 | 553,410 |
| | 968,127 | 974,218 | 838,241 | | 454,705 | 489,214 | 539,379 |
| **avg.** | **776,266** | **1,008,394** | **822,456** | | | 524,927 | 528,157 |
| **stdev.** | **153,203** | **69,445** | **131,126** | **avg.** | **601,942** | **657,067** | **698,306** |
| **95% CI** | **134,286** | **60,870** | **114,935** | **stdev.** | **125,524** | **172,709** | **178,982** |
| | | | | **95% CI** | **110,025** | **151,383** | **156,882** |

| | 2 Weeks Top 1 | | | | 4 Weeks Top 1 | | |
|---|---|---|---|---|---|---|---|
| | Bare Ti | S/RGDS Hybrid | S(P)/RGDS Hybrid | | Bare Ti | S/RGDS Hybrid | S(P)/RGDS Hybrid |
| | 844,872 | 1,213,101 | 1,114,810 | | 909,310 | 526,274 | 1,098,041 |
| | 710,093 | 1,018,938 | 1,362,779 | | 755,927 | 1,187,922 | 876,427 |
| | 947,890 | 1,151,694 | 882,748 | | 797,449 | 797,022 | 844,692 |
| | 641,564 | 994,503 | 727,335 | | 499,421 | 964,324 | 704,005 |
| | 1,187,328 | 1,158,378 | 861,782 | | 566,518 | 506,921 | 585,994 |
| **avg.** | **866,350** | **1,107,323** | **989,891** | | | 809,648 | 560,083 |
| **stdev.** | **215,106** | **95,269** | **250,738** | **avg.** | **705,725** | **798,685** | **778,207** |
| **95% CI** | **188,545** | **83,505** | **219,777** | **stdev.** | **169,056** | **260,153** | **203,170** |
| | | | | **95% CI** | **148,182** | **208,162** | **162,567** |

Top 2 = the 2 slides per implant with the most amount of new bone.

Top 1 = the slide per implant with the most amount of new bone.

The data shown are the number of pixels counted.

**Table B.2 Total mineralized tissue formed within the porous implant**

| | 2 Weeks Ingrowth | | | | 4 Weeks Ingrowth | | |
|---|---|---|---|---|---|---|---|
| | Bare Ti | S/RGDS Hybrid | S(P)/RGDS Hybrid | | Bare Ti | S/RGDS Hybrid | S(P)/RGDS Hybrid |
| | 0.602 | 0.723 | 0.600 | | 0.598 | 0.566 | 0.590 |
| | 0.533 | 0.678 | 0.586 | | 0.735 | 0.431 | 0.676 |
| | 0.613 | 0.667 | 0.618 | | 0.598 | 0.784 | 0.713 |
| | 0.647 | 0.772 | 0.564 | | 0.767 | 0.681 | 0.597 |
| | 0.726 | 0.826 | 0.737 | | 0.557 | 0.661 | 0.757 |
| **avg.** | **0.624** | **0.733** | **0.621** | | | 0.675 | 0.659 |
| **stdev.** | **0.071** | **0.067** | **0.068** | **avg.** | **0.651** | **0.633** | **0.665** |
| **95% CI** | **0.062** | **0.058** | **0.059** | **stdev.** | **0.094** | **0.121** | **0.065** |
| | | | | **95% CI** | **0.082** | **0.106** | **0.057** |

Data shown as fraction of porosity visible filled with tissue.

**Table B.3 Total bone formed immediately adjacent to implant from cortical bone**

| | 2 Weeks Rim Formation | | | | 4 Weeks Rim Formation | | |
|---|---|---|---|---|---|---|---|
| | Bare Ti | S/RGDS Hybrid | S(P)/RGDS Hybrid | | Bare Ti | S/RGDS Hybrid | S(P)/RGDS Hybrid |
| | 0.636 | 0.623 | 0.361 | | 0.679 | 0.770 | 0.537 |
| | 0.548 | 0.657 | 0.613 | | 0.627 | 0.642 | 0.727 |
| | 0.643 | 0.690 | 0.662 | | 0.830 | 0.750 | 0.860 |
| | 0.585 | 0.916 | 0.410 | | 0.479 | 0.662 | 0.597 |
| | **0.677** | **0.822** | **0.765** | | | 0.888 | 0.749 |
| **avg.** | **0.618** | **0.742** | **0.562** | | | **0.745** | **0.849** |
| **stdev.** | **0.051** | **0.123** | **0.171** | **avg.** | **0.654** | **0.743** | **0.720** |
| **95% CI** | **0.045** | **0.108** | **0.150** | **stdev.** | **0.145** | **0.088** | **0.131** |
| | | | | **95% CI** | **0.127** | **0.070** | **0.105** |

Data shown as fraction of porosity visible filled with tissue.

# VITA

Timothy David Sargeant was born on February 17th, 1979 to David and Diane Sargeant in North York, Ontario, Canada. He was raised, along with his sister Amanda, in Brampton, Ontario, Canada, and then in Moody, British Columbia, Canada. Tim attended Port Moody Senior Secondary School and graduated with Honours in 1997.

Tim then attended The University of British Columbia in Vancouver, British Columbia, and entered the Department of Metals and Materials Engineering in his second year. During his time at The University of British Columbia, Tim was an active student-athlete, playing first on the Varsity Hockey team, and later joining the Varsity Rowing program for 2 years. Tim also participated in the Engineering Co-op program, working for 8 months at the National Research Council of Canada in the Tribology Group in Vancouver, BC; then 3 months at the University of Maryland in the Materials Science & Engineering department Summer Undergraduate Research Fellowship in College Park, Maryland; and finally 8 months at SMI-Texas Steel Mill in the Melt Shop in Seguin, Texas. Tim completed his Bachelor of Applied Science in Metals and Materials Engineering on the Dean's list in 2002.

In September 2002, Tim began his graduate studies at Northwestern University in the Department of Materials Science & Engineering in Evanston, Illinois, USA. He joined the research group of Prof. Samuel I. Stupp and worked in the area of self-assembling nanomaterials for biomedical applications. Tim has presented his work at the iBIO IndEx (Feb. 2007) and the Society for Biomaterials (Apr. 2007) with Honorable Mention. After completing his degree, Tim intends to enter the biomedical industry and work in research and development.